Semiconductor Disk Laser Pumped Cr^{2+}:Chalcogenide Lasers

Nils Hempler

A thesis presented in fulfilment
of the requirements for the degree of
Doctor of Philosophy
to the University of Strathclyde, Department of Physics

2010

Copyright

This thesis is the result of the author's original research. It has been composed by the author and has not been previously submitted for examination which has led to the award of a degree.

The copyright of this thesis belongs to the author under the terms of the United Kingdom Copyright Acts as qualified by University of Strathclyde Regulation 3.50. Due acknowledgement must always be made of the use of any material contained in, or derived from, this thesis.

Signed: N. Hempler Date: 19/12/2010

To Aleksandra

Abstract

Divalent chromium-doped chalcogenides have become an established material for mid infrared (2-3 μm) laser sources. They provide the potential for multi-Watt output powers and ultrashort pulses over a very wide tuning range of around 1 μm in the shortwave mid-infrared waveband. Furthermore, with an absorption band between 1.5-2.0 μm, various types of laser source can be exploited as pump sources.

In this work, the semiconductor disk laser (SDL) has been investigated as a novel pump source for chromium:chalcogenide lasers. For this, GaSb-based SDLs emitting at 1.9 and 2.0 μm SDLs were developed. In continuous-wave (cw) operation output powers of up to 6 W were obtained from the 2.0 μm SDL resulting in 1.8 W of 2.5 μm radiation from a Cr^{2+}:ZnSe laser. The results of this system were compared to a 1.9 μm SDL-pumped Cr^{2+}:ZnSe laser and a Tm^{3+}:$YAlO_3$ laser - a more conventional pump source for Cr^{2+}:chalcogenide laser. Particular emphasis was put on the respective intensity noise properties of these systems.

To investigate the pulsed operation of Cr^{2+}:II-VI lasers, an SDL chip designed for 2.3 μm was used as a controllable saturable absorber to passively Q-switch a Cr^{2+}:ZnSe laser. In this way, Q-switched operation was achieved with a pulse duration of ~90 ns. By pumping the saturable absorber, state switching between cw and Q-switched operation was achieved with a transitional time constant of ~50 μs.

The use of pulsed-pumped SDLs as a pump source for gain-switched Cr^{2+}:ZnSe laser embodiments was also investigated. Here, 1.9 and 2.0 μm SDLs were pumped with low-cost pulsed diode lasers emitting up to 75 W of on-time power with nominal pulse duration of up to 200 ns. The resulting SDL pulses showed a spectral shift over the pulse duration, and this was investigated in detail and underlined using thermal finite element analysis. Using the 1.9 μm SDL having an on-time power of 20 W, a gain-switched Cr^{2+}:ZnSe laser was demonstrated. The results of this study were compared to a numerical model and used to investigate the potential of this novel system.

Acknowledgements

This dissertation would not have been possible without the guidance and the help of a number of individuals who in one way or another contributed and extended their valuable assistance in the preparation and completion of this study.

First and foremost, my utmost gratitude to my supervisor Dr. David Burns whose encouragement, guidance and support helped me find my way to completing this work. The countless hours of working together in the lab and fruitful lunch time discussions were of indispensable value.

I would also like to thank Dr. John-Mark Hopkins for all his help and more so for being a good friend. His scientific as well as personal guidance along the way is something I will never forget.

Furthermore, my special thanks to Dr. Alan Kemp who significantly contributed to the modelling sections of this work and who was kind enough to correct the first draft of this thesis.

Dr. Walter Lubeigt for being the best lab-mate one can wish for. His willingness to keep up with days and days in the darkness and never ending hours of *traditional* German music are much appreciated.

In addition, I would like to thank Dr. Alexander MacLean, Dr. Stephane Calvez and Dr. Nicolas Laurand for all the discussions and advice along the way.

Paul Hynd and Lisa Muir, our technicians, for all always being particularly fast with manufacturing all those little bits I required.

Last but not least, I would like to express particular gratitude to my parents and my girlfriend who always supported me throughout the years and who were the backbone of the success of this work.

Table of Contents

Chapter One

Chapter Two

Chapter Three

Chapter Four

Chapter Five

Chapter Six

Chapter Seven

Chapter One

Introduction

1.1 Introduction

For a long time the visible and near infrared were the main areas of interest for application-focused laser development. Even though the short-wave mid-infrared wavelength band in the range of 2-5 µm is potentially a better alternative for some of these applications, the limited availability of detectors, and moreover, laser sources in this spectral region favoured the use of shorter wavelength laser sources due to their maturity and superior practicality. However, with advances in detectors [1,2] and the ongoing development of laser sources in the short-wave mid-infrared (mid-IR), this wavelength band is becoming increasingly important. The challenge to harnessing and fully exploiting the mid-IR spectral region is to develop laser systems that meet the demands of applications.

In this chapter, an introduction to mid-IR laser sources is given. After a brief definition of the term *mid-infrared*, the advantages and disadvantages of the most common coherent light sources for this waveband are discussed. Finally, the divalent chromium-doped chalcogenide materials in particular are discussed with emphasis on the pump sources used for these systems.

1.2 The mid-infrared wavelength band

The limits of the mid-IR band are somewhat ill-defined but in the context of this work, the term mid-IR is used to refer to the region between 2-5 µm. This range of the spectrum is of particular interest for spectroscopic applications as many molecules have fundamental vibrational absorption resonances in this wavelength band. As a consequence, the mid-IR is often referred to as the *molecular fingerprint region*. Figure 1.1 shows a subset of the spectral absorption line data (for a threshold spectral line intensity of $1*10^{-25}$ $cm^{-1}/(mol\cdot cm^{-2})$ [3]) obtained from the HITRAN 2008 database between 0.17 to 5 µm [4]. The plot was generated using Spectralcalc, a convenient browsing solution for the HITRAN database [5], rather than the more typical JAVAHAWKS platform. Above ~2 µm the number of molecular absorption lines significantly increases and includes compounds such as methane and carbon dioxide.

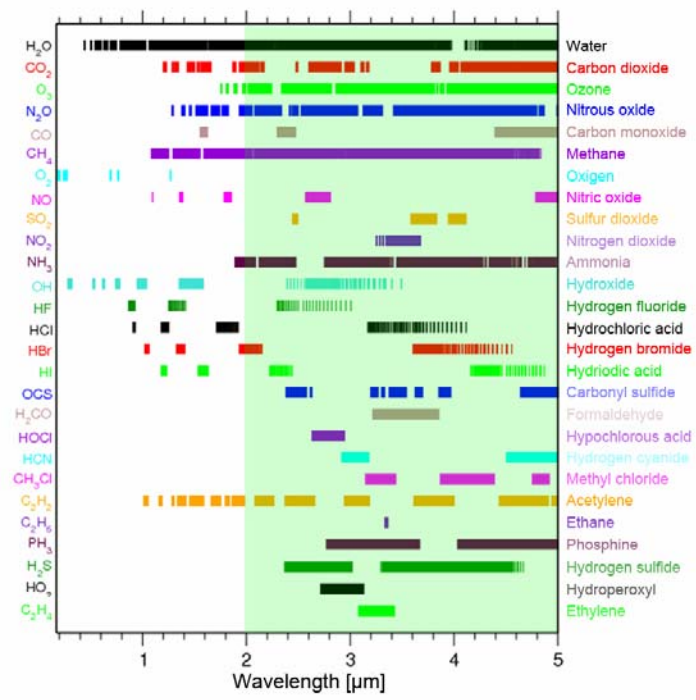

Figure 1.1 Subset of the line position data for various molecules between 0.17-5 µm, obtained from the HITRAN 2008 database. For a threshold spectral line intensity of $1 \cdot 10^{-25}$ cm^{-1}/(mol·cm^{-2}).

But it is not only the absorption of target molecules that is important for applications but also the presence of water transmission windows [6]. When considering free space communication for example, the reduced water absorption is mandatory as this allows longer transmission ranges. To visualise this, the line position data for water between 0.17 and 5 µm for an intensity threshold of $1 \cdot 10^{-22}$ cm^{-1}/(mol·cm^{-2}) is plotted in Figure 1.2. One can argue that there are multiple water transmission windows in the near infrared; however, the advantage of the mid-IR region is that it combines these windows with the *eye-safe* properties of this range of wavelengths and the enhanced molecular absorptions discussed above.

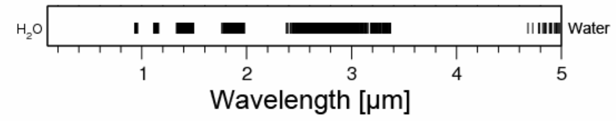

Figure 1.2 Line position data for water molecules between 0.17-5 µm for a threshold spectral line intensity of $1 \cdot 10^{-22}$ cm^{-1}/(mol·cm^{-2}).

1.3 Mid-infrared laser sources

This strong interest in mid-IR applications has resulted in the development of a variety of different approaches to create light sources in this wavelength range [7]. In this section, these various laser sources and their advantages and disadvantages will be discussed.

1.3.1 Gas lasers

The most important mid-IR gas lasers are the carbon monoxide (CO) and carbon dioxide (CO_2) lasers - the CO laser being of interest for the 2-5 μm band and the CO_2 laser operating at longer wavelengths [8,9]. In this type of laser, an electrical discharge is used to pump a gaseous gain medium (see Figure 1.3) [10]. The CO laser typically emits on a variety of lines between 5.0-6.0 μm. However, overtone emission has been demonstrated leading to line tuning between 2.6 and 3.9 μm on a total of 45 lines [11]. The advantage of these systems is mainly the relatively inexpensive active medium; hence large volumes of material can be used to obtain high powers. A major drawback, however, is the degradation of performance over time [12]. Besides this, the CO overtone laser specifically suffers from lower efficiencies (<5%).

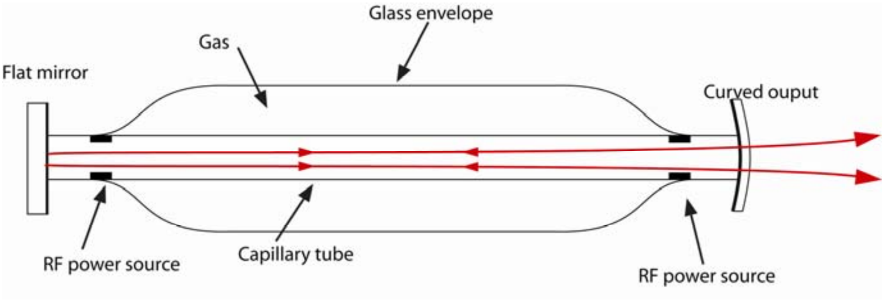

Figure 1.3 Schematic of a gas laser consisting of a gas filled capillary tube with mirrors at the end. The excitation is achieved via the RF power source contacts.

1.3.2 Semiconductor lasers

There are a promising number of semiconductor lasers that emit in the mid-infrared. The most important of which are quantum well and quantum cascade lasers.

Depending on the band-gap alignment, quantum well semiconductor lasers are termed type I or type II structures [7]. The quantum wells, providing carrier confinement and gain, are typically implemented in a waveguide layer that ensures that the light is constrained to the gain region of the device. Figure 1.4 shows a schematic of a type I and a type II quantum well laser.

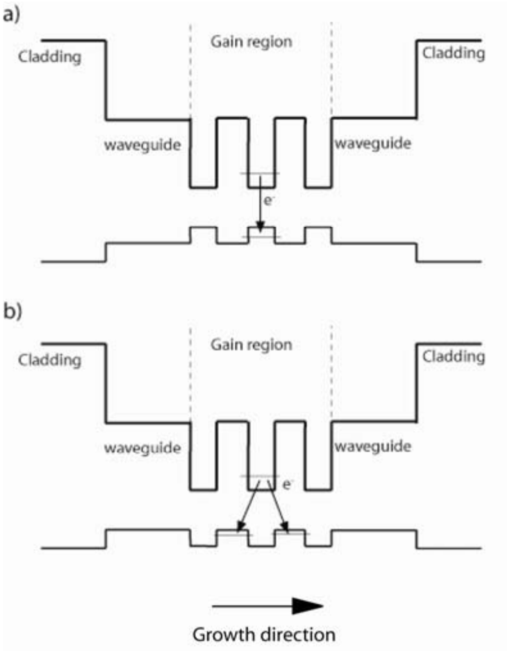

Figure 1.4 Structure of quantum well semiconductor lasers. a) type I configuration and b) type II configuration.

In type I designs, the transitions take place within one material layer between its valence and conduction bands (direct transition). The minimum possible photon energy (and so its wavelength) is therefore determined, to first order at least, by the band-gap of the material. In type II structures, transitions take place between the valence and conduction band of two adjacent layers, effectively separating electron and hole confining layers (indirect transition). Therefore, the wavelength of these devices is determined by the properties of two materials giving more design flexibility. When longer wavelengths are desired, type II structures are more suitable as the reduced hole confinement in type I structures leads to greatly reduced efficiency and poor thermal performance. Type II transitions are intrinsically less efficient than type I transitions, but represent a more effective solution for longer wavelength quantum well lasers [13].

Type I lasers, comprising antimonide or lead-salt based materials have been realised in various forms such as the semiconductor disk laser (SDL) format, Vertical Cavity Surface Emitting Lasers (VCSEL) and edge-emitting diode lasers.

Using type I and II structures, antimonide-based systems allow wavelength coverage between 1.9-4.0 µm [14-20], and with lead-salt based devices this range can be extended to 3-30 µm [21,22].

A second class of a semiconductor based mid-IR lasers are the so called quantum cascade or intersubband lasers (QCL) [23]. These lasers consist of many thin layers that vary (a)periodically in their material and thicknesses. By suitable design of these layers, multistage gain regions can be created. Gain in these devices does not arise due to carrier transitions between the conduction and valance band but through intersubband energy level transitions within this highly designed semiconductor structure. The figure below shows a simplified schematic of the function of a quantum cascade laser.

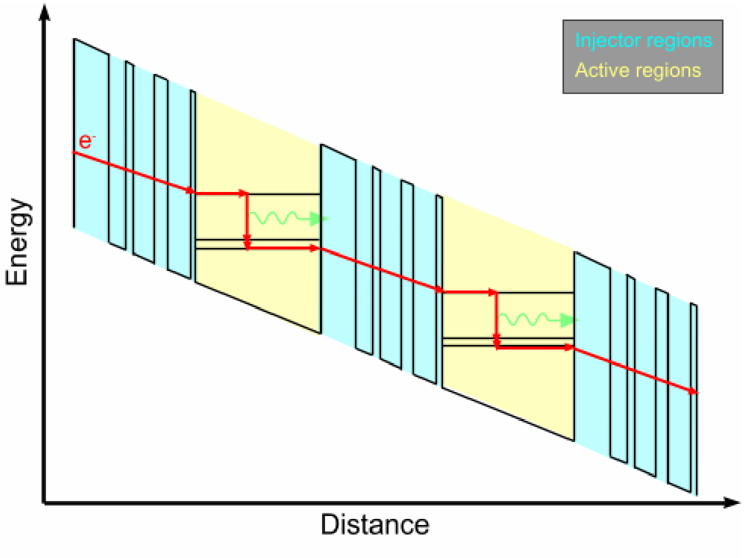

Figure 1.5 Simplified energy transition and tunnelling behaviour of a quantum cascade laser.

When an electrical field is applied to a QCL structure an electron undergoes a transition and can then *tunnel* through specially designed *injector regions* into the upper energy state of the next gain section and undergo a further optical transition. A major advantage of the QCL format is that the operational wavelength is mainly controlled by the design of the structure rather than the materials used. By varying the structure, emission from 150 µm down to 3 µm can be achieved [24-27]. Despite their excellent efficiency and wide wavelength coverage, QCLs have multiple drawbacks. The infrared power is usually limited to the mW range and they often require cryogenic cooling or operate in the pulsed regime. Additionally high performance operation below 5 μm is difficult.

Another potential drawback is the complex growth required for these structures [28]. Because of the high number of very thin layers that are required in a device, growth is time consuming and complex. Good repeatability is often difficult to achieve and very precise calibration of the growth is required.

On the whole, mid-IR semiconductor lasers offer great compactness and efficiency as well as the option of tailoring for specific wavelengths. However, despite these advantages, multiple drawbacks for many applications, such as low power, poor quality output beams and cryogenic cooling requirements remain in the 2-5 μm wavelength region.

1.3.3 Rare-earth

Another format of mid-IR laser sources are solid-state lasers incorporating rare-earth (lanthanide) active ions. These include ions such as Nd^{3+}, Yb^{3+}, Er^{3+}, Tm^{3+}, Ho^{3+}, Pr^{3+} and Ce^{3+} contained in crystalline or glass hosts such as garnets, vanadates and fluorides. High energy pulsed operation, ultra-short pulse generation and high output powers as well as moderate tuning (when typically used with glass hosts) are available from these sources.

The properties of these lasers are defined in the main by the properties of the active ion. This is because the electronic transitions occur in the f-shells of the ions. These orbitals are relatively strongly shielded against the influences of the surrounding lattice structure by the fully populated 5s and 5p shells. Therefore, the optical properties do not vary radically from host to host. This is only the case, however, when doped into crystalline structures. (The random ion orientations in glass hosts typically give rise to broader spectral features). Both types of hosts, glass and crystalline, can be advantageous: crystalline hosts often have superior thermal properties which promote power scaling; glass hosts typically provide broader tuning ranges.

The most widely used rare-earth transitions lie in the 1-2 μm band; however, some materials allow emission above this. For these lasers it is of particular importance that the host materials have low phonon energy to prevent multi-phonon relaxation from the upper laser level that would reduce the efficiency of such a laser. In recent years, a number of fibre and crystalline hosts have been investigated and an overview of these is given in Table 1.1.

Material	Max. Phonon Energy [cm^{-1}]	Transparency [μm]	References
Silica	1100	<2.5	[29]
ZBLAN	580	<6	[29]
GLS	425	<8	[30]
YAG	865	<5.5	[31,32]
PbGaS	324	<20	[33]
KPB	140	<20	[34,35]
RPB	140	<20	[34]

Table 1.1 Overview of common fibre and crystalline materials for mid-infrared lasers and their respective phonon energy cut-offs and infrared transparencies.

In the area of fibre lasers, Silica, ZBLAN (**Zr**F$_4$-**B**aF$_2$-**L**aF$_3$-**A**lF$_3$-**N**aF), and gallium lanthanum sulphide (GLS) fibres are of particular interest [29,30]. In addition, crystalline hosts such as lead-thiogallate (PbGaS) and the lead bromides (KBP and RGP) showed promise as low phonon hosts [33,34]. Incorporated into these and some of the more conventional hosts, various rare-earth dopants have shown emission in the mid-IR. An overview of these with their respective emission and main absorption wavelengths is given in Table 1.2 [33,36-40].

Active ion	λ-Emission [μm]	Transition	λ-Absorption [μm]	Laser action	Reference
Tm^{3+}	1.9	${}^{3}H_{4} \longrightarrow {}^{3}H_{6}$	0.79	yes	[36]
Tm^{3+}	2.3	${}^{3}F_{4} \longrightarrow {}^{3}H_{5}$	0.79	no	[36]
Tm^{3+}	3.8	${}^{3}H_{5} \longrightarrow {}^{3}H_{4}$	0.79	no	[36]
Er^{3+}	2.9	${}^{4}I_{11} \longrightarrow {}^{4}I_{13}$	0.98	yes	[37]
Ho^{3+}	2.1	${}^{5}I_{7} \longrightarrow {}^{5}I_{8}$	1.9	yes	[38]
Ho^{3+}	2.9	${}^{5}I_{6} \longrightarrow {}^{5}I_{7}$	1.9	no	[38]
Ho^{3+}	4.9	${}^{5}I_{4} \longrightarrow {}^{5}I_{5}$	1.9	no	[38]
Dy^{3+}	2.7	${}^{6}H_{13} \longrightarrow {}^{6}H_{15}$	1.3	yes	[39]
Dy	4.4	${}^{6}H_{11} \longrightarrow {}_{6}H_{13}$	1.3, 1.6	yes	[33]
Tb	4.8	${}^{7}F_{5} \longrightarrow {}^{7}F_{6}$	4.5	no	[36]
Pr	4.6	${}^{3}H_{5} \rightarrow {}^{3}H_{4}$	1.5	no	[40]

Table 1.2 Overview of various rare-earth ions for the generation of mid-infrared radiation and their emission wavelengths, energy transition and absorption.

The most commonly used dopants to date are thulium [36], holmium [38] and erbium [37] which emit at wavelengths between 1.9-3.0 μm but other rare-earth elements have also shown great promise. Dysprosium [33] and terbium [36] have gained interest due to their emission in the 4.x μm range and initial spectroscopic investigations have been carried out on praseodymium [40] emitting on its $^3H_5 \rightarrow {}^3H_4$ transition at 4.6 µm.

Despite the variety of ion/host combinations, only limited wavelength coverage is offered by each solution, with different material combinations required for different applications. In addition, the relative large quantum defect in many of these systems causes restrictions in power scaling.

1.3.4 Nonlinear conversion techniques

Given the applications-rich nature of the mid-IR, one particularly attractive feature of laser sources in this regime is broad tunability. As few laser sources offer this directly, frequency conversion in nonlinear optical materials has become a powerful tool. The typically used second-order nonlinear effects are shown Figure 1.6.

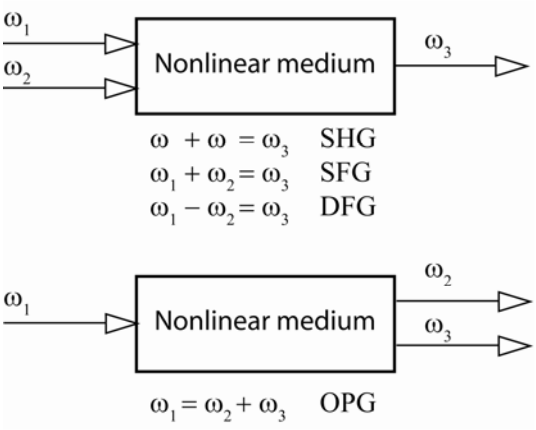

Figure 1.6 Some of the possible interactions of light within a nonlinear medium.

The processes that can take place include second harmonic generation (SHG), sum frequency generation (SFG), difference frequency generation (DFG) and optical parametric generation (OPG) [41]. Utilizing these process can lead to great tunability and coverage of wavelength. For the mid infrared band DFG and OPG/OPO (optical parametric generation/oscillation) are the most important nonlinear conversion techniques. A short overview will be given in this section.

For all nonlinear processes discussed here, the phase matching of the beams is critical in order to optimise nonlinear conversion. To fulfil this criterion, the sum of the wave vector of signal and idler beams has to be equal to the wave vector of the pump beam. To achieve this, two types of phase matching are typically used, i.e. birefringent phase matching (BPM) [42] or quasi-phase matching (QPM) [42]. BPM can be achieved by type I & II phase matching. In type I, the idler and signal beam are polarised along the same crystal axis, while in type II, the two beams are polarised perpendicular to each other. Typically phase matching is achieved by temperature, wavelength or angle tuning of the nonlinear crystal. It should be noted, however, that the phase matching condition does not usually result in access to the highest nonlinear coefficient. This results in a compromise in overall conversion efficiency. To counteract this problem, or if the birefringent properties of the nonlinear crystal prevent phase matching, QPM can be used as alternative. In this case the relative phase of the beams is corrected at regular intervals using a structural periodicity, which prevents the destructive interference of the light with the newly generated radiation after each coherence length. Essentially the periodic structure causes a sign change of the nonlinearity of the crystal and thereby allows for constructive interference.

Pump Laser	**Signal laser**	**λ_P [µm]**	**λ_S [µm]**	**λ_{DFG}**	**Ref.**
Ti:Sa	Ti:Sa	0.69-0.75	0.91-1.05	2.3-2.8	[43]
OPA	OPA	1.1-1.6	1.6-2.93	2.4-1.2	[44]
Ti:Sa	OPG/OPA	0.81	1.2-1.5	2.5-7.6	[45]
ECDL	HeNe	1.5-1.58	3.39	2.68-2.95	[46]
Ti:Sa	Nd:YAG	0.77-0.82	1.06	3.0-3.6	[47]
Nd:YAG	OPO	1.06	1.43-1.6	3.2-4.2	[48]
OPO	OPO	1.7-2.1	2.26-2.84	5.0-18.0	[49]

Table 1.3 Overview of DFG-based laser systems in the mid-IR and laser types, pump / signal wavelength (λ_P & λ_S) idler wavelength (λ_{DFG}) and nonlinear crystal used. Ti:Sa=titanium-doped sapphire, ECDL= external cavity diode laser.

A summary of the DFG systems emitting in the mid-IR is given in Table 1.3. The used pump and signal laser types are listed along with the pump, signal and idler wavelengths. From this it can be seen that this technique allows the coverage of a wide range of wavelengths in the mid-IR and beyond. However, pump sources with broad tuning ranges are required to obtain the desired wavelength coverage from the DFG process. The systems are therefore often complex and expensive.

Optical parametric oscillators are another common type of coherent light source in the mid-IR. In this arrangement, an incoming pump photon is split in two less energetic photons (the signal and idler) - the sum of the energies of which equals the pump photon energy. It can therefore also be regarded as the reverse of SFG. In the same way as in DFG, phase matching of the beams is critical.

Crystals typically used are lithium niobate ($LiNbO_3$), potassium titanyl phosphate (KTP), potassium titanyl arsenate (KTA) and rubidium titanyl arsenate (RTA), all of which have also been demonstrated in periodically-poled arrangements.

For the mid-IR, periodically-poled lithium niobate (PPLN) has received considerable attention, largely due to its high nonlinear coefficient and the availability of high quality $LiNbO_3$ [50]. Both cw and pulsed operation has been demonstrated in this material with a wavelength coverage (using various systems) from 1.6 to 4.8 µm [50-52]. Due to the relatively low photorefractive damage threshold, however, output powers are typically limited. It was found, however, that the operation at higher temperatures (~200 °C) or by co-doping with magnesium oxide (MgO) would counteract this limitation and enable multi-Watt output powers from these devices [53-55].

Zinc germanium phosphide ($ZnGeP_2$) is another well established nonlinear crystal for mid-IR OPOs. It's high nonlinearity, high thermal conductivity, relatively high damage threshold make it advantageous for high power applications, however, the phase matching requirements are not met for wavelengths of 1 or 1.5 µm which limits the choice of high power pump sources. The development of high peak power Tm- and Ho-based laser sources, however, has helped scaling the output power of these devices. An alternative to overcome this issue and enable the use of high-energy neodymium lasers is to use a two step process in which 1 µm radiation is first converted to 2 µm before being used for OPG [56]. With its advantageous thermal mechanical and optical properties, ZGP OPOs have been demonstrated with output powers of multiple tens of Watts with spectral tuning over a range of 3-5 µm [57].

Aside the various dielectric materials used for nonlinear conversion techniques, QPM semiconductor materials have started to show promise, for example orientation-patterned gallium arsenide (OP-GaAs). Its high nonlinearity, large thermal conductivity and low absorption losses at ~2 µm make it a very good alternative to ZGP for high power 3-5 µm OPOs [57,58]. Since the first demonstration of OPGaAs as a nonlinear crystal in OPOs by Vodopyanov et al. in 2004, the availability of material with sufficient thickness has limited the progression of this material [59]. However, with the advances in growth technologies, samples with sufficient length for efficient OPO operation have been grown, resulting in output powers of ~0.5 W [60].

Compared to the DFG sources, OPO systems are somewhat less complex as they only require the use of one pump source; however, the requirement for high powers to achieve efficient nonlinear conversion persists, making cw operation more difficult. While pulsed embodiments work at relatively high efficiencies, the complexity of these systems can potentially impose a disadvantage on application-focused laser sources. For this reason, the direct generation of the required light would be advantageous.

1.3.5 Transition-metal doped crystalline lasers

A promising alternative for compact and widely tunable sources covering the mid-IR region are the transition-metal lasers. Compared to the rare-earth solid-state lasers described earlier, they offer wider tuning ranges. The origins of this wide emission is their so-called vibronic behaviour [61]. Crucially, here, the optical transitions take place in the d-shell of the ion rather than the f-shell, as is the case in rare-earth ions. The d-shell electrons being the outermost electrons therefore experience a strong interaction with the lattice, hence the energy level structure is perturbed producing a broad variation in potential optical transitions.

For emission in the mid-infrared, chalcogenide materials are often used as hosts for transition-metal ions such as Cr^{2+} and Fe^{2+}. Chalcogenides are compounds containing at least one chalcogen ion – i.e. the elements of the 16th group of the periodic table (essentially selenides, sulphides, and tellurides. Notably oxides are typically not referred to as chalcogenides). In combination with elements such as zinc or cadmium from the second group of the periodic table, these hosts are often referred to as the chalcogenides or II-VI compounds (N.B. this nomenclature effectively ignores the transition metal elements).

When doped with chromium, these materials are often pumped in the 1.5-2.0 µm regime and emit between 2-3 µm [62]. Fe^{2+} based materials have been shown to provide continuous tuning between 3.77 and 5.05 µm [63], however these materials require to be pumped around 2.5-4.5 µm.

In recent years, Cr^{2+} lasers have stimulated a lot of research, resulting in operation at room temperature [62], modelocking with pulses as short as ~100 fs [64], diode-pumping [65] and very broad tunability between 1.8-3.1 µm [66].

The possibility of broad tunability or the utilisation of this bandwidth to create ultrashort pulses, while maintaining the stability, flexibility and efficiency of solid-state lasers, builds a good foundation for practical applications-focused sources. With a bandwidth relative to their central wavelength that is similar to that of titanium-doped sapphire, the chromium chalcogenides have great promise to become mid-IR laser materials as important as Ti:sapphire has been in the near-infrared. The following sections and chapters will therefore concentrate on the development of chromium-doped chalcogenide lasers.

1.4 Chromium-doped chalcogenide lasers

As already mentioned briefly in the previous section, divalent chromium-doped chalcogenide gain media are vibronic laser crystal where strong interactions of the active ion with the lattice of the host crystal strongly influence the optical transitions. It is not only the ion-host interaction that is responsible for the broad absorption (~500 nm) and emission (~1000 nm) bandwidths. Jahn-Teller interactions add to the width of the transition by splitting the degenerate energy states and decrease the overall energy of the crystalline complex [67]. This results in very broad absorption and emission spectra which typically range, for example, from 1.5-2.1 µm and 1.8-3.1 µm respectively for Cr^{2+}:ZnSe (see Figure 1.7).

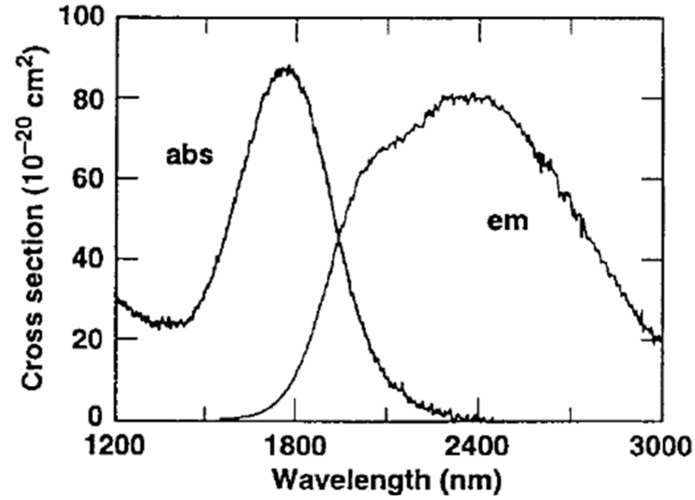

Figure 1.7 Absorption and emission spectrum of Cr^{2+}:ZnSe (after Page et al. [68]).

The transitions between the different energy levels represent a 4-level structure, as typical for vibronic gain media (see Figure 1.8). While the absorption of the pump radiation from the ground state into the excited state is an electronic transition, it is phonon assisted transitions within the upper energy level that enables the decay into the upper level of the laser transition. After the radiative transition, the electron undergoes further phonon assisted transitions to repopulate the ground state.

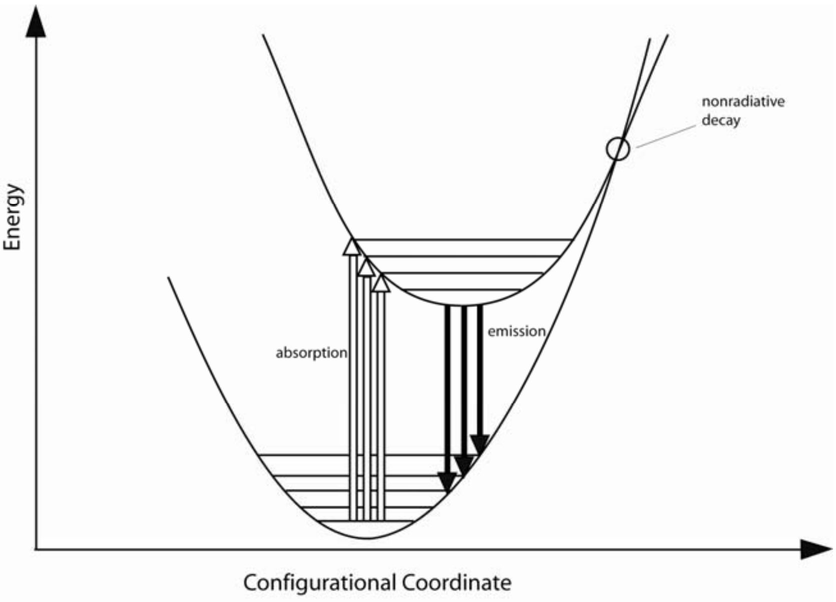

Figure 1.8 Energy diagram of a vibronic laser such as Cr^{2+} chalcogenide.

While the combination of phonon assisted transitions is advantageous for the formation of the broad energy bands, it should be noted that it is important that the phonon cut off of the host material is low enough to prevent non-radiative depletion of the excited state due to phonon-phonon interactions.

1.4.1 Chalcogenide hosts

As a consequence of the previously discussed interaction of the electronic transitions with the lattice structure, the host significantly influences the laser properties of a vibronic laser. This stimulated a lot of research into various II-VI hosts, the most important ones of which are summarized in Table 1.4.

The first laser operation of a chromium-chalcogenide material was demonstrated in 1996 by DeLoach et al. using Cr^{2+}:ZnSe as the active medium [69]. Since then Cr^{2+}:ZnSe has been the most studied of all the chalcogenide hosts, mainly due to its favourable combination of thermal, optical and spectroscopic properties compared to the other chalcogenide hosts.

	Cr^{2+}:ZnSe	**Cr^{2+}:ZnS**	**Cr^{2+}:CdSe**	**Ti^{3+}:Al_2O_3**
Peak emission wavelength [µm]	2.45 [69]	2.41 [70]	2.6 [71]	780 [72]
Relative bandwidth ($\Delta\lambda/\lambda$)	0.56 [73]	0.34 [70]	0.51 [71]	0.41 [72]
Peak absorption wavelength [µm]	1.78 [69]	1.67 [74]	1.9 [71]	490 [72]
Emission cross section [10^{-20} cm^2]	110 [75]	100 [75]	194 [75]	39 [72]
Absorption cross section [10^{-20} cm^2]	350 [75]	350 [75]	440 [75]	65 [72]
Radiative lifetime [µs]	11 [69]	8 [69]	3 [69]	3.2 [72]
Thermal conductivity [W/m·K]	19 [76]	27 [76]	4 [77]	28 [68]
Thermal expansion coefficient [10^{-6} 1/K]	6.4 [77]	7.3 [77]	4.9 [77]	5 [72]
Thermal shock resistance [W/√m]	5.3 [68]	7.1 [68]	no data	22 [68]
dn/dT [10^{-6} 1/K]	70 [68]	46 [68]	98 [77]	12 [68]

Table 1.4 Overview of the most developed chalcogenide hosts used for chromium-doped mid-IR lasers. Values for Ti^{3+}:Al_2O_3 are provided for comparison.

In the subsequent years, the crystal quality improved significantly, and as a result cw output powers and efficiencies increased to values exceeding 12 W [75] and 60 % [78] respectively. Another way to enable higher peak output powers in Cr^{2+}:ZnSe was the use of gain switched embodiments which resulted in an output power of 18.5 W [79]. In addition, the thin disk arrangement has been investigated [80], providing 4 W of output power.

Aside from the power scaling of Cr^{2+}:ZnSe laser which is potentially interesting for military applications, other modes of operation have gained interest too: single frequency [81] as well as active [82] and passive [83] mode-locked arrangements with the shortest pulse duration being <100 fs [84] were developed. A very broad tuning range has also been demonstrated, covering a spectral range of 1.8-3.1 µm using multiple mirror sets [66]. However, recently, the operation of a Cr^{2+}:ZnSe laser tunable over the range of 1973 to 3349 nm using a single mirror set was demonstrated [73]. To address the demand of affordable sources, microchip arrangements have also been investigated [85] where an output power of 100mW and slope efficiencies of 20 % have been observed.

Despite the considerable interest in Cr^{2+}:ZnSe, other hosts have found interest too, e.g. chromium-doped zinc-sulphide (ZnS). Amongst the chalcogenides, the ZnS hosts has the highest thermal conductivity, optical damage threshold and hardness combined with the lowest level of thermal lensing [86] and therefore is potentially more suitable for scaling the output power of chromium-doped chalcogenide lasers.

Since the first demonstration of Cr^{2+}:ZnS in 2002 by Sorokina et al. [87] further development of these crystals has led to output powers exceeding 10 W [88]. Compared to Cr^{2+}:ZnSe, the emission and absorption bands are shifted towards shorter wavelengths by ~100 nm. This could especially be useful if erbium-based laser pumping is employed as the Cr^{2+}:ZnS absorption peak is now closer to the 1.53 µm radiation of the erbium laser compared to Cr^{2+}:ZnSe.

If shifting the absorption and emission wavelength of chromium-doped chalcogenides towards longer wavelengths is desirable, cadmium-based chalcogenides such as cadmium-selenide (CdSe) can be used [71]. With an absorption band centred at 1.9 µm, pumping with Tm-based lasers is advantageous. The emission peak on the other hand is shifted to 2.6 µm. Tuning between 2.26 and 3.61 µm, Cr^{2+}:CdSe has the longest emission wavelength of any chromium chalcogenide laser. However, the presence of strong thermal lensing has restricted its development since the first room temperature operation in 1999 [89] and it was not until 2007, that cw operation was demonstrated with an output power of 1 W [90].

In addition to the chalcogenide hosts mentioned in the previous section, various other hosts such as $Cr^{2+}:Cd_{0.85}Mn_{0.15}Te$ [91], $Cr^{2+}:Cd_{0.55}Mn_{0.45}Te$ [92], Cr^{2+}:CdTe [93], Cr^{2+}:CdZnTe [94], Cr^{2+}:CdS [95] and $Cr^{2+}:ZnS_xSe_{1-x}$ [79] has been demonstrated. These are, however, significantly less developed compared to the previously mentioned materials. A brief overview of the achievements using these materials is given in Table 1.5.

Material	Absorption peak	Emission	Operation	Output power/Energy
$Cr^{2+}:Cd_{0.85}Mn_{0.15}Te$	1.91	2.3–2.6	pulsed	250 µJ
$Cr^{2+}:Cd_{0.55}Mn_{0.45}Te$	1.91	2.17–3.01	pulsed	n.a.
Cr^{2+}:CdTe	1.91	2.54	pulsed	132 µJ
Cr^{2+}:CdZnTe	1.89	2.0-2.6	cw	3 mW
Cr^{2+}:CdS	1.85	2.2–3.3	pulsed	4mJ
$Cr^{2+}:ZnS_xSe_{1-x}$	1.68	2.1–2.7	cw	50mW

Table 1.5 Overview of various less developed chromium-doped chalcogenide lasers.

1.4.2 Growth of Cr^{2+}:II-VI materials

Cr^{2+}-doped chalcogenide materials can be prepared in various ways. One scheme is to diffusion dope chromium ions into the polycrystalline ZnSe that is available for mid-infrared components such as optical windows and lenses [96]. This relatively simple process gives good quality Cr^{2+}:ZnSe. The thermal diffusion, however, causes the doping concentration within the ZnSe to be inhomogeneous. Specific details of the thermal-diffusion doping process are reported in [97,98]. The gradients in doping limit the manufacture of large Cr^{2+}:ZnSe crystals for power scaling of these systems. This problem has recently been addressed by systematic studies of the diffusion parameters, i.e. temperature and time [99] which led to the preparation of Cr^{2+}:ZnSe with good doping uniformity.

Current, however, the most widely used method of preparing Cr^{2+}-doped chalcogenide crystals with uniform doping is physical vapour transport (PVT) growth. A schematic of the arrangement of such a growth facility (after [100]) can be seen in Figure 1.9.

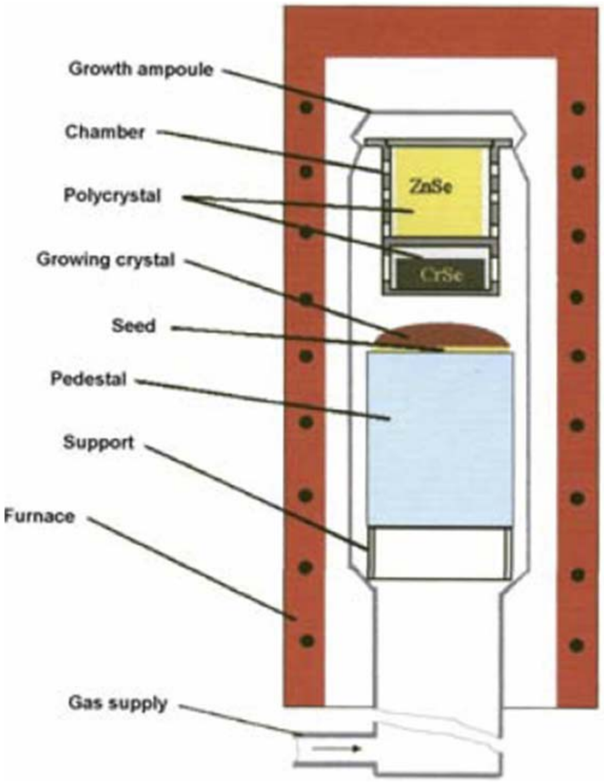

Figure 1.9 Schematic of the PVT process for growing single-crystal chromium-doped chalcogenides after [100].

Here, the polycrystalline host and dopant are positioned in two separate chambers within the furnace. By heating of the furnace, transport of the II-VI compound and the chromium to the seed takes place. The host-to-dopant ratio can be varied by the difference in perforation of the different chambers. In this way, homogeneous, single crystal material of very good quality and reasonable size (~40 mm) has been grown.

An alternative method for producing single crystal Cr^{2+}:chalcogenides is the use of the vertical Bridgman method [101]. In this technique, a mixture of II-VI compounds and CrSe powders are melted in a furnace and exposed to a temperature gradient. The solidification of the melt is seeded by a piece of single crystal material, which stimulates the formation of single crystalline material once the melt cools down. In this way, high quality Cr^{2+}:ZnSe crystal boules have been manufactured with a diameter of 50 mm and a length of 100 mm [102]. The quality of this material was confirmed by the demonstration of the highest slope efficiency (66 % in cw operation, 70 % in pulsed) ever demonstrated in a chromium-doped chalcogenide laser [103].

In recent years, the preparation of ceramic materials has gained interest. Since the initial demonstration of ceramic laser materials in 1966 [104], the Nd:YAG ceramics have been the main focus of this interest [105]. The advantage of ceramic over single crystalline material is mainly the possibility to produce large size samples on mass-market scales with good sample to sample uniformity. The first demonstration of a laser using hot-pressed ceramic Cr^{2+}:ZnSe was in 2006 by Gallian et al. [106], operating in gain-switched mode. The authors first mixed ZnSe and CrSe powders and then ground this mixture to reduce the grain size to <10 µm. The powder was then pressed into briquettes at room temperature and afterwards pressed at high temperature (900 °C) into the final form. While cw operation has also been demonstrated [107], the quality of chromium-chalcogenide ceramics is still relatively poor. However, it can be expected that with growing expertise in this field, the preparation of Cr^{2+}:chalcogenide ceramics will become as successful as demonstrated in other material systems.

1.4.3 Pump sources for Cr^{2+}:II-VI lasers

From the previous sections it is clear, that since the initial demonstration of Cr^{2+}:chalcogenides in 1996, chromium-doped chalcogenides have developed into an attractive laser material for the generation of mid-IR radiation. A practical and compact laser source as required by many applications, however, also demands a pump laser that meets these requirements. While the width of the absorption spectrum of chromium chalcogenide lasers (>500 nm) might suggest that appropriate pump sources should be plentiful, in fact only a limited number of pump sources are available in this wavelength band.

1.4.3.1 Co:MgF2 lasers

In the early years of the chromium-chalcogenide lasers, pulsed Co:MgF_2 [108] lasers were typically used as pump sources [68,69]. With tuning between 1.6 and 2.4 µm and millijoule-type output energies, these laser systems were ideal for investigating the early Cr^{2+}:chalcogenide materials. Aside the pulsed operation, the Co:MgF_2 laser was also used as a cw pump source with output powers of the order of 1.6 W [109,110]. An issue observed when using these pump sources was the sensitivity to feedback. In the work reported by Sorokina et al. [110] retro-reflection to double pass the pump in a chromium-chalcogenide laser caused feedback into the Co:MgF_2 pump laser. This resulted in spiking of the Co:MgF_2 and chromium laser outputs – the authors claimed this to be a consequence of the Cr^{2+}:ZnSe crystal acting as a saturable absorber. To counteract this issue, optical isolation using a Faraday-isolator would need to be implemented into the system which would reduce practicality and increase the cost.

Following the use of Co:MgF_2 lasers for the initial demonstration of the Cr^{2+}:ZnSe laser it was soon recognized that this pump source was too complex and unpractical as it required cryogenic cooling and an unconventional pump source (i.e. a Nd:$Y_3Al_5O_{12}$ laser tuned to 1.3 µm [111]).

1.4.3.2 Thulium-based lasers

For the first demonstration of a cw Cr^{2+}:ZnSe laser, a Tm^{3+}:$YAlO_3$ laser emitting at 1.94 µm was used as the pump source [78]. At that time, the available output power of the pump was limited to 1 W, however, even so, 250 mW of cw output power was achieved from the Cr^{2+}:ZnSe laser.

Since then various other groups have used crystalline thulium-based lasers with output powers in the multi-Watt regime, resulting in chromium-chalcogenide lasers having output powers approaching the Watt level [80,112,113]. While the thulium lasers are more suitable for cw operation compared to the Co:MgF_2 laser, feedback-related instabilities are also present and need to be addressed [80].

As an alternative to the crystalline thulium-doped lasers, fibre-lasers have also been used [114,115]. While it has been reported that these also suffer from feedback-related instabilities [114], high power embodiments having output powers in excess of 100 W are now commercially available (e.g. TLR series from IPG Photonics [116]) and are suitable for power scaling of Cr^{2+}:II-VI lasers.

1.4.3.3 Erbium-doped lasers

While thulium-based laser systems (emitting at 1.95 μm) are red-shifted with respect to the absorption peak of Cr^{2+}:ZnSe, erbium lasers (@ ~1.55 μm) are blue shifted and so introduce a significantly higher quantum defect (63 % for erbium compared to 79 % for thulium). Even so, this has not prevented their use as a pump source for Cr^{2+}:ZnSe due to ready availability and excellent performance characteristics.

While the use of crystalline erbium-doped YAG and YAP lasers is largely limited to pulsed embodiments, erbium-doped fibre lasers have proven to be invaluable pump sources for high power chromium-chalcogenide lasers. Indeed, the highest output power ever achieved from a chromium-chalcogenide laser lasers was obtained using an erbium fibre laser emitting 30 W of output power [88]. However, the authors reported problems with the unpolarised output of the pump laser. When using the Cr^{2+}:II-VI crystal at Brewster's angle, the unpolarised light led to significant losses from the vertically polarised component of the light at the crystal surface. In addition, polarisation-based beam attenuators could not be used to adjust the incident pump power which imposed problems with polarisation switching of the erbium laser when changing its pump diode laser current. To counteract this problem, a 9 W erbium fibre laser using a polarisation maintaining fibre has been used to pump a Cr^{2+}:ZnSe laser to an output power level of >3 W [117]. In addition to the polarisation related problems of these lasers, feedback resistance is, again, a potential problem. Especially when the chromium-doped crystal is placed at normal incidence to the pump beam, Fresnel reflections of the pump light can cause instabilities of the pump laser as was observed when using a 2 W, unpolarised erbium fibre laser to pump Cr^{2+}:ZnSe and Cr^{2+}:ZnS microchip lasers [85].

1.4.3.4 Direct diode laser pumping

During the very early years of the Cr^{2+}:chalcogenide development, the use of direct diode laser pumping was suggested. It was initially proposed by Page et al. in 1997 [68] and demonstrated in the same year using InGaAsP diode lasers emitting at 1.65 µm [65]. A few years later, the use of a fibre-coupled, 400 mW diode laser emitting at 1.54 µm was demonstrated, resulting in output powers from the chromium laser of 15 mW.

As an alternative to InGaAsP diode lasers, Mond et al. used (AlGaIn)(AsSb)-based diode lasers emitting 1 W of radiation at 1.9 and 2.0 µm . With the emission shifted towards lower quantum defects and closer to the absorption peak of Cr^{2+}:chalcogenide laser, the output power of the Cr^{2+}:ZnSe laser was ~100 mW. Intrinsic to these diode lasers, however, is the relative poor beam quality. The result is that the output beam of these diode lasers is elliptical with a beam propagation parameter of close to diffraction limited and >10 in the highly divergent (fast axis) and low divergence axis (slow axis) respectively. In case of the 1.9 and 2.0 µm diode lasers, the beam propagation parameter was 1.3 and 25 for the fast and slow axes respectively. As a consequence, a more complex beam conditioning lens arrangement is typically required to focus the radiation onto the laser crystal. Another drawback of the low brightness of these diode lasers is that more complex pumping geometries such as multi-pass pumping are more difficult to implement.

1.4.3.5 The ideal pump source

When considering an ideal pump source, many of the aspects of the individual pump sources discussed in the previous section become important. Wavelength, output power and compactness might be considered the most important properties of a pump source, but beam quality, feedback resistance, efficiency and flexibility could also be considered as important. The actual specification of an ideal pump source therefore depends on the specification of the laser that is being pumped.

Two major development routes for chromium-doped chalcogenide lasers are currently being pursued: one is high power embodiments, largely stimulated by military applications such as laser countermeasures. For these applications, high power pump sources such as erbium and thulium fibre lasers are ideal as they can offer large pump powers in a relatively compact format. The other route of laser development is towards scientific lasers, with applications such as spectroscopy in mind. For these lasers, power levels in the multi-Watt regime are typically sufficient but the added functionality such as mode-locked and single frequency operation are considered more important. For these purposes, a pump source with moderate output power is often sufficient but requirements such as high brightness, low intensity noise and feedback resistance become essential. However, in all cases, a simple, compact and reliable pump source is desirable.

While the development of high power Cr^{2+}:II-VI laser is steadily advancing, less attention has been paid to the development of practical pump sources for the laser systems in the multi-Watt regime. The aim of this work is therefore to investigate novel pump sources for the chromium-chalcogenide laser family for scientific applications with emphasis on practicality and flexibility to cater the wide range of applications of Cr^{2+}:II-VI sources. A summary of the desired properties for a cw and pulsed pump sources are given in Table 1.6.

Continuous Wave		**Pulsed**	
Parameter	**Value**	**Parameter**	**Value**
Power [W]	Watt-level	Peak Power [W]	Watt-level
Wavelength [μm]	1.6-2.1	Wavelength [μm]	1.6-2.1
M^2	<5	Pulse Duration	ns-ms
RMS Intensity noise [%]	<2	Energy	μJ-mJ
Feedback sensitivity	low	Repetition rate	> 1 kHz

Table 1.6 Overview of the demands for a cw and pulsed pump source for Cr^{2+}:II-VI lasers.

A potential candidate as a novel pump source for chromium-doped II-VI laser is the semiconductor disk laser (SDL) [118], a class of laser that combines multi-Watt output powers from a wavelength engineerable format with the flexibility of adding intra-cavity elements, typical of solid-state lasers. The investigations of material systems such as (AlGaIn)(AsSb) opens the route for SDLs to generate radiation in the mid-IR around 2 μm and therefore could make this an ideal candidate as a novel pump source for Cr^{2+}:II-VI lasers. The development of these sources and their use as pump source for chromium-doped chalcogenide lasers will be the main body of this work.

1.5 Conclusion

Laser sources in the short wave mid-infrared range are of increasing interest due to the important atmospheric gases and aerosols that have characteristic absorptions in this range. While a number of laser sources are already available in this wavelength band, only the transition-metal doped chalcogenide lasers, specifically the chromium-doped chalcogenide lasers, can combine multiple Watt output power, broad tunability, practicality and simplicity along with the ability to generate ultrashort pulses or single frequency operation.

A variety of II-VI hosts such as ZnSe, ZnS and CdSe have been investigated. Cr^{2+}:ZnSe which has its emission centred at 2.45 μm is currently the most developed of the chromium doped II-VI materials. Its vibronically broadened energy level system allows tuning over more than 1μm from 1.9-3.1 μm. With the possibility of generating mode-locked pulses with durations in the femtosecond regime, this laser system is often referred to as the *mid-infrared Ti:Sapphire*.

While the broad absorption between 1.5 and 2.1 μm allows the use of various pump sources, e.g. erbium- and thulium-doped crystalline and fibre lasers, Co:MgF_2 and diode lasers. None of these, however, satisfies the demands of a truly practical and flexible pump source for scientific chromium-chalcogenide lasers.

The semiconductor disk laser is a potential alternative pump source especially since multi-watt power levels have recently been reached from (AlGaIn)(AsSb)-based systems emitting around ~2 μm.

This thesis will therefore focus on the investigation of (AlGaIn)(AsSb)-based semiconductor disk lasers emitting around 2 μm as pump sources for the chromium--chalcogenide laser. For comparison, a more conventional pump system, i.e. the Tm^{3+}:$YAlO_3$ laser will be discussed in chapter 2. After the introduction of the semiconductor disk laser and the demonstration of high power 1.9 and 2.0 μm embodiments in chapter 3, the pulsed operation of these lasers using low-cost pulsed diode lasers as pump sources will be detailed in chapter 4.

In chapter 5 the use of the cw SDLs as pump sources for a Cr^{2+}:ZnSe laser will be outlined and the potential advantages and disadvantages of the SDL as a pump source discussed. In chapter 6, pulsed-pumped Cr^{2+}:ZnSe arrangements will be described. The 7th chapter will then conclude this work and give suggestions for further research directions in this field.

References

[1] A. Krier et al., "A room temperature photovoltaic detector for the mid-infrared (1.8-3.4 μm) wavelength region," Semiconductor Science and Technology **13**, 950 (1998).

[2] Lambda Photometrics Ltd, http://www.lambdaphoto.co.uk, (05-2010).

[3] L. S. Rothman, A. Barbe, D. Chris Benner, L. R. Brown, C. Camy-Peyret, M. R. Carleer, K. Chance, C. Clerbaux, V. Dana, V. M. Devi, A. Fayt, J. M. Flaud, R. R. Gamache, A. Goldman, D. Jacquemart, K. W. Jucks, W. J. Lafferty, J. Y. Mandin, S. T. Massie, V. Nemtchinov, D. A. Newnham, A. Perrin, C. P. Rinsland, J. Schroeder, K. M. Smith, M. A. H. Smith, K. Tang, R. A. Toth, J. Vander Auwera, P. Varanasi, and K. Yoshino, "The HITRAN molecular spectroscopic database: edition of 2000 including updates through 2001," Journal of Quantitative Spectroscopy and Radiative Transfer **82**, 5. (2004)

[4] L.S. Rothman, (Atomic Molecular Division, Harverd University, 2004).

[5] Spectral Calculator , http://www.spectralcalc.com, (GATS, Inc.), (2007).

[6] H. A. Gebbie, W. R. Harding, C. Hilsum, A. W. Pryce, and V. Roberts, "Atmospheric Transmission in the 1 to 14 μm Region," Proceedings of the Royal Society of London. Series A. Mathematical and Physical Sciences **206**, 87 (1951).

[7] I. T. Sorokina and K.L. Vodopyanov, *Solid-State Mid-Infrared Laser Sources*. Springer, Berlin, Heidelberg, New York, p.557 (2003).

[8] C. K. N. Patel, "CW laser on vibrational-rotational transitions of CO," Appl. Phys. Lett. **7**, 246 (1965).

[9] C. K. N. Patel, "Continuous-Wave Laser Action on Vibrational-Rotational Transitions of CO_2," Physical Review **136**, A1187 (1964).

[10] A. E. Siegman, in *Lasers*, edited by A. Kelly University Science Books, Sausalito, CA, pp. 62 (1986).

[11] Y. G. Utkin, M. Goshe, I. V. Adamovich, and J. W. Rich, "Compact overtone band carbon monoxide laser," Opt. Commun. **263**, 105 (2006).

[12] C. Freed, "Sealed-off operation of stable CO lasers," Appl. Phys. Lett. **18**, 458 (1971).

[13] A. Joullié and P. Christol, "GaSb-based mid-infrared 2-5 μm laser diodes," Comptes Rendus Physique **4**, 621 (2003).

[14] L. A. Coldren and S. W. Corzine, *Diode Lasers and Photonic Integrated Circuits*., WileyBlackwell, p.624 (1995).

[15] C. Mermelstein, A. Rattunde, J. Schmitz, S. Simanowski, R. Kiefer, M. Walther, and J. Wagner, in *Progress in Semiconductor Materials for Optoelectronic Applications*, edited by E. D. Jones, O. Manasreh, K. D. Choquette et al. Materials Research Society, Warrendale, Vol. 692, pp. 365 (2002).

[16] J. G. Kim, L. Shterengas, R. U. Martinelli, G. L. Belenky, D. Z. Garbuzov, and W. K. Chan, "Room-temperature 2.5 μm InGaAsSb/AlGaAsSb diode lasers emitting 1 W continuous waves," Appl. Phys. Lett. **81**, 3146 (2002).

[17] N. Schulz, J. M. Hopkins, M. Rattunde, D. Burns, and J. Wagner, "High-brightness long-wavelength semiconductor disk lasers," Laser Photonics Rev. **2**, 160 (2008).

[18] N. Hempler, J. M. Hopkins, and M. Rattunde, "Tuning and brightness optimisation of high-performance GaSb-based semiconductor disk lasers from 1.86 to 2.80 μm," presented at the European Conference on Lasers and Electro-Optics, Munich (2009).

[19] L. Cerutti, A. Ducanchez, G. Narcy, P. Grech, G. Boissier, A. Garnache, E. Tournie, and F. Genty, "GaSb-based VCSELs emitting in the mid-infrared wavelength range (2-3 μm) grown by MBE," J. Cryst. Growth **311**, 1912 (2009).

[20] H. K. Choi, G. W. Turner, M. J. Manfra, and M. K. Connors, "175 K continuous wave operation of InAsSb/InAlAsSb quantum-well diode lasers emitting at 3.5 μm," Appl. Phys. Lett. **68**, 2936 (1996).

[21] L. Partin Dale and M. Thrush Christopher, "Wavelength coverage of lead-europium-selenide-telluride diode lasers," Appl. Phys. Lett. **45**, 193 (1984).

[22] H. Preier, "Physics and applications of IV-VI compound semiconductor lasers," Semiconductor Science and Technology **5**, S12 (1990).

[23] J. Faist, F. Capasso, D. L. Sivco, C. Sirtori, A. L. Hutchinson, and A. Y. Cho, "Quantum Cascade Laser," Science **264**, 553 (1994).

[24] G. Scalari, C. Walther, M. Fischer, R. Terazzi, H. Beere, D. Ritchie, and J. Faist, "THz and sub-THz quantum cascade lasers," Laser & Photonics Review **3**, 45 (2009).

[25] Q. K. Yang, W. Bronner, K. Kohler, and J. Wagner, "Short-wavelength quantum-cascade lasers," Photon. Spectra **41**, 64 (2007).

[26] S. Y. Zhang, D. G. Revin, J. W. Cockburn, K. Kennedy, A. B. Krysa, and M. Hopkinson, "$\lambda \sim 3.1$ μm room temperature InGaAs/AlAsSb/InP quantum cascade lasers," Appl. Phys. Lett. **94**, 031106 (2009).

[27] R. Köhler, A. Tredicucci, F. Beltram, H. E. Beere, E. H. Linfield, A. Giles Davies, and D. A. Ritchie, "Low-threshold quantum-cascade lasers at 3.5 THz ($\lambda = 85$ μm)," Opt. Lett. **28**, 810 (2003).

[28] F.-Q. Liu, Quan-Sheng Zhang, Y.-Z. Zhang, D. Ding, B. Xu, and Z.-G. Wang, "Growth and characterization of InGaAs/InAlAs quantum cascade lasers," Solid-State Electronics **45**, 1831 (2001).

[29] F. Auzel and Y. H. Chen, "The effective frequency in multiphonon processes: Differences for energy transfers or side-bands and non-radiative decay," J. Lumin. **66-67**, 224 (1995).

[30] T. Schweizer, "Rare-earth-doped gallium lanthanum sulphide glasses for mid infrared fibre lasers," PhD Thesis, University of Hamburg (1998).

[31] M. Klimczak, M. Malinowski, J. Sarnecki, and R. Piramidowicz, "Luminescence properties in the visible of Dy:YAG/YAG planar waveguides," J. Lumin. **129**, 1869 (2009).

[32] Crystran Ltd., http://www.crystran.co.uk/yttrium-aluminium-garnet-yag.htm, (2010).

[33] M. E. Doroshenko, T. T. Basiev, V. V. Osiko, V. V. Badikov, D. V. Badikov, H. Jelínková, P. Koranda, and J. Sulc, "Oscillation properties of dysprosium-doped lead thiogallate crystal," Opt. Lett. **34**, 590 (2009).

[34] K. Rademaker, W. F. Krupke, R. H. Page, S. A. Payne, K. Petermann, G. Huber, A. P. Yelisseyev, L. I. Isaenko, U. N. Roy, A. Burger, K. C. Mandal, and K. Nitsch, "Optical properties of Nd^{3+}- and Tb^{3+}-doped KPb_2Br_5 and $RbPb_2Br_5$ with low nonradiative decay," J. Opt. Soc. Am. B **21**, 2117 (2004).

[35] M. C. Nostrand, R. H. Page, S. A. Payne, L. I. Isaenko, and A. P. Yelisseyev, "Optical properties of Dy^{3+}- and Nd^{3+}-doped KPb_2Cl_5," J. Opt. Soc. Am. B **18**, 264 (2001).

[36] T. Schweizer, B. N. Samson, J. R. Hector, W. S. Brocklesby, D. W. Hewak, and D. N. Payne, "Infrared emission and ion-ion interactions in thulium- and terbium-doped gallium lanthanum sulfide glass," J. Opt. Soc. Am. B **16**, 308 (1999).

[37] V. Zharikov Evgeny, V. I. Zhekov, L. A. Kulevskii, T. M. Murina, V. Osiko Vyacheslav, A. M. Prokhorov, A. D. Savel'ev, V. Smirnov Valery, B. P. Starikov, and M. I. Timoshechkin, "Stimulated emission from Er^{3+} ions in yttrium aluminum garnet crystals at λ = 2.94 μm," Soviet Journal of Quantum Electronics, 1039 (1975).

[38] T. Schweizer, B. N. Samson, J. R. Hector, W. S. Brocklesby, D. W. Hewak, and D. N. Payne, "Infrared emission from holmium doped gallium lanthanum sulphide glass," Infrared Physics & Technology **40**, 329 (1999).

[39] Yuen H. Tsang, Atalla E. El-Taher, Terence A. King, and Stuart D. Jackson, "Efficient 2.96 μm dysprosium-doped fluoride fibre laser pumped with a Nd:YAG laser operating at 1.3 μm," Opt. Express **14**, 678 (2006).

[40] P. Amedzake, E. Brown, U. Hömmerich, S. B. Trivedi, and J. M. Zavada, "Crystal growth and spectroscopic characterization of Pr-doped KPb_2Cl_5 for mid-infrared laser applications," J. Cryst. Growth **310**, 2015 (2008).

[41] W. Koechner, in *Springer Series in Optical Sciences*, edited by W. T. Rhodes Spring Science + Business Media, Inc., New York, pp. 587 (2006).

[42] J. A. Armstrong, N. Bloembergen, J. Ducuing, and P. S. Pershan, "Interactions between Light Waves in a Nonlinear Dielectric," Physical Review **127**, 1918 (1962).

[43] Takamasa Momose, Tomonari Wakabayashi, and Tadamasa Shida, "Tunable-narrow-linewidth continuous-wave mid-infrared light generation by difference-frequency mixing," J. Opt. Soc. Am. B **13**, 1706 (1996).

[44] B. Golubovic and M. K. Reed, "All-solid-state generation of 100 kHz tunable mid-infrared 50 fs pulses in type I and type II $AgGaS_2$," Opt. Lett. **23**, 1760 (1998).

[45] H.-K. Nienhuys, P. C. M. Planken, R. A. van Santen, and H. J. Bakker, "Generation of mid-infrared pulses by X^3 difference frequency generation in CaF_2 and BaF_2," Opt. Lett. **26**, 1350 (2001).

[46] D. Hofmann, G. Schreiber, C. Haase, H. Herrmann, W. Grundkötter, R. Ricken, and W. Sohler, "Quasi-phase-matched difference-frequency generation in periodically poled Ti:LiNbO$_3$ channel waveguides," Opt. Lett. **24**, 896 (1999).

[47] J. Hong, A. D. O. Bawagan, S. Charbonneau, and Albert Stolow, "Broadly tunable femtosecond pulse generation in the near and mid-infrared," Appl. Opt. **36**, 1894 (1997).

[48] D. L. Fenimore, K. L. Schepler, D. Zelmon, S. Kück, U. B. Ramabadran, P. Von Richter, and D. Small, "Rubidium titanyl arsenate difference-frequency generation and validation of new Sellmeier coefficients," J. Opt. Soc. Am. B **13**, 1935 (1996).

[49] K. S. Abedin, S. Haidar, Y. Konno, C. Takyu, and H. Ito, "Difference Frequency Generation of 5-18 μm in a AgGaSe$_2$ Crystal," Appl. Opt. **37**, 1642 (1998).

[50] L. E. Myers, R. C. Eckardt, M. M. Fejer, R. L. Byer, W. R. Bosenberg, and J. W. Pierce, "Quasi-phase-matched optical parametric oscillators in bulk periodically poled LiNbO$_3$," J. Opt. Soc. Am. B **12**, 2102 (1995).

[51] L. E. Myers, R. C. Eckardt, M. M. Fejer, R. L. Byer, and W. R. Bosenberg, "Multigrating quasi-phase-matched optical parametric oscillator in periodically poled LiNbO$_3$," Opt. Lett. **21**, 591 (1996).

[52] G. Hansson and D. D. Smith, "Mid-Infrared-Wavelength Generation in 2 μm Pumped Periodically Poled Lithium Niobate," Appl. Opt. **37**, 5743 (1998).

[53] G. D. Miller, R. G. Batchko, W. M. Tulloch, D. R. Weise, M. M. Fejer, and R. L. Byer, "42 % efficient single-pass cw second-harmonic generation in periodically poled lithium niobate," Opt. Lett. **22**, 1834 (1997).

[54] D. A. Bryan, G. Robert, and H. E. Tomaschke, "Increased optical damage resistance in lithium niobate," Appl. Phys. Lett. **44**, 847 (1984).

[55] W. R. Bosenberg, A. Drobshoff, J. I. Alexander, L. E. Myers, and R. L. Byer, "93% pump depletion, 3.5 W continuous-wave, singly resonant optical parametric oscillator," Opt. Lett. **21**, 1336 (1996).

[56] G. Rustad, E. Lippert, G. Arishol, M. Haakestad, S. Nicolas, H. Fonnum, and K. Stenersen, "Infrared laser sources with high power and high pulse energy through nonlinear conversion in zinc germanium phosphide," presented at the Middle Infrared Coherent Light Sources, Trouville, France (2009).

[57] P. G. Schunemann, K.T. Zawilski, L. A. Pomeranz, and L. Mohnkern, "Advances in nonlinear optical crystals for efficient mid-infrared frequency conversion," presented at the Middle Infrared Coheren Light Sources, Trouville, France (2009).

[58] T. Skauli, K. L. Vodopyanov, T. J. Pinguet, A. Schober, O. Levi, L. A. Eyres, M. M. Fejer, J. S. Harris, B. Gerard, L. Becouarn, E. Lallier, and G. Arisholm, "Measurement of the nonlinear coefficient of orientation-patterned GaAs and demonstration of highly efficient second-harmonic generation," Opt. Lett. **27**, 628 (2002).

[59] K. L. Vodopyanov, O. Levi, P. S. Kuo, T. J. Pinguet, J. S. Harris, M. M. Fejer, B. Gerard, L. Becouarn, and E. Lallier, "Optical parametric oscillation in quasi-phase-matched GaAs," Opt. Lett. **29**, 1912 (2004).

[60] G. Schunemann Peter, D. Setzler Scott, Mohnkern Lee, M. Pollak Thomas, F. Bliss David, Weyburne David, and O'Hearn Kevin, "2.05 μm-Laser-Pumped

Orientation-Patterned Gallium Arsenide (OPGaAs) OPO," presented at the Conference on Lasers and Electro-Optics/Quantum Electronics and Laser Science and Photonic Applications Systems Technologies (2005).

[61] W. Koechner, in *Springer Series in Optical Sciences*, edited by W. T. Rhodes Spring Science + Business Media Inc., New York, pp. 38 (2006).

[62] R.H. Page, L.D. DeLoach, K.I. Schaffers, F.D. Patel, R.J. Beach, S.A. Krupke Payne, W.F., and A. Burger, in *Advanced Solid-State Lasers*, edited by C. Pollock S.A. Payne Optical Society of America, Washington, D.C., Vol. 1, pp. 130 (1996).

[63] V. V. Fedorov, S. B. Mirov, A. Gallian, D. V. Badikov, M. P. Frolov, Y. V. Korostelin, V. I. Kozlovsky, A. I. Landman, Y. P. Podmar'kov, V. A. Akimov, and A. A. Voronov, "3.77-5.05 µm tunable solid-state lasers based on Fe^{2+}-doped ZnSe crystals operating at low and room temperatures," IEEE J. Quantum Eelect. **42**, 907 (2006).

[64] I.T. Sorokina and E Sorokin, "Femtosecond pulse generation from a SESAM mode-locked Cr:ZnSe laser," Optical Society of America (2005).

[65] R. H. Page, J.A. Skidmore, K. I. Schaffers, R.J. Beach, S. A. Payne, and W. F. Krupke, in *Advanced Solid-State Lasers*, edited by C. R. Pollock and W.R. Bosenberg Optical Society of America, Washington, D.C., Vol. 10, pp. 208 (1997).

[66] U. Demirbas and A. Sennaroglu, "Intracavity-pumped Cr^{2+}:ZnSe laser with ultrabroad tuning range between 1880 and 3100 nm," Opt. Lett. **31**, 2293 (2006).

[67] G. Goetz, H. Zimmermann, and H.-J. Schulz, "Jahn-Teller interaction at Cr^{2+} (d4) centres in tetrahedrally coordinated II-VI lattices studied by optical spectroscopy," Z. Angew. Phys. **91**, 429 (1992).

[68] R. H. Page, K. I. Schaffers, L. D. DeLoach, G. D. Wilke, F. D. Patel, J. B. Tassano, S. A. Payne, W. F. Krupke, K. T. Chen, and A. Burger, "Cr^{2+}-doped zinc chalcogenides as efficient, widely tunable mid-infrared lasers," IEEE J. Quantum Eelect. **33**, 609 (1997).

[69] L. D. DeLoach, R. H. Page, G. D. Wilke, S. A. Payne, and W. F. Krupke, "Transition metal-doped zinc chalcogenides: Spectroscopy and laser demonstration of a new class of gain media," IEEE J. Quantum Eelect. **32**, 885 (1996).

[70] D. M. Simanovskii, H. A. Schwettman, H. Lee, and A. J. Welch, "Midinfrared Optical Breakdown in Transparent Dielectrics," Physical Review Letters **91**, 107601 (2003).

[71] V. A. Akimov, V. I. Kozovskii, Y. V. Korostelin, A. I. Landman, Y. P. Podmar'kov, Y. K. Skasyrskii, and M. P. Frolov, "Efficient pulsed Cr^{2+}:CdSe laser continuously tunable in the spectral range from 2.26 to 3.61 µm," Quantum Electron. **38**, 205 (2008).

[72] P. F. Moulton, "Spectroscopic and laser characteristics of Ti:Al_2O_3," J. Opt. Soc. Am. B **3**, 125 (1986).

[73] E. Sorokin, I. T. Sorokina, M. S. Mirov, V. V. Fedorov, I. S. Moskalev, and S. B. Mirov, "Ultrabroad Continuous-Wave Tuning of Ceramic Cr:ZnSe and Cr:ZnS Lasers," presented at the ASSP, San Diego, CA, USA, (2010).

[74] I. T. Sorokina, E. Sorokin, S. Mirov, V. Fedorov, V. Badikov, V. Panyutin, A. Di Lieto, and M. Tonelli, "Continuous-wave tunable Cr^{2+}:ZnS laser," Appl. Phys. B **74**, 607 (2002).

[75] S. B. Mirov, V. V. Fedorov, I. S. Moskalev, D. V. Martyshkin, and C. Kim, "Progress in Cr^{2+} and Fe^{2+} dopded Mid-IR Laser Materials," Laser Photonics Rev. **DOI 10.1002/Ipor.200810076** (2009).

[76] I. S. Moskalev, V. V. Fedorov, and S. B. Mirov, "10 Watt, pure continuous-wave, polycrystalline Cr^{2+}:ZnS laser," Opt. Express **17**, 2048 (2009).

[77] J.B. Goodenough, A. Hamnett, G. Huber, F. Hullinger, M. Leiß, S.K. Ramasesha, and H. Werheit, *Non-Tetrahedrally Bonded Binary Compounds* (Springer, Berlin, 1989).

[78] G. J. Wagner, T. J. Carrig, R. H. Page, K. I. Schaffers, J. O. Ndap, X. Y. Ma, and A. Burger, "Continuous-wave broadly tunable Cr^{2+}:ZnSe laser," Opt. Lett. **24**, 19 (1999).

[79] T. J. Carrig, A. Zakel, G. J. Wagner, and W. J. Alford, "Chromium-doped chalcogenide lasers," 2005 IEEE LEOS Annual Meeting Conference Proceedings (LEOS), 260 (2005).

[80] K. L. Schepler, R. D. Peterson, P. A. Berry, and J. B. McKay, "Thermal effects in Cr^{2+}:ZnSe thin disk lasers," IEEE J. Sel. Top. Quantum Electron. **11**, 713 (2005).

[81] G. J. Wagner, B. G. Tiemann, W.J Alford, and T. J. Carrig, "Single-Frequency Cr:ZnSe Laser," presented at the Advanced Solid-State Photonics, Santa Fe, New Mexico, (2004).

[82] T. J. Carrig, G. J. Wagner, A. Sennaroglu, J. Y. Jeong, and C. R. Pollock, "Mode-locked Cr^{2+}:ZnSe laser," Opt. Lett. **25**, 168 (2000).

[83] C. R. Pollock, N.A. Brilliant, D. Gwin, T. J. Carrig, and W.J Alford, "Mode locked and Q-switched Cr:ZnSe laser using a Semiconductor Saturable Absorbing Mirror (SESAM)," presented at Advanced Solid State Photonics (2005).

[84] I. T. Sorokina and E Sorokin, "Chriped-mirror dispersion controlled femtosecond Cr:ZnSe laser," presented at the Advanced Solid State Photonics, Paper WA7 (2007).

[85] S. B. Mirov, V. V. Fedorov, K. Graham, I. S. Moskalev, V. V. Badikov, and V. Panyutin, "Erbium fiber laser-pumped continuous-wave microchip Cr^{2+}:ZnS and Cr^{2+}:ZnSe lasers," Opt. Lett. **27**, 909 (2002).

[86] S. Kasap, H. Ruda, P. Capper, Cyril Koughia, S. O'Leary, S. Irvine, J. Wang, and M. Isshiki, *Springer Handbook of Electronic and Photonic Materials,* Springer (2006).

[87] I. T. Sorokina, E. Sorokin, S. Mirov, V. Fedorov, V. Badikov, V. Panyutin, and K. I. Schaffers, "Broadly tunable compact continuous-wave Cr^{2+}:ZnS laser," Opt. Lett. **27**, 1040 (2002).

[88] I. S. Moskalev, V. V. Fedorov, and S. B. Mirov, "10 Watt, pure continuous-wave, polycrystalline Cr^{2+}:ZnS laser," Opt. Express **17**, 2048 (2009).

[89] J. McKay, K. L. Schepler, and G. C. Catella, "Efficient grating-tuned mid-infrared Cr^{2+}:CdSe laser," Opt. Lett. **24**, 1575 (1999).

[90] V. A. Akimov and et al., "Efficient cw lasing in a Cr^{2+}:CdSe crystal," Quantum Electron. **37**, 991 (2007).

[91] J. T. Seo, U. Hommerich, S. B. Trivedi, S. W. Kutcher, R. J. Chen, C. C. Wang, and H. Zong, "Spectroscopy and tunable mid-infrared lasing of a novel gain medium: Cr^{2+}-doped $Cd_{0.85}Mn_{0.15}Te$," J. Korean Phys. Soc. **34**, 221 (1999).

[92] J. T. Seo, U. Hommerich, H. Zong, S. B. Trivedi, S. W. Kutcher, C. C. Wang, and R. J. Chen, "Mid-infrared lasing from a novel optical material: Chromium-doped $Cd_{0.55}Mn_{0.45}Te$," Phys. Status Solidi A **175**, R3 (1999).

[93] A. Bluiett, U. Hömmerich, R. Shah, S. Trivedi, S. Kutcher, and C. Wang, "Observation of lasing from Cr^{2+}:CdTe and compositional effects in Cr^{2+}-doped II-VI semiconductors," J. Electron. Mater. **31**, 806 (2002).

[94] P. Cerný, H. Sun, D. Burns, U. N. Roy, and A. Burger, "Spectroscopic investigation and continuous-wave laser demonstration utilizing single crystal Cr^{2+}:CdZnTe," presented at the Advanced Solid-State Photonics (2005).

[95] V. Akimov, M. Frolov, Y. Korostelin, V. Kozlovsky, A. Landman, Y. Podmar'kov, Y. Skasyrsky, and A. Voronov, "Pulsed broadly tunable room-temperature Cr^{2+}:CdS laser," Applied Physics B: Lasers and Optics **97**, 793 (2009).

[96] E. M. Gavrushchuk, "Polycrystalline Zinc Selenide for IR Optical Applications," Inorganic Materials **39**, 883 (2003).

[97] A. Burger, K. Chattopadhyay, J. O. Ndap, X. Ma, S. H. Morgan, C. I. Rablau, C. H. Su, S. Feth, Ralph H. Page, Kathleen I. Schaffers, and Stephen A. Payne, "Preparation conditions of chromium doped ZnSe and their infrared luminescence properties," J. Cryst. Growth **225**, 249 (2001).

[98] J. O. Ndap, K. Chattopadhyay, O. O. Adetunji, D. E. Zelmon, and A. Burger, "Thermal diffusion of Cr^{2+} in bulk ZnSe," J. Cryst. Growth **240**, 176 (2002).

[99] U. Demirbas, A. Sennaroglu, and M. Somer, "Synthesis and characterization of diffusion-doped Cr^{2+}:ZnSe and Fe^{2+}:ZnSe," Opt. Mater. **28**, 231 (2006).

[100] V. A. Akimov, M. P. Frolov, V. Korostelin Yu, V. I. Kozlovsky, A. I. Landman, P. Podmar'kov Yu, and A. A. Voronov, "Vapour growth of II-VI single crystals doped by transition metals for mid-infrared lasers," physica status solidi (c) **3**, 1213 (2006).

[101] S. B. Trivedi, C.-C. Wang, S. Kutcher, U. Hommerich, and W. Palosz, "Crystal growth technology of binary and ternary II-VI semiconductors for photonic applications," J. Cryst. Growth **310**, 1099 (2008).

[102] M. E. Doroshenko, P. Koranda, H. Jelínková, J. Scaronulc, N. M, ecaron, mec, T. T. Basiev, V. K. Komar, A. S. Gerasimenko, and V. M. Puzikov, "Cr:ZnSe prism for broadly tunable mid-infrared laser radiation generation," Laser Physics Letters **4**, 503 (2007).

[103] P. Koranda, H. Jelínková, J. Sulc, M. Nemec, M. E. Doroshenko, T. T. Basiev, V. K. Komar, and M. B. Kosmyna, "ZnSe:Cr^{2+} coherently pumped laser," Opt. Mater. **30**, 149 (2007).

[104] E. Carnall, S.E. Hatch, and W.F. Parson, "Optical studies on hot-pressed Polycrystalline CaF_2 with clean grain boundaries," Mater. Sci. Res. **3**, 165 (1966).

[105] J. Lu, H. Yagi, K. Takaichi, T. Uematsu, J. F. Bisson, Y. Feng, A. Shirakawa, K. I. Ueda, T. Yanagitani, and A. A. Kaminskii, "110 W ceramic Nd^{3+}:$Y_3Al_5O_{12}$ laser," Applied Physics B: Lasers and Optics **79**, 25 (2004).

[106] A. Gallian, V. V. Fedorov, S. B. Mirov, V. V. Badikov, S. N. Galkin, E. F. Voronkin, and A. I. Lalayants, "Hot-pressed ceramic Cr^{2+}: ZnSe gain-switched laser," Opt. Express **14**, 11694 (2006).

[107] S. B. Mirov, V. V. Fedorov, I. S. Moskalev, and D. V. Martyshkin, "Recent progress in transition-metal-doped II-VI mid-IR lasers," IEEE J. Sel. Top. Quantum Electron. **13**, 810 (2007).

[108] P. Moulton, "An investigation of the Co:MgF_2 laser system," Quantum Electronics, IEEE Journal of **21**, 1582 (1985).

[109] A. Di Lieto and M. Tonelli, "Development of a cw polycrystalline Cr^{2+}:ZnSe laser," Opt. Lasers Eng. **39**, 305 (2003).

[110] I. T. Sorokina, E. Sorokin, A. Di Lieto, M. Tonelli, R. H. Page, and K. I. Schaffers, "Efficient broadly tunable continuous-wave Cr^{2+}: ZnSe laser," J. Opt. Soc. Am. B-Opt. Phys. **18**, 926 (2001).

[111] A. Di Lieto, "Development of a cw Co : MgF_2 laser," Opt. Lasers Eng. **39**, 309 (2003).

[112] A. V. Podlipensky, V. G. Shcherbitsky, N. V. Kuleshov, V. I. Levchenko, V. N. Yakimovich, M. Mond, E. Heumann, G. Huber, H. Kretschmann, and S. Kuck, "Efficient laser operation and continuous-wave diode pumping of Cr^{2+}:ZnSe single crystals," Appl. Phys. B **72**, 253 (2001).

[113] H. Jelínková, P. Koranda, M. E. Doroshenko, T. T. Basiev, J. Scaronulc, N. M, ecaron, mec, P, Ccaron, erný, V. K. Komar, and M. B. Kosmyna, "Cr^{2+}:ZnSe laser pumped by 1.66 µm or 1.97 µm radiations," Laser Physics Letters **4**, 23 (2007).

[114] A. Sennaroglu, U. Demirbas, N. Vermeulen, H. Ottevaere, and H. Thienpont, "Continuous-wave broadly tunable Cr^{2+}:ZnSe laser pumped by a thulium fiber laser," Opt. Commun. **268**, 115 (2006).

[115] Y. Yang, "Tm-Doped Fibre Laser Pumped Cr^{2+}:ZnSe Poly-Crystal Laser," Chinese Physics Letters **25**, 116 (2008).

[116] IPG Phoptonics, http://www.ipgphotonics.com, (2010).

[117] I. S. Moskalev, V. Fedorov, and S. Mirov, "Single-Frequency, Widely-Tunable, and Multi-Watt Polycrystalline CW Cr^{2+}:znSe Laser," presented at Advanced Solid State Photonics (2008).

[118] M. Kuznetsov, F. Hakimi, R. Sprague, and A. Mooradian, "High-power (>0.5 W CW) diode-pumped vertical-external-cavity surface-emitting semiconductor lasers with circular TEM_{00} beams," IEEE Photonic Tech. L. **9**, 1063 (1997).

Chapter Two

Consideration of a Tm^{3+}:$YAlO_3$ laser as a pump source for Cr^{2+}-laser

---

2.1 Introduction

The most commonly used pump sources for Cr^{2+}:chalcogenide lasers to date have been the thulium and erbium based solid-state lasers. These systems operate at different wavelengths but have similar upper-state lifetimes (on the order of milliseconds) and both exhibit three-level laser behaviour. To be able to evaluate the use of semiconductor disk lasers as pump sources for Cr^{2+}:II-VI lasers, this chapter will discuss the characteristics of a Tm^{3+}:$YAlO_3$ laser as a representation of more commonly used pump sources.

The use of the rare-earth element thulium in a crystalline laser gain medium was first demonstrated in 1966 in a sensitised holmium-doped yttrium aluminium perovskite (YAP, chemical formula $YAlO_3$) crystal with an emission wavelength of 2.1µm [1,2]. After this initial demonstration, trivalent thulium was doped into $YAlO_3$ without the addition of holmium resulting in a laser emission around 1.9-2.0 µm [2]. Also alternative hosts, such as yttrium lithium fluoride (YLF, chemical formula $LiYF_4$) and yttrium aluminium garnet (YAG, chemical formula $Y_3Al_5O_{12}$) have been used [3,4]. The use of $Y_3Al_5O_{12}$ is advantageous for high power laser embodiments due to its large thermal conductivity, mechanical robustness and good optical quality. However, its cubic structure imposed a significant disadvantage, i.e. the absence of natural birefringence. As a result, thermally induced birefringence associated with the absorption of pump light can lead to depolarisation losses which can impose significant problems in high power lasers [5]. However, $YAlO_3$ and $LiYF_4$ hosts effectively resolve this problem with their biaxial, orthorhombic structure [6].

While both, $YAlO_3$ and $LiYF_4$ show natural birefringence, $LiYF_4$ has a lower thermal fracture limit which makes it less suitable for end-pumped, high-power lasers. It also shows polarisation dependent thermal lensing with a negative thermal lens. This negative lens can potentially be advantageous for high power lasers as it can compensate for bulging of crystal surfaces resulting in a crystal without any lensing properties [7]. On the other hand, asymmetric thermal lensing introduces astigmatism into the output beam of the laser which can be disadvantageous when the system is used as pump source. With a symmetric thermal lens and the capability of producing >10 W of output power [8], Tm^{3+}:$YAlO_3$ is a promising choice as gain medium for a pump laser for chromium-chalcogenide.

Initially, Tm^{3+}:$YAlO_3$ was pumped using flash lamps [2]; however, soon solid-state lasers (Ti:sapphire) were used [9] and nowadays the preferred method of using diode laser pumping has become established [10].

Typically grown by the Czochralski method, Tm^{3+}:$YAlO_3$ has three kinetically favoured forms, hexagonal, orthorhombic and cubic, known as $YAlO_3$-I, $YAlO_3$-II, $YAlO_3$-III, respectively [11], with the most typically used form being orthorhombic [12,13]. In this form, the crystals have 3 different crystallographic symmetry axes, i.e. the a, b and c orientation. As a consequence the absorption and gain of Tm^{3+}:$YAlO_3$ are polarisation dependent and can be influenced by the orientation of the crystal [9]. The absorption and emission spectrum recorded by Stoneman et al. can be seen in Figure 2.1 [9]. This shows, that the strongest absorption of Tm^3+:$YAlO_3$ can be found at 795 nm for the a- and b-cut crystals while the c-cut crystals show a double peak in the absorption spectrum at 793 and 799 nm. The emission is centred at ~1.9 μm and can, depending on the crystal cut, be tuned between ~1.85 and 1.95 μm.

Within the crystalline structure, the trivalent thulium populates the Y^{3+} sites. The active ion is located in the ^4F electron site which is typical for rare-earth ions. As these electron sites are shielded by the outer ^3D shells, ion-host interactions are small contrary to transition-metal ions such as chromium. The energy levels of the laser transition are therefore not greatly broadened and show relatively narrow absorption and emission features compared to their transition-metal counterparts.

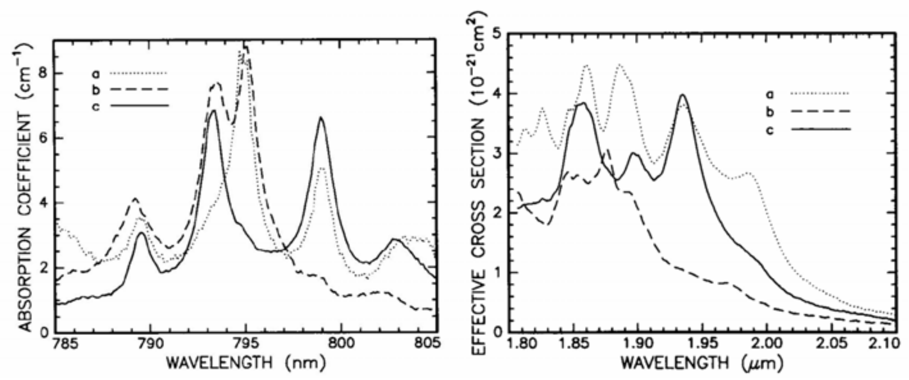

Figure 2.1 Absorption (left) and emission spectrum (right) of Tm^{3+}:YAlO$_3$ for the different polarisation orientations for a 4 % doped crystal (after Stoneman et al. [9]).

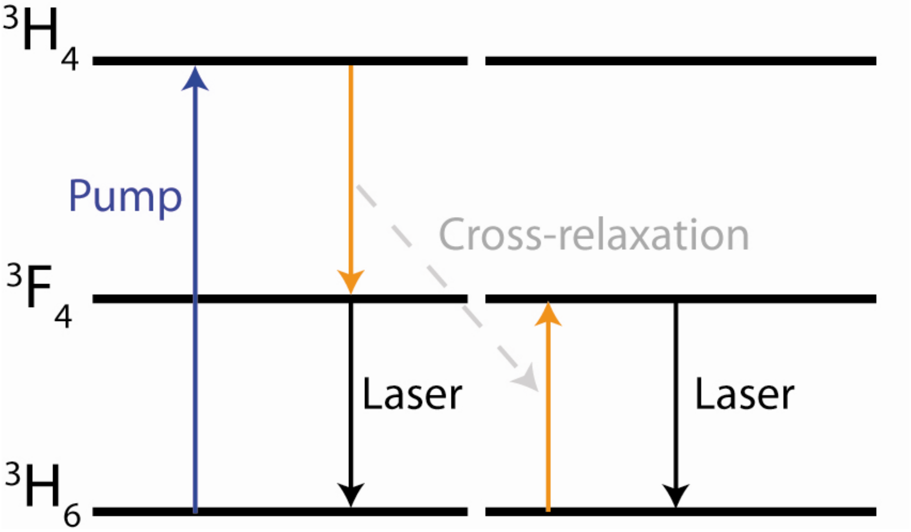

Figure 2.2 Simplified energy diagram of the transitions in a Tm^{3+}:YAlO$_3$ active host.

A simplified energy diagram of Tm^{3+}:YAlO$_3$ can be seen in Figure 2.2. One property of this energy diagram is that it exhibits a quasi-3-level behaviour [14]. The pump radiation excites the ions in the crystal to the $^3H_4$ energy level multiplet from where they decay non-radiatively into the upper laser level $^3F_4$ multiplet. This transition is fast compared to the lifetime of the upper laser level $^3F_4$ (4 ms) [15]. This is important because otherwise a population inversion could not be achieved in the $^3F_4$ level. From this level, the electrons relax back into the ground state multiplet. Due to the quasi-3-level nature of this material, the ground state is not a single state but a band of energy levels that are closely spaced. As a consequence, their population follows the Boltzmann distribution [16]. Contrary to the 4-level energy diagram, a population inversion is not reached after the first ion is excited as the population of the lower laser level within the ground energy band needs to be overcome. However, this system is more correctly described as a quasi 3-level system and so the population inversion does not require as much as 50 % of the total population to be excited as would be the case in a pure 3-level system.

The relatively long upper-state lifetime of Tm^{3+}:YAlO$_3$ results in relatively large amounts of stored energy in the gain medium. This can be advantageous for Q-switched lasers; however, for a continuous-wave (cw) laser, this can potentially introduce strong intensity fluctuations, which is a well known drawback of these lasers [17]. A solution to this issue will be discussed in section 2 of this chapter.

Another noteworthy point in Tm^{3+}:YAlO$_3$ is the process of cross-relaxation which is typically seen for doping levels exceeding ~3 % [18]. When a photon is absorbed and excites the valence electron from the ground state to the $^3H_4$ multiplet, the relaxation of this electron to the upper laser level ($^3F_4$) releases sufficient energy to excite another electron in a neighbouring ion. As a result, a single pump photon can generate two excited ions in the upper laser level leading to a quantum efficiency of almost two. Aside from the increased efficiency of the system, this also effectively reduces the large quantum defect of 60 % to 15 %.

In this chapter, a Tm^{3+}:YAlO$_3$ lasers using two different crystals cut along the a- and b-axis will be investigated. The experimental arrangement of the laser will be discussed in section 2 of this chapter with emphasis on an active stabilisation loop that allows the compensation of intensity noise spikes in the laser output when running cw. Section 3 will discuss the experimental results and compare the a- and b-cut geometry.

2.2 Experimental arrangement

The experimental configuration was based on the one demonstrated by Cerny et al. in 2005 [19]. The crystals used for the experiments were thulium-doped YAlO$_3$ rods obtained from Scientific Materials, Inc. (Bozeman, MT) [20]. Both samples had a diameter of 3 mm and were anti-reflection coated for the pump and oscillating wavelength. While sample 1 was cut along the a-axis and 5 mm long, sample 2 was a b-cut crystal with a length of 8 mm. The doping concentration for both of these samples was 4 % at.

The pump source for this system was a fibre-coupled (600 µm core diameter) diode laser with a maximum output power of 25 W (Thales TH-1725-F6). The laser emitted radiation at around 795 nm and was driven using a Glassman LP 20-60 power supply. A Coherent Field Mate power meter in combination with a Coherent PM10 thermopile head was used to record the current to power conversion for this diode (Figure 2.3). To increase the lifetime of the pump laser, the driver current was limited to 36 A, resulting in a maximum available pump power of 20 W. With the base plate temperature of the diode laser stabilised to 20 °C (using a recirculating water bath chiller) the output spectrum of the laser was centred at 796.5 nm with a full width half maximum (FWHM) of 2.7 nm (see inset of Figure 2.3).

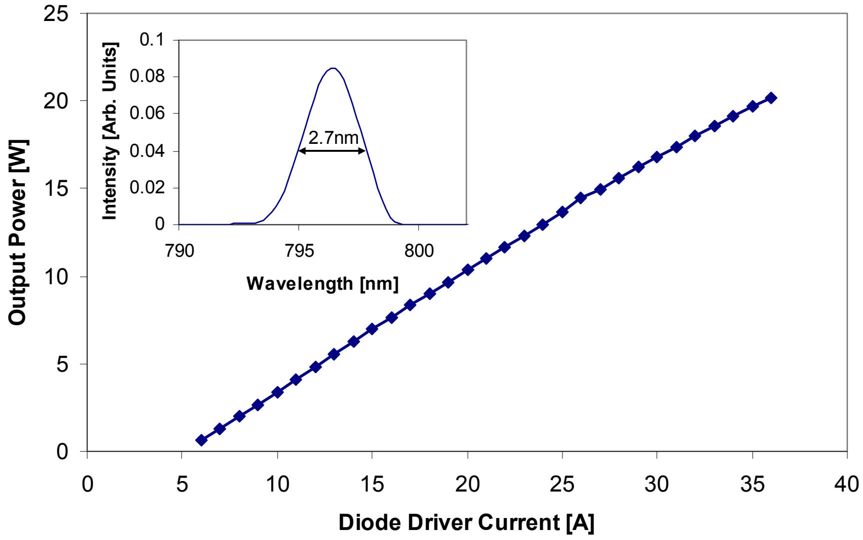

Figure 2.3 Current to power conversion characteristics of the 800 nm diode laser pump source for the Tm^{3+}:$YAlO_3$ laser. **Inset:** Spectral width of the diode laser at 20 W of output power.

As the relatively narrow absorption feature of Tm^{3+}:$YAlO_3$ is centred at 795.6 nm for both, the a- and b-cut crystals, the emission wavelength of the diode laser was crucial to achieve a maximum absorption of the pump radiation. When leaving the base plate temperature of the laser set to 20 °C, the wavelength of the laser changed between 788-796.5 nm (Figure 2.4) over the diode driver current range. To tune the wavelength to the absorption peak of Tm^{3+}:$YAlO_3$ the temperature of the diode laser base plate needed to be adjusted accordingly. The inset of Figure 2.4 shows the required temperature to maintain an output wavelength of 795.6 nm over the range of the driver current.

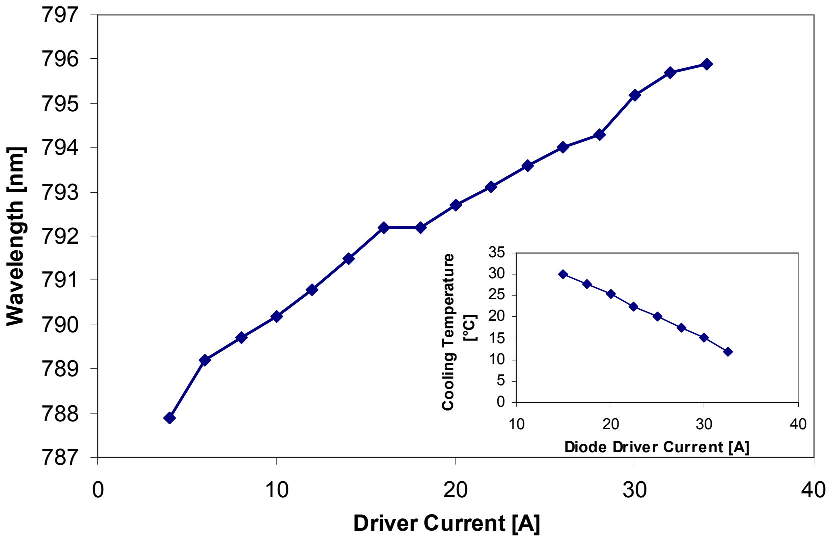

Figure 2.4 Wavelength drift of the diode laser with increasing drive current when temperature stabilised to 20 °C**. Inset:** Water bath temperature required for emission of 795.6 nm with changing pump current.

To pump the Tm^{3+}:$YAlO_3$ crystals using this diode laser, the radiation was conditioned using two 40 mm focal length lenses, one for collimation of the fibre output and one to focus the radiation into the crystal.

The experimental arrangement (see Figure 2.5) of the Tm^{3+}:$YAlO_3$ resonator comprised two curved mirrors M_1 and M_2 with 300 and 500 mm radius of curvature respectively. Both of these mirrors were coated for high reflectivity at 1.94 µm and high transmission at the pump wavelength. The cavity was completed using plane output coupling mirrors with reflectivity values between 80-98 %. A photograph of the laser can be seen in Figure 2.6.

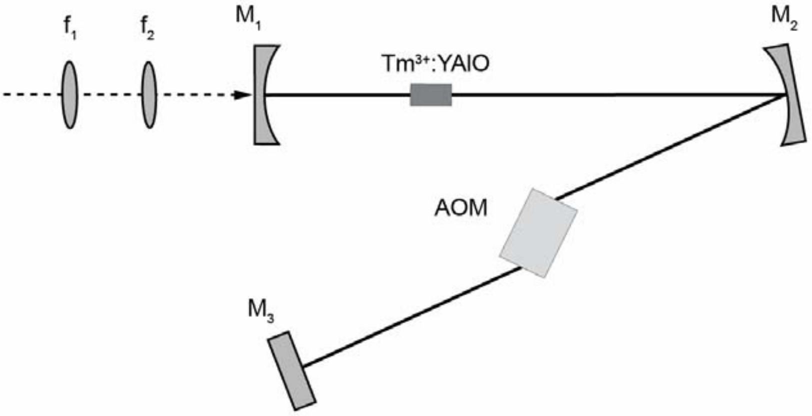

Figure 2.5 Schematic of the Tm^{3+}:$YAlO_3$ laser comprising a 300 mm and a 500 mm radius of curvature mirror (M_1 and M_2) and a plane output coupler (M_3). To stabilise the output intensity, an acousto-optical modulator is used.

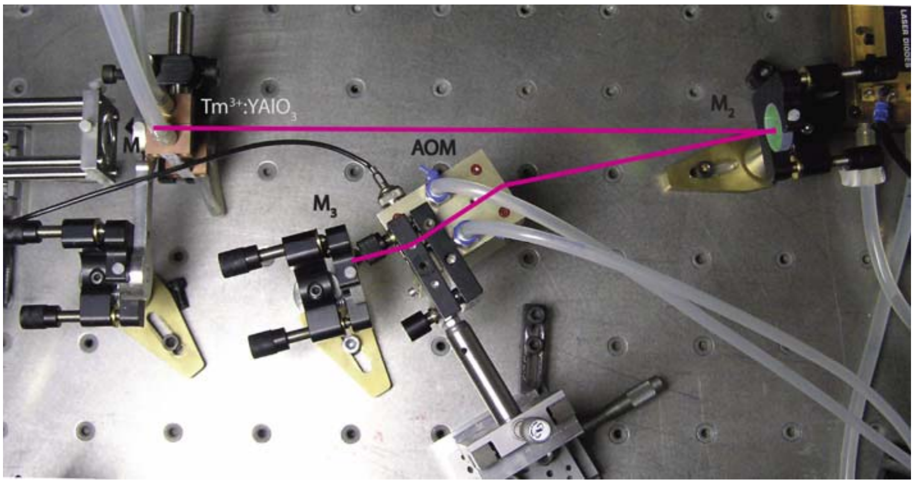

Figure 2.6 Photograph of the Tm^{3+}:$YAlO_3$ laser comprising of a 300 mm and 500 mm radius of curvature mirror (M_1 and M_2), a plane output coupler (M_3) and an acusto optical modulator (AOM).

Using the resonator modelling software WinLase (version 2.1 Professional) the beam propagation inside of the resonator was determined and is shown in Figure 2.7. This shows that the resonator waist was actually not positioned at the crystal but behind it. This was done to optimize the overall mode-match of the pump and resonator beam for the pump focusing lenses used.

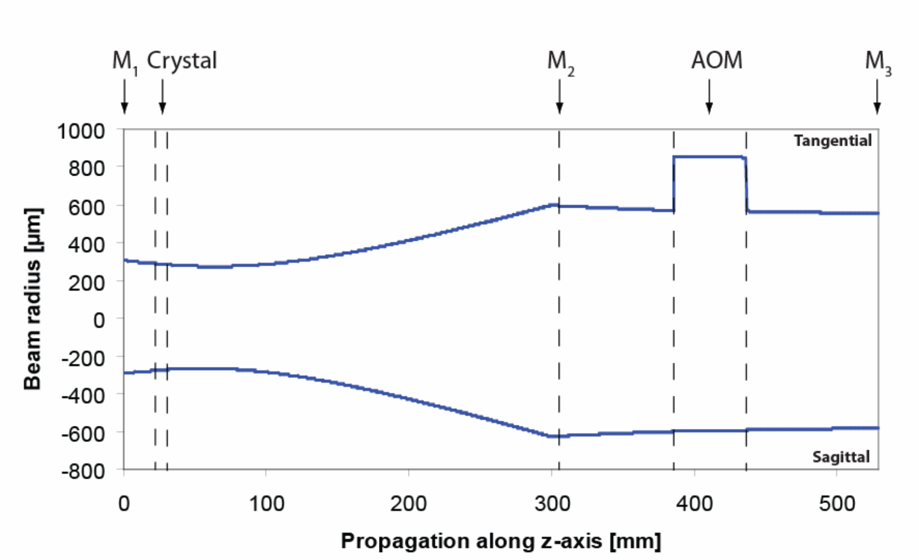

Figure 2.7 Winlase diagram of the Tm^{3+}:$YAlO_3$ resonator for the sagittal and tangential plane.

It was already mentioned in the introduction that the long upper-state lifetime in Tm^{3+}:$YAlO_3$ combined with its quasi-3-level energy characteristics causes the output intensity to fluctuate strongly. The large amount of energy storage enables noise in the cavity to be amplified and form strong spiking and relaxation oscillations [21].

This can damage the Tm-laser itself or any laser which it is being used to pump. In order to alleviate this problem, an intracavity acousto-optic modulator (AOM) was driven by an active feedback loop [17] as depicted in the block-diagram in Figure 2.8.

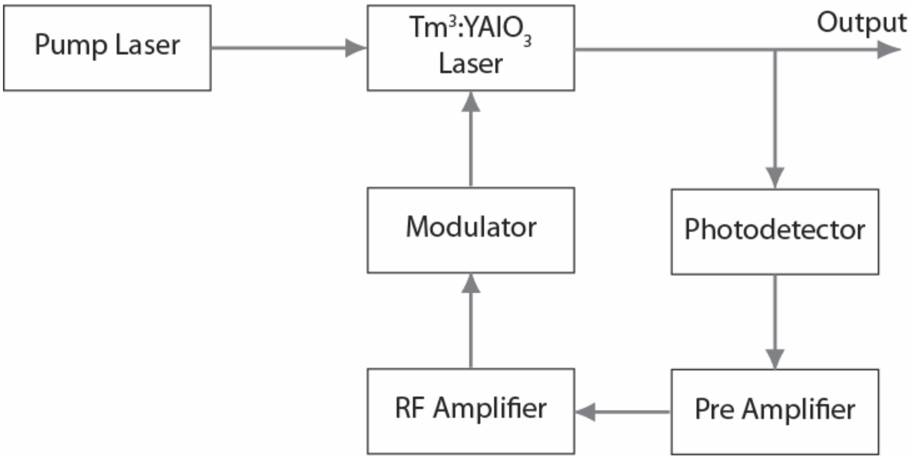

Figure 2.8 Block diagram of the control loop implemented into the laser to stabilise the output intensity.

Here, some residual light that passes through one of the high reflecting mirrors is used to detect the intensity variation of the intracavity field. A simple in-house-build DC operational amplifier as shown in Figure 2.9 was used as a variable gain pre-amplifier to condition the signal before injecting it into the RF amplifier (Intra Action Corp., GE-2725).

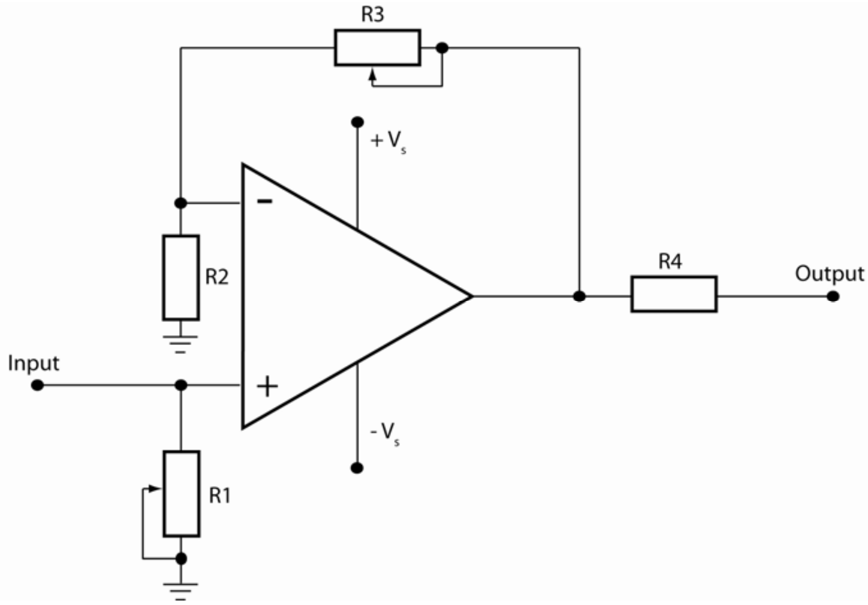

Figure 2.9 Schematic of the preamplifier circuit based on an operational amplifier and resistors R1-R4.

The main component of the pre-amplifier is a low noise (0.9 nV/√Hz) operational amplifier (Analogue Devices AD797) with a bandwidth of 280 kHz. In the circuit, the potentiometer R1 (100 kΩ) is used to adjust the input impedance of the circuit while the fixed resistor R4 sets the output impedance to 50 Ω. The ratio of the resistor R2 (1 kΩ) and the potentiometer R3 (<500 kΩ) set the gain of the amplifier.

After preconditioning of the signal and injecting it into the RF amplifier that drives the AOM, losses proportional to the intensity fluctuations are added to the cavity. This counteracts the build-up of noise spikes and therefore stabilises the intra-cavity field. It should be noted that the pre-amplifier was DC-coupled. As a consequence a constant signal is present at the AOM as soon as the laser oscillates. This results in a non-zero loss inside the resonator for a steady-state condition, which enables the modulation of the signal field in both directions.

2.3 Experimental discussion

2.3.1 A-cut Tm^{3+}:$YAlO_3$ crystal

The first experimental investigations of the Tm^{3+}:$YAlO_3$ laser were carried out using the a-cut crystal.

While the laser was oscillating, the pump absorption was measured for incident pump powers from 2-20 W. The result of the measurement can be seen in Figure 2.10. While the absorption is not fully linear, a consequence of a poorly stabilised wavelength of the pump diode, no absorption saturation was observed. On average, ~80 % of the incident pump power was absorbed inside the crystal. Using the Lambert-Beer law of absorption given in equation 2.1, the resulting absorption coefficient was calculated to be 11 cm^{-1}.

$$I_1 = I_0 \cdot e^{-\alpha \cdot l} \qquad \textbf{Equation 2.1}$$

In this equation, I_0 and I_1 are the incident and transmitted intensities (or power in this case), l the length of the crystal and α the absorption coefficient. It is worth noting, that absorbing less than 100 % of the incident pump light is important in the context of quasi-3-level laser systems, as transparency is only achieved throughout the whole crystal if the whole length is being pumped strongly enough. Crystals are therefore typically designed to be 2-3 absorption lengths long, i.e. between 87-95 % pump absorption.

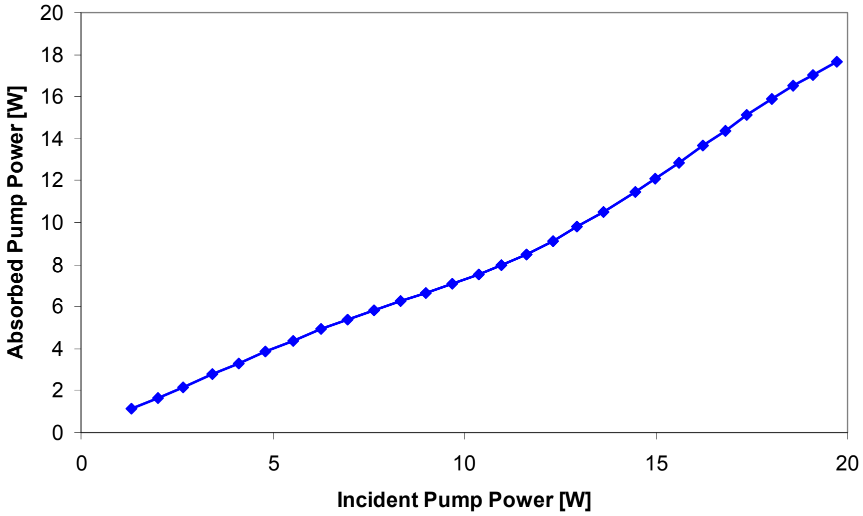

Figure 2.10 Pump absorption measurement for the a-cut Tm^{3+}:YAlO$_3$ crystal when oscillating.

Using the absorbed pump power as reference, power transfer curves were recorded for various output couplers with reflectivities between 80-98 %. These are shown in Figure 2.11.

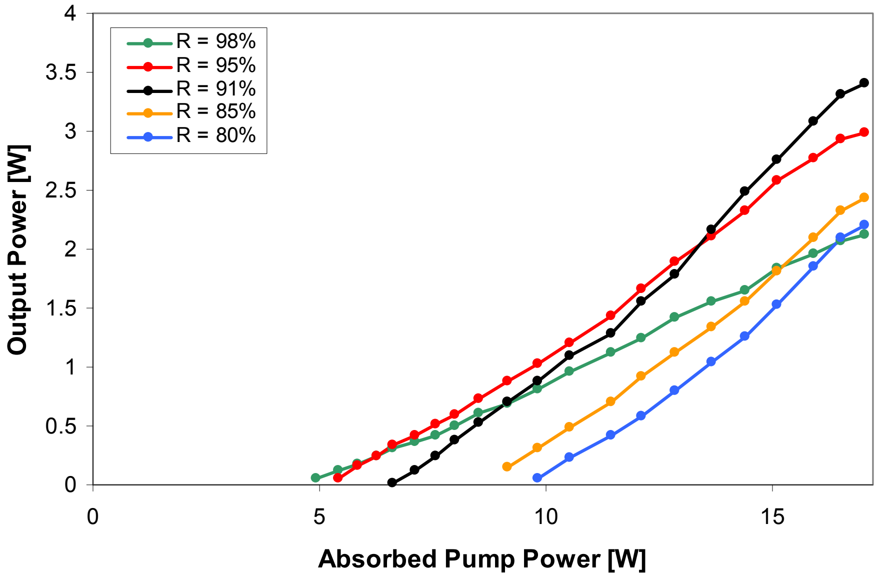

Figure 2.11 Power transfer characteristics of the Tm^{3+}:YAlO$_3$ laser using various output couplers with reflectivities between 80-98 %.

The result indicates that for the maximum pump power, an optimum output coupler reflectivity of R=91 % was found. This gave a maximum output power of 3.4 W for an absorbed pump power of 17.5 W (20 W of incident power). The maximum slope efficiency was found to be 35 % and the threshold 6.6 W.

As mentioned earlier in this chapter, the wavelength of the diode laser is crucial to obtain optimum overall system performance. To investigate the strength of this effect, the output power was monitored for a variation in the base plate temperature of the diode laser from 12-30 °C. The result of the measurement can be seen in Figure 2.12. A significant power drop from 2.5 to 0.8 W was observed over the full range of temperature variation. The result also indicates that cooling the diode laser to lower temperatures could be advantageous, as no isolated peak was observed as would be expected. However, further cooling was not done to prevent water condensation on the diode laser.

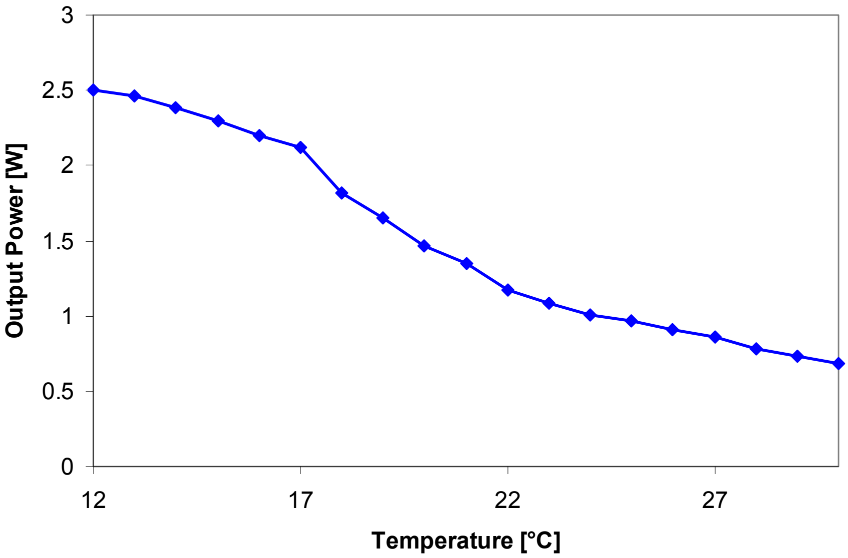

Figure 2.12 Output power variation with changing diode laser base plate temperature for the a-cut crystal.

For the analysis of the intensity noise stabilisation using the AOM arrangement discussed previously, the output of the laser was attenuated and recorded using a photodiode (Teledyne Judson Technologies, J23-5I-R03M-2.6) and oscilloscope (Agilent Infiniium 54830B). To stimulate intensity noise spikes inside the Tm^{3+}:$YAlO_3$ resonator, the 20 W output radiation of the pump laser was modulated using a mechanical chopper to initiate relaxation oscillation. The result of the comparison – with and without the stabilisation loop - can be seen in Figure 2.13.

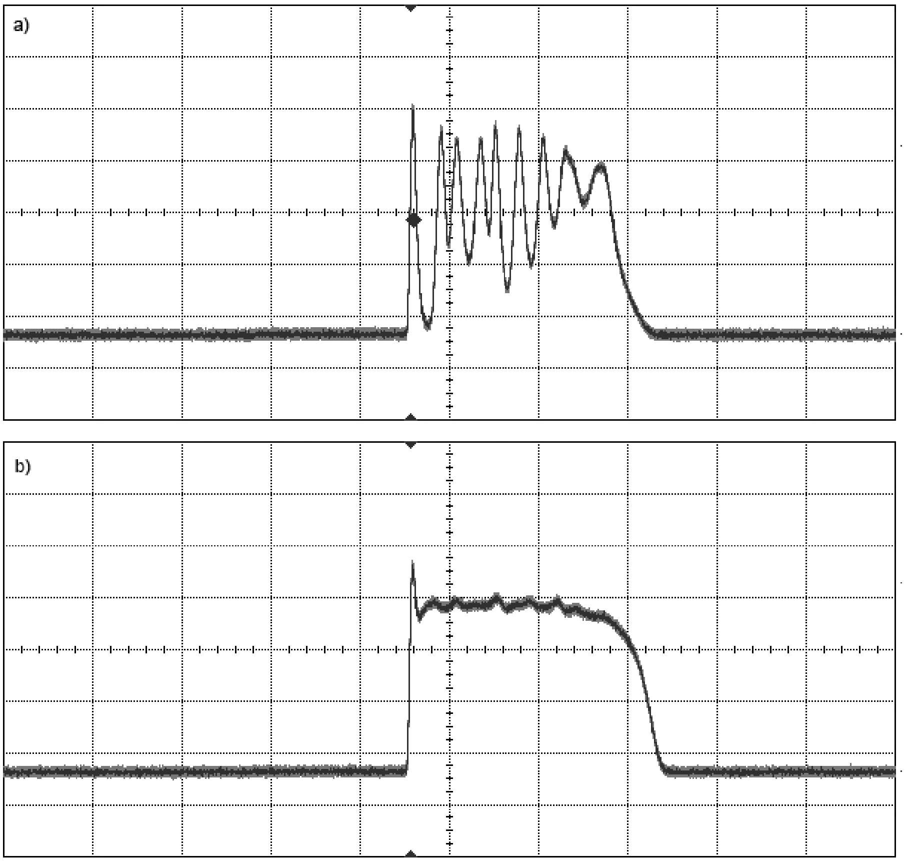

Figure 2.13 Output signal of the Tm^{3+}:$YAlO_3$ laser when pumped in quasi-cw mode without the active stabilisation (a) and with the stabilisation loop activated (b).

From this data it can be seen that significant spiking and intensity noise fluctuations are present without the stabilisation turned on (Figure 2.13a). For the stabilised laser, the output was optimised by carefully positioning the AOM and adjusting the amplifier gain. This strongly damped the fluctuating of the output signal and improved its stability (Figure 2.13b), an important property when considering the Tm^{3+}:$YAlO_3$ laser a pump source.

To investigate the tunability of the output wavelength of the Tm^{3+}:$YAlO_3$ laser, a 2 mm thick crystalline quartz plate was inserted into the resonator at Brewster's angle to act as birefringent filter (BRF). This allowed tuning of the laser between 1.88 and 2.02 μm (Figure 2.14). The insertion of the BRF, however, reduced the output power of the laser to 2.8 W. It was also observed, that no smooth tuning was obtained. This effect was already reported in the literature. Especially before the introduction of a-cut crystals, crystals cut along the b-axis had problems with smooth tuning. In the case of these experiments, the tuning was restricted by two broad H_2O and CO_2 absorption bands.

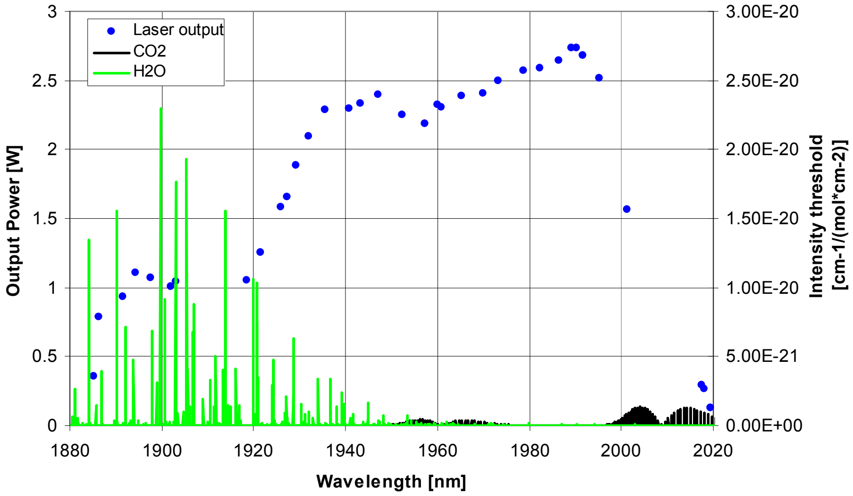

Figure 2.14 Tuning curve of the Tm^{3+}:$YAlO_3$ laser (blue) and the H_2O (green) and CO_2 (black) absorption lines obtained from the HITRAN 2004 database.

Polarisation losses due to birefringence were also investigated. This was considered as the insertion of the BRF, i.e. a polarisation defining element, reduced the output power of the laser by 18 %, indicating that depolarisation losses were present. Therefore a crystal mount with fine adjustment for the rotation around the optical axis was employed. This allowed precise alignment of the crystal and its associated birefringence axis with the polarisation plane of the resonator (defined by the intracavity BRF). This, however, did not solve the problem but the unsmooth tuning remained. Subsequent communication with colleagues in the Czech Republic have revealed that this effect is present to varying degrees in Tm-hosts and is currently not well understood [22]. As the precise control of the emission wavelength is not required for pumping of chromium-chalcogenide lasers, it was decided not to currently investigate this problem further.

2.3.2 B-cut Tm^{3+}:$YAlO_3$ crystal

For the b-cut crystal, again, the absorption coefficient was determined. The result of the measurement can be seen in Figure 2.15. The absorption of the 8 mm crystal was found to be 92 % on average over the range of available pump powers. This equates to an absorption coefficient of 6.7 cm^{-1}. Again, slight nonlinearities can be observed that were associated with the temperature drift of the diode laser.

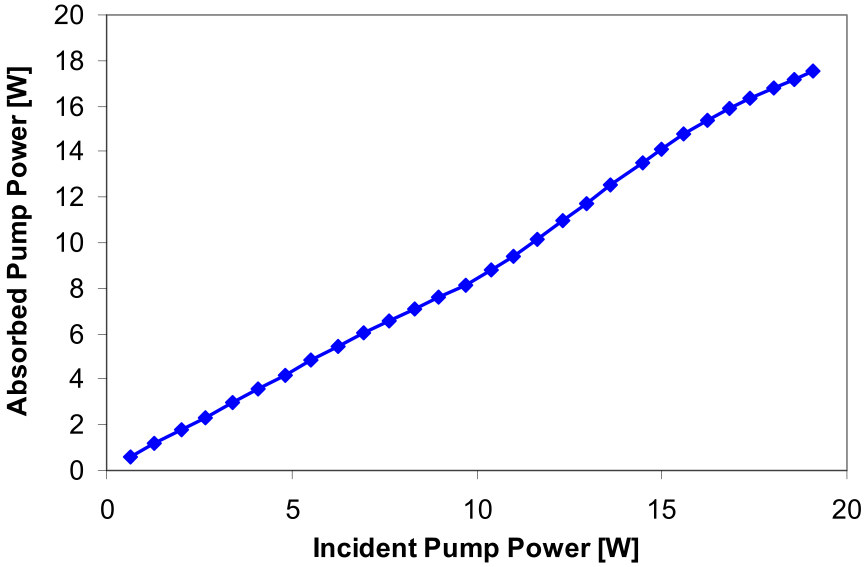

Figure 2.15 Absorption measurement results for the b-cut Tm^{3+}:$YAlO_3$ crystal when oscillating.

Comparing the power transfer curves (Figure 2.16) for the b-cut crystal and the a-cut crystal reveals a significantly lower output power from the b-cut crystal (1.8 rather than 3.5 W). This can be attributed to a lower slope efficiency as well as a higher threshold which is in the order of 1.5 times higher in case of the b-cut crystal. This difference is associated with increased reabsorption losses at around 1.94 μm [19].

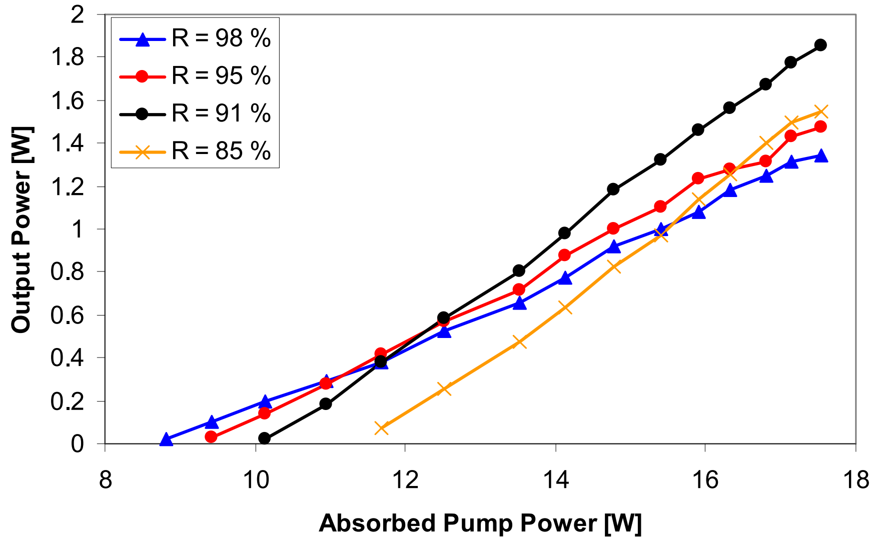

Figure 2.16 Power transfer characteristic for the Tm^{3+}:$YAlO_3$ laser using the b-cut crystal and output couplers with values between 85-98 %.

Again, the tuning curve was recorded using a grating monochromator. The results are plotted in Figure 2.17. Here even stronger modulation of the tuning curve compared to the a-cut crystal is obvious. With a tuning curve ranging from 1.91-1.99 µm and a peak at ~1.94 µm, the overall output spectrum is centred at shorter wavelength compared to the centre at 1.98 µm for the a-cut result. In addition, the tuning range of the b-cut crystal is 80 nm; significantly smaller compared to the a-cut crystal (140 nm). This can be associated with the different crystal length used in these experiments and the resulting performance difference which is clearly evident from the reduced peak output power of the b-cut crystal compared to the a-cut one. This clearly limits the tuning boundaries of the b-cut crystal contrary to what can be expected from the literature [9]. For the purpose of pumping Cr^{2+}:chalcogenide lasers, the difference in the peak position should not be considered a major disadvantage. Indeed, the shorter output wavelength of the b-cut crystal could be considered beneficial as it is closer to the absorption peak of Cr^{2+}:ZnSe. This, however, can potentially be offset by the increased performance of the a-cut crystal.

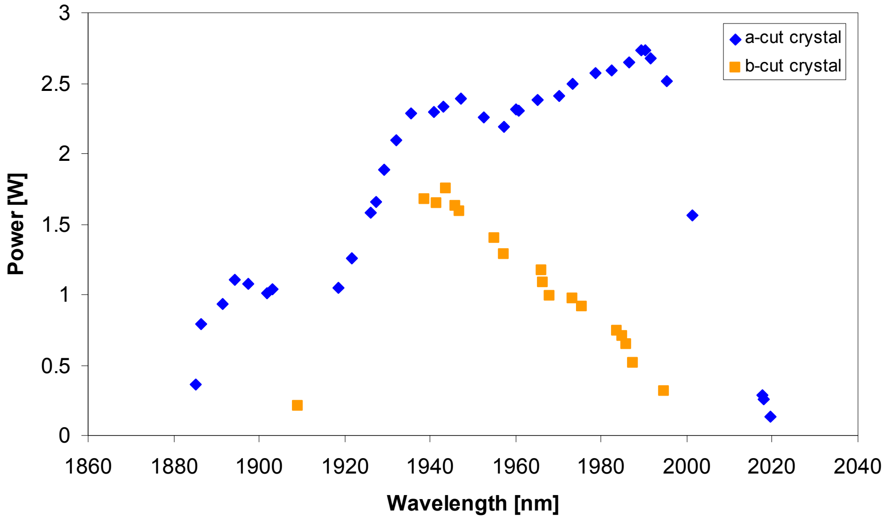

Figure 2.17 Tuning curve of the Tm^{3+}:YAlO$_3$ laser using the 8 mm long b-cut crystal (orange curve). For comparison, the results of the a-cut crystal are shown as well.

2.4 Conclusion

A Tm^{3+}:YAlO$_3$ laser was investigated as a representative of pump sources typically used for chromium-chaclogenide laser. In this context, a- and b-cut Tm^{3+}:YAlO$_3$ crystals were investigated. The a-cut crystal exhibited up to 3.4 W of output power with a slope efficiency of 38 % and a threshold of 6.6 W for an output coupler reflectivity of 91 %. Using a 2 mm thick quartz birefringent filter, tuning was achieved between 1.88 and 2.02 µm. However, the tuning was found to be strongly modulated rather than smooth, an effect known in $YAlO_3$ hosts but not fully understood yet. This effect is even stronger in the b-cut crystal where the tuning curve was shifted towards lower wavelength with its peak emission at 1.94 µm. The spectral range covered from this crystal was 1.91-1.99 µm.

The maximum output power of the b-cut crystal was significant lower than the one of the a-cut crystal with a maximum of 1.8 W. This reduced performance was attributed to increased reabsorption losses at the lower operating wavelength of 1.94 µm.

The observed intensity noise issues with Tm^{3+}:$YAlO_3$ were reduced by employing an active feedback loop into the laser. This was based on an acusto-optical modulator that added losses proportional to the intracavity intensity noise to the intracavity field. This reduced the spiking behaviour of the laser significantly which is considered beneficial when using this laser as a pump source.

With multi-Watt output powers and the stabilised output, the Tm^{3+}:$YAlO_3$ laser should be ideal of pumping of Cr^{2+}:chalcogenide crystals. With the emission shifted towards 2.0 µm in case of the a-cut crystal, the emission is moving further away from the absorption peak of Cr^{2+}:chalcogenides (e.g. 1.79 µm for Cr^{2+}:ZnSe). This reduced absorption, however, can be compensated for by the increased output power of the a-cut crystal compared to the b-cut arrangement. Additionally, the reduced absorption coefficient can be mitigated by increasing the crystal length of the chromium laser or employing pump retro-reflection. Therefore the a-cut arrangement was used in the subsequent work.

Table 2.1 shows the comparison of the obtained experimental results with the demands for an ideal pump source outlined in chapter 1.

Parameter	**Required**	**Achieved**
Power [W]	Watt-level	3.4
Wavelength [µm]	1.6-2.1	1.98
RMS Noise [%]	<2	Quantification required
Sensitivity towards feedback	low	unknown

Table 2.1 Comparison of desired properties of a pump source for chromium-doped chalcogenide lasers and the Tm^{3+}:$YAlO_3$ discussed in this chapter.

References

[1] L. F. Johnson, J. E. Geusic, and L. G. Van Uitert, "Efficient, high-power, coherent emission from Ho^{3+} ions in yttrium aluminum garnet, assisted by energy transfer," Appl. Phys. Lett. **8**, 200 (1966).

[2] M. J. Weber, M. Bass, Varitimo.Te, and D. P. Bua, "Laser Action from Ho^{3+}, Er^{3+}, and Tm^{3+} in Yalo$_3$," IEEE J. Quantum Eelect. **QE 9**, 1079 (1973).

[3] P. A. Budni, L. A. Pomeranz, M. L. Lemons, C. A. Miller, J. R. Mosto, and E. P. Chicklis, "Efficient mid-infrared laser using 1.9 µm-pumped Ho:YAG and ZnGeP2 optical parametric oscillators," J. Opt. Soc. Am. B **17**, 723 (2000).

[4] P. J. M. Suni and S. W. Henderson, "1 mJ/pulse Tm:YAG laser pumped by a 3 W diode laser," Opt. Lett. **16**, 817 (1991).

[5] W. Koechner, in *Springer Series in Optical Sciences*, edited by W. T. Rhodes Spring Science + Business Media, Inc., New York, pp. 535 (2006).

[6] I. F. Elder and M. J. P. Payne, "YAP versus YAG as a diode-pumped host for thulium," Opt. Commun. **148**, 265 (1998).

[7] X. M. Duan, B. Q. Yao, Y. J. Zhang, C. W. Song, L. L. Zheng, Y. L. Ju, and Y. Z. Wang, "Diode-pumped high efficient Tm:YLF laser output at 1908 nm with near-diffraction limited beam quality," Laser Physics Letters **5**, 347 (2008).

[8] X. Cheng, F. Chen, G. Zhao, and J. Xu, "High-efficiency, high-power, diode-pumped continuous-wave Tm:YAlO$_3$ slab lasers," Appl. Phys. B **97**, 639 (2009).

[9] R. C. Stoneman and L. Esterowitz, "Efficient 1.94 µm Tm:YAlO Laser," IEEE J. Sel. Top. Quantum Electron. **1**, 78 (1995).

[10] R. C. Stoneman, L. Esterowitz, and B. J. Feldman, in *Leos '95 - Ieee Lasers and Electro-Optics Society 1995 Annual Meeting - 8th Annual Meeting Conference Proceedings, Vols. 1 & 2* I E E E, New York, pp. B453 (1995).

[11] B. Basavalingu, H. N. Girish, K. Byrappa, and Kohei Soga, "Hydrothermal synthesis and characterization of orthorhombic yttrium aluminum perovskites (YAP)," Materials Chemistry and Physics **112**, 723 (2008).

[12] M. J. Weber, M. Bass, K. Andringa, R. R. Monchamp, and E. Comperchio, "Czochalski growth and properties of YAlO$_3$ laser crystals," Appl. Phys. Lett. **15**, 342 (1969).

[13] Y. L. Lu, J. Wang, Y. Yang, Y. B. Dai, A. P. Dong, and B. D. Sun, "Growth and optical properties of Tm:YAlO single crystals with different Tm concentrations," J. Alloy. Compd. **429**, 296 (2007).

[14] W. Koechner, in *Springer Series in Optical Sciences*, edited by W. T. Rhodes Spring Science + Business Media, Inc., New York, pp. 27 (2006).

[15] I. F. Elder and J. Payne, "Diode-pumped, room-temperature Tm:YAP laser," Appl. Opt. **36**, 8606 (1997).

[16] W. Koechner, in *Springer Series in Optical Sciences*, edited by W. T. Rhodes Spring Science + Business Media, Inc., New York, pp. 25 (2006).

[17] P. Cerny, G. J. Valentine, and D. Burns, "Actively stabilised diode pumped Tm : YAIO laser," Electron. Lett. **40**, 1061 (2004).

[18] W. Koechner, in *Springer Series in Optical Sciences*, edited by W. T. Rhodes Spring Science + Business Media, Inc., New York, pp. 94 (2006).

[19] P. Cerny and D. Burns, "Modeling and experimental investigation of a diode-pumped Tm : YAlO$_3$ Laser with a- and b-cut crystal orientations," IEEE J. Sel. Top. Quantum Electron. **11**, 674 (2005).
[20] Scientific Materials Ltd., http://www.scientificmaterials.com.
[21] A. E. Siegman, in *Lasers*, edited by A. Kelly University Science Books, Sausalito, CA, pp. 962 (1986).
[22] P. Cerny and H. Jelinkova, Czech Technical University in Prague 2009.

Chapter Three

GaSb-based semiconductor disk lasers

3.1 Introduction

In the previous chapter, a Tm^{3+}:$YAlO_3$ laser was discussed as a representative of a class of conventional sources used to pump Cr^{2+}:chalcogenide lasers. In this chapter, the optically-pumped semiconductor disk laser (SDL) will be introduced as a novel type of laser source that can be used to pump Cr^{2+}:II-VI lasers.

The SDL, also known as vertical external-cavity surface-emitting laser (VECSEL), is a category of laser that is similar in many respects to the optically-pumped doped-dielectric disk laser [1]. Here, a thin semiconductor platelet is optically pumped and used as the active medium inside an optical resonator (see Figure 3.1).

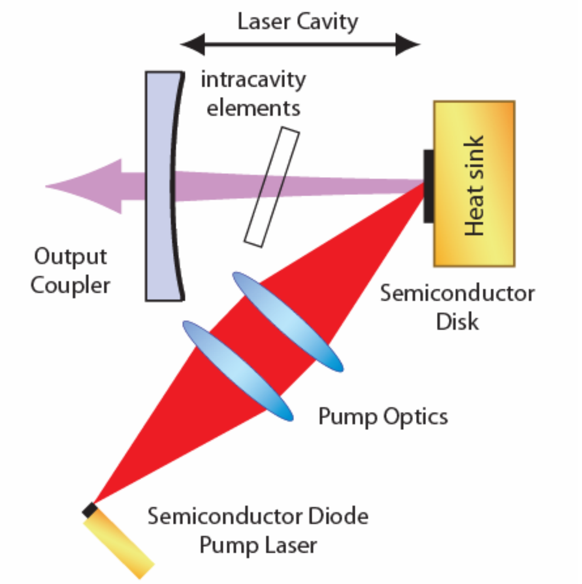

Figure 3.1 Schematic of a semiconductor disk laser including the semiconductor pump diode laser, the active semiconductor chip, an external output coupling mirror as well as any optional intracavity element.

The laser that would now be recognised as an SDL was first demonstrated in 1966 [2] but it was not until the end of the 20th century that the full potential of this laser format was realised [3]. In contrast to the gain medium in typical doped-dielectric lasers, the semiconductor chip is not a homogeneous piece of material but a complex epitaxial structure made of an integrated distributed Bragg reflector (DBR), pump absorbing barriers and quantum wells and is thus more similar to vertical-cavity surface-emitting lasers (VCSELs) [4,5] but without the top DBR. However, the SDL utilises optically pumping instead of the electrical pumping used in VCSELs. This, combined with the external cavity, allows for control of the cavity and pump mode and therefore enables power scaling [6] as well as brightness optimisation [7]. Additionally, the external cavity allows for the use of intra-cavity elements that enable a wide range of operational modes such as active and passive modelocking [8], narrow linewidth operation [9] and intracavity frequency conversion techniques [10].

Intracavity frequency conversion is one way of extending the emission range of these lasers into the UV and visible [6,11-15]; however, direct generation of radiation in various wavelength bands is also possible utilising the wide range of semiconductor materials available.

For the visible, e.g. (AlInP)(AlGaInP)(GaAs) has been used to generate direct emission in the red [16] while for the important telecommunication band, GaInNAs and InGaAsP-based SDLs have been developed emitting at various wavelengths between 1.2 and 1.55 µm [17-20]. For a summary of the state of the art values in respect to emission wavelength and output powers see Figure 3.2.

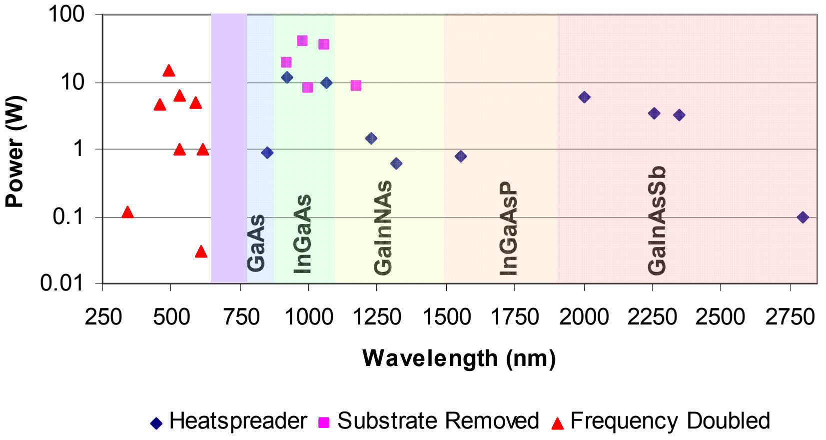

Figure 3.2 Overview of wavelength coverage of the SDL technology by fundamental and harmonic generation of radiation and the maximum output power achieved.

In the context of this work, the (AlGaIn)(AsSb) material system was chosen to gain access to the very important molecular fingerprint region above 2 µm. So far, emission from this material system has been demonstrated at various wavelengths between 2.0 and 2.8 µm [7,21-23]. Initially limited to a few milliwatts [21], careful design of the structures and appropriate heat management has resulted in output levels of multiple watts [24-26].

In this chapter (AlGaIn)(AsSb)-based SDLs emitting at 2.0 and 1.9 µm with multi-Watt continuous-wave (cw) output powers will be presented. After introducing the design of the semiconductor chips, the very important aspect of heat management will be discussed, followed by the characterisation and optimisation of the 2.0 and 1.9 µm SDLs in respect to power, wavelength tuning and brightness. In the last section, the use of multichip arrangements to scale the output power beyond that achieved with a single chip will be discussed.

3.2 Semiconductor disk laser chip design

When designing a semiconductor chip for a specific wavelength, the choice of material is not only important for the target emission wavelength of the SDL but also the mechanical aspects of the material composition. This requires that the lattice constant of the components are matched to reduce structural stress and therefore allow high quality single crystal growth, hence a chip with good mechanical integrity.

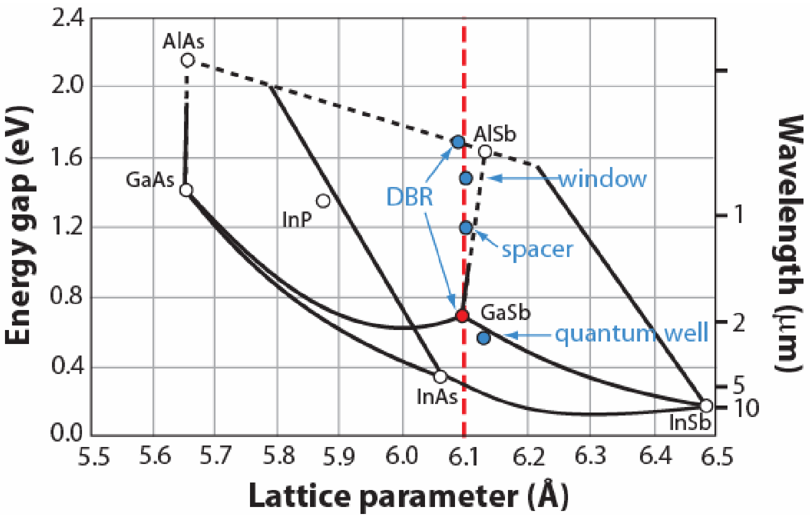

Figure 3.3 Energy bandgap diagram of various III-V semiconductor materials (based on reference [27]). Elements used in the 1.9 and 2.0 µm SDLs are shown as blue spots along the red line, indicating similar lattice constant, hence low mechanical stress in the final structure.

The (AlGaIn)(AsSb) material system satisfies this demand while allowing the coverage of a wide range of wavelength by using different ternary and quaternary quantum wells (see Figure 3.3). In case of the 2.0 and 1.9 µm SDLs used in this work, the chip is a ~10 µm thick semiconductor structure that is grown monolithically onto a 500 µm thick 2 in. diameter GaSb waver by molecular beam epitaxy. Figure 3.4 and Figure 3.5 show the schematics of the layer structure and energy diagram of an SDL.

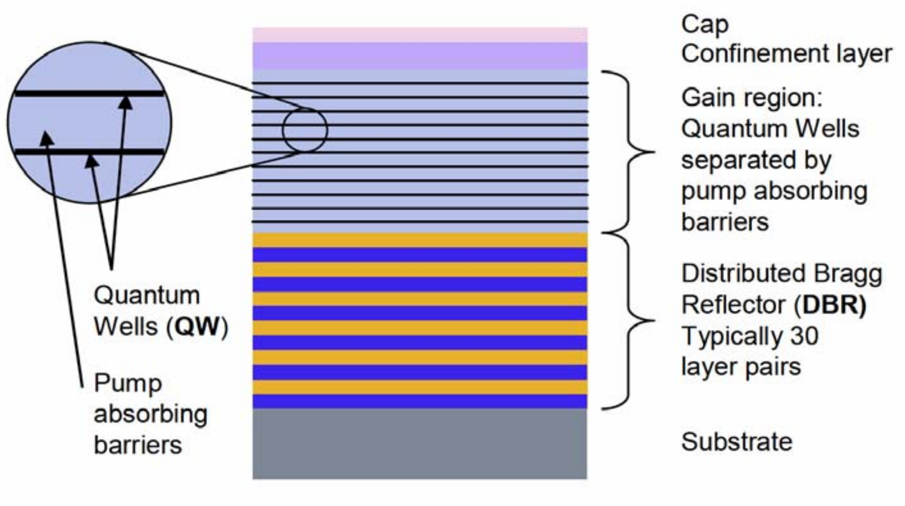

Figure 3.4 Layer structure of a semiconductor disk laser chip consisting of the substrate, Distributed Bragg Reflector, gain region (consisting of quantum wells and pump absorbing barriers) and cap/confinement layer.

The DBR is a series of 21.5 pairs of λ/4 thick layers of alternating high and low refractive index material ($AlAs_{0.08}Sb_{0.92}/GaSb$) which creates a mirror with a reflectivity R>99.5% at the design wavelength. The 2 µm thick active region consists of $Al_{0.30}Ga_{0.70}As_{0.02}Sb_{0.98}$ pump absorbing barriers and ten compressively strained (1.3 %), 10 nm thick, $Ga_{0.74}In_{0.26}Sb$ quantum wells. On top of this, a 350 nm thick $Al_{0.85}Ga_{0.15}As_{0.06}Sb_{0.04}$ window layer and 13 nm GaSb cap are grown to respectively prevent carrier recombination and oxidation of the aluminium-rich layers.

The thickness between the DBR and the top surface is typically designed to be an integer number of half the emission wavelength so that a micro-cavity is formed which results in a standing wave field inside the chip. For increased gain, the quantum wells are distributed at the antinodes of the standing wave optical field, forming a resonant periodic gain configuration (RPG) to increase the small signal gain [28].

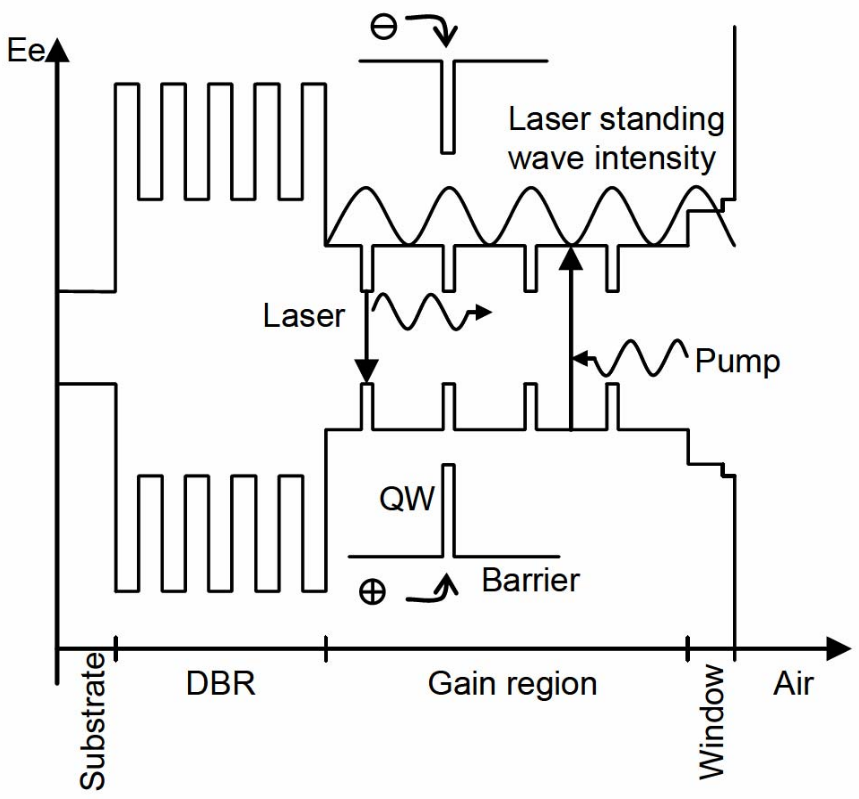

Figure 3.5 Schematic energy diagram of the semiconductor disk laser layer structure showing the DBR, active region (consisting of quantum wells and pump absorbing barriers) and the window layer. In most SDLs oscillation will tend to be at the wavelength of the resonance of the micro-cavity between the DBR and the front surface of the chip.

3.3 Thermal management of semiconductor disk lasers

A major concern when developing high power SDLs is the management of heat that originates from the quantum defect associated with the pump and emission wavelength. From this heating of the chip, two potential problems arise: one is the change of refractive index with temperature which in turn red shifts the micro-cavity resonance; the other is that the quantum well peak emission shifts due to an increase in temperature of the quantum wells themselves which results in a reduction of the bandgap that in turn increases the emission wavelength [29]. Both of these temperature related drifts happen at different speeds (see Figure 3.6). While the micro-cavity shift is about 0.3 $\mathrm{nm \cdot K^{-1}}$, the quantum well emission shifts at a rate of 0.1 $\mathrm{nm \cdot K^{-1}}$. Therefore the quantum-well gain peak and the sub-cavity resonance will eventually become spectrally misaligned, causing the SDL to stop oscillating: an effect commonly called *thermal rollover*. To delay this until higher power levels, the room temperature quantum well peak emission wavelength is chosen such that it is blue-shifted with respect to the micro-cavity resonance to compensate for thermal heating of the device at operating temperature. This is an essential design consideration when designing high power SDLs [30-32].

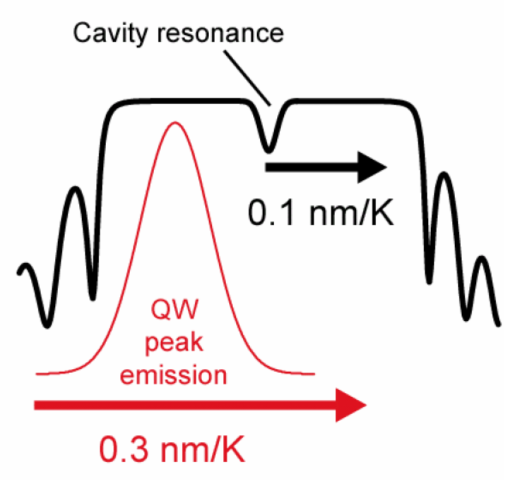

Figure 3.6 Shift of cavity resonance and quantum well (QW) peak emission with temperature. N.B. Both shift at different rates

This design feature on its own, however, does not enable high power operation in SDLs as the pump induced heating range of the chip would be sufficient to heat the device beyond the point where quantum well peak emission and micro-cavity resonance are spectrally aligned. Further steps to remove the heat from the active region inside the SDL into an appropriate heat sink are required. To achieve this, two main approaches have been developed: substrate removal (and bonding to a high conductive heat sink) [6] and the use of intracavity heatspreader [33,34]. The principles of both of these techniques are shown in Figure 3.7. In case of the substrate removal, the SDL structure is grown upside down with the cap layer grown first followed by the gain section and then the DBR. The surface is then metallised and soldered to a heat sink. The final step is to remove the substrate using selective chemical etching. Using this technique it is possible to minimize the material, and hence the thermal impedance, between the active region and the heat sink, and thereby improve the heat extraction (Figure 3.7b). This *thin device* approach has been very useful in InGaAs-(Al)GaAs-based SDLs emitting at around 1 μm due to the relatively higher thermal conductivity of the materials used for the DBR.

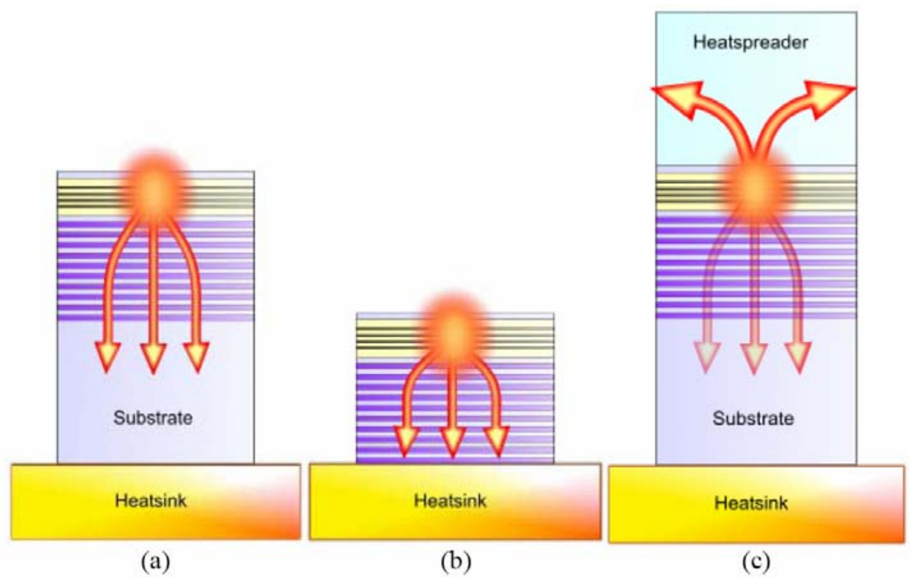

Figure 3.7 Techniques for improving heat removal from the semiconductor chip. a) Original design without improved heat extraction; b) substrate removed; c) intracavity heatspreader.

For (AlGaIn)(AsSb)-based SDLs emitting at 2.X µm, however, it has been shown that this technique does not work as well due to the increased thickness of the required DBRs and the lower thermal conductivity of the materials [35]. Therefore an alternative method, the use of an intra-cavity heatspreader, can be employed to improve heat extraction. For this method the chip is grown in the conventional order, DBR first, followed by the active region and the cap layer. The substrate does not need to be removed, but instead a highly thermally conductive heatspreader is optically contacted by a liquid assisted process onto the chip that extracts the heat more efficiently from the active region into a surrounding heat sink (Figure 3.7c) [33]. First results using this technique were obtained using sapphire heatspreaders [36] but silicon carbide and diamond soon become favoured due to their higher thermal conductivity [18,37]. When using a heatspreader, one has to bear in mind though that the intracavity element introduces an etalon filter function. This can potentially be a disadvantage if an unmodulated output spectrum and smooth tuning is required; however, in the context of single frequency operation this property can also be advantageous [38].

3.4 The 2 µm semiconductor disk laser

3.4.1 Experimental set-up

For the experiments carried out in the context of this work, an SDL based on the 2.0 µm structure described in section 3.2 was set up. Therefore a ~4x4 mm piece was cleaved from the 2 in. semiconductor waver and capillary bonded to a 250 µm thick diamond heatspreader (see Figure 3.8, left).

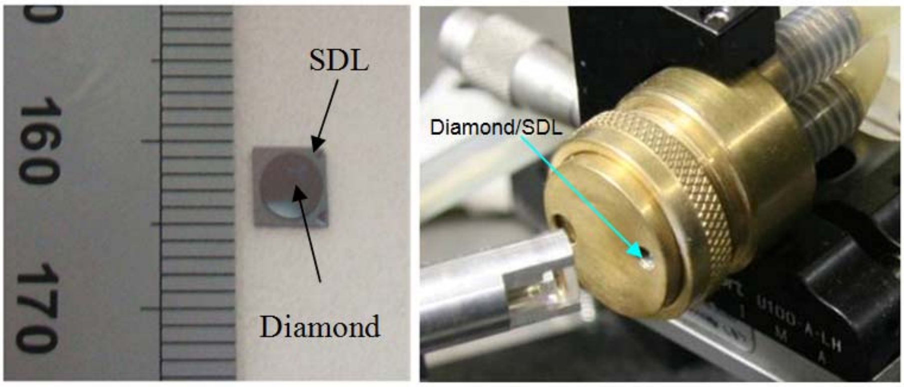

Figure 3.8 Picture of the 4x4 mm semiconductor chip bonded to a 250 µm thick piece of diamond (left) and the chip-diamond assembly mounted in water-cooled brass mount (right). The right picture also shows the focusing lens of the pump assembly.

This assembly was then placed into a water-cooled brass mount (see Figure 3.8, right) and pumped using a fibre-coupled edge-emitting diode laser. Contrary to more conventional doped-dielectric lasers that often require a very precise pump wavelength, the pump wavelength for an SDL merely needs to be smaller than the wavelength associated with the band gap energy of the barrier material; thereby allowing the choice of a wide range of commercially available diode lasers. Pumping into the barriers is typically called *barrier-pumping*, however, it should be noted that it is strictly speaking a combination of both, absorption in the barriers and a small fraction also in the quantum-wells. Alternatively, one can also pump directly into the quantum-wells alone, a technique called *in-well-pumping* which can be used to reduce the quantum defect [39,40]. For the arrangement used in this work (see Figure 3.9), barrier-pumping at 980 nm using a fibre-coupled (100 µm core) diode laser was chosen. The pump optics comprised of two aspheric lenses, f_1 and f_2, with 11 mm focal length which image the core of the 100 µm fibre onto the chip. The resonator was completed using a 100 mm radius of curvature mirror M_1, coated with a high reflective coating (R>99.9 %) for 2.02 µm, and different output couplers M_2 with various reflectivities between 99 and 75 % (Figure 3.8).

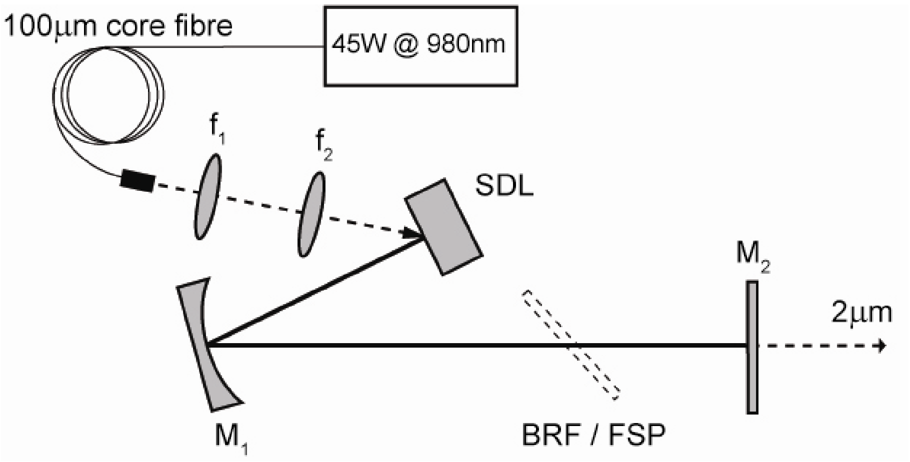

Figure 3.9 Schematic of the semiconductor disk laser consisting of a fibre-coupled diode pump laser, two pump lenses f_1 and f_2, a curved mirror M_1 and a plane output coupler M_2. Optionally, a birefringent filter (BRF) or fused silica plate (FSP) could be added into the resonator for added functionality.

For tuning the output wavelength of the laser, a quartz birefringent plate (BRF) [41] was inserted into the resonator at Brewster's angle. If tuning was not necessary, a 5 mm thick fused silica plate could be inserted to act as polarisation defining element. Either of these two elements will pin the polarisation inside the resonator which can potentially cause problems when using diamond as a heatspreader. This is because diamond can have natural stress induced birefringence that can elevate losses inside the resonator [34]. By careful positioning of the diamond or by using synthetic diamond, this effect can be minimised.

Using the laser resonator modelling software *WinLase 2 Professional*, the spacing between the semiconductor disk and mirror M_1 was optimized to be ~60 mm while the distance between M_1 and M_2 was ~260 mm (see Figure 3.10). This resulted in a cavity radius of ~50 µm which matched the pump spot radius of ~50 µm.

For fine tuning of the arrangement, the cavity and pump mode overlap at the SDL chip could be adjusted by defocusing of the pump by translating the pump optics assembly f_1 and f_2. This is possible because of the quasi-2-dimensional absorption profile of the SDL chip due to its relatively thin active region (2 µm) compared to the pump and cavity spot sizes. It should be noted that for maximum output power it was favourable to run with larger pump spot sized which favour transverse multimode operation of the resonator. In this configuration, the gain of the chip is exploited more efficiently resulting in higher output powers but also a degeneration of the mode quality. This aspect will be further discussed in section 3.6.

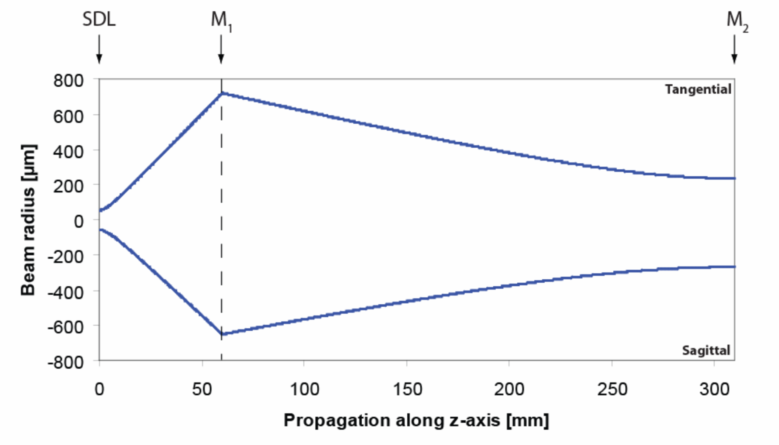

Figure 3.10 ABCD matrix model of the semiconductor disk laser resonator. The chip is at the left-hand boundary of the plot, the line at 60 mm along the z-axis represents the 100 mm radius of curvature mirror and the right-hand boundary represents the plane output coupler. The resulting cavity radius at the chip is ~50 µm.

3.4.2 Experimental results

Initially, a nominally 25 W diode laser coupled into an SMA-mounted 100 µm fibre (LIMO FI-A-P-0025) was used to pump the semiconductor disk laser. For the experiments, the diode was driven by a LIMO laser diode driver (LDD100-3) with up to 35 A and the laser diode delivered 22.3 W of output power (see Figure 3.11).

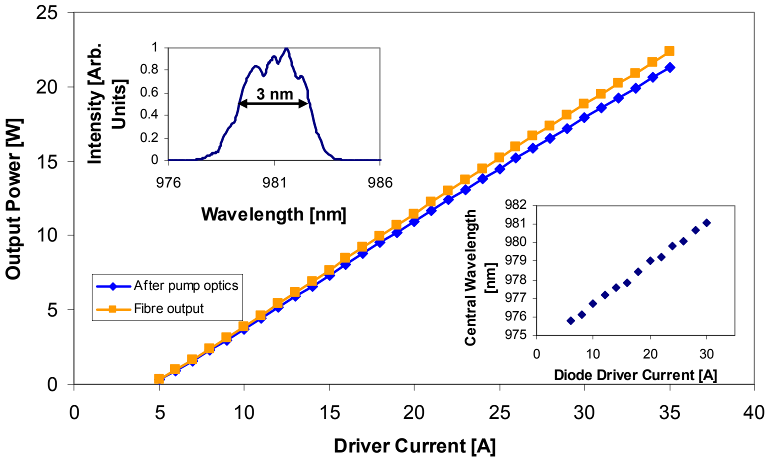

Figure 3.11 Power output characteristic of the 25 W diode laser. The maximum output power after the fibre is 22.3 W which reduces to 21.2 W after the focusing optics. Inset on the left shows the spectrum of the emission at full power and the right inset shows the shift of the central wavelength with increasing pump current.

The threshold current was measured to be 4.7 A and the slope efficiency 40 %. The pump optics f_1 and f_2 reduced the available pump power by 5 % to 21.2 W, associated with losses due surface reflections. As one can see in the right inset of Figure 3.11, the emission wavelength of the diode changed with pump current and hence junction temperature between 975.5-981 nm. The free running spectrum has a full width half maximum (FWHM) of ~3 nm at the maximum output power (left inset of Figure 3.11).

For the power transfer experiments, no BRF or Brewster-angled plate was inserted into the cavity to prevent polarisation losses associated with the birefringence of the diamond. It is possible to linearly polarise the output while maintaining maximum output power; however, more care has to be taken when choosing the diamond and aligning the cavity.

At first, the optimum output coupling for the given pump power and cavity arrangement was determined empirically. Therefore power transfer characteristics were carried out using different output couplers between R=85-97.8 % (see Figure 3.12).

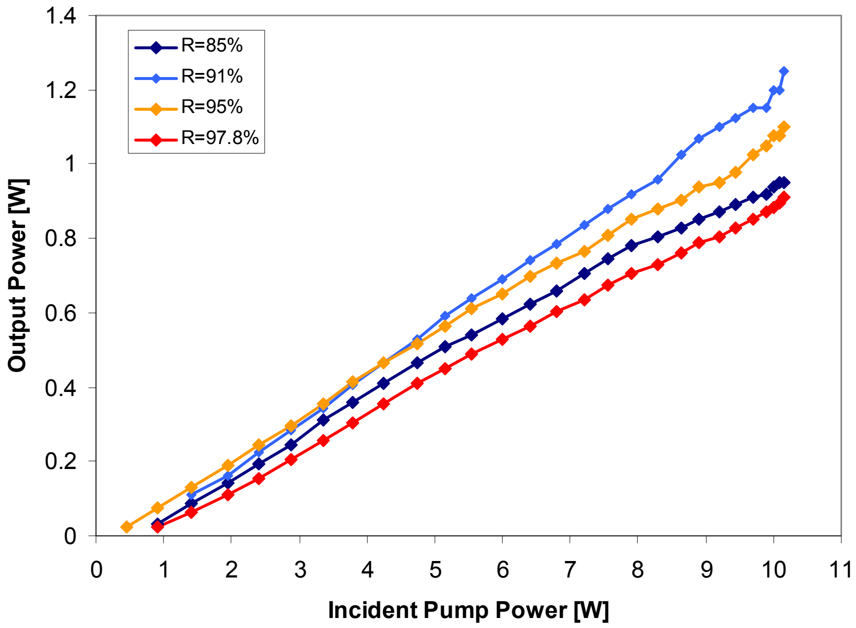

Figure 3.12 Power transfer characteristics of the 2.0 µm semiconductor disk laser using different output couplers between 85-98 % reflectivity. The optimum output coupler reflectivity was found to be 9 % with a maximum output power of 1.25 W.

From this it was found that the optimum output coupler reflectivity for this system was R=91 %. At maximum pump power, this configuration led to 3.2 W of output power with a slope efficiency of 17 % and a threshold of 1.6 W with respect to the incidence pump power (see Figure 3.12).

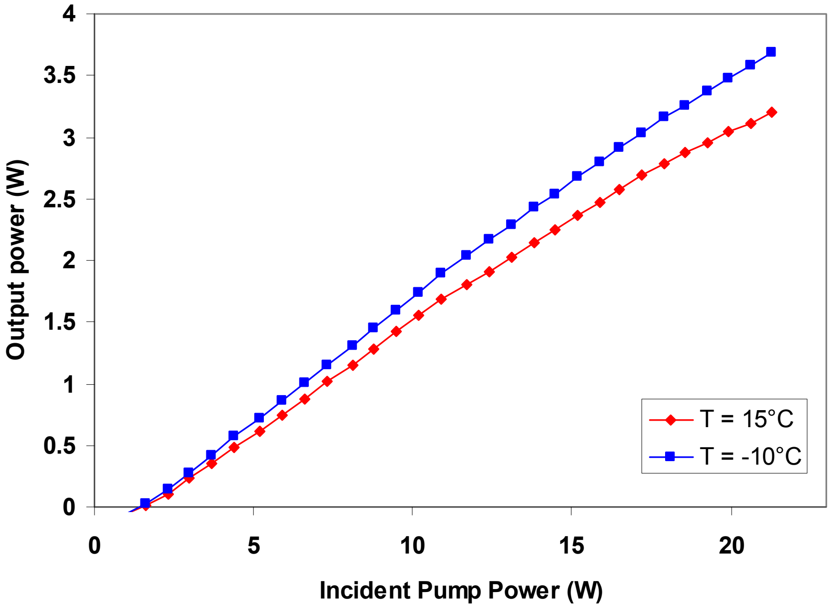

Figure 3.13 Power transfer characteristics for the 2.0 μm SDL pumped by a nominal 25 W, fibre-coupled diode laser. The maximum obtained output power at 15 °C and -10 °C was 3.2 and 3.7 W respectively with a maximum slope efficiency of 17 % for the 15 °C curve and 19 % for the -10 °C curve. In both cases the threshold is ~1.6 W with respect to the incident pump power.

It should be noted that the slope efficiency reduces at the high end of the 15 °C curve which is associated with thermal rollover. To increase the performance of the SDL it was possible to reduce the temperature of the brass mount the chip was held in. As a result of reducing the temperature to -10 ºC the output power increased to 3.7 W with a maximum slope efficiency of 19 % and a threshold of 1.6 W.

To further increase the output power of the SDL, a nominally 45 W, fibre-coupled diode laser (QPC Laser, Inc., BrightLase Ultra-100) replaced the 25 W laser. It was driven using a Glassman LP 20-60 power supply and delivered a maximum power of 38 W at 36 A diode driver current (see Figure 3.14). If this pump power is to be converted to additional output power from the SDL, it is important to delay the degradation of the slope efficiency due to thermal effects to higher incident powers. Therefore, the pump spot size had to be increased to keep a constant pump intensity on the chip. Rather than using different resonator optics it was possible to adjust the cavity spot sizes by changing the spacing between the chip and the curved mirror M_1 to ~58 mm and the arm length between the curved mirror M_1 and the output coupling mirror M_2 to 250 mm which in turn increased the cavity mode to 61 µm and thereby the area by a factor of 1.5. The pump mode was matched to this defocusing the pump spot on the SDL chip.

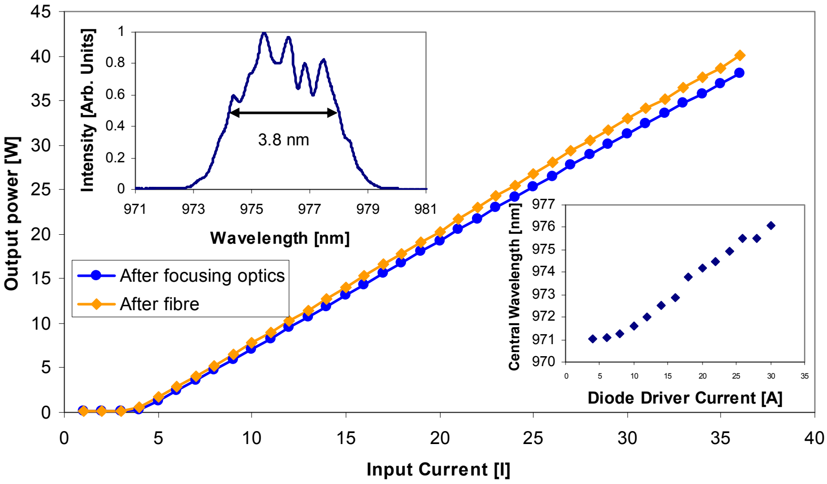

Figure 3.14 Power output characteristic of the 45 W diode laser. The inset on the left shows the spectrum of the emission and the right hand inset shows the shift of the central wavelength with increasing pump current.

With the more powerful pump source and the brass mount of the chip held to 21 ºC, the SDL provided up to 3.28 W of output power with a slope efficiency of 18 % and a threshold of ~1.6 W (see Figure 3.15). When cooled to -15 ºC, the SDL power was increased by 60 % to 5.82 W with an increased slope efficiency of 22 %.

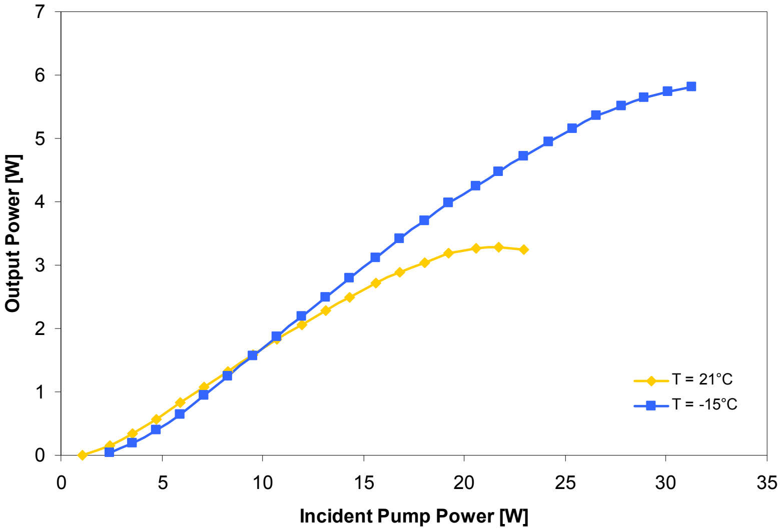

Figure 3.15 Power transfer characteristics for the 2.0 µm SDL pumped by a nominal 45 W, fibre-coupled diode laser.

In all cases, the highest power was achieved at the expense of output beam quality. Using a automated scanning slit beam profiler (Beam Scope P8) the beam quality factor (M^2) was measured to be in the order of $M^2 = 6$. This is possibly due to an increased pump spot size which results from adjusting the laser towards higher power. The increased pump spot size favours higher-transverse mode operation of the SDL which would lead to improved extraction efficiency of the gain and thereby increase the output power. In turn, the higher order mode operation, however, results in a deterioration of the brightness of the system. In section 3.6, a full analysis of the beam quality factor of the SDL will be presented and ways for improving the brightness of the system will be discussed.

Figure 3.15 also shows that the roll over occurs before the maximum pump power is applied onto the chip. Larger pump and cavity mode radii were tried in attempt to increase the output power; however, this did not lead to an improvement of the system. The reason for this is that even though heat flow in a disk laser geometry is usually considered to be one-dimensional, the heat dissipation is actually 3-dimensional. This arises from the fact that the heat flow into the diamond heatspreader is three-dimensional as it removes the heat out of the pumped region and dissipates it radially [35]. Therefore the thin disk criterion is not fulfilled anymore, resulting in a limit of the power scaling capability.

3.4.3 Spectral characterisation

The free running spectrum of the SDL was to be measured using a large frame grating spectrometer (Jobin Yvon HR 460) in conjunction with a thermo electrically cooled InAs detector (1-3.55 μm) (see Figure 3.16).

Figure 3.16 shows the 8 spectral mode groups associated with the etalon effect of the intracavity diamond heatspreader that reach threshold at an output power of 2.8 W. The separation of the adjacent mode groups is given by the free spectral range of the diamond heatspreader which in case of the 250 μm thick piece of diamond used for this laser is 3 nm.

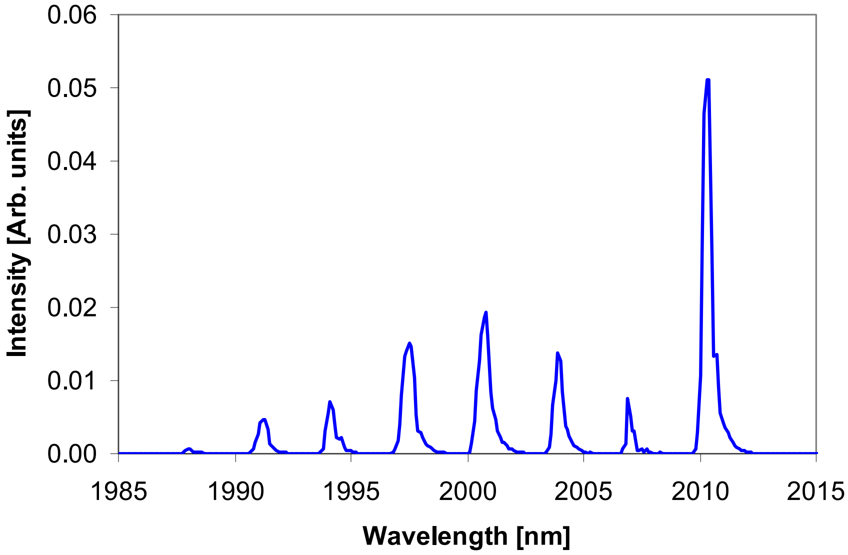

Figure 3.16 Spectral output of the 2.0 µm SDL in free-running operation showing the modulation associated with the etalon effect of the diamond heatspreader.

To investigate the ability to tune the central wavelength of the SDL, a 2 mm thick quartz BRF was inserted into the resonator to allow the emission wavelength of the SDL to be tuned. Initially a tuning curve was recorded for a pump current of 30.9 A with an output coupler transmission of 7 %. This resulted in wavelength coverage of 80 nm from 1962 to 2042 nm (Figure 3.17, black curve).

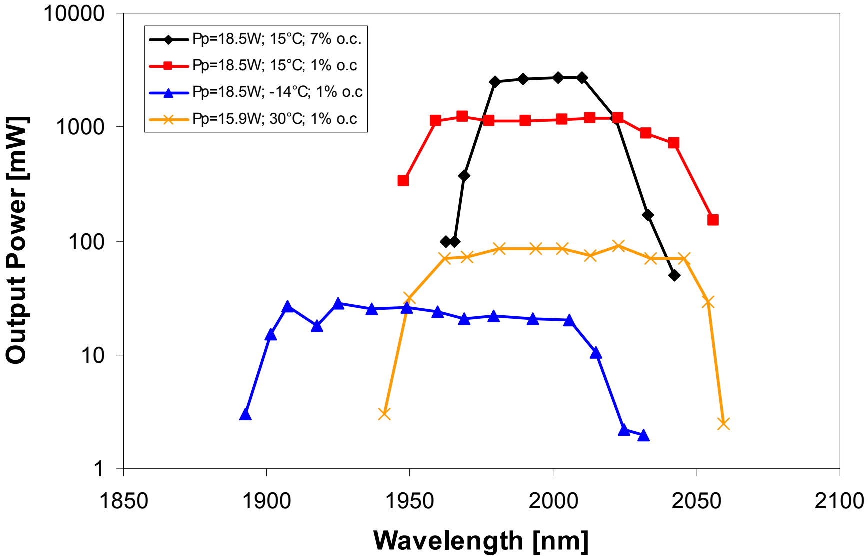

Figure 3.17: Tuning curves of the 2.0 µm SDL for maximum output power (black curve), reduced output coupling (red curve) and temperature tuned (blue curve).

It was possible to extend this tuning range by reducing the amount of output coupling and thereby reduce the threshold wavelengths in the wings of the gain band. This can be seen in the red curve in Figure 3.17 where an output coupler with 1 % transmission was used which reduced the maximum output power of the SDL but increased the spectral tuning by 38 nm to 108 nm, ranging from 1948 to 2056 nm. Ultimately, the maximum tuning was achieved when using a high reflecting mirror instead of an output coupler; however, this greatly reduced the output power of the SDL. Another way of tuning the device was to change the temperature the chip was held at. By reducing this from 15 °C to -14 °C, the tuning range was shifted to shorter wavelengths by 56 nm. This was in part associated with the shifts of the microcavity resonance and the quantum well peak emission towards shorter wavelength; however, at a maximum rate of change of 0.3 nm/K, the 29 K temperature difference only equates to a shift of the wavelength by 8.7 nm. It was expected that the larger wavelength shift was possible because of the width of the microcavity resonance. For the 6 µm long microcavity that was formed between the DBR (R=99.5 %) and the diamond heatspreader interface (R=17.5 %) the theory of Fabry Perot resonators discussed in reference [42] suggests a width of the resonance of ~11 nm. In combination with the microcavity resonance and quantum well peak emission drift, this led to a total theoretical shift of the wavelength by ~20 nm and therefore doesn’t account for the total 56 nm shift observed experimentally. To fully understand the mechanisms involved in the temperature induced wavelength tuning, additional investigations are required.

Towards higher temperatures, it was not possible to observe a shift in the tuning range because the coatings of the external mirrors limited the range of operation.

Using these various techniques, it was possible to cover a total wavelength range of 167 nm from 1.892 to 2.059 µm.

3.5 The 1.9 µm semiconductor disk laser

3.5.1 Experimental results

The 1.9 µm SDL was first characterised in respect to its power transfer properties. The experimental set up used for this was identically to the one described in section 3.4.1. The pump source was the 45 W, fibre-coupled diode laser described in section 3.4.2. The result of the power transfer analysis is shown in Figure 3.18.

It can be seen that the optimum output coupler transmission is again found to be 9 %. In this configuration the SDL delivered a maximum output power of 3.03 W with a slope efficiency of ~17 % and a threshold of ~1.3 W. When reducing the temperature of the brass mount from 20 to -10 °C the maximum output power was increased to 4.33 W with a slope efficiency of 18 % (see Figure 3.19).

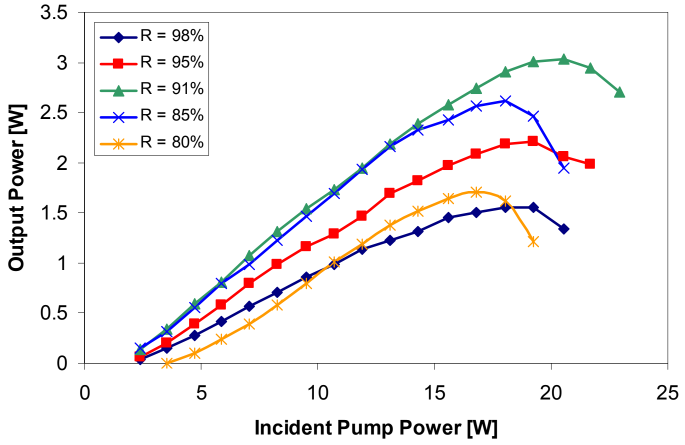

Figure 3.18 Power transfer characteristics of the 1.9 µm SDL with a maximum power of 3.03 W at 9 % output coupler transmission and a threshold of 1.3 W.

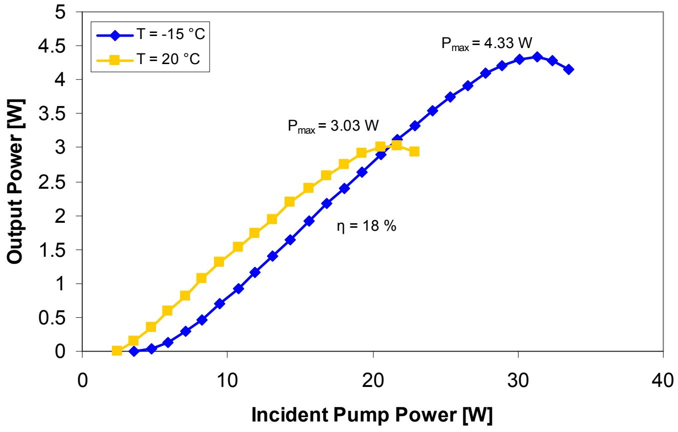

Figure 3.19 Power transfer of 1.9 µm semiconductor disk laser delivering a maximum output power of 3.03 W and 4.33 W at a chiller temperature of 20 °C and -15 °C respectively.

Compared to the 2.0 µm sample the 1.9 µm SDL exhibits significantly lower output power while the slope efficiency with 18 % is similar to the 22 % of the 2.0 µm sample. The difference in maximum output power was attributed to a difference in the designed offset between micro-cavity resonance and quantum well peak emission of the two samples. The small difference in the slope efficiency can potentially be associated with the microcavity and peak emission wavelength offset too; a consequence of a change of the cavity Q-factor and coupling of the pump radiation. The change in the slope efficiency induced by differences in the designed offset, however, only slightly changes the overall performance of the SDL while it is the thermally induced rollover that can have detrimental effects on the power transfer characteristics of the SDL if not designed correctly.

3.5.2 Spectral characterisation

For tuning purposes, a 2mm thick quartz BRF was again inserted into the cavity at Brewster's angle. Using an output coupler with 91 % reflectivity, tuning between 1885-1970 nm was achieved (see Figure 3.20).

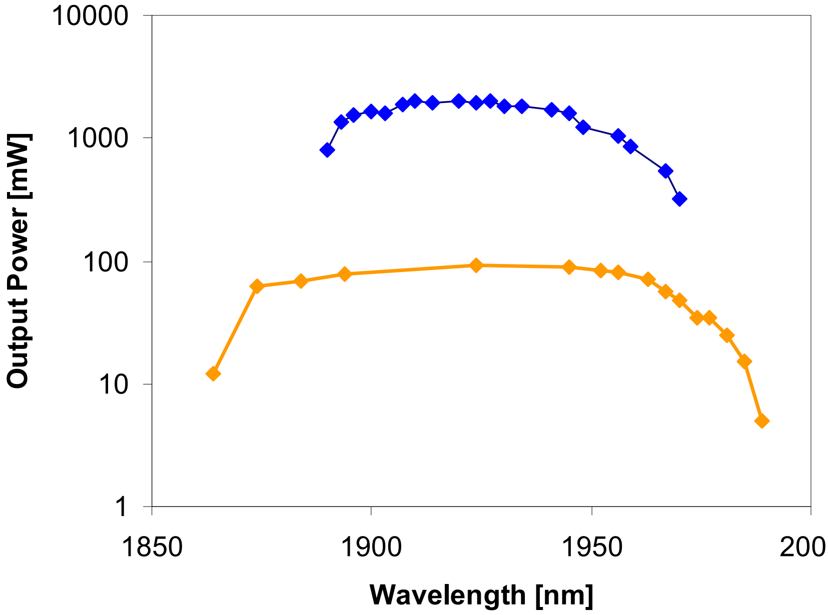

Figure 3.20 Tuning curve of the 1.9 µm SDL. At optimum output coupling of 9 % the maximum tuning was 85 nm from 1885 to 1970 nm (blue curve). When using a high reflector (orange curve) the tuning range was increased to cover a total of 125 nm from 1864 to 1989 nm.

It was possible to extend this range to a maximum tuning range of 125nm from 1864 to 1989 nm by using a high reflective mirror instead of the output coupler.

3.6 Brightness optimisation of semiconductor disk lasers

As mentioned previously, the highest power operation of SDLs is achieved at the expense of beam quality which is due to higher order transverse modes having better overlap with the pump. Another phenomenon that can deteriorate the beam quality of the SDL is the *soft-aperture* effect which results from the Gaussian beam profile of the pump sources used. Because of the Gaussian shape, a change in pump power will change the area within which the quantum wells are pumped to transparency. The result is a gain-aperture that changes the mode overlap between the pump and cavity with power. The principle of this is depicted in Figure 3.21.

To investigate this effect, the 2.0 µm SDL was analysed in respect to its beam quality by using an automated, scanning-slit beam profiler (DataRay Beamscope P8). The output beam of the SDL was focused using a 70 mm focal length lens and the beam profile around the focus measured by the scanning-slit profiler (see Figure 3.22). From this measurement the DataRay software was able to calculate the beam quality factor (M^2).

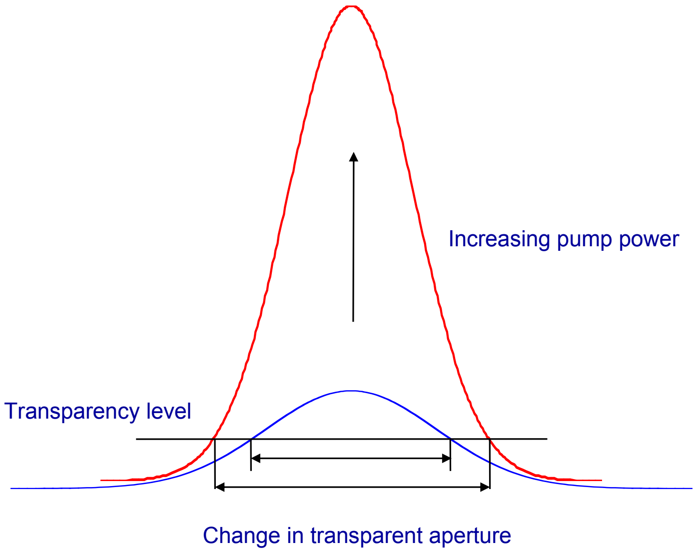

Figure 3.21 Principle of a soft aperture where an increase in pump power causes a larger area of the chip to be bleached (change in aperture).

At first the beam quality was measured at maximum SDL power. This revealed an M^2 value of ~6. The variation in beam radius around the focal point as well as the beam profile at the focus can be seen in Figure 3.23.

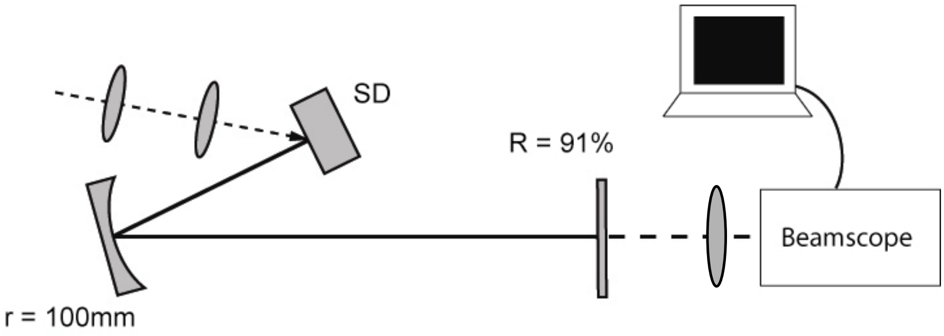

Figure 3.22 Schematic of the experimental arrangement to measure the beam propagation parameter of the 2.0 µm SDL.

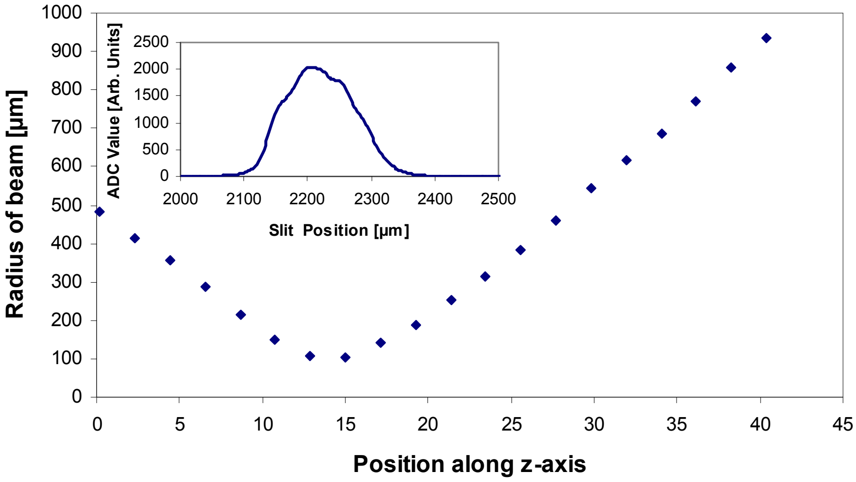

Figure 3.23 Beam propagation of the focused SDL at 3.6 W output power. **Inset:** Beam profile at focus [plotted is Analogue-Digital-Converter (ADC) value versus slit position].

The first approach to reduce the beam quality factor was by inserting an aperture into the cavity to limit the transverse mode of the oscillating field. In addition to improving the beam propagation parameter, however, this also reduces the output power of the SDL as some of the intracavity field is sacrificed when restricting the mode with the aperture. The results of this measurement are shown in Figure 3.24. It was possible to improve the output beam quality significantly from $M^2=6$ to $M^2 \sim 1$. While this also results in a significant power drop of 87% from 3 to <0.5 W the brightness of the system is still enhanced by a factor of 6.

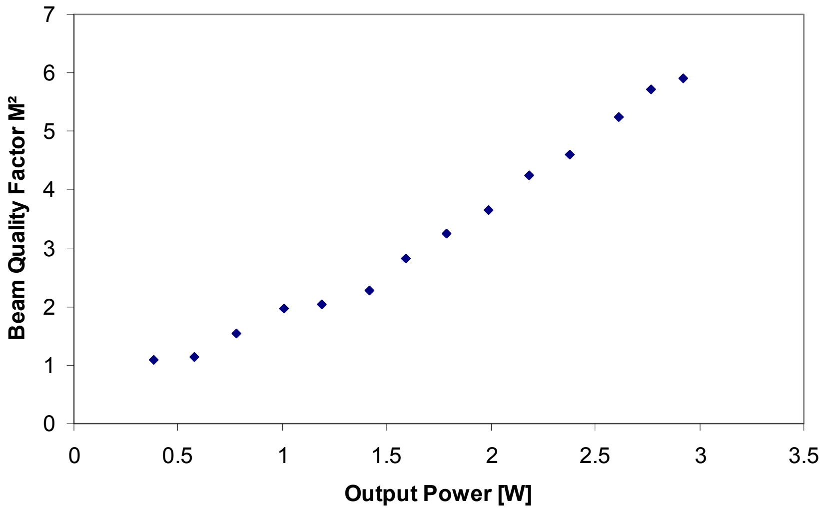

Figure 3.24 Change of beam quality factor (M^2) with varying output power.

As alternative way to optimize the brightness of the SDL, it is possible to improve the mode overlap of laser and pump. As mentioned in section 3.4.2, aligning of the laser for maximum power often results in a larger pump spot which in turn leads to multi transverse-mode operation of the laser. Rather than restricting the higher order modes by using an aperture, it is possible to pump only the fundamental mode of the laser so that higher order modes are not being excited.

To investigate this further, the beam quality factor of the SDL was measured for different ratios of pump to cavity mode size (ω_c/ω_p). A three-mirror resonator was set up with the same optics used in the previous sections. The cavity waist on the chip was then varied by adjusting the length of the resonator arm comprising of the output coupler. The three-mirror resonator had the advantage of supporting a wide range of cavity waist radii ω_c compared to a two mirror resonator as it can be seen from Figure 3.25.

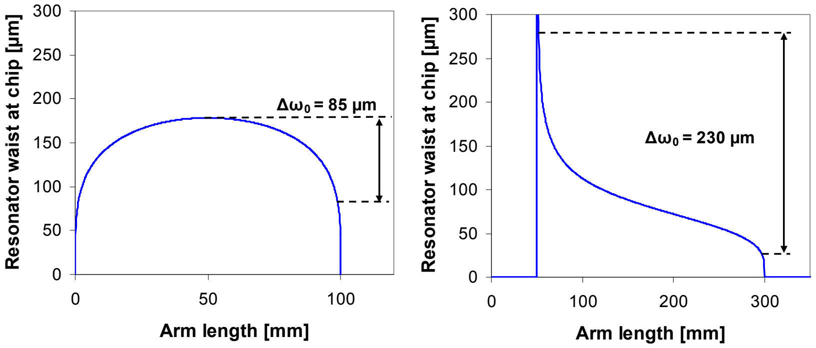

Figure 3.25 Change in cavity waist size against change in arm length of a two-mirror resonator using a 50 mm radius of curvature mirror (left) and three-mirror resonator using a 100 mm radius of curvature folding mirror (right).

To determine (ω_c/ω_p), the $1/e^2$ pump mode size on the chip (when the laser was aligned for maximum power) had to be determined. Therefore the pump focus was analysed using a knife edge measurement [43] at multiple points along the beam propagation and around the focus (see Figure 3.26). A Gaussian beam profile was then fitted to each position using the algorithm suggested by de Araujo et al. [44]. To this series of points a Gaussian fit for the propagation along the z-axis was calculated.

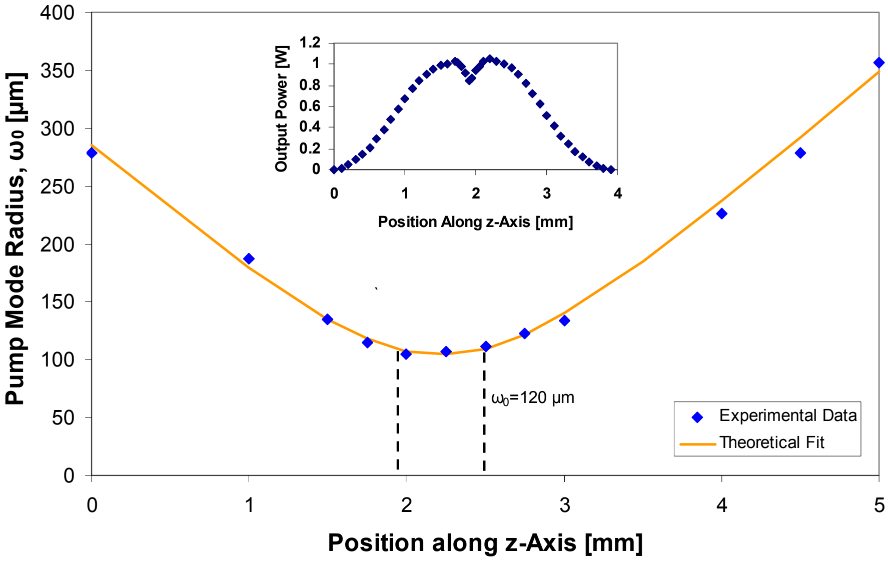

Figure 3.26 Knife edge measurement of the pump mode. **Inset:** SDL output power against translation of the SDL pump optics along the optical axis (z-axis).

The pump focal position relative to the front surface of the SDL chip then had to be determined. This was done by translating the pump optics along their z-axis (while the SDL was oscillating) to locate the two peaks in the output power of the SDL (one where the focus of the pump is before the face of the chip, one where it is inside the chip) that can be seen in the inset of Figure 3.26. Between these two maxima the laser showed reduced performance due to the increased heat load density directly at the focus. The point of operation was then found at the point where the output reached a local maximum. From this position the distance to the pump focus position was obtained and using the result of the knife edge measurement, the pump waist ω_0 was determined to be ~120 µm radius.

In the next step the pump to cavity mode radius ratio of the system was changed incrementally by changing the length of the resonator arm between 50 and 250 mm.

This arm length variation changed the resonator waist size between ~50-300 μm which equates to a change in cavity to pump spot ratio from 0.44-2.45 (using the previously determined value of 120 μm for the pump waist). For every 10 mm of arm length change the M^2 value and power were measured and plotted against the cavity to pump mode ratio (see Figure 3.27).

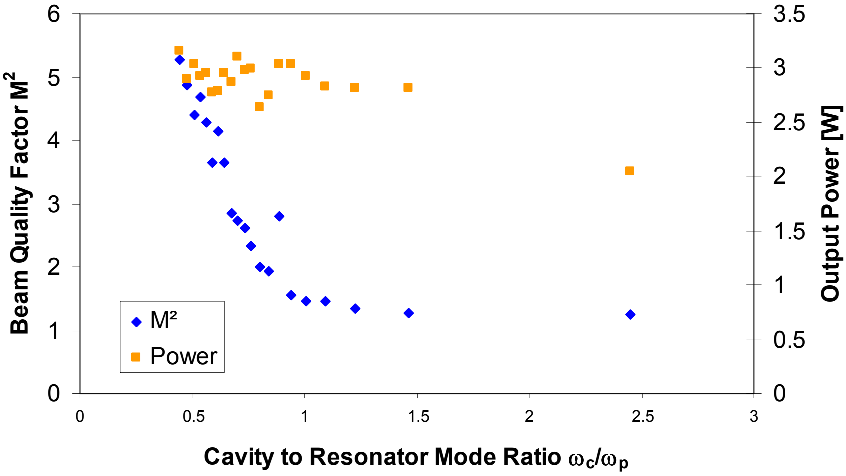

Figure 3.27 Change of power and beam quality factor over the changing ratio of resonator to cavity waist.

The maximum output power of 3.16 W was obtained in conjunction with a relatively high M^2 value of ~5.25. At this point the pump mode was more than twice the cavity mode radius. By increasing the resonator mode radius waist the M^2 value improves until a near diffraction limited output beam is obtained at the point where ω_c/ω_p is close to one. The best beam quality factor of M^2=1.3 (see Figure 3.28) was achieved with ω_c/ω_p~1.5 resulting in a 6 % drop in the maximum output power. For a value of 2.45, the beam quality remained good; however, the reduced mode overlap resulted in a significant reduction of the output power.

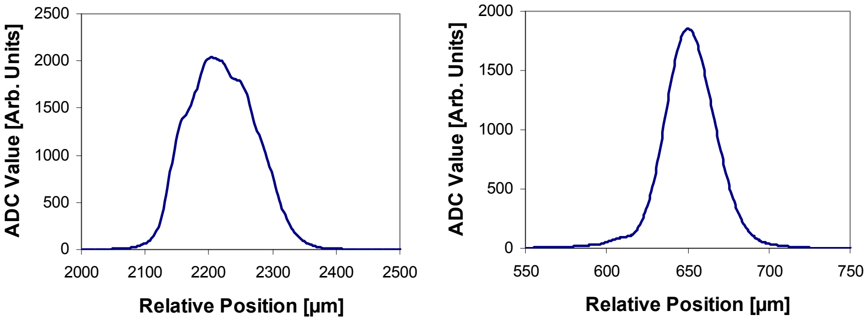

Figure 3.28 Beam profile of the SDL at the focus created by the 70 mm focal length les. **Left:** Before optimization (M^2 ~5.25) **right:** After optimizing the cavity to pump waist ratio (M^2~1.3).

In this fashion, it was possible to improve the brightness of the SDL output by a factor of 15 which shows that the SDL is a flexible format, not only in respect to wavelength engineerability and functionality but also in respect to its beam quality at high output power. While in most cases good quality beams is preferred, an easily adjustable beam quality might be of interest in the context of an SDL as pump source for other lasers. This aspect will be further discussed in chapter 5.

3.7 Multi-chip semiconductor disk lasers

When the power obtained from a single chip is not enough for a certain application, it is possible to divide the pump power and heat between multiple chips within the same resonator and thereby increase the output power [6]. In this section the possibility of using the 2 μm SDL in a dual chip configuration is investigated.

As mentioned in section 3.4.2, the power scalability of SDLs, by increasing the spot size of the pump and cavity mode, is not indefinite. There are multiple factors such as amplified spontaneous emission in the epitaxial plane that increases with larger spot sizes, surface defects and impurities of the chip and the previously mentioned lateral heat flow in the diamond that contribute to the ultimate limit of spot size scalability [45]. At this point a multi-chip configuration can help to overcome these issues and enable scaling to higher powers. In previous work [46-48], one of the SDL chips was used as a folding mirror inside the cavity while the other one was used as an end mirror in the same way as described in the earlier sections of this chapter. Using an SDL chip at non-normal incidence, however, reduces the efficiency as the effective layer thicknesses in the chip are now different. This reduces the micro-cavity resonance as the spacing between the DBR and the surface is not an integer of the wavelength anymore. Additionally it misaligns the quantum wells in respect to the intracavity standing wave and adds losses due to increased reflectivity off the surface of the chip. The last mentioned can be counteracted by using antireflection coatings but this will reduce the performance of the chip as the micro-cavity resonance and therefore the RPG is further reduced in strength. To eliminate these issues the resonator used in the context of this work was a four-mirror resonator as shown in Figure 3.29 in which the two chips were placed as end mirrors of the resonator so that the intracavity mode was at normal incidence to them. It was therefore essentially a mirrored version of the arrangement discussed in section 3.4.1 with the difference that one of the curved mirrors was used as an output coupler. This also ensured that the spot sizes on the chip were identically (see Figure 3.30). It should be noted, that the use of a folding mirror as output coupler resulted in two output beams. While this could be addressed by combining the output beams to form a single one or by other means of output coupling, this was not addressed in the context of this work as the fundamental power transfer characteristics of the laser would not change.

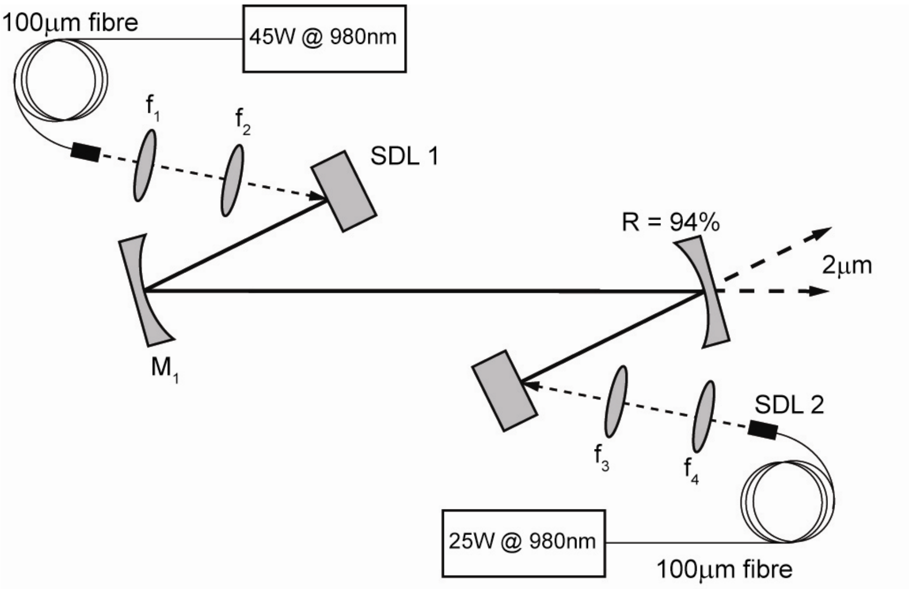

Figure 3.29 Experimental arrangement of the 2.0 μm SDL using two chips that are pumped independently. Output coupling was achieved using a curved output coupler resulting in two output beams.

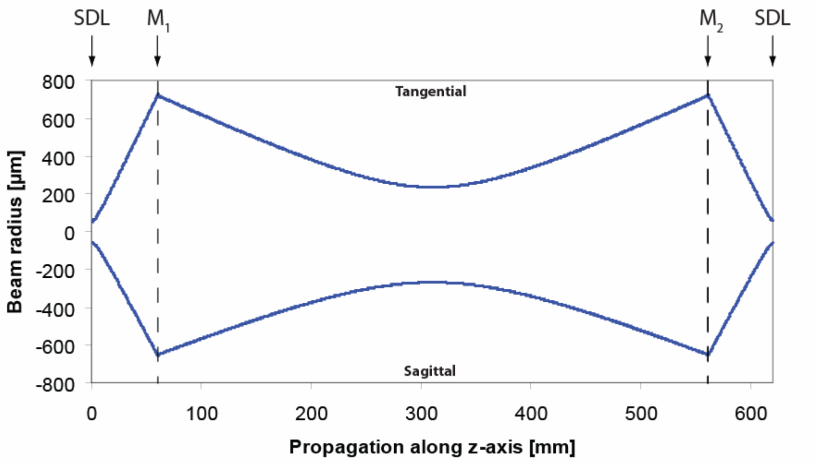

Figure 3.30 ABCD-Matrix model of the dual chip four-mirror resonator. The spot sizes on the chips being the same as in section 3.4.1.

As only a limited range of curved output couplers was available, an R = 94 % output coupler (which equate to overall output coupling of 12 % per roundtrip) was used for maximum output power.

To accurately compare the dual chip laser with a single chip resonator it was important not to interfere with the alignment of the dual chip system as small changes in the position on the SDL chips can result in significant power changes. It was also desirable to remove the unpumped chip from the system as this would act as an absorber in the cavity which would add losses and therefore reduce the efficiency of the system. It was therefore chosen to place a 9 % output coupling mirror in the symmetry point of the resonator to form single chip resonators whose cavity and pump spot sizes were identical to the dual chip layout. However, for one of the single-chip resonators the curved output coupler had to be replaced with a high reflective mirror of the same curvature.

The power transfer characteristics of the dual chip SDL as well as the individual chips are shown in Figure 3.31. Chip 1 and chip 2 delivered up to 4.5 and 3.8 W with slope efficiencies of 22 and 20 % respectively. When operating in the dual chip arrangement the maximum output power was 8.1 W which is close to the sum of the two individual chips.

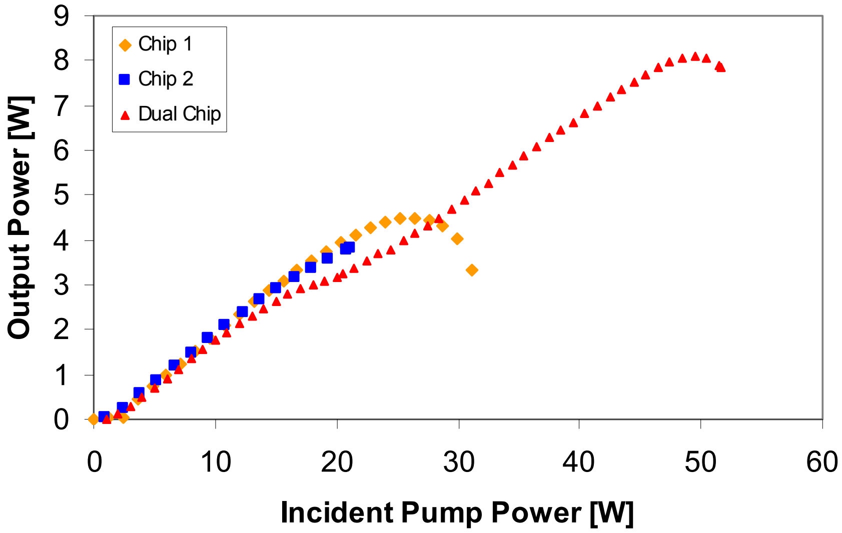

Figure 3.31 Power transfer characteristics of the individual chips and the dual chip 2.0 μm SDL demonstrating the combination of the individual powers (3.8 and 4.5 W) to an output power of 8.1 W for the dual-chip arrangement.

As demonstrated in [46], the use of two chips should increase the small signal gain per roundtrip which should in turn result in an increase in the optimum output coupling, thus increasing the threshold but also the slope efficiency. However, this could not be fully verified due to the limitation in available output couplers. When a slightly higher output coupling of 12 % (compared to 9 % of the single chip arrangement) was used, the threshold in the dual-chip arrangement increased from 1 to 2.3 W. However, the slope efficiency actually decreased slightly to 19 % on the linear part of the upper end of the power transfer curve and 20 % on the lower part of the curve. Aside the total of 12 % output coupling, 14 and 8% output coupling were tried as well which did not improve the performance of the system.

With the summation of the individual single chip powers of 3.8 and 4.5 W in the dual chip arrangement to a total output power of 8.1 W, it has been shown that the division of pump induced heating onto multiple chips allows the significant scaling of the output power of the laser in an almost linear fashion. In the context of a pump source, the two separate output beams generated would need to be combined and conditioned. Alternatively, the use of other resonator geometries with a single output beam would solve this problem.

3.8 Conclusion

Multi-watt, cw operation of a (AlGaIn)(AsSb) semiconductor disk lasers emitting at 1.9 and 2.0 µm has been demonstrated. The 1.9 µm sample delivered up to 3.03 W with a slope efficiency of 18 % and a threshold of 1.1 W with the chip being thermally stabilised at 20 °C. When cooled to -15 °C the power was increased to 4.33 W. The 2.0 µm sample delivered up to 3.28 W of output power with slope efficiencies of 18 % and a threshold of 1.6 W at a temperature of 21 °C. When cooled to -15 °C the device delivered up to 5.82 W of output power with a maximum slope efficiency of 22 % and a threshold of 1.6 W.

Tuning of the two lasers was possible using a 2 mm thick quartz BRF. For the 1.9 µm sample this resulted in a maximum tuning range of 125 nm from 1.864 to 1.989 µm while the 2.0 µm SDL allowed tuning over a range of 130 nm from 1.892 to 2.031 µm. On the example of the 2.0 µm SDL it was also shown that the emission of the individual devices can be shifted by varying the temperature the chip was held it. This extended the total wavelength coverage of the 2.0 µm SDL to 167 nm.

Furthermore, the beam quality factor of the lasers was determined revealing a relatively poor beam quality of M^2>5.25 when running at maximum power. However, a detailed investigation of the beam quality factor relation to the mode overlap of pump and resonator revealed that this can be greatly improved to M^2<1.3 by careful alignment of the laser with only sacrificing 6 % of the maximum output power.

To be able to scale the SDL format further in power, a dual-chip arrangement has been demonstrated, using two independent 2.0 µm SDL chips in a single resonator to distribute the pump power and its associated heat onto multiple chips. In this way it was possible to combine the individual output powers of the chips in one resonator resulting in an output power from the dual chip SDL of 8.1 W.

Parameter	Required	Achieved
Power [W]	Watt-level	5.8 (8)
Wavelength [µm]	1.6-2.1	2.0
M2	<5	1.3
Intensity noise [%]	<2	Requires quantification
Sensitivity towards feedback	low	unknown

Table 3.1 Comparison of desired properties of a pump source for chromium-doped chalcogenide lasers and the SDL discussed in this chapter.

With these results, the GaSb-based semiconductor disk laser format emitting at 1.9 and 2.0 µm has shown great potential as a cw pump source for chromium-chalcogenide lasers (see Table 3.1). In the next chapter, the SDL format will further be investigated for pulsed operation and in the following chapters, the use of this laser as pump source for chromium-doped chalcogenide laser will be discussed.

References

[1] A. Giesen, H. Hugel, A. Voss, K. Wittig, U. Brauch, and H. Opower, "Scalable Concept for Diode-Pumped High-Power Solid-State Lasers," Appl. Phys. B **58**, 365 (1994).

[2] G. E. Stillman, M. D. Sirkis, J. A. Rossi, M. R. Johnson, and N. Holonyak, Jr., "Volume excitation of an ultrathin single-mode CdSe laser," Appl. Phys. Lett. **9**, 268 (1966).

[3] M. Kuznetsov, F. Hakimi, R. Sprague, and A. Mooradian, "High-power (>0.5 W CW) diode-pumped vertical-external-cavity surface-emitting semiconductor lasers with circular TEM_{00} beams," IEEE Photonic Tech. L. **9**, 1063 (1997).

[4] H. Soda, K. Iga, C. Kitahara, and Y. Suematsu, "Gainasp-Inp Surface Emitting Injection-Lasers," Japanese Journal of Applied Physics **18**, 2329 (1979).

[5] M. A. Hadley, G. C. Wilson, K. Y. Lau, and J. S. Smith, "High single-transverse-mode output from external-cavity surface-emitting laser diodes," Appl. Phys. Lett. **63**, 1607 (1993).

[6] J. Chilla, S. Butterworth, A. Zeitschel, J. Charles, A. Caprara, M. Reed, and L. Spinelli, "High power optically pumped semiconductor lasers," Solid State Lasers Xiii: Technology and Devices **5332**, 143 (2004).

[7] N. Hempler, J. M. Hopkins, and M. Rattunde, "Tuning and brightness optimisation of high-performance GaSb-based semiconductor disk lasers from 1.86 to 2.80 µm," presented at the European Conference on Lasers and Electro-Optics, Munich, (2009).

[8] M. A. Holm, P. Cusumano, D. Burns, A. I. Ferguson, and M. D. Dawson, "Mode-locked operation of a diode-pumped, external-cavity GaAs/AlGaAs surface emitting laser," presented at the Conference on Lasers and Electro-Optics, Baltimore, (1999).

[9] M. A. Holm, A. I. Ferguson, and M. D. Dawson, "Actively stabilized single-frequency vertical-external-cavity AlGaAs laser," IEEE Photonic Tech. L. **11**, 1551 (1999).

[10] T. D. Raymond, W. J. Alford, M. H. Crawford, and A. A. Allerman, "Intracavity frequency doubling of a diode-pumped external-cavity surface-emitting semiconductor laser," Opt. Lett. **24**, 1127 (1999).

[11] S. Calvez, J. E. Hastie, M. Guina, O. Okhotnikov, and M. D. Dawson, "Semiconductor disk lasers for the generation of visible and ultraviolet radiation," Laser Photonics Rev. **DIO 10.1002** (2009).

[12] J. Chilla, Q. Z. Shu, H. L. Zhou, E. Weiss, M. Reed, and L. Spinelli, "Recent advances in optically pumped semiconductor lasers - art. no. 645109," Solid State Lasers XVI: Technology and Devices **6451**, 45109 (2007).

[13] A. J. Maclean, A. J. Kemp, S. Calvez, J. Y. Kim, T. Kim, M. D. Dawson, and D. Burns, "Continuous tuning and efficient intracavity second-harmonic generation in a semiconductor disk laser with an intracavity diamond heatspreader," IEEE J. Quantum Eelect. **44**, 216 (2008).

[14] J. Rautiainen, A. Harkanen, V. M. Korpijarvi, P. Tuomisto, M. Guina, and O. G. Okhotnikov, "2.7 W tunable orange-red GaInNAs semiconductor disk laser," Opt. Express **15**, 18345 (2007).

[15] A. Harkonen, J. Rautiainen, M. Guina, J. Konttinen, P. Tuomisto, L. Orsila, M. Pessa, and O. G. Okhotnikov, "High power frequency doubled GaInNAs semiconductor disk laser emitting at 615 nm," Opt. Express **15**, 3224 (2007).

[16] J. E. Hastie, S. Calvez, M. D. Dawson, T. Leinonen, A. Laakso, J. Lyytikainen, and M. Pessa, "High power CW red VECSEL with linearly polarized TEM00 output beam," Opt. Express **13**, 77 (2005).

[17] J. Konttinen, A. Harkonen, P. Tuomisto, M. Guina, J. Rautiainen, M. Pessa, and O. Okhotnikov, "High-power (> 1 W) dilute nitride semiconductor disk laser emitting at 1240 nm," New J. Phys. **9** (2007).

[18] J. M. Hopkins, S. A. Smith, C. W. Jeon, H. D. Sun, D. Burns, S. Calvez, M. D. Dawson, T. Jouhti, and M. Pessa, "0.6 W CW GaInNAs vertical external-cavity surface emitting laser operating at 1.32 µm," Electron. Lett. **40**, 30 (2004).

[19] C. Symonds, J. Dion, I. Sagnes, M. Dainese, M. Strassner, L. Leroy, and J. L. Oudar, "High performance 1.55 µm vertical external cavity surface emitting

laser with broadband integrated dielectric-metal mirror," Electron. Lett. **40**, 734 (2004).

[20] H. Lindberg, A. Strassner, E. Gerster, and A. Larsson, "0.8 W optically pumped vertical external cavity surface emitting laser operating CW at 1550 nm," Electron. Lett. **40**, 601 (2004).

[21] L. Cerutti, A. Garnache, F. Genty, A. Ouvrard, and C. Alibert, "Low threshold, room temperature laser diode pumped Sb-based VECSEL emitting around 2.1 µm," Electron. Lett. **39**, 290 (2003).

[22] L. Cerutti, A. Garnache, A. Ouvrard, and F. Genty, "High temperature continuous wave operation of Sb-based vertical external cavity surface emitting laser near 2.3 µm," J. Cryst. Growth **268**, 128 (2004).

[23] A. Ouvrard, A. Garnache, L. Cerutti, F. Genty, and D. Romanini, "Single-frequency tunable Sb-based VCSELs emitting at 2.3 µm," IEEE Photonic Tech. L. **17**, 2020 (2005).

[24] J. M. Hopkins, N. Hempler, B Rösener, N. Schulz, M. Rattunde, C. Manz, K Köhler, J. Wagner, and D. Burns, "High-power, (AlGaIn)(AsSb) semiconductor disk laser at 2.0 µm," Opt. Lett. **33**, 201 (2008).

[25] B. Rosener, N. Schulz, M. Rattunde, C. Manz, K. Kohler, and J. Wagner, "High-power high-brightness operation of a 2.25 µm (AlGaIn)(AsSb)-based barrier-pumped vertical-external-cavity surface-emitting laser," IEEE Photonic Tech. L. **20**, 502 (2008).

[26] A. Harkonen, M. Guina, O. Okhotnikov, K. Rossner, M. Hummer, T. Lehnhardt, M. Muller, A. Forchel, and M. Fischer, "1 W antimonide-based vertical external cavity surface emitting laser operating at 2 µm," Opt. Express **14**, 6479 (2006).

[27] B. R. Bennett, R. Magno, J. B. Boos, W. Kruppa, and M. G. Ancona, "Antimonide-based compound semiconductors for electronic devices: A Review," Solid-State Electronics **49**, 1875 (2005).

[28] S. W. Corzine, R. S. Geels, J. W. Scott, R. H. Yan, and L. A. Coldren, "Design of Fabry-Perot Surface-Emitting Lasers with a Periodic Gain Structure," IEEE J. Quantum Eelect. **25**, 1513 (1989).

[29] I. Vurgaftman, J. R. Meyer, and L. R. Ram-Mohan, "Band parameters for III-V compound semiconductors and their alloys," J. Appl. Phys. **89**, 5815 (2001).

[30] B. Tell, K. F. Browngoebeler, R. E. Leibenguth, F. M. Baez, and Y. H. Lee, "Temperature-Dependence of GaAs-AlGaAs Vertical Cavity Surface Emitting Lasers," Appl. Phys. Lett. **60**, 683 (1992).

[31] D. B. Young, J. W. Scott, F. H. Peters, M. G. Peters, M. L. Majewski, B. J. Thibeault, S. W. Corzine, and L. A. Coldren, "Enhanced Performance of Offset-Gain High-Barrier Vertical-Cavity Surface-Emitting Lasers," IEEE J. Quantum Eelect. **29**, 2013 (1993).

[32] N. Schulz, M. Rattunde, C. Ritzenthaler, B. Rosener, C. Manz, K. Kohler, and J. Wagner, "Effect of the cavity resonance-gain offset on the output power characteristics of GaSb-based VECSELs," IEEE Photonic Tech. L. **19**, 1741 (2007).

[33] Z. L. Liau, "Semiconductor wafer bonding via liquid capillarity," Appl. Phys. Lett. **77**, 651 (2000).

[34] F. van Loon, A. J. Kemp, A. J. Maclean, S. Calvez, J. M. Hopkins, J. E. Hastie, M. D. Dawson, and D. Burns, "Intracavity diamond heatspreaders in lasers: the effects of birefringence," Opt. Express **14**, 9250 (2006).

[35] A. J. Kemp, J. M. Hopkins, A. J. Maclean, N. Schulz, M. Rattunde, J. Wagner, and D. Burns, "Thermal management in 2.3 µm semiconductor disk lasers: A finite element analysis," IEEE J. Quantum Eelect. **44**, 125 (2008).

[36] W. J. Alford, T. D. Raymond, and A. A. Allerman, "High power and good beam quality at 980 nm from a vertical external-cavity surface-emitting laser," J. Opt. Soc. Am. B-Opt. Phys. **19**, 663 (2002).

[37] J. E. Hastie, J. M. Hopkins, S. Calvez, C. W. Jeon, D. Burns, R. Abram, E. Riis, A. I. Ferguson, and M. D. Dawson, "0.5 W single transverse-mode operation of an 850 nm diode-pumped surface-emitting semiconductor laser," IEEE Photonic Tech. L. **15**, 894 (2003).

[38] J. M. Hopkins, A. J. Maclean, D. Burns, E. Riis, N. Schulz, M. Rattunde, C. Manz, K. Kohler, and J. Wagner, "Tunable, single-frequency, diode-pumped 2.3 mu m VECSEL," Opt. Express **15**, 8212 (2007).

[39] M. Schmid, S. Benchabane, F. Torabi-Goudarzi, R. Abram, A. I. Ferguson, and E. Riis, "Optical in-well pumping of a vertical-external-cavity surface-emitting laser," Appl. Phys. Lett. **84**, 4860 (2004).

[40] N. Schulz, M. Rattunde, C. Ritzenthaler, B. Rosener, C. Manz, K. Kohler, and J. Wagner, "Resonant optical in-well pumping of an (AlGaIn)(AsSb)-based vertical-external-cavity surface-emitting laser emitting at 2.35 µm," Appl. Phys. Lett. **91** (2007).

[41] B. Lyot, "Optical apparatus with wide field using interference of polarized light," C.R. Acad. Sci., 1593 (1933).

[42] O. Svelto, in *Principles of Lasers*, edited by D. C. Hanna Springer, New York, pp. 140 (1998).

[43] J. M. Khosrofian and B. A. Garetz, "Measurement of a Gaussian laser beam diameter through the direct inversion of knife-edge data," Appl. Opt. **22**, 3406 (1983).

[44] M. A. C. de Araujo, R. Silva, E. de Lima, D. P. Pereira, and P. C. de Oliveira, "Measurement of Gaussian laser beam radius using the knife-edge technique: improvement on data analysis," Appl. Opt. **48**, 393 (2009).

[45] A. J. Maclean, R. B. Birch, P. W. Roth, A. J. Kemp, and D. Burns, "Limits on Efficiency and Power Scaling in Semiconductor Disk Lasers with Diamond Heatspreaders," Submitted to Journal of the Optical Society of America B: Optical Physics (2009).

[46] L. Fan, M. Fallahi, J. Hader, A. R. Zakharian, J. V. Moloney, J. T. Murray, R. Bedford, W. Stolz, and S. W. Koch, "Multichip vertical-external-cavity surface-emitting lasers: a coherent power scaling scheme," Opt. Lett. **31**, 3612 (2006).

[47] L. E. Hunziker, Q. Z. Shu, D. Bauer, C. Ihli, G. J. Mahnke, M. Rebut, J. R. Chilla, A. L. Caprara, H. L. Zhou, E. S. Weiss, and M. K. Reed, "Power-scaling of optically-pumped semiconductor lasers - art. no. 64510A," Solid State Lasers XVI: Technology and Devices **6451**, A4510 (2007).

[48] B. Rosener, M. Rattunde, R. Moser, C. Manz, K. Kohler, and J. Wagner, "GaSb-Based Optically Pumped Semiconductor Disk Laser Using Multiple Gain Elements," IEEE Photonic Tech. L. **21**, 848 (2009).

Chapter Four

Pulsed-pumped semiconductor disk lasers

4.1 Introduction

In the previous chapter, the multi-Watt continuous-wave operation of (AlGaIn)(AsSb)-based semiconductor disk lasers (SDL) emitting at 1.9 and 2 µm was introduced as a potential pump sources for chromium-doped chalcogenide lasers. When cw radiation of a laser source is not required, pulsed-pumping can be a beneficial technique for the design of efficient and practical laser sources. In this chapter, the pulsed-operation of SDLs emitting at 1.9 and 2.0 µm is discussed with the aim of creating a pump source that can be used for pulsed-pumped chromium-doped chalcogenide lasers.

In the previous chapter, the cw output power of a single chip laser was ultimately limited by thermal effects which reduced the efficiency of the laser and caused thermal rollover. In this context, using heatspreaders was the key element to allow the up-scaling of output powers. An alternative route to thermal management in semiconductor disk lasers is pulsed-pumping [1]. Rather than being concerned with the removal of heat, pulsed-pumping reduces the amount of heat that is introduced into the system. For this approach, a pump source generating pulses of radiation is required. This can be achieved mechanically, optically or electrically.

For the mechanical approach one way is to use a cw laser source and place a spinning disk into the beam path either intracavity or externally. This spinning disk contains of holes which chop the cw beam resulting in the formation of pulses [2]. Such devices are often referred to as a *mechanical chopper*. When chopping is done extracavity, the resulting pulse consists of the properties of the cw-signal and does not change over the duration of the pulse. This mode of operation is therefore often referred to as quasi-cw. When chopped intracavity, the pulse shape is determined by the dynamics of the resonator and the gain media and can, depending on the lifetime of the gain material, show strong signs of relaxation oscillation [3]. In these configurations, the pulse duration and duty cycle can easily be adjusted by design of the chopper blade. Even though these devices can offer a quick way of generating pulses from an already established cw-system, they are often not appropriate due to their limitation in maximum speed, lack of practicality, and additional costs. Furthermore, this technique sacrifices significant amounts of the cw radiation of the pump source, making the overall system less efficient.

When high repetition rates or very short pulses are required, an alternative is the use of laser oscillators that use optical effects to create pulse, e.g. Q-switching and modelocking [4,5]. The concept of Q-switching relies on the storage of energy while oscillation of the resonator is prevented by means of passive or active intracavity components [6,7]. Once the oscillation is enabled again, the stored energy will quickly get depleted by stimulated emission, resulting in a short light pulse. In this way, pulses in the order of tens of nanoseconds and kHz repetition rates are possible [3]. The process of modelocking uses active or passive components that interact with the optical field inside the resonator [8,9]. Here, however, the different longitudinal modes of the optical field are locked in phase. The resulting interference of these modes results in the formation of short pulses whose length is directly related to the number of modes locked together. The repetition rate is determined by the roundtrip time of the resonator. In this way, pulses with durations in the femto- and picosecond regime can be achieved with MHz repetition rates [10]. The downside of these systems is, however, that they are complex laser oscillators and are typically large and expensive.

In contrast to the pulses generated by a mechanical choppers, the output pulses of modelocked and Q-switched lasers systems are not square in shape and quasi-cw in their properties but determined by optical effects inside the resonators [11,12].

As alternative to mechanical and optical means of generating pulses, the electrical generation of pulses is possible, e.g. by using electrically modulated diode lasers. In this case, the electrical circuit that is driving the diode laser is modulated to generate pulsed electrical currents. Because of the short lifetime of semiconductors [13], the optical signal follows the electrical field closely. Therefore the characteristics of the pulses are mainly dictated and limited by the driver electronics. The advantage of these systems is that the pulse duration and pulse can be adjusted electrically, therefore making these systems very flexible source.

Pumping semiconductor disk lasers with pulsed-pump sources has so far only been demonstrated using 10 ns pulses generated by a Q-switched Nd:YAG laser to pump a 1.3 μm SDL [14]. The results are promising; however, using a complex pump source such as a Q-switched Nd:YAG laser greatly limits the practicality of such systems for real world applications due to the resulting size and cost.

The increasing use of pulsed diode laser in automotive collision systems has resulted in higher power devices that have recently become available at very low cost. One of these types of diode lasers is the OSRAM SPL PL90 series (see Figure 4.1). These devices are stacks of multiple edge emitting diode lasers, designed to operate at high peak powers (up to 150 W from a single package) while emitting short pulses (several 100 ns with repetition rates of up to 10 kHz). Because of the low duty cycle and short pulse durations, no heat management is required which allows the packaging of these devices in low-cost plastic and metal housings making them a very cost effective (~£1 to £20 depending on volumes) choice for various applications.

Figure 4.1 Picture of the OSRAM SPL PL90_3 nanostack laser (www.osram-os.com).

In this chapter, the use of an OSRAM SPL PL90_3 to pump 1.9 and 2.0 μm SDL is discussed. After the characterisation of the OSRAM SPL PL90_3, the power transfer and pulse characteristics of the pulsed-pumped SDL are presented. The following sections will then discuss the spectral properties of the SDL pulses and the thermal properties of the devices during the pump pulse. The prospect for extending the pulse duration of these devices will also be discussed and the observations underlined with a section about thermal modelling.

4.2 OSRAM SPL PL90_3 as pump source for SDLs

The OSRAM SPL PL90_3 used in this work is a stack of three edge emitting diode laser arrays with a total emitter size of 200x10 µm. It provides up to 75 W *on-time* power in a square pulse. The spectrum of the output of this device is centred at 905 nm and therefore makes this device suitable for barrier pumping of the (AlGaIn)(AsSb)-based SDLs used in the context of this work.

Figure 4.2 Driver board from Dr. Heller Elektronik for the OSRAM SPL PL90_3 pulsed diode laser.

The driver for the diodes were two commercially available avalanche transistor circuits from Dr. Heller Elektronik KG, Germany. This allowed the pulse duration to be adjusted between 15-180 ns and the frequency between 1-10kHz. It was also possible to trigger the board externally using a signal generator to increase or reduce the repetition rate beyond the limits of the board. In the context of this work, the board was triggered externally by a TTi TG120 signal generator. Unless stated otherwise, a pulse duration of ~180 ns with a pulse repetition rate of 10kHz was used. To power the driver board and diode, a dual-channel laboratory power supply with a maximum voltage of 30 V and a current of 3 A was used: one channel was used to power the board with 12 V; the second channel was connected to the diode power adjustment pin (Vs, see Figure 4.2) and enabled direct control of the output power of the pulsed diode laser. It should be noted that it was not the voltage across the diode that was varied but a control voltage on the board which the electronics converted to a proportional supply current to the diode laser.

The output power characteristics of the OSRAM SPL PL90_3 can be seen in Figure 4.3. The on-time power was determined by measuring the average output power using a laser power meter (Coherent Fieldmate) with a thermopile sensor (Coherent PM10) and dividing this value by the product of the pulse repetition rate and pulse duration.

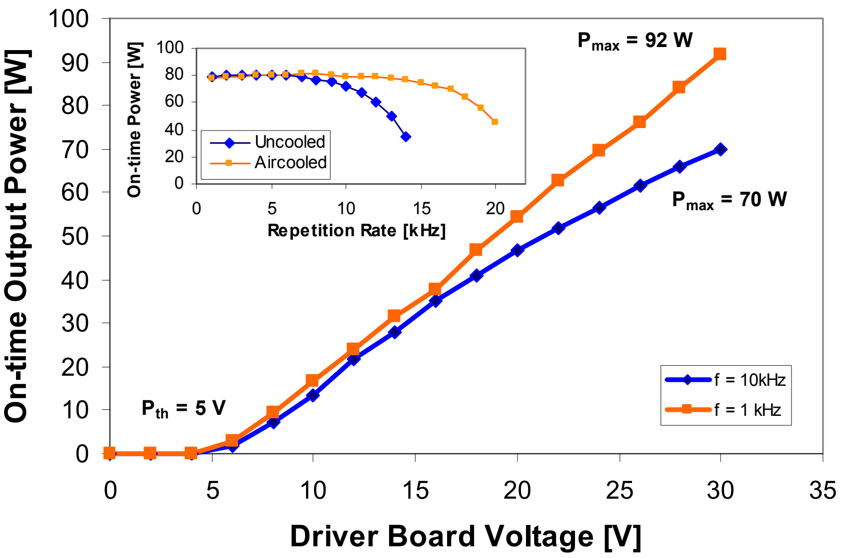

Figure 4.3 Output power characteristics of the OSRAM SPL PL90_3 nanostack laser at 1 and 10 kHz with no cooling applied **Inset:** Dependence of the output power at 30 V pump voltage on the repetition rate for an uncooled and a forced air cooled driver board.

The maximum output power of the device was found to be 70 W at a driver voltage of 30 V and the threshold was measured to be at 5 V. This was obtained at a repetition rate of 10 kHz (blue curve in Figure 4.3). The shape of the curve shows a clear reduction of the slope efficiency at higher driver board voltages. For comparison, the voltage-power transfer at 1 kHz repetition rate was taken too (orange curve in Figure 4.3). This did not show any signs of roll-over. To investigate this further, the maximum on-time power at 30 V pump voltage was recorded for repetition rates of 1-20 kHz (blue curve in inset of Figure 4.3). For each measurement, the system was left to thermally stabilize for 1-2 minutes. This measurement clearly shows a reduction in actual output power with repetition rates >5 kHz. This is not, however, associated with the diode laser but with heating of the transistors on the driver board. It was therefore possible to reduce the effect of power reduction by active air cooling of the board. In this way, the repetition rate could be extended to >20 kHz. With more sophisticated cooling geometries for the transistors, it should be possible to increase the repetition rate further. Additionally the pump voltage could be reduced which, at the expense of output power, would reduce the heat load on the transistors.

After investigating the power characteristics of the OSRAM SPL PL90_3 and the driver board, it was necessary to investigate the spatial properties of the output beam of the pulsed diode laser to choose appropriate beam conditioning optics. Because of the difference in emitter size in the two emission planes, the beam is not symmetrical, but has a low and high divergence plane, called the *slow axis* and *fast axis* respectively. When conditioning an asymmetric beam like this, a major concern is to prevent clipping of the light at the optics. This often requires for lenses that have high numerical apertures (NA); defined as the sine of the half angle divergence angle the lens can capture.

To calculate the required NA for a lens suitable to collect the light of the SPL PL90_3, the divergence angle (to the $1/e^2$ half width) of the fast axis was first measured. Figure 4.4 shows the data collected at different points along the beam propagation for the fast and slow axis. From a linear fit to this data a divergence half angle of 16 and 8 degree in the fast and slow axis respectively were determined (see inset of Figure 4.4). It should be noted that the given distances are not the actual distances to the facet of the diode laser but relative distances the pinhole and photodetector were translated. The actual position of the facet can be determined from the linear fit to the data and was found to be at z = -10.6 mm.

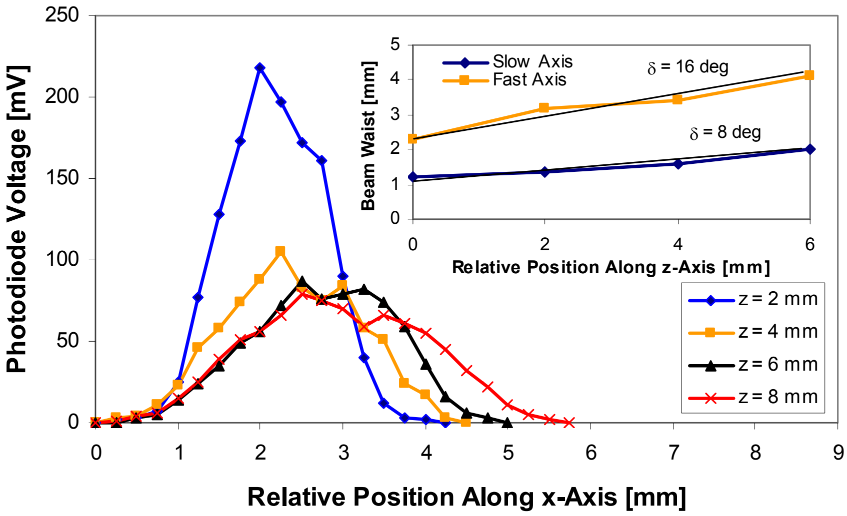

Figure 4.4 Divergence measurement for the OSRAM SPL PL90_3 the beam profile at 4 different positions along the fast axis separated by 2 mm. **Inset:** Beam waist over propagation along z-axis.

The divergence of 8 and 16 degree in the slow and fast equate to an NA of 0.14 and 0.07 respectively. A lens to collect the light of the fast axis and collimate it would therefore need to have an NA larger than 0.14.

In the following section the chosen experimental arrangement for the pulsed diode laser and its use as pump source for the 1.9 and 2.0 μm SDL is described.

4.3 Experimental arrangement

For the experiments, an arrangement as shown in Figure 4.5 was chosen. To collect the radiation, an achromatic, 8 mm focal length lens with an NA of 0.5 was employed. This NA was sufficient to effectively collimate the fast axis. The slow axis, however, was not collimated with this lens but its divergence only reduced. Therefore the slow axis could be divergence matched to the fast axis so that a square spot with the same dimensions in both planes was formed at the position of the focusing lens (see Figure 4.6). At this point, an 11 mm lens was placed to focus the radiation onto the SDL chip. Because of its thin active region, the SDL format does not require mode matching over an extended distance along the optical axis as typically known from doped-dielectric laser. The relatively low brightness of the pump diodes was therefore not found to be a problem.

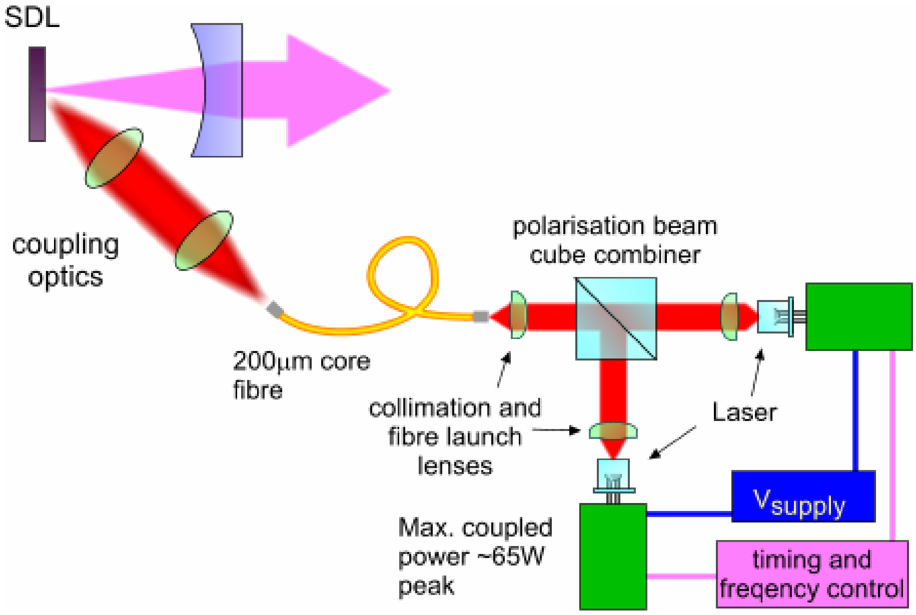

Figure 4.5 Experimental configuration of the pulsed-pumped SDL. The collimation and focussing lenses were 8 mm and 11 mm focal length respectively and the resonator mirror was a 50 mm radius of curvature output coupling mirror.

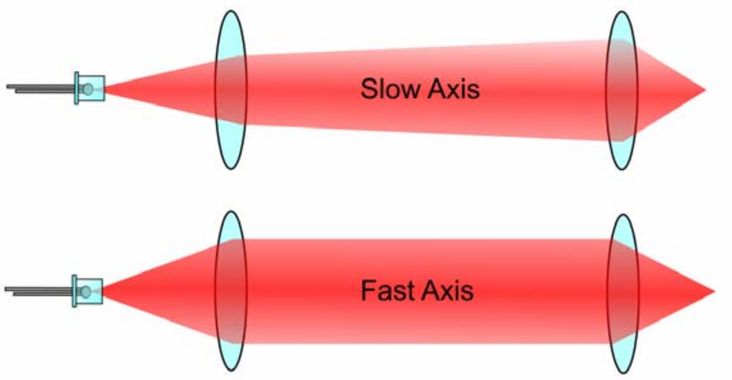

Figure 4.6 Schematic of the fast and slow axis beam propagation conditioned using 8 and 11 mm lenses.

To increase the available pump power, two of the OSRAM diode lasers were used. This was possible using polarisation coupling. This requires the light of the diodes to be polarised which is a property edge emitting diode lasers possess as the asymmetry of the emitter planes favours TE polarised light [15]. The combination of the two beams is achieved by using a polarising beam cube that allows transmission of a tangential polarised beam while reflecting sagittal polarised beam. This enabled superimposing the beams onto each other, resulting in a beam with equal amounts of both polarisations. This can potentially be a problem for laser systems where the active medium has a polarisation dependent absorption. However, in the context of pumping SDLs this is not a problem. In this way, the individual power of both diodes could be combined delivering up to 120 W on-time power (Figure 4.7) and thereby doubling the available pump power.

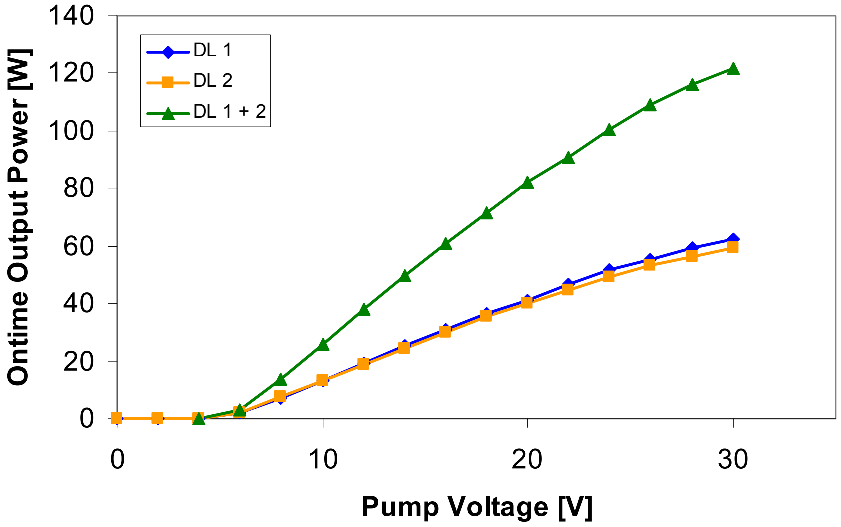

Figure 4.7 Output power characteristics of the OSRAM SPL PL90_3 beam conditioning arrangement. Shown are the individual powers from diode laser 1 and 2 (LD 1 & LD 2) and their polarisation combined power after the focusing lens. The maximum output power is >120 W. The repetition rate was set to 10 kHz.

To deliver the light of the pulsed-diode arrangement to the SDL chip it was initially chosen to couple the radiation into a 200 µm core diameter fibre. This enabled flexible delivery of the pump light to the SDL chip by using the optical arrangement used when cw-pumping the SDL. Fibre-coupling of the radiation, however, reduced the available pump power by ~50 % to around 62 W due to coupling losses. After the fibre, the radiation was delivered onto the chip using two additional aspheric lenses. These imaged the fibre facet 1:1 onto the SDL creating a pump spot of ~200 µm diameter on the chip.

The SDL resonator was a simple near-hemispheric 2-mirror cavity. The 1.9 or 2.0 µm SDL acted as an active plane-mirror while a 50 mm radius of curvature mirror completed the resonator. The separation between the two mirrors was set to 45 mm which corresponded to a fundamental resonator mode waist on the chip of 100 µm (200 µm diameter) which matched the pump mode. It should be noted that for these experiments, the heatspreaders used in the cw work were still in place; however, no water cooling of the brass mount was employed.

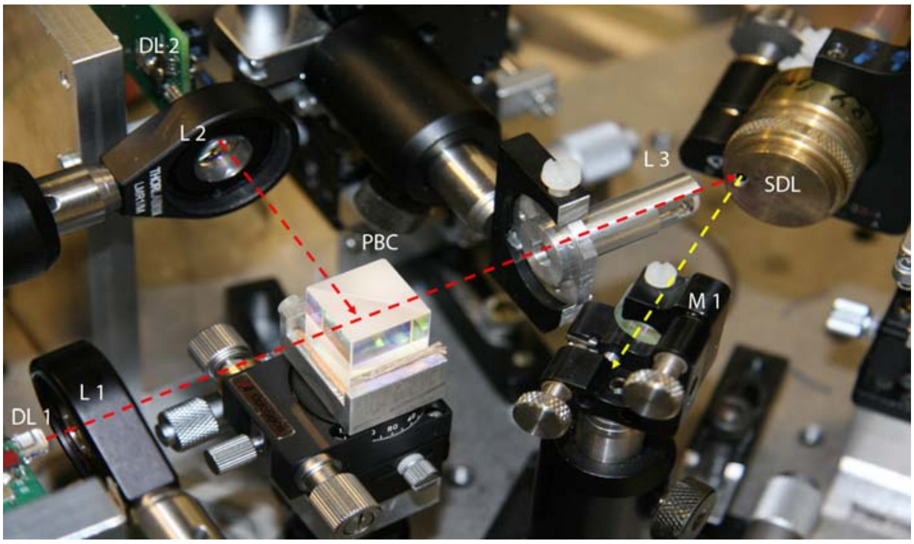

Figure 4.8 Photograph of the directly pulsed-pumped 1.9 µm SDL using two OSRAM SPL PL90_3 diode lasers (DL 1 & DL 2) collimated by lenses L1 & L2 and polarisation combined by the polarising beam splitter cube (PBC). The radiation was focused onto the semiconductor disk (SDL) by another lens L3. The SDL cavity was completed using a curved output coupler M1.

If higher pump powers are required, the radiation of the pulsed diode lasers can also be delivered directly to the SDL. Doing this increased the incident on-time power at the SDL to ~120 W as no losses associated with the fibre coupling were introduced. Aside the improvement in power, the compactness of the system was also increased (see Figure 4.8).

4.4 Experimental results

4.4.1 Power transfer characteristics

Pumping the 1.9 and 2.0 µm SDL with the arrangement described in the previous section led to oscillation of the SDLs. The traces of the pump and output pulses were recorded using a digital oscilloscope (Agilent Infiniium 54830B) and an amplified InGaAs photodetector (Thorlabs PDA10D-EC, 15 MHz bandwidth). To resolve the pulses fully it was important to focus all the light onto the chip of the detector and prevent light from hitting the surrounding electronics of the photodetector chip which caused the signal to be distorted. For this purpose a lens with 30 mm focal length was chosen and the signal attenuated using colour filters to prevent the detector from saturation. Stable output pulses were observed with full width half maximum (FWHM) pulse durations of 160 ns and 147 ns for the 1.9 and 2.0 µm SDLs respectively with the pump pulse duration being 180 ns. Due to the previously mentioned short carrier lifetime of the semiconductor material [13], the output pulses of the SDLs closely mirrored the pump pulses (see Figure 4.9). However, a turn on delay of the pulse was observed.

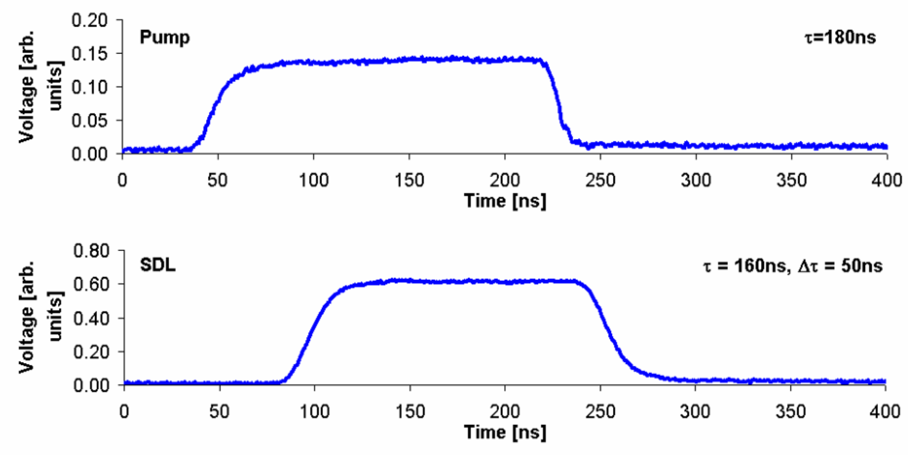

Figure 4.9 Timing diagram of the 1.9 µm pulsed-pumped SDL. The full width half maximum pulse duration was measured to be 160 ns. A turn on delay Δτ=50 ns was observed which is attributed to the SDL chip heating up to operating temperature as to overcome the offset between micro-cavity resonance and quantum well peak emission.

One might expect that this delay was associated with the resonance build-up time of the resonator. This, however, was falsified by calculating the resonator build-up time T_b using equation 4.1 [16].

$$T_b \approx \frac{t_c}{r-1} \ln \cdot \left(\frac{I_{ss}}{I_0} \right) \qquad \textbf{Equation 4.1}$$

Here, t_c is the cavity lifetime, I_{ss} the steady state oscillation level, I_0 the initial noise level and r the normalised inversion ratio. According to [16] the ratio of I_{ss} to I_0 varies between 10^8 and 10^{12} depending on the laser. For the SDL an average value of 10^{10} was assumed. The inversion ratio r of the pulsed-pumped SDL is relatively high due to the high on-time pump powers. As a consequence, T_b is with ~3.5 ns relatively short. The turn-on delay between the pump and SDL pulse therefore had to be attributed to another mechanism. In the later section of this chapter it will be shown that this delay is indeed attributed to the heating of the SDL chip that was necessary to overcome the offset between micro-cavity resonance and quantum well peak emission. In the case of the 1.9 μm SDL this delay was found to be 50 ns while in the case of the 2.0 μm SDL the turn on delay was found to be 63 ns. The difference between these two values is an indication for a difference in the micro-cavity offset. Recalling the results of the cw-pumping, it was observed that, compared to the 1.9 μm SDL, the 2.0 μm SDL was able to withstand higher pump powers without rolling over thermally. This would be expected only if the micro-cavity resonance offset was larger as this would enable more heating of the device before the micro-cavity resonance and quantum well peak emission are spectrally aligned. In the pulsed regime, however, a small or zero offset might be more advantages as it would result in faster turn on.

In addition to the turn-on delay, a delay in the turn-off was observed too. This was attributed to a combined effect of the photon lifetime and the energy storage in the quantum wells for the duration of the carrier lifetime (multiple nanoseconds). In addition, the falling edge of the pump pulse was distorted by the speed of the detection system, dictated by the Thorlabs PDA10D-EC photodetector bandwidth of 15 MHz, and could not fully be resolved.

To record power transfer characteristics for the fibre delivered 1.9 μm pulsed-pumped SDL, the Thorlabs PDA10D-EC photodetector was used as the average power of the pulsed-pumped SDL was too low to be accurately measured using the available thermopile power meters. The photodiode was calibrated using the Coherent Fieldmate with the PM10 thermopile head. Beforehand, however, it was important to check the linearity of the photodetector. Therefore 2.0 μm cw radiation was focused onto the photodetector and the photodetector voltage plotted against the incident power. To prevent saturation, colour glass filters were put into place to attenuate the beam. The result of this measurement can be seen in Figure 4.10. It shows that the photo detector has a linear response over its whole range of operation as long as it was not saturated.

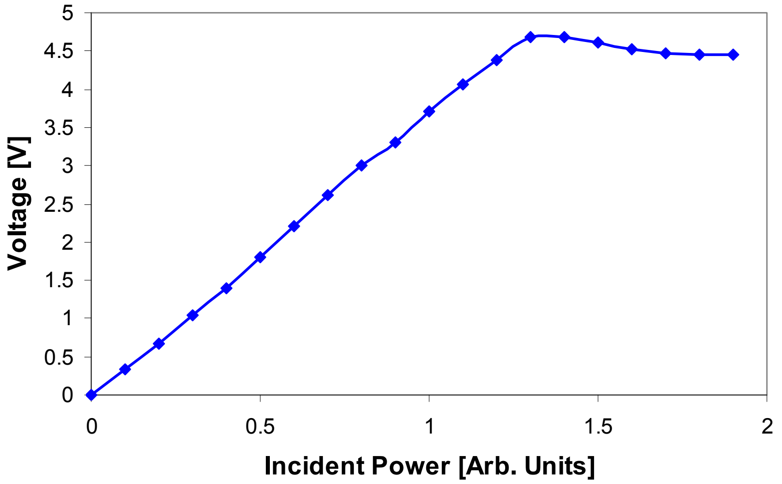

Figure 4.10 Output voltage of Thorlabs PDA10-EC versus incident power. Linearity is given throughout the full range until the point of saturation is reached.

The power transfer measurements of the pulsed-pumped SDL revealed an optimum output coupling of 4 % which is significantly different compared to the 9 % output coupling that was found to be best when operating the SDL in cw mode.

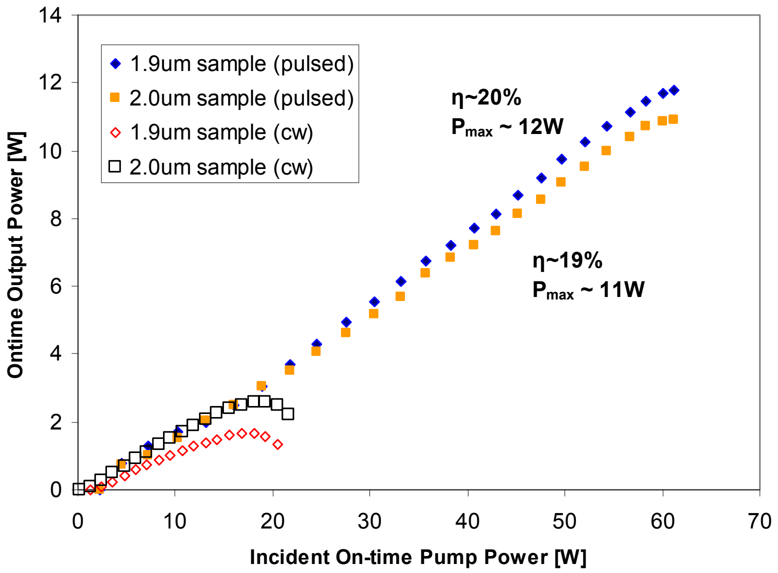

Figure 4.11 Power transfer characteristic for the pulsed-pumped 1.9 and 2.0 µm SDL with fibre-coupled arrangement. The maximum on-time output power was 12 W and 11 W for the 1.9 and 2.0 µm SDL respectively. The maximum slope efficiencies were 20 and 19 %.

For the pulsed-pumped configuration maximum on-time output powers of 12 W in case of the 1.9 µm sample were obtained with a slope efficiency of 20 % (see Figure 4.11) with respect to the incident pump power. For the 2.0 µm SDL the maximum on-time output power was found to be 11 W with a slope efficiency of 19 %. For comparison, the cw operation of exactly the same resonator geometry was recorded (using the 25 W diode laser used in the cw experiments). As the optimum output coupling for the pulsed and cw case is different, however, a 9 % output coupler was used for the cw-operation. Comparing the results, it can be seen that an improvement by a factor of 7 in the on-time output power was achieved. It should be noted that this comparison is disadvantageous for the pulsed-pumped results as the pulsed-pump source was emitting at 905 nm compared to 980 nm which results in an increase in the quantum defect from 47 to 51 %.

The high end of the pulsed-pumped power transfer curve shows a slight roll over of the efficiency. Whether this was the indication of the system reaching an upper limit due to thermal effects was investigated by employing a retro-reflector to reflect the residual pump light that got reflected off the diamond, back onto the chip. This increased that maximum output power by 15 % without increasing the strength of the rollover, indicating that the system was not yet thermally limited.

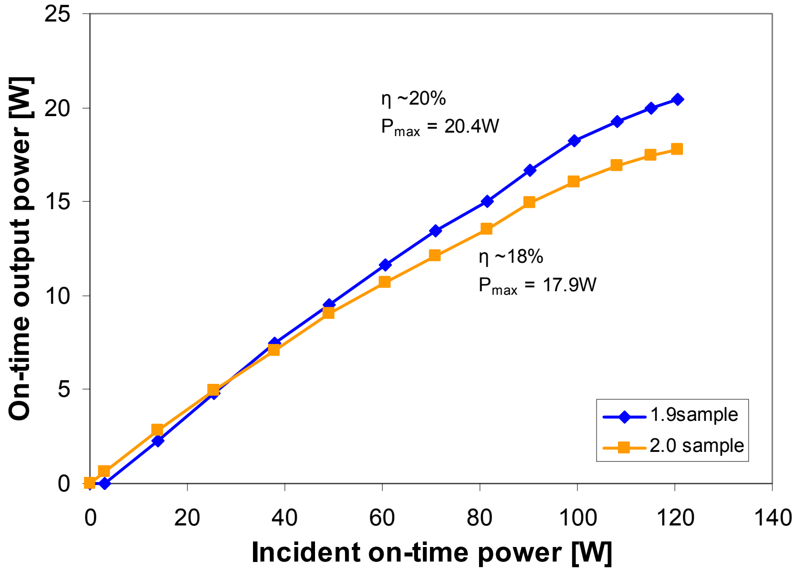

Figure 4.12 Power transfer characteristics of the directly pulsed-pumped 1.9 and 2.0 µm SDLs.

To investigate this further, the fibre coupling was removed from the system and the 1.9 and 2.0 µm chip pumped directly. Utilizing the full 120 W of pump power, the on-time output power of the SDL was increased significantly to over 20 W for the 1.9 µm SDL and 18 W for the 2.0 µm sample (Figure 4.12). The respective maximum slope efficiencies were measure to be 20 and 18 %. Here the onset of a rollover indeed starts to show, however, not as strong as in the lower power cw results but a rather slow rollover as known from pulsed SDLs [1].

To determine the beam propagation parameter of the pulsed-pumped SDLs the same experiment as described in chapter 3 (section 3.6) was carried out using the DataRay Beamscope. The fact that the beam was pulsed rather than cw was not found to be a problem as the integration time of the detector inside the Beamscope P8 head was long enough to sample over the duration of multiple pulses. The arm length, hence the ratio of cavity to pump mode, was again varied and the beam propagation parameters as well as the powers recorded for each position. The result of the measurement can be seen in the left graph of Figure 4.13. Contrary to the experiments in chapter 3, the resonator was not changed to a 3-mirror layout but stayed the same as used in the previous experiments.

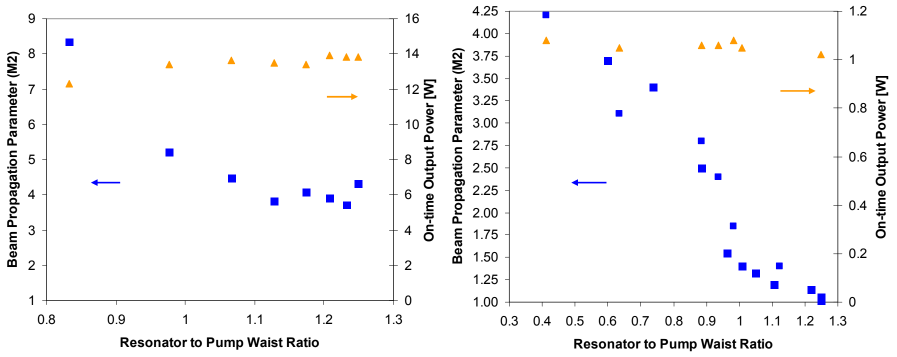

Figure 4.13 Beam-quality factor of the pulsed pumped SDL (left) and a 2.0 cw operated SDL (right) in a 2-mirror resonator. While the cw laser is capable of running at M² values of close to 1 the pulsed system has a minimum M^2 of 4.5.

While an M² value of 4.5 was found at maximum power, it was not possible to improve the beam quality of the laser in the same way as was possible with the cw 3-mirror resonator. This, however, is not a consequence of the 2-mirror resonator arrangement used for the pulsed-pumped set-up but a result of the mode of operation, i.e. the pulsed-pumping. For comparison, the beam propagation parameter variation was determined for a cw-pumped 2.0 µm 2-mirror SDL and is shown on the right hand side in Figure 4.13. It can be seen that a clear improvement of the beam propagation parameter to M^2~1 was achieved in a similar manner as observed in the 3-mirror arrangement used in chapter 3. One possible explanation for the difference in M^2 between the two different modes of operation was assumed to be related to the transient temperature rise of the chip observed in the spectral characterisation later in this chapter. The intensity profile of the pump beam heats the chip with a variation in the radial dimension. This may introduce an aperture effect, which would result in a change of mode overlap over the pulse duration and thereby change the M^2 in a transient fashion. As the integration time of the DataRay Beamscope was longer than the pulse duration, this effect would not be resolved. To investigate this possibility, a transient beam propagation parameter measurement was carried out using the knife edge approach [17].

If the M^2 would change during the pulse duration then the same would apply to the beam waist. As the knife edge is then translated into the beam, distortion of the pulse shape should be observed, as the different waist sizes during the pulse should clip at the knife edge at different moments in time. It would therefore be possible to collect the beam profiles at different moments during the pulse. If this is done at multiple points along the beam propagation around the focus created by a lens, the transient beam propagation parameter can be determined.

When this experiment was carried out, however, the pulse shape did not get distorted when translating the knife edge into the beam, indicating that the M^2 value does not change during the pulse duration. Further investigations are needed to ascertain the origin of the relatively poor beam quality.

4.4.2 Spectral characterisation

To investigate the spectral properties of the pulses, a grating monochromator was used. In this way the etalon mode groups associated with the diamond heatspreader bonded onto the chips could be fully resolved. When cw-pumping, one would expect the etalon mode groups to form a steady-state. When pulsed-pumping, however, the spectrum does not reach equilibrium during the 180 ns duration of the pulse.
Therefore the temporal evolution of all the 9 etalon mode groups of the 1.9 µm SDL at a pump power of 62 W was recorded. A schematic of this measurement is shown in Figure 4.14.

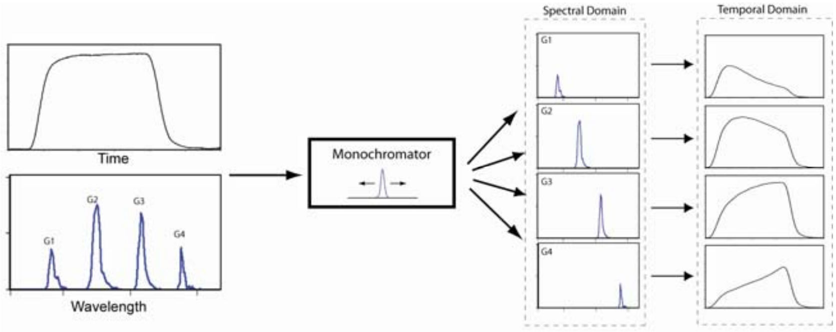

Figure 4.14 Principle of recording the spectral evolution of the SDL output using a grating monochromator as variable filter.

The data recorded in this way is shown in Figure 4.15. Here it can be seen that none of the mode groups are constant in intensity throughout the duration of the square pulse. The quasi-cw pulse shape is therefore made up of the cumulative intensities of the individual spectral modes.

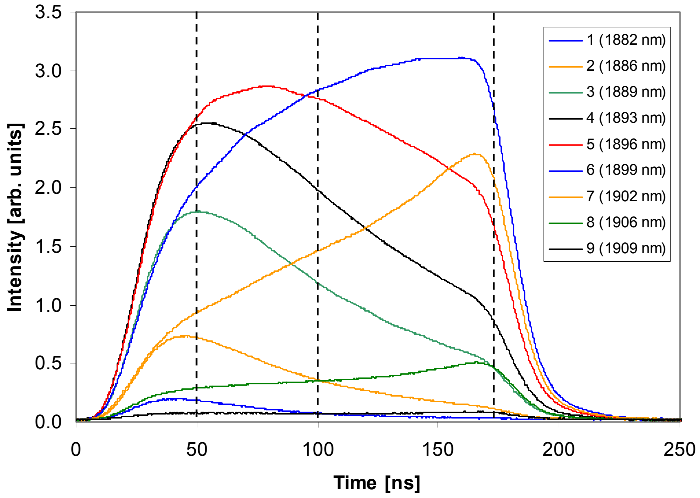

Figure 4.15 Spectral evolution of the 9 etalon mode groups of the 1.9 µm SDL associated with diamond heatspreader. The peaks are numbered from 1 to 9 in the order they reach threshold during the pulse. The dotted lines show the times where quasi-instantaneous spectrums were extracted for further analysis (see Figure 4.16).

To gain more information about the evolution of the etalon mode groups, the instantaneous spectra at different times throughout the pulse were extracted from the previous data. A subset of these is depicted in Figure 4.16.

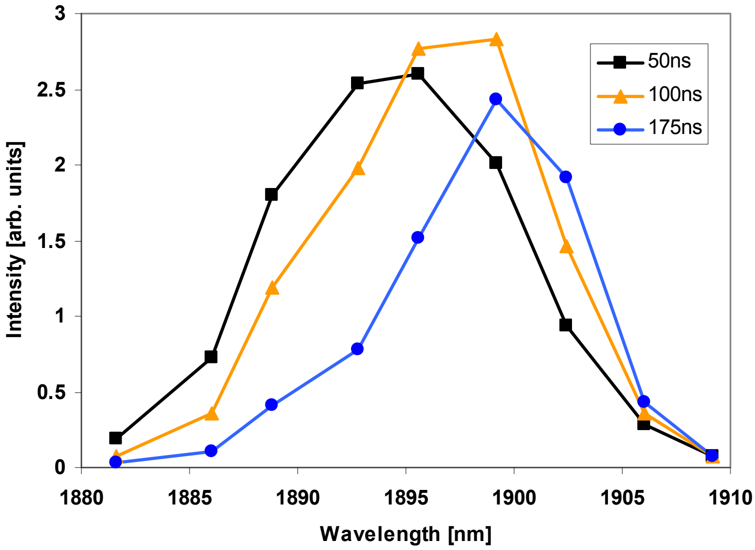

Figure 4.16 Subset of the quasi-instantaneous spectrum at different times (50, 100, 175 ns) from the output of the pulse derived from the etalon mode evolution (Figure 4.15).

Here a clear red shift of the spectrum throughout the pulse is visible. Remembering the observations made in the tuning characterisation discussed in chapter 3 this red shift can be attributed to heating of the device which causes the micro-cavity resonance to shift, thereby tuning the wavelength. To quantify this wavelength shift, the change of wavelength over the pulse duration can be plotted (see Figure 4.1)

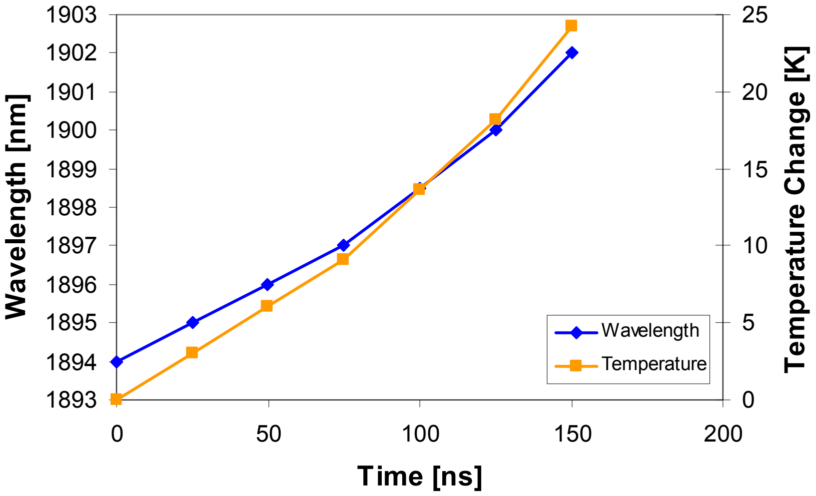

Figure 4.17 Wavelength (blue curve) and temperature (orange curve) variation over time during the pulse of the 1.9 µm pulsed-pumped SDL.

A clear wavelength shift of 8 nm from 1894 to 1902 nm occurred during the 150 ns. Taking the rate of change of the micro-cavity resonance into of ~0.33 nm/K into consideration [18], this wavelength shift equates to a total temperature rise of 24K.

From this we can obtain a heating rate of 0.15 K/ns for the 1.9 µm. In the same way, a heating rate of 0.16 K/ns was determined for the 2.0 µm SDL. From this, one can determine the additional temperature rise during the delay between the start of the pump and laser pulse to a total device temperature rise of 29 and 33K for the 1.9 and 2 µm samples respectively.

The relationship between wavelength and temperature can be further exploited to change the central emission wavelength of the SDLs. Even though active cooling of the SDL chips is not required for efficient operation, temperature control of the chips allowed the variation of the wavelength. In this work, the temperature of the chip was changed by varying the cooling water temperature. Alternatively, thermoelectric coolers could used to obtain a more practical solution. The result of this experiment can be seen in Figure 4.18 and reveals that the rate of change of the wavelength with temperature is 0.33 nm/K.

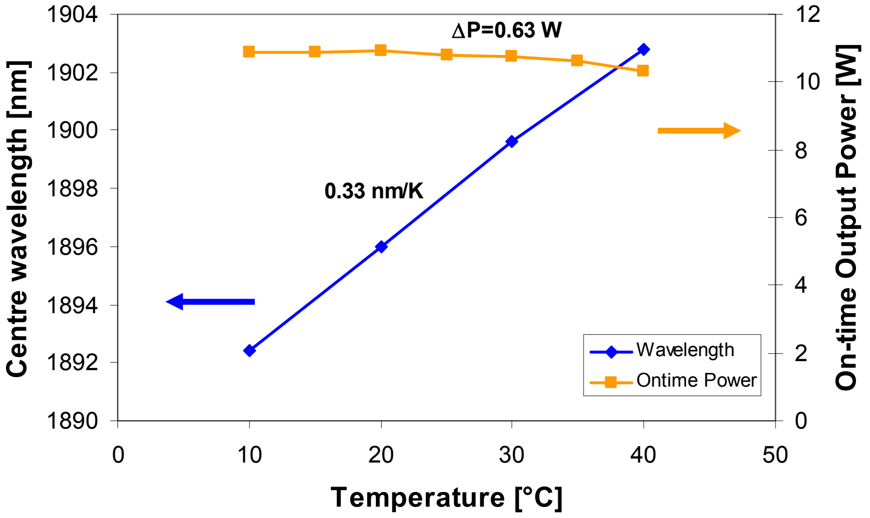

Figure 4.18 Tuning of the pulsed-pumped 1.9 µm SDL by changing the temperature the chip was held at. Tuning between 1892 and 1903 was obtained with an overall power drop of 0.63 W.

In addition to the wavelength, the on-time output power is plotted over the temperature. It can be seen that a 6 % drop of on-time power results from the increased temperature. This heat related reduction in output power will increase significantly if the temperature is increased to tune to longer wavelengths. The temperature tuning is therefore only feasible when small wavelength changes are required.

4.5 Operation with extended pulse durations

4.5.1 Power characteristics and temporal properties

Even though the specifications for the driver board and the pulsed diode lasers set the upper limit of the pulse duration to 200 ns, it was of interest to investigate the possibility to extend the pulse duration beyond this value. As this was not possible with the factory configuration, the control board was modified by replacing the potentiometer that was responsible for the adjustment of the pulse duration. The original 1 kΩ potentiometer was replaced with a 10 kΩ potentiometer, allowing the pulse duration to be extended to up to 1.3 μs. When operating at these extended pulse durations, however, it was found that the repetition rate of the diode laser needed to be reduced significantly or heat related effects started to reduce the maximum on-time output power. For the initial investigations, the pulse repetition rate was therefore set to 100 Hz and the on-time output power limited to 30 W per diode laser.

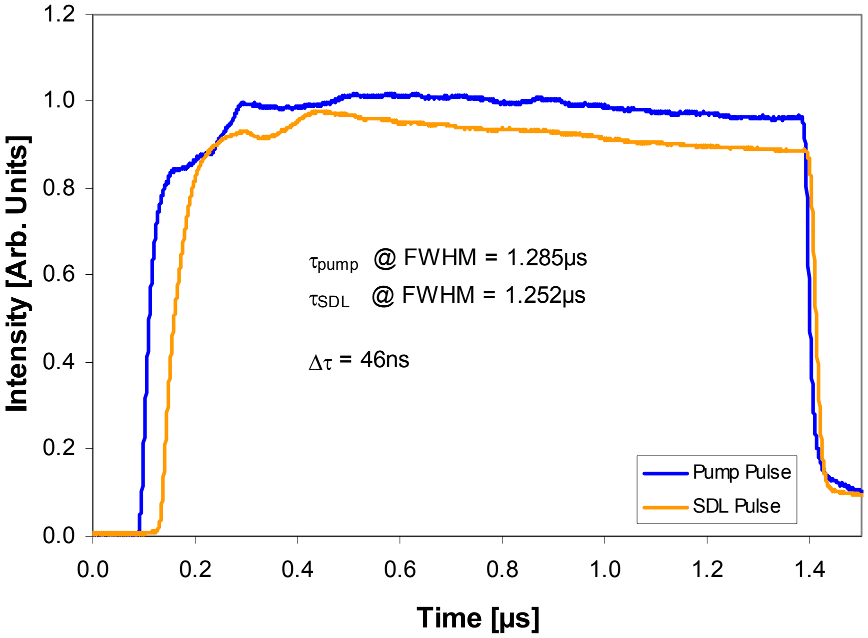

Figure 4.19 Single pulse of the OSRAM SPL PL90_3 nanostack laser operating with an extended pulse duration of ~1.285 μs (blue line). The orange line shows the output pulse of the 1.9 μm SDL pumped with the ~1.3 μs pulse. The turn on delay Δt reduces the pulse duration of the SDL to 1.252 μs.

Having a closer look at the shape of the diode laser pulse reveals an irregularity of the pulse shape after around 200 ns where a steep rise in intensity occurs. After this, the pulse shows the flat top shape again. The longest pulse duration at maximum power was found by progressively increasing the pulse duration from 200 ns onwards until breakdown of the device occurred at 1.1 µs. At this point, a sudden drop in output power was observed to ~1/3rd of the maximum power, an indication that 2 of the 3 emitters of the nanostack were damaged.

With the pulse duration of the diode laser set to 1.3 µs it was used to pump the 1.9 µm SDL. The output pulse of the SDL is shown in Figure 4.19. The SDL pulses still mirror the shape of the pump pulse closely. The previously observed turn-on delay is also still present.

Even though the on-time power of the pulses did not change with the increased pulse duration, the pulse energy of the pulses increased significantly. Compared to full power with pulse duration of ~200 ns, the pulse energy was increased by a factor of 3.25 from 4 to 13 µJ when operating at half the maximum power and with a pulse duration of 1.3 µs. With the pulse duration set to 1 µs and maximum power an energy increase by a factor of 5 to 20 µJ is obtained.

When considering using these devices as a pump source for Cr^{2+}:chalcogenide lasers, this increase in energy can be of great benefit as the upperstate lifetime (e.g. Cr^{2+}:ZnSe t ~ 4 µs) allows the full energy to be harvested at extended pulse durations. This would not be the case if the upperstate lifetime of a laser was significantly shorter than the pump pulse duration, as spontaneous emission would start to deplete the upper laser level.

4.5.2 Spectral characterisation

The spectral behaviour of the extended pump pulse duration (set to 1 µs) was investigated using the grating monochromator to resolve the etalon mode groups. The result of this measurement can be seen in Figure 4.20

Again, it was observed that the different etalon mode groups turn on at different moments during the pulse. However, a significant difference occurs after ~500 ns. Unlike with pulses of ~200 ns duration, it can be seen that in this case the different frequency components start to come to an equilibrium. This is even more obvious in the instantaneous spectra (Figure 4.21) and the resulting temperature and wavelength change over time (Figure 4.22).

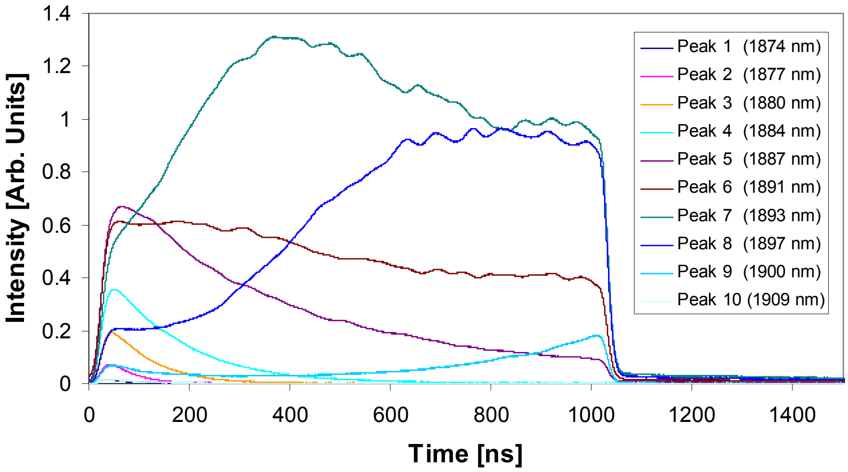

Figure 4.20 Spectral evolution of the 10 etalon mode groups of the 1.9 µm SDL, associated with the 250 µm thick diamond heatspreader. The peaks are numbered from 1 to 10 in the order they reached threshold during the pulse and the wavelengths in brackets give the centre wavelength of each of the etalon mode group peaks.

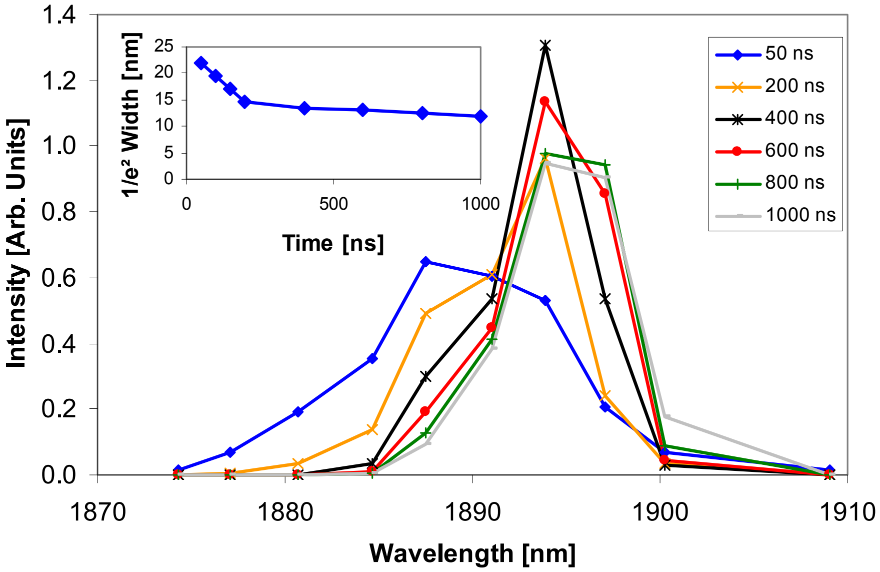

Figure 4.21 Instantaneous spectra of the 1.9 µm pulsed-pumped SDL at various times during the 1 µs pulse. **Inset:** Narrowing of the spectrum is observed from 200 ns onwards.

The instantaneous spectra clearly show an overlap at a wavelength of ~1895 nm without any further shift. Additionally, the spectrum also narrows (see inset of Figure 4.21) which is an indication for the stabilisation of the output spectrum.

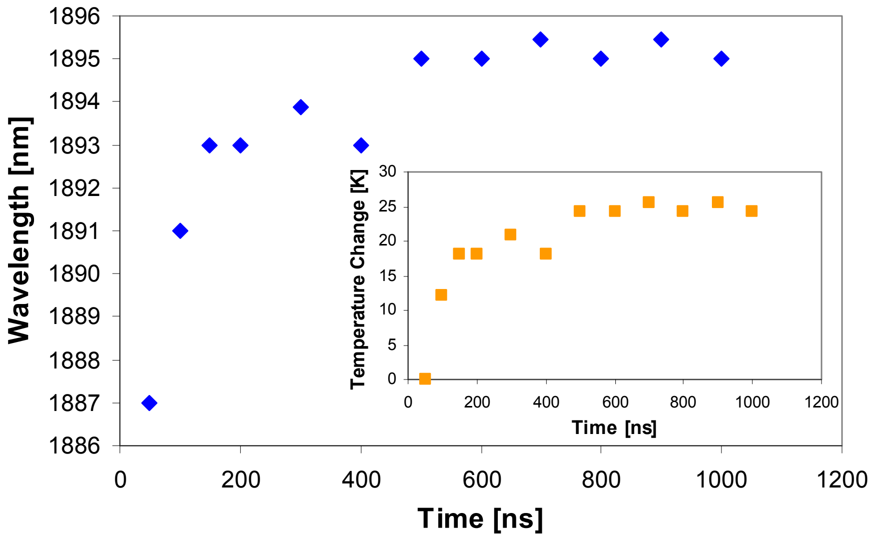

Figure 4.22 Wavelength shift during the pulse duration of the 1.9 µm SDL. **Inset:** Temperature change associated with the 0.33nm/K drift rate of the SDL.

The temperature and wavelength change over time indicate a stabilisation of the output wavelength and temperature of the chip after a pulse duration of 500 ns. Before 200 ns, in the region investigated in the short pulsed-pumped arrangement, the rate of wavelength change is with 0.18 nm/ns almost the identically to the 0.15 nm/ns of the previous measurement and well within the uncertainty of the measurement. To investigate this further a thermal model for the SDL was developed using finite element analysis (FEA) software. The modelling and the results are discussed in section 4.7.

If output pulses consisting of the steady state part only without the transient period at the beginning are required, it is possible to delay the turn-on of the pulse artificially until the device has heated to overcome the initial chirp. In this work, this was achieved by inserting a variable aperture into the resonator that allowed varying the level of loss introduced into the resonator mode. Therefore it was possible to increase the threshold of the resonator and in turn increase the turn-on delay. The results of this can be seen in Figure 4.23. The picture shows that the output pulse of the SDL was delayed significantly by ~400 ns. Using a grating monochromator, the bottom trace was recorded, which shows stable spectrum centred at 1910 nm.

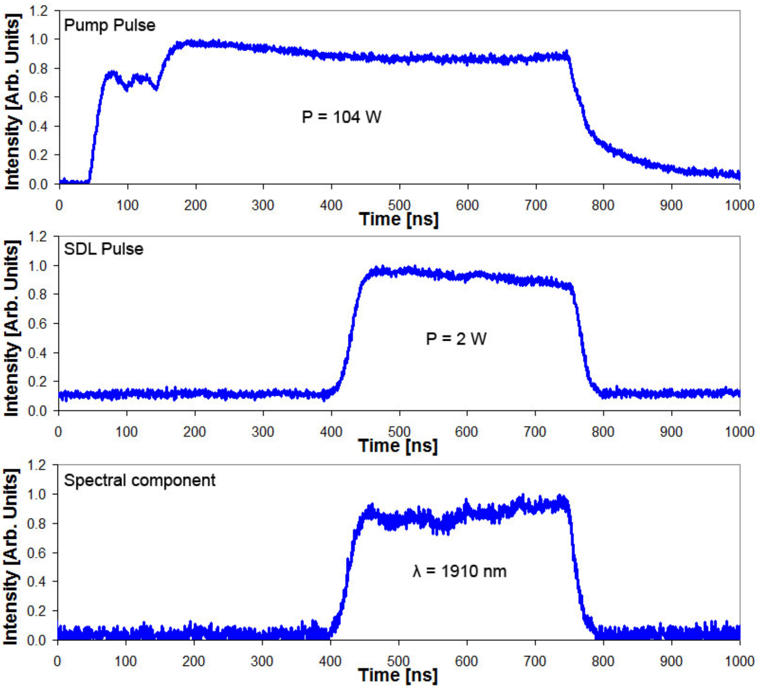

Figure 4.23 Chirp-free output of the 1.9 µm pulsed-pumped SDL. **Top:** 905 nm pump pulse; **Middle:** Output pulse from the SDL; **Bottom:** Spectral evolution of the output pulse.

As this technique significantly reduces the on-time output power by, 87 % (from 16 to 2 W with pump voltage set to 25 V), it might be advantageous to envisage other solutions to delay the resonator turn on. One of these could for instance be the use of an additional pulsed diode that heats the chip while being low enough in power that the SDL does not reach threshold. It might also be possible to tune the laser to the etalon mode group that switches on last by using an additional etalon. Alternatively, it would also be possible to increase the resonator length, spot sizes or output coupling to increase the cavity build-up time and thereby increase the turn on delay of the pulse. Last, the implementation of active or passive Q-switches could be used to delay the pulse turn-on.

Earlier in this chapter the possibility to tune the output wavelength of the laser by means of varying the temperature of the chip was discussed. As an alternative it is possible to insert a birefringent filter (BRF) into the laser and use this to tune the output wavelength of the SDL [19]. Doing this experimentally, it was found that the pulse shape still mirrored the pump pulse closely; however, a small reduction of the pulse duration from 1001 to 968 ns was observed. When analysing the spectral evolution of the individual pulses it was observed that the chirp of the pulse was not preserved but the output wavelength limited to one etalon mode group. By turning the BRF it was possible to tune this mode group between 1862 and 1930 nm (see Figure 4.24).

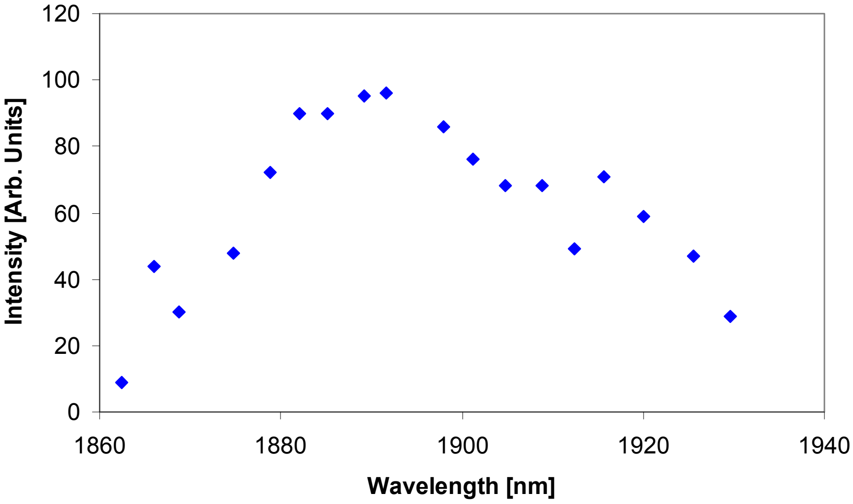

Figure 4.24 Tuning curve of the 1 µs pulsed-pumped 1.9 µm SDL using a birefringent filter. A tuning range of 68 nm between 1862 and 1930 nm was obtained.

4.7 Finite element analysis of the pulsed-pumped semiconductor disk laser

With the computational power of today's computers, the use of finite element analysis (FEA) allows one to investigate complex numerical systems that are difficult to solve analytically. The flow of heat inside the pulsed-pumped SDL is one problem that can be solved using this technique. The FEA software divides the whole structure into small sub volumes which are calculated independently and their relationship between each other computed at finite time steps (Figure 4.25). A heat load can then be introduced into some of these volumes, in the case of the pulsed-pumped system, representing the heat introduced by a pump source. To obtain a final solution, the heat of a volume is determined by the absorbed pump power per discrete time interval Δt and the energy transfer between adjacent volumes. If this is iterated, a solution for the temperature distribution is found when steady state is reached.

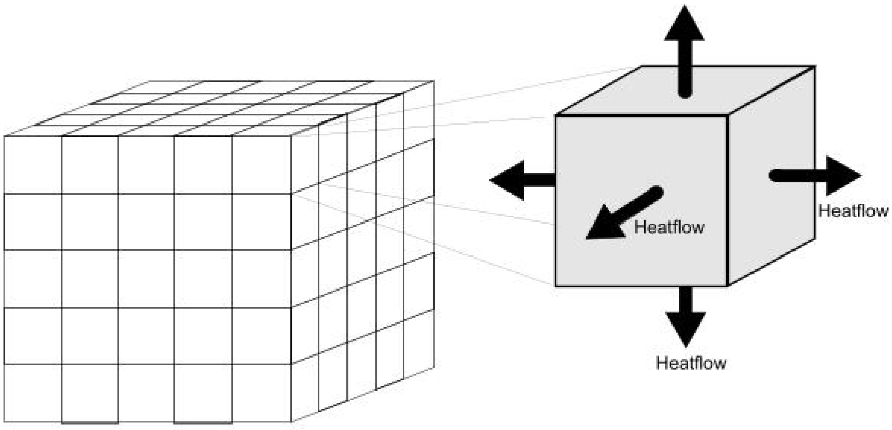

Figure 4.25 Schematic of a finite element analysis approach splitting up the volume in sub elements whose properties can be calculated independently.

To model the heat evolution inside the pulsed-pumped 1.9 µm SDL, the software COMSOL Multiphysics (version 3.5.0.494) was used. The chip was modelled together with the brass mount as well as indium layers that were used when mounting the chip. The model of the assembly and the grid of the various areas can be seen in Figure 4.26. To reduce processing times, the grid density was varied, placing high grid densities in important areas that require high spatial resolution.

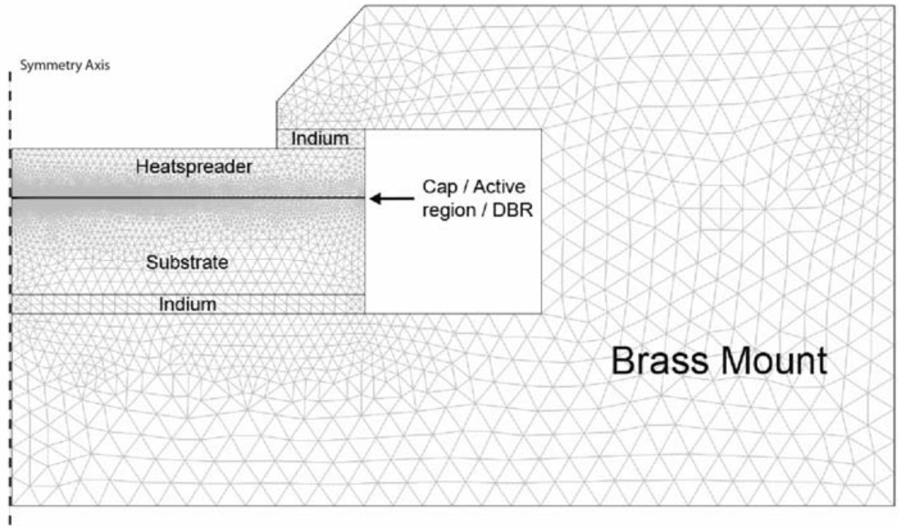

Figure 4.26 SDL chip assembly for the FEA analysis showing the different components and the grid for the calculations.

For the calculations, the layer structure and their associated thicknesses t, thermal conductivities k and absorption coefficients α were required. For the transient model, the heat capacity and densities were also required The values for the thickness were obtained from the design of the structure while the thermal conductivities and absorption coefficients were obtained from references [20-22]. For the heat capacity and density, the values for GaSb, i.e. $5.61 \cdot 10^{-6}$ kg/m^3 and 250 J/kg·K respectively, were used for the layers of the structure [23].

Layer	Material	t [nm]	k [W/m·K]	α [mm-1]
Cap	GaSb	15	0.033 [20]	3359.6 [21]
Window	$Al_{0.85}Ga_{0.15}As_{0.068}Sb_{0.932}$	275	0.0091 [20]	Transparent
Quantum well	$Ga_{0.74}In_{0.26}Sb$	100	0.0571 [22]	5178 [24]
Barrier	$Al_{0.3}Ga_{0.7}As_{0.02}Sb_{0.98}$	1456	0.012 [20]	1997.5 [25]
DBR	GaSb	2514	0.033 [20]	3359.6 [21]
	$As_{0.08}Sb_{0.92}$	3265	0.098 [25]	Transparent
Substrate	GaSb	500000	0.033 [20]	3359.6 [21]

Table 4.1 Material properties of the different layers of the 1.9 μm SDL with their respective thermal conductivities k and absorption coefficients α.

To decrease the computing time for the model, the active region and DBR were simplified by averaging the sub layer properties over the thickness of the total thickness of the active region and DBR respectively.

For the thermal conductivity an average value needed to be found for both, the radial and axial directions as the grown structure is anisotropic. For the calculations, equations 4.2 and 4.3 for the radial (k_p) and perpendicular (k_z) thermal conductivities were used [26].

$$k_p = \frac{\sum_{n=1}^{N} d_{z,n} \cdot k_n}{\sum_{n=1}^{N} d_{z,n}}$$ **Equation 4.2**

$$k_z = \frac{\sum_{n=1}^{N} d_{z,n}}{\sum_{n=1}^{N} \frac{d_{z,n}}{k_n}}$$ **Equation 4.3**

Here, d_z and k_n represent the thickness and thermal conductivities of layer number n respectively, and N is the total number of layers.

For the absorption coefficient of the active region and the DBR the sum of the absorption of the individual layers was used (equation 4.4).

$$e^{-\bar{\alpha}\cdot\bar{t}} = e^{\alpha_1\cdot t_1}\cdot e^{\alpha_2\cdot t_2}\ldots\cdot e^{\alpha_n\cdot t_n} \qquad \text{Equation 4.4}$$

which leads to equation 4.5.

$$\bar{\alpha} = \frac{\sum_i \alpha_i\cdot t_i}{\sum_i t_i} \qquad \text{Equation 4.5}$$

A list of the parameters of the SDL chip used for the model is shown in Table 4.2.

	t_{tot} [nm]	**k_z [W/m·K]**	**k_p [W/m·K]**	**$\alpha_{avg.}$ [mm^{-1}]**
Cap	15	0.033	0.033	3359.6
Window	275	0.0091	0.0091	Transparent
Active Region	1556	0.0148	0.444	19024
DBR	5750	0.0304	0.0224	1820
Substrate	5000	0.0091	0.0091	3359.6

Table 4.2 Material parameters for the thermal model of the pulsed pumped 1.9 µm SDL giving the total thickness t_{tot}’ thermal conductivity k_p and k_r.

The parameters used for the heatspreader materials in the model are shown in Table 4.3.

Material	**C [J/kg.K]**	**ρ [g/cm^3]**	**k [W/mm.K]**	**Reference**
Brass	380	8.55	0.109	[27]
Indium	234 [28]	7.3 [28]	0.084	[28]
Diamond	520	3.5	2	[27]
Sapphire	830	3.98	0.0351	[27]
Silicon carbide	690	3.21	0.49	[27]

Table 4.3 Heat capacity C, density ρ and thermal conductivity k of the additional materials used for the model [27,28].

For the final calculation, the heat load density at each point within the SDL structure is required. This can be derived from the energy conservation

$$\int Q \cdot dV = \eta \cdot P_p \qquad \textbf{Equation 4.6}$$

where Q is the heat load, V the volume in which the incident pump power P_p is absorbed considering the absorption efficiency η.

From this the heat load at any point of the rotational symmetric SDL chip can be determined with consideration of the Gaussian distribution of the pump light and the Lambert-Beer law of absorption.

$$Q_p = k \cdot e^{\frac{-2 \cdot r^2}{w_p}} \cdot e^{-\alpha(z)} \qquad \textbf{Equation 4.7}$$

Here, k is a constant, r is the radial coordinate, w_p the pump waist on the chip, z the propagation along axial direction of the chip and α the absorption coefficient. Integration of equation 4.7 then leads to

$$\int Q \cdot dV = \eta \cdot P_p = k \cdot \int_0^\infty e^{\frac{-2 \cdot r^2}{w_p}} \cdot dr \cdot \int_0^\infty e^{-\alpha(z)} \cdot dz \qquad \textbf{Equation 4.8}$$

where dV is defined as

$$dV = 2 \cdot \pi \cdot r \cdot dr \cdot dz\,. \qquad \textbf{Equation 4.9}$$

From this, one can now determine the constant k using the following equation.

$$\frac{k \cdot \pi \cdot w_p^{\;2}}{2 \cdot \alpha} = \eta \cdot P_p\,. \qquad \textbf{Equation 4.10}$$

Rewriting equation 4.10 and substituting it into equation 4.7 then results in the local heat load Q_p.

$$Q_p = \frac{2 \cdot \alpha \cdot \eta \cdot P_p}{\pi \cdot w_p^{\;2}} \cdot e^{\frac{-2 \cdot r^2}{w_p}} \cdot e^{-\alpha(z)} \qquad \textbf{Equation 4.11}$$

From this heat load density, the model can now generate the heat flow through the structure and give the heat distribution at any point in time during the pulse. Figure 4.27 shows an example of the temperature distribution after 1 μs of pumping with

60 W incident power, a spot size of 120 μm and the chip being bonded to a 250 μm thick diamond heatspreader.

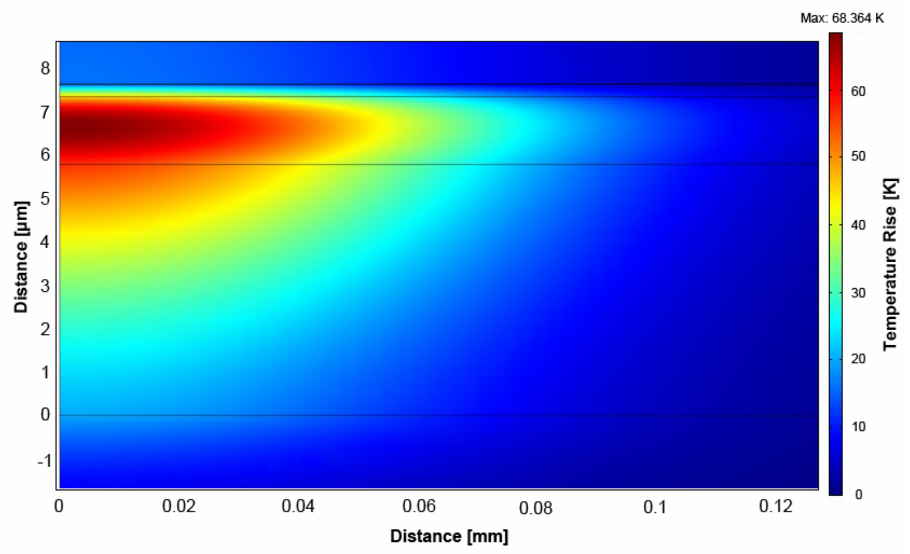

Figure 4.27 Temperature distribution inside the 1.9 μm SDL when pulsed-pumped with 1 μs pulse duration and 60 W on-time output power.

This plot shows that the SDL chip heats up significantly (a maximum of 70 K) inside the active region over the duration of the pump pulse. The laser mode, however, interacts with a finite volume of the chip. An average temperature over the spot size of the resonator mode inside the active region was therefore determined. For an approximation, the resonator mode was assumed to have the same size as the pump mode. A weighted average was determined using the following expression:

$$T_{ave} = \frac{\int T(r,z) \cdot I_p(r) \cdot dv}{\int I_P(r) \cdot dV} \qquad \textbf{Equation 4.12}$$

To investigate the agreement with the experimental results, the model was run in a transient mode to show the evolution of the temperature inside the active region of the chip over the duration of the pump pulse. The modelled peak and average temperature as well as the experimental temperature rise of the chip can be seen in Figure 4.28.

From this it becomes obvious that neither the average nor the peak temperatures are in perfect agreement with the experimental results. This can be assumed to be due to various reasons: The pump spot size was taken from the knife edge measurement of the pump radiation around the focus. While the focus was found to be 220 µm in width, the SDL may not have been operated exactly at the focus. As only a small increase of the pump spot size to ~280 µm (equivalent to a ~0.5 mm defocusing) is sufficient to fit the modelled peak temperature to the experimental data, this could be one source for the difference between the experimental and modelled data. In addition, uncertainty in the material data and heat load could influence the modelled results.

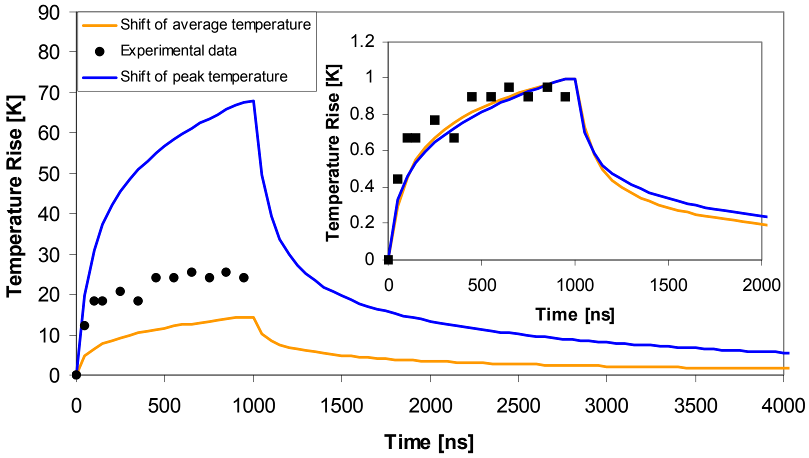

Figure 4.28 Thermal response of the SDL chip for the experimental data and the FEM model taking into account the average and peak temperature of the chip. **Inset:** Normalised variation of the modelled peak and average temperature as well as the experimental results.

The model is not in perfect agreement with the experimental results, however, normalising the data (see inset of Figure 4.28) shows that the time constant of the thermal rollover is almost identical for the experimental and modelled results. The model therefore underlines the experimentally observed spectral evolution and indicates that the cause of the thermal (and hence the wavelength) rollover is associated with the time constants of the thermal diffusion into the heatspreader.

To investigate how this behaviour could be modified, the thermal response of the same chip without a heatspreader, and with diamond, silicon carbide and sapphire heatspreader in place was modelled (see Figure 4.29). This shows a very similar initial rate of temperature rise but with the device settling to very different temperatures. While the model underlines the importance in heatspreader material choice, it also shows that the heat extraction is strongly depending on the pump pulse duration; the shorter the pump pulses, the less difference in performance between the different heatspreader materials. This is especially true for pulse durations of less than 150 ns where no significant difference between the different heatspreader materials and no heatspreader is present (see Figure 4.30). This indeed renders the heatspreader superfluous for these pulse durations.

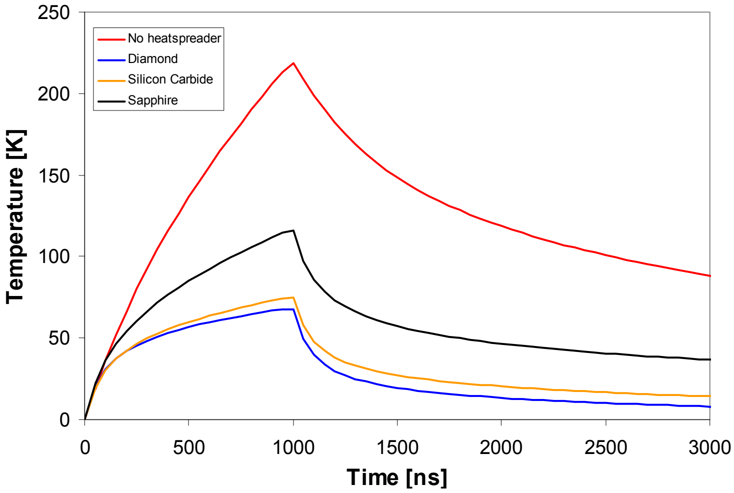

Figure 4.29 Comparison of time resolved FEM data (peak temperature) for various heatspreader materials.

The fact that the time constant for the heat dissipation is in the order of 100-200ns also suggests, that within this time frame the SDL chip is truly power scalable by increasing the pump and cavity spot sizes which is typically not indefinitely applicable to cw SDLs using intracavity heatspreaders [29].

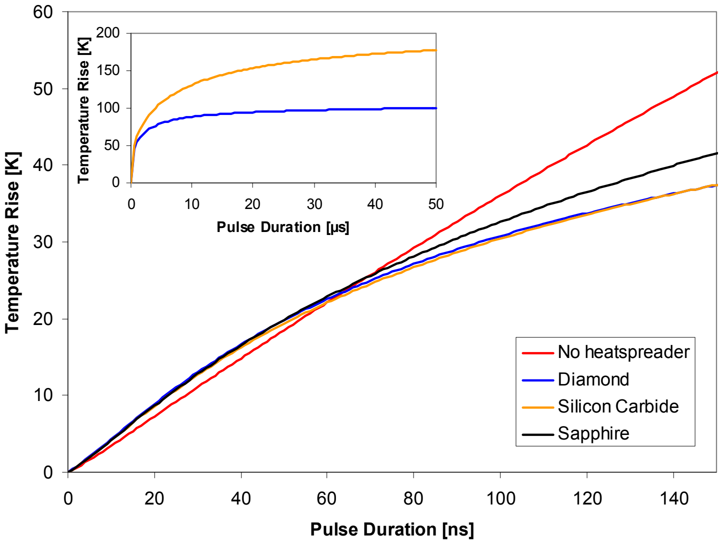

Figure 4.30 Temperature rise for no heatspreader and the use of diamond, silicon carbide and sapphire heatspreaders for pulse durations of less than 150 ns. **Inset:** Comparison of temperature rise using silicon carbide and diamond as heatspreader for pulse durations up to 50 µs.

The almost linear wavelength shift over longer pulse durations that was obtained for the case without heatspreader could potentially be advantageous for spectroscopic applications, where larger wavelengths shifts could be desired. It should be noted, however that the chirp will then ultimately be limited by the overlap of microcavity resonance and quantum well emission, since once this is significantly misaligned, no oscillation of the SDL can be obtained.

While the different heatspreader materials do not cause strong changes in performance for pulse durations below 1 μs, using the model to predict the temperature evolution over longer pulse durations (50 μs) shows that the choice of heatspreader material becomes increasingly importance for longer pulse durations. For this, the modelled thermal response of the most commonly used heatspreaders, i.e. diamond and silicon carbide, was compared (see inset of Figure 4.30). From the previous data, it can be seen that for a pulse duration of 1 μs the superior thermal properties of diamond only result in a temperature reduction of 10 % compared to silicon carbide. When investigating significantly longer pulses of 50 μs, however, the temperature reduction compared to the silicon carbide is 45 %. This further underlines the importance for heatspreader material choice with the pump pulse duration in mind and gives room for more specifically tailored SDLs.

4.8 Conclusion

The quasi-cw operation of a compact 1.9 and 2.0 μm SDL was demonstrated using low-cost pulsed nanostack diode lasers. Polarisation coupling of two diodes delivered a maximum of 120 W of on-time pump power. Pumping the SDL with this, oscillation was readily achieved resulting in output powers >20 W with pulse durations from 15-200 ns with repetition rates of 1-10 kHz. It was possible to extend the pulse duration of the pulsed diode lasers by modifying the driver boards, resulting in a maximum pulse duration of 1 μs at maximum power, and 1.3 μs at a reduced pump power and pulse repetition rate.

With no active cooling of the SDL chip, the pump induced heating did not reduce the efficiency of the laser over the duration of the pulse. However, for the case of the 200 ns pulse duration, a linear wavelength chirp of the output radiation in the order of 8 nm revealed a significant temperature rise of the SDL by ~24 K. For pulse durations >200 ns the rate of wavelength change reduced significantly, approaching a steady state condition, resulting in a true quasi-cw state.

These experimental investigations were underlined by FEA. While the data was not in agreement with the experimental results, the origin for this thermal rollover was found to be attributable to the time constant associated with the thermal diffusion of the material.

Parameter	**Required**	**Achieved**
Peak Power [W]	Watt-level	20
Wavelength [μm]	1.6-2.1	1.9 / 2.0
Pulse Duration	ns-ms	0.1-1 μs
Energy	> 1 μJ	20 μJ
Repetition rate	> 1 kHz	0.1-10 kHz

Table 4.4 Comparison of desired properties of a pulsed pump source for chromium-doped chalcogenide lasers and the properties of the SDL discussed in this chapter.

Table 4.4 shows the key properties of the pulsed-pumped SDL and the comparison to the requirements for a cost-effective pump source outlined in the introduction. While the highest output energy was only achieved in conjunction with fairly low pulse repetition rates, this might not necessarily be a problem for certain applications. The obtained pulse energy from these devices is not large in a scale of solid-state lasers, however the attractiveness of the low-cost and compact format allow to envisage the use of these devices in short distance spectroscopic applications like process monitoring or breath-analysis, where high pulse energies are not required.

For further development, this arrangement could potentially be reduced further in size by replacing the bench top components with engineered solutions. One might also consider microchip arrangements for the SDL as well as more compact optics for the beam conditioning and beam combining, potentially enabling this to be a highly compact, cost-effective and practical system.

References

[1] N. Hempler, J. M. Hopkins, A. J. Kemp, N. Schulz, M. Rattunde, J. Wagner, M. D. Dawson, and D. Burns, "Pulsed pumping of semiconductor disk lasers," Opt. Express **15**, 3247 (2007).
[2] G. W. Hoffmann and T. M. Jovin, "Nanosecond Rise-Time Mechanical Chopper for Laser Light," Appl. Opt. **10**, 218 (1971).
[3] A. E. Siegman, in *Lasers*, edited by A. Kelly University Science Books, Sausalito, CA, pp. 962 (1986).

[4] R. W. Hellwarth, "Theory of the Pulsation of Fluorescent Light from Ruby," Physics Review Letters **6**, 9 (1961).

[5] W. E. Lamb, "Theory of an Optical Maser," Physical Review **134**, A1429 (1964).

[6] F. J. McClung and R. W. Hellwarth, "Giant Optical Pulsations from Ruby," J. Appl. Phys. **33**, 828 (1962).

[7] A. M. Bonch-Bruevich, N. N. Kostin, V. A. Khodovoi, and V. V. Khromov, "Passive Q-switching and frequency stabilization of ruby laser using molecular rubidium vapor," Journal of Experimental and Theoretical Physics Letters, 242 (1970).

[8] L. E. Hargrove, R. L. Fork, and M. A. Pollack, "Locking of He-Ne laser modes induced by synchronous intracavity modulation," Appl. Phys. Lett. **5**, 4 (1964).

[9] B. K. Garside and T. K. Lim, "Laser Mode-Locking Using Saturable Absorbers," J. Appl. Phys. **44**, 2335 (1973).

[10] C. Spielmann, P. F. Curley, T. Brabec, and F. Krausz, "Ultrabroadband Femtosecond Lasers," IEEE J. Quantum Eelect. **30**, 1100 (1994).

[11] L. Jingang, S. Deyuan, T. Siu-Chung, and L. Yee-Loy, "Modeling pulse shape of Q-switched lasers," Quantum Electronics, IEEE Journal of **37**, 888 (2001).

[12] W. Koechner, in *Springer Series in Optical Sciences*, edited by W. T. Rhodes Spring Science + Business Media, Inc., New York, pp. 535 (2006).

[13] L. A. Coldren and S. W. Corzine, *Diode Lasers and Photonic Integrated Circuits.*, WileyBlackwell, p.624 (1995).

[14] K. W. Su, S. C. Huang, A. Li, S. C. Liu, Y. F. Chen, and K. F. Huang, "High-peak-power AlGaInAs quantum-well 1.3 µm laser pumped by a diode-pumped actively Q-switched solid-state laser," Opt. Lett. **31**, 2009 (2006).

[15] I. Sakuma, H. Yonezu, K. Nishida, Kobayash.K, F. Saito, and Y. Nannichi, "Continuous Operation of Junction Lasers at Room Temperature," Japanese Journal of Applied Physics **10**, 282 (1971).

[16] A. E. Siegman, in *Lasers*, edited by A. Kelly University Science Books, Sausalito, CA, pp. 492 (1986).

[17] J. M. Khosrofian and B. A. Garetz, "Measurement of a Gaussian laser beam diameter through the direct inversion of knife-edge data," Appl. Opt. **22**, 3406 (1983).

[18] N. Schulz, M. Rattunde, C. Ritzenthaler, B. Rosener, C. Manz, K. Kohler, and J. Wagner, "Effect of the cavity resonance-gain offset on the output power characteristics of GaSb-based VECSELs," IEEE Photonic Tech. L. **19**, 1741 (2007).

[19] B. Lyot, "Optical apparatus with wide field using interference of polarized light," C.R. Acad. Sci., 1593 (1933).

[20] T. Borca-Tasciuc, D. W. Song, J. R. Meyer, I. Vurgaftman, M. J. Yang, B. Z. Nosho, L. J. Whitman, H. Lee, R. U. Martinelli, G. W. Turner, M. J. Manfra, and G. Chen, "Thermal conductivity of $AlAs_{0.07}Sb_{0.93}$ and $Al_{0.9}Ga_{0.1}As_{0.07}Sb_{0.93}$ alloys and (AlAs)(1)/(AlSb)(11) digital-alloy superlattices," J. Appl. Phys. **92**, 4994 (2002).

[21] M. Munoz, K. Wei, F. H. Pollak, J. L. Freeouf, and G. W. Charache, "Spectral ellipsometry of GaSb: Experiment and modeling," Phys. Rev. B **60**, 8105 (1999).

[22] S. Adachi, "Lattice thermal conductivity of group-IV and III-V semiconductor alloys," J. Appl. Phys. **102** (2007).

[23] Ioffe Physical Technical Institute, (Ioffe, 1998-2001).

[24] S. Adachi, "Optical dispersion relations for GaP, GaAs, GaSb, InP, InAs, InSb, $Al_xGa_{1-x}As$, and $In_{1-x}Ga_xAs_y]P_{1-y}$," J. Appl. Phys. **66**, 6030 (1989).

[25] M. Rattunde, Institute of Applied Solid State Physics, Freiburg (2008).

[26] H. Lindberg, M. Strassner, E. Gerster, J. Bengtsson, and A. Larsson, "Thermal management of optically pumped long-wavelength InP-based semiconductor disk lasers," IEEE J. Sel. Top. Quantum Electron. **11**, 1126 (2005).

[27] http://www.engineeringtoolbox.com, (2010).

[28] https://www.goodfellow.com, (2010).

[29] R. G. Bedford, M. Kolesik, J. L. A. Chilla, M. K. Reed, T. R. Nelson, and J. V. Moloney, "Power-limiting mechanisms in VECSELs," presented at the Enabling Photonics Technologies for Defense, Security, and Aerospace Applications, Orlando, FL, USA (2005).

Chapter Five

SDL-pumped Cr^{2+}:II-VI laser

5.1 Introduction

After the discussion of the $Tm^{3+}:YAlO_3$ laser as a conventional pump source for chromium-doped chalcogenide lasers and the introduction of the 1.9 and 2.0 µm semiconductor disk laser as a novel source, this chapter will discuss the use of these lasers to pump continuous-wave (cw) chromium chalcogenide lasers, utilising their advantage as potentially compact, high brightness and low-noise multi-Watt pump sources.

While the technology has advanced significantly with respect to single crystalline Cr^{2+}:ZnSe growth, a more established method of preparing Cr^{2+}:chalcogenides is the doping of polycrystalline bulk chalcogenide material. For many years, polycrystalline materials have provided superior output power and efficiency mainly due to the availability of technological advanced low-cost polycrystalline ZnSe for mid-infrared components. Another chalcogenide material available in good quality was CdZnTe, typically used in x- and gamma-ray applications and therefore well understood in respect to the growth of large single crystal material with high uniformity and quality [1].

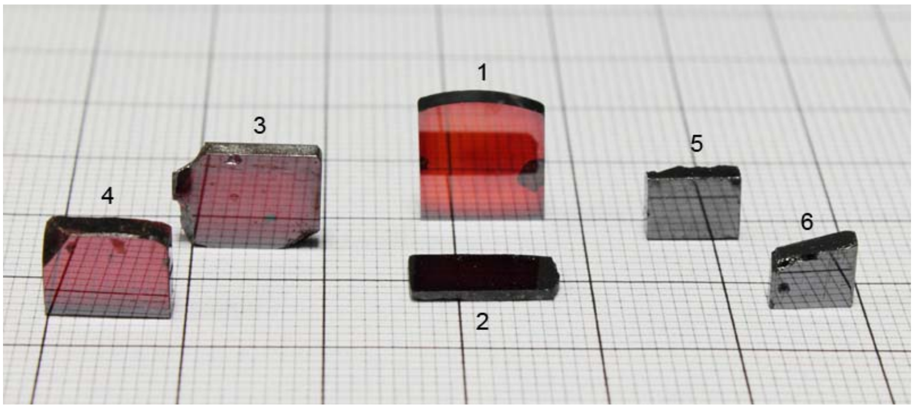

Figure 5.1 Different Cr^{2+}:ZnSe (1-4) and Cr^{2+}:CdZnTe samples (5,6) used throughout this work.

While in recent years the quality of other chalcogenide materials such as Cr^{2+}:ZnS has greatly been improved, the experiments in this chapter will concentrate on the use of well established Cr^{2+}:ZnSe as well as novel Cr^{2+}:CdZnTe [2]. Therefore, a series of crystals were obtained from various sources (Figure 5.1). Samples 1 and 2 were obtained from Dr. Arnold Burger, Department of Physics, Fisk University, USA and were polycrystalline ZnSe that were diffusion doped for 5 days at a temperature of 950 °C. The thickness of sample 1 was 1.3 mm and sample 2 was cut to 3 mm length.

Sample 3 was also Cr^{2+}:ZnSe and obtained from Dr. William Krupke from the Lawrence Livermore National Laboratory. Its physical dimensions were 11x8x2 mm (where 2 mm is the thickness).

Sample 4 was obtained from Prof. Sergey Mirov, Department of Physics, University of Alabama, USA (also at Photonics Innovations Inc.) who diffusion-doped CVD grown material obtained from II-VI, Inc. [3,4]. The dimensions of the sample were 3x7x8 mm (where 3 mm is the thickness).

The Cr^{2+}:CdZnTe (samples 5 and 6) used for this work were also obtained from Arnold Burger and were the same ones as used in [5,6]. For their preparation, $Cd_{1-x}Zn_xTe$, x=0.04 crystals (dimensions 7x7x24 mm) were purchased from eV Products and used for Cr diffusion. For this, high purity pre-synthesised CrSe was used as the source for the chromium and placed together with the CdZnTe into an evacuated (under vacuum at 2x 10-7 torr) and sealed quartz ampoule. The diffusion was carried out over 15 days at a temperature of 900 °C.

In the following sections, the quality and laser efficiency of these samples will be investigated using the Tm^{3+}:$YAlO_3$ laser and the 1.9/2.0 µm SDLs as pump sources. After the description of the experimental arrangement for the chromium laser in section 5.2, section 5.3 and 5.4 will discuss the power transfer and tuning characteristics of the systems.

5.2 Experimental arrangement

For the experiments in this chapter, two resonator arrangements were chosen, i.e. a 3- and 4-mirror resonator. For the power transfer characteristics of the samples, a

3-mirror cavity was used, while a 4-mirror arrangement was used to add a prism for tuning of the resonator. Figure 5.2 shows the typical arrangement of the laser.

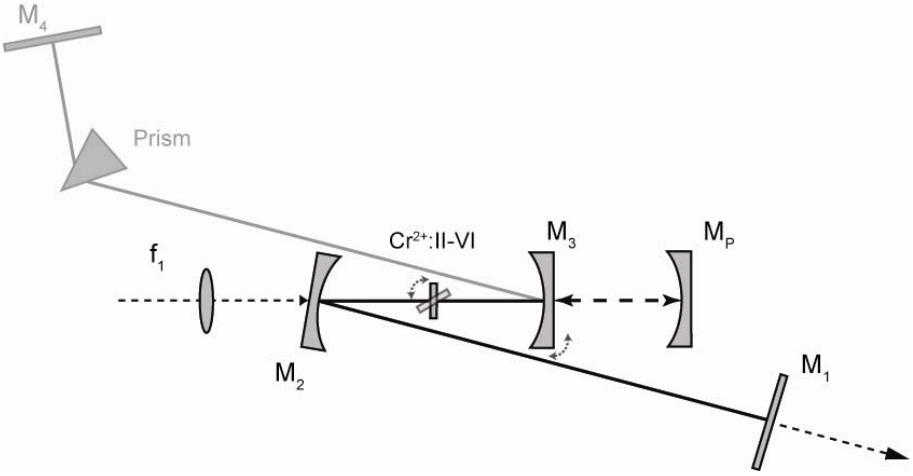

Figure 5.2 Experimental configuration of the 3- and 4-mirror resonator. For the 3-mirror resonator the following mirrors were chosen: mirror M_3 r=50 mm; mirror M_2 r=100 mm; output coupler (M_1). For the 4-mirror resonator, the end mirror M3 was tilted and replaced with a r=100mm radius of curvature mirror to establish a second arm, which was terminated by a plane, highly reflecting end mirror M_4.

For the 3-mirror resonator, an r=50 mm radius of curvature (ROC) mirror was used as the end mirror (M_3) of the resonator while the folding mirror M_2 was chosen to be of r=100 mm. Both these mirrors were placed 50 mm away from the gain element. The distance between the folding mirror and the output coupling mirror (M_1) was set to 300 mm. The beam propagation predicted by ABCD-Matrix analysis (using WinLase 2.1 Professional) inside the resonator with the crystal being placed at Brewster's angle can be seen in Figure 5.3.

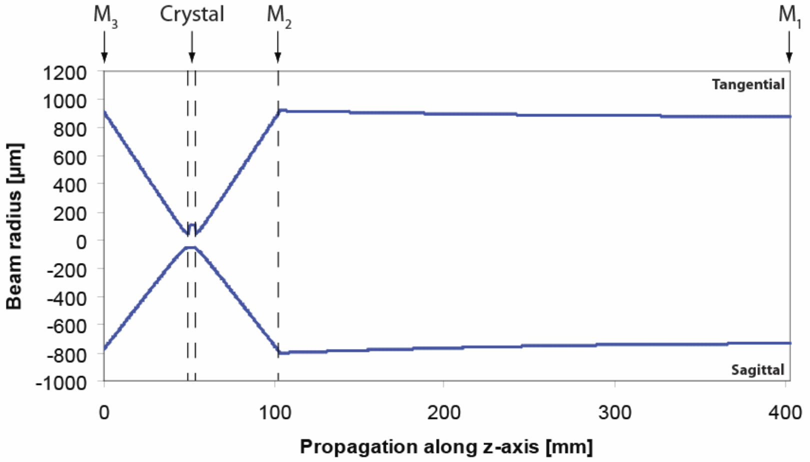

Figure 5.3 ABCD matrix model of the 3-mirror Cr^{2+}:ZnSe resonator for the crystal being placed at Brewster's angle.

For the 4-mirror resonator, the mirror M_3 was replaced with a r=100 mm ROC mirror that allowed to add a second arm into the resonator which allowed for the insertion of additional elements (such as prisms) without displacing the output beam of the resonator when tuning the output wavelength. The predicted beam propagation suggests a beam radius at the resonator waist of 40x93 μm (see Figure 5.4).

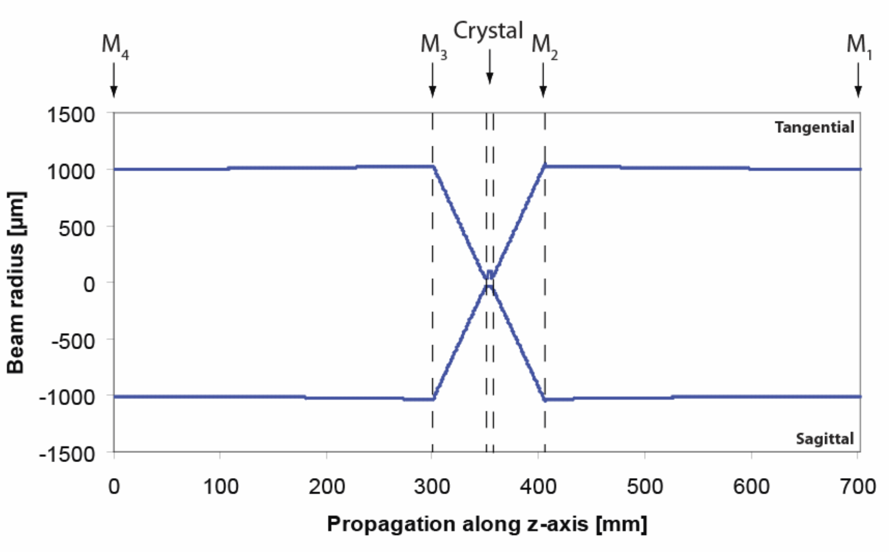

Figure 5.4 ABCD matrix model of the 4-mirror Cr^{2+}:ZnSe resonator for the crystal being placed at Brewster's angle.

As none of the crystals was specifically designed for the given pump power wavelength not all of the available pump radiation was absorbed. Hence, a retro reflecting mirror (M_p) was used to reflect the remaining pump light back into the chromium crystal, increasing the overall pump absorption in the crystal.

As the crystals were used at normal incidence or Brewster's angle, the resonator arms were set to an angle where the difference in path length of the tangential and sagittal plane, i.e. astigmatism, introduced by the Brewster-angled element is compensated for and the resulting output beam of the laser is circular. Using ABCD matrix analysis of the resonator geometry, the angle at which astigmatism is compensated was found to be 11.8° resulting in a circular waist at the output coupler (M_1) with the dimension of ~2 mm diameter.

When the crystal was turned to be sited at normal incidence, the angles for the astigmatism compensation created a slightly distorted beam shape. As this could only be compensated using small folding angles in the resonator, this distortion was left unadjusted as it did not introduce any variation of the power transfer or tuning characteristics of the laser.

For the above described resonator arrangement, the resonator modelling software WinLase 2.1 Professional, predicted a resonator waist radius of 50x100 µm if the crystal was orientated at Brewster's angle and ~50x50 for normal incidence.

The mirrors used for the laser came from different manufactures, i.e. LASEROPTIK GmbH and Casimir Optics [7,8]. All of the mirrors were centred at 2.45 µm with a reflectivity band stretching from 2.3 to 2.5 µm. The output coupling mirrors available for this work were of 99, 98, 92, and 87 % nominal reflectivity. For higher output coupling, the resonator arm between the curved folding and output coupler was folded using combinations of various output couplers.

To hold the crystals in place, an in-house built brass mount was used (see Figure 5.5). To allow for basic temperature control of the crystals, the brass mount was cooled using a recirculating water bath chiller.

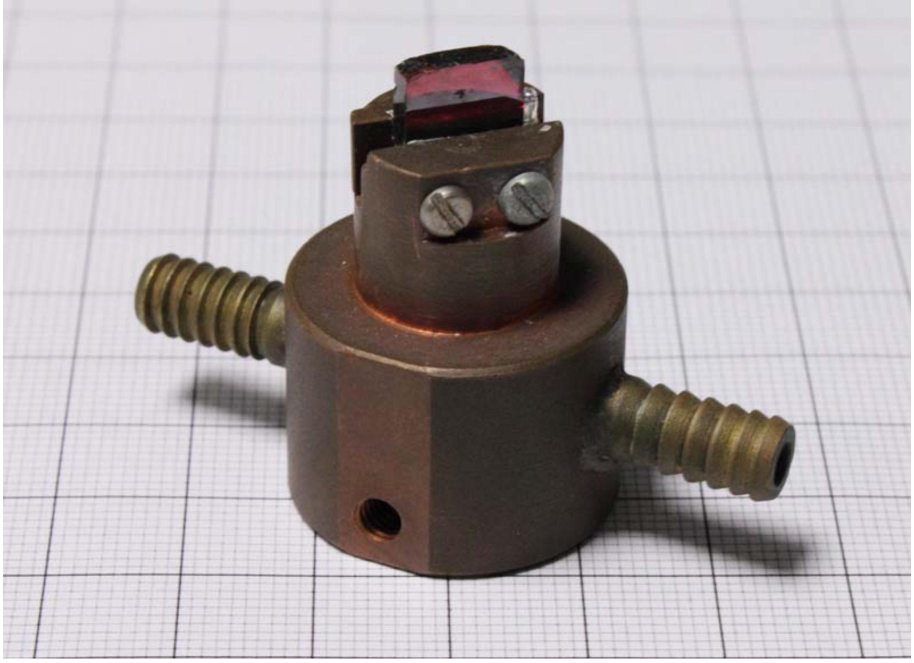

Figure 5.5 Picture of the brass mount used to hold the chromium chalcogenide crystals. The adapters to the left and right allow for water cooling.

To condition the beams of the Tm^{3+}:$YAlO_3$ and SDLs it was chosen to use the divergence properties of the pump laser. The size of a focus produced by a lens is directly proportional to the focal length of the lens and the beam size at the lens for a given divergence of the incident beam. It was therefore possible to adjust the beam radius at the focus by varying the distance between the pump and the focusing lens. The divergence of the pump laser changed the beam size on the lens, and hence the beam radius of the focus.

5.3 Power characterisation

5.3.1 Tm^{3+}:$YAlO_3$ pumping of Cr^{2+}:chalcogenides

For the initial chromium laser experiments, the Tm^{3+}:$YAlO_3$ laser was used in the arrangement discussed in chapter 2. Because solid-state lasers tend to change their output beam shape with varying pump power due to changes in the thermal lens inside the gain medium, the diode laser pump power to the Tm^{3+}:$YAlO_3$ was kept at a constant value. This also prevented that the sensitive active stabilisation system of the Tm^{3+}:$YAlO_3$ laser failed due to a required change of gain with changing power. To change the pump power to the chromium laser, the pump beam was attenuated using a half-wave plate (HWP) and a thin film polarizer (TFP). To allow for easier alignment of the laser and pump mode, two beam steering mirrors were used to align the pump beam. These were two highly reflecting mirrors (M_1 and M_2) coated for 1.94 µm at 45 ° angle of incidence. A schematic of the entire arrangement can be seen in Figure 5.6.

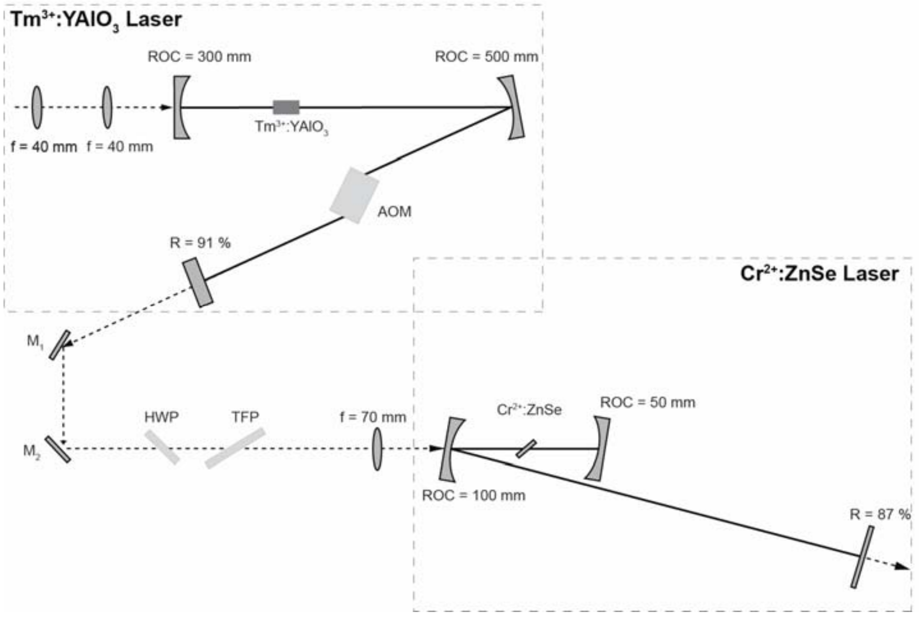

Figure 5.6 Experimental arrangement of the Tm^{3+}:$YAlO_3$ laser pumped Cr^{2+}:ZnSe laser using a half-wave plate (HWP) and a thin film polariser (TFP) for variation of the pump power and two steering mirrors (M_1 and M_2) for alignment.

The only Cr^{2+}:ZnSe crystals available at the time this part of the work was done, were sample 1, 2 and 3. With an incident pump power of 3.5 W at the crystal, oscillation from the chromium laser was only obtained using sample 2 and 3, with 50 and 200 mW output power respectively.

Systematic investigation of the crystals was not possible due to problems with the Tm^{3+}:$YAlO_3$ laser. While operating the chromium laser, strong drops of the output power of the Tm^{3+}:$YAlO_3$ laser were observed. Major realignment of the Tm^{3+}:$YAlO_3$ laser was required to regain the previously achieved maximum power. Further investigations suggested that this was associated with damage of the Tm^{3+}:$YAlO_3$ crystal facets. Indeed, when investigating the crystal surfaces under a microscope, circular damage marks were visible, an indication for laser induced damage (Figure 5.7).

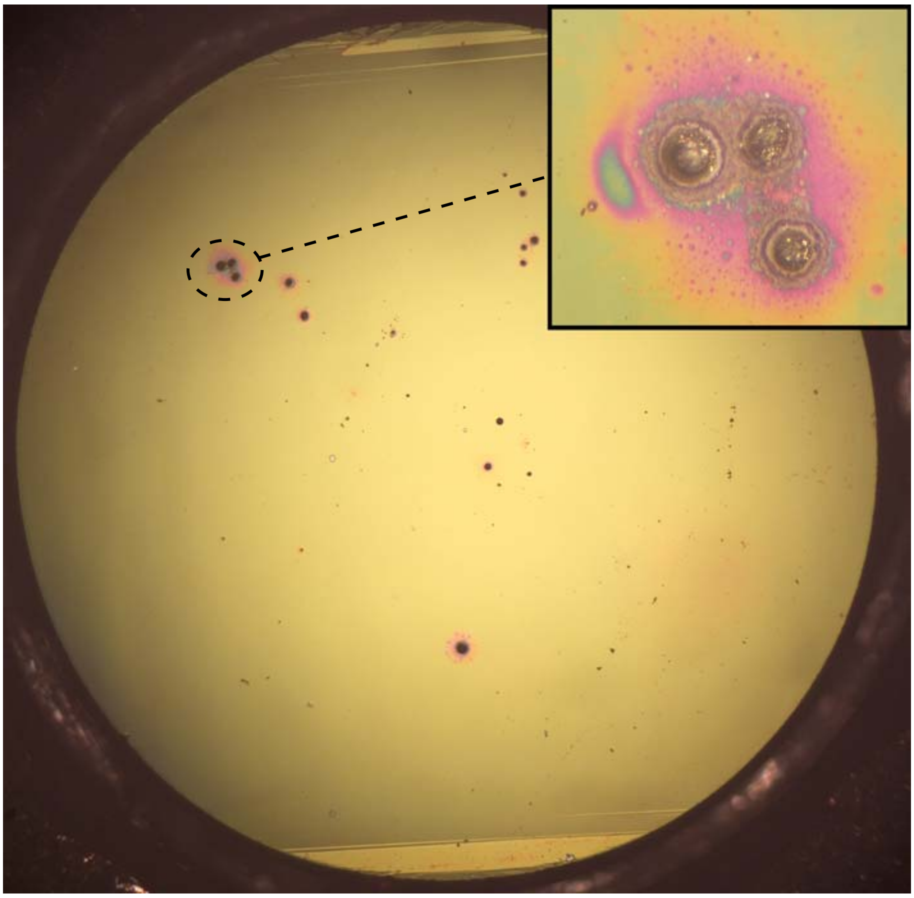

Figure 5.7 Photograph of the coated Tm^{3+}:$YAlO_3$ crystal showing the damage caused be strong intensity fluctuations.

This was a consequence of reflections from the chromium laser mirrors that injected 1.9 µm radiation back into the Tm^{3+}:$YAlO_3$ laser, causing the active stabilisation to fail. This resulted in Q-switching like behaviour that caused strong intensity fluctuations of the intracavity field, damaging the components inside the resonator. Satisfactory operation of the $Tm^{3+}:YAlO_3$ laser as pump source would therefore have required optical isolation. This was considered but the considerable cost and reduced practicality meant that alternative approaches were more attractive. In addition to the high cost of these isolators, the small effective aperture (typically a few millimetres) limited the practicality. Large aperture isolators have just recently become available through companies such as Lambda Photometrics Ltd [9].

It should also be noted that the initial powers obtained from the various samples were not obtained from a fully optimised system as the restricted time of operation due to damage of the $Tm^{3+}:YAlO_3$ laser did not allow full optimization.

Due to these issues, the SDL was considered as an alternative pump sources for chromium chalcogenide lasers. The experimental results from SDL-pumped chromium II-VI lasers will be discussed in the following sections.

5.3.2 1.9 and 2.0 µm SDLs as pump source for Cr^{2+}:ZnSe

SDL do not suffer from strong thermal lensing the way that solid-state lasers do. The half-wave plate and thin film polarizer were therefore removed for the adjustment of the incident pump power. Instead, the driver current of the diode laser pumping the SDL could be adjusted directly. For this, however, it was important to investigate the stability of the SDL mode with changing pump diode driver currents. Therefore the mode size and shape of the output beam for increasing diode driver currents was recorded using a laser beam diagnostic camera (SPIRICON Pyrocam II). From this data, the $1/e^2$ radius in the far field was recorded. The normalized data is shown in Figure 5.8. Here it can be seen that the output beam changes significantly over the first 5-10 A but then becomes stable. After this stabilisation, the mode size varies by less than 4 %, except for a small dip at 22 A driver current which is likely to be associated with a change of the resonator mode. The inset of the graph shows a subset of the actual data recorded using the SPIRICON camera. Here it can be seen that the mode changes from a circular mode near threshold to a highly multimode beam. In the following, the 2.0 µm SDL will be investigated as pump source for the different chromium crystals. Based on the previous experiments using the

$Tm^{3+}:YAlO_3$ laser as pump source, it was decided that only sample 3 will be used, as sample 1 and 2 were not as good in quality. In addition, samples 4-6 will be discussed and compared to sample 3.

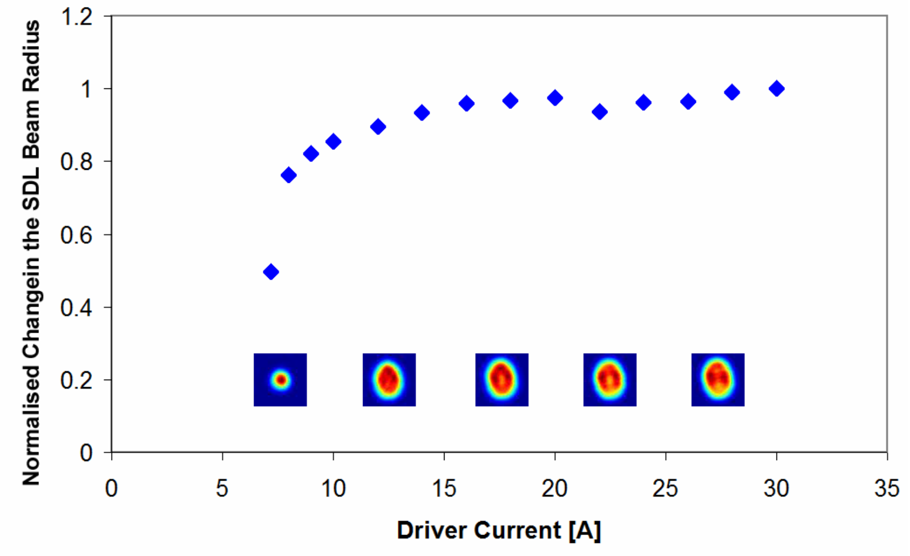

Figure 5.8 Normalized change of the 1/e² output beam size of the 2.0 µm SDL with changing driver current. The insets show the recorded beam profile using the SPIRICON Pyrocam II.

5.3.2.1 2.0 µm SDL pumping of Cr^{2+}:ZnSe

For the initial experiments, sample 3 was used and placed at Brewster's angle into the 3-mirror resonator. Stable oscillation was readily achieved from the chromium laser and no drops in output power of the SDLs were observed as were when using the $Tm^{3+}:YAlO_3$ laser as pump source. This indicates that the SDL does not show any significant signs of feedback sensitivity which can be explained by the short upper-state lifetime in the order of nanoseconds which reduces energy storage and eliminates the build-up of the relaxation oscillation. The low noise aspect of the SDL pumped Cr^{2+}:ZnSe laser will further be elaborated in section 5.5 .

The output power of the laser was recorded using a laser power meter (Coherent Fieldmate) in conjunction with a thermopile head (Coherent LM 10). To determine the absorbed pump power inside the crystal for the power transfer curves, the power was measured behind the crystal for each measurement point of the power transfer curves. By subtracting the transmitted power from the incident power and by taking into account the losses associated with the resonator optics, the absorbed pump power was obtained (see Figure 5.9). For this measurement, it was important, that the transmitted power was recorded when the chromium laser was oscillating, as absorption saturation changes the fraction of the pump power absorbed for the oscillating and not oscillating case (see Figure 5.9).

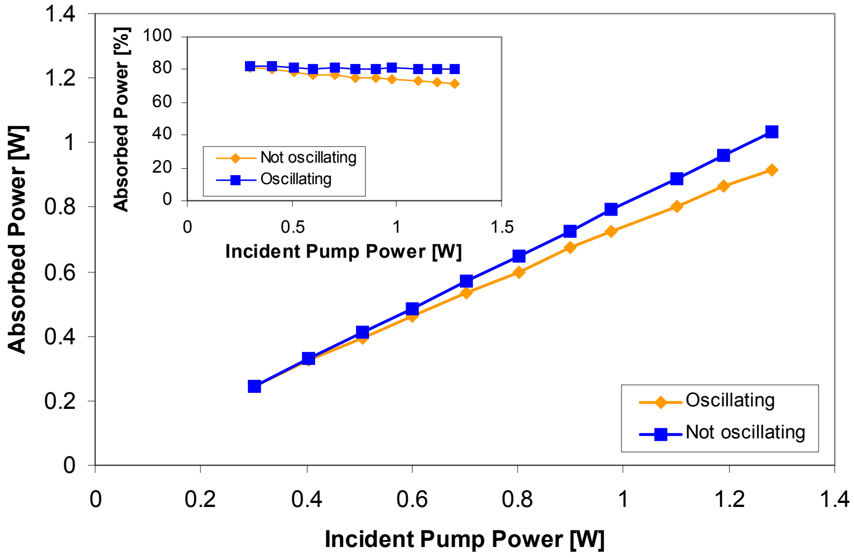

Figure 5.9 Absorption of the Cr^{2+}:ZnSe crystal for the oscillating and not oscillating case. **Inset:** Percentage of absorbed pump light for the oscillating and not oscillating case.

The inset of Figure 5.9 shows the percentage of the pump power absorbed for the oscillating and not oscillating case. Here it can be seen, that bleaching effects deteriorate the absorption significantly when the laser is not oscillating with an observed maximum reduction of 9 %. When the resonator is oscillating, the absorption reduces from 82 to 81 %, which is insignificant in respect to the overall performance of the system. From these values, the average absorption coefficient for the crystal was determined to be 5.6 cm^{-1}.

The power transfer curves were recorded using the 3-mirror resonator design described in section 5.2 using various output couplers with reflectivities between R=87 % and R=99 %. As the absorption of the crystal was reasonably high, the pump retro reflector (M_P) was not employed. The results of the power transfer experiments can be seen in Figure 5.10. The experiment revealed a maximum output power of 285 mW for an absorbed pump power of 1.03 W (limited by the diode laser power of the SDL) and a slope efficiency of 36 % using the R=87 % output coupler. The lowest threshold was found to be 124 mW when using the R=99 % output coupler.

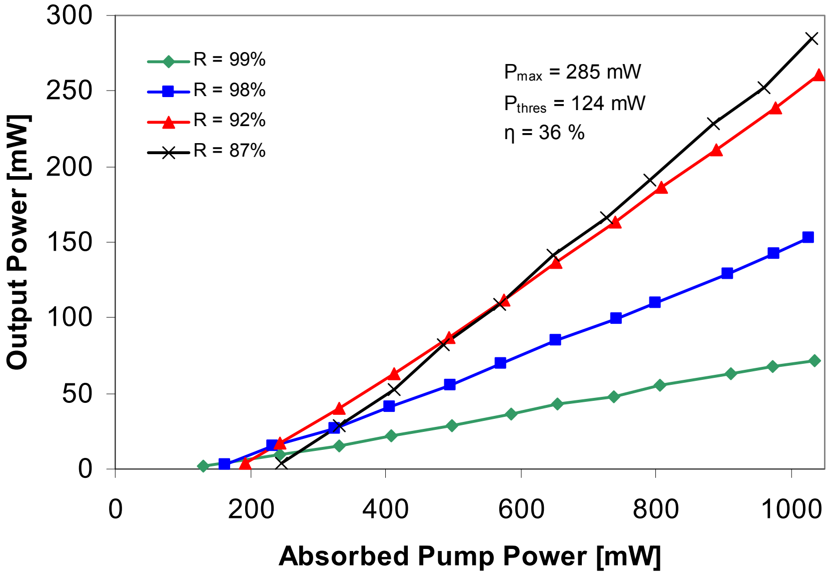

Figure 5.10 Power transfer characteristic of sample 3 using output couplers with reflectivities between 87-99 % using the 2.0 µm SDL as pump source.

This data was used to carry out a Findlay-Clay analysis [10,11]. The result of this is shown in Figure 5.11. It reveals a round trip loss of 11 % with a calculated error of ±0.3 %. As the Findlay-Clay analysis, however, takes into consideration the threshold at different output couplers and from this interpolates the final loss value, the accuracy of the threshold values is crucial for a realistic loss estimate. In these experiments the cavity alignment was optimised for high power operation which inevitably results in a different cavity alignment than would be the case for low threshold operation. The accuracy of the Findlay-Clay plot is therefore questionable.

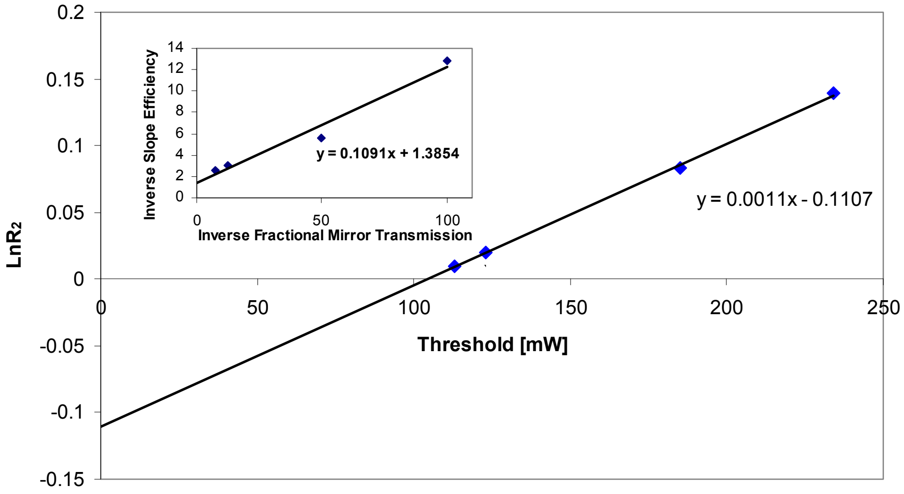

Figure 5.11 Data for the Findlay-Clay analysis and the linear fit to this data to determine the intracavity loss of the resonator. **Inset:** Data for the Caird analysis and it's linear fit.

For this reason, a Caird analysis was carried out too [11]. Instead of taking the threshold into consideration, the method suggested by Caird uses the slope efficiencies of the power transfer curves and thereby gives a better loss estimate for a laser that is optimised for maximum output power. Compared to the 11 % of loss resulting from the Findlay-Clay analysis, the Caird method reveals a loss value of 7.9 %. The limited amount of data points, however, resulted in a relatively large error of ±4.3 %. It should be noted, that generally a discrepancy of the two techniques can be expected for vibronic systems and is typically attributed to ground-state absorption [12]. While it is not possible to directly compare the two results due to the large error of the Caird analysis, they both indicate that relatively high losses are present in the resonator. Assuming that losses associated with the resonator optics are negligible, this result suggests that the Cr^{2+}:ZnSe crystal introduces these losses. This can be related to surface imperfection and bulk losses of the material. As a result one can expect significant improvements of the laser performance by utilising gain media of higher optical quality.

In addition to the loss analysis, the power transfer characteristics can also be used to determine the optimum output coupling for a given pump power. E.g. for a pump power of less than 200 mW one would use the R=99 % or R=98 % output couplers, as higher output coupling would result in a threshold higher than the available pump power. As the pump power increases, however, it is possible to sacrifice more of the pump power to a higher threshold as higher slope efficiency is gained.

During these initial experiments it was observed, that the performance of the laser was strongly dependent on the positioning of the crystal relative to the pump and resonator mode. This was associated with surface losses due to imperfection of the facets of the crystal. Due to the Brewster angle, it became more difficult to position the crystal as the angle reduced the effective aperture. As an alternative approach, the crystal was therefore placed at normal incidence. This removes the polarisation discrimination of the Brewster's angle and increases the Fresnel reflection but enables better control over the positioning of the crystal. Stable oscillation was readily achieved with the crystal at normal incidence. The two scenarios were compared by carrying out another power transfer analysis for the crystal placed at normal incidence. The result of this can be seen in Figure 5.12.

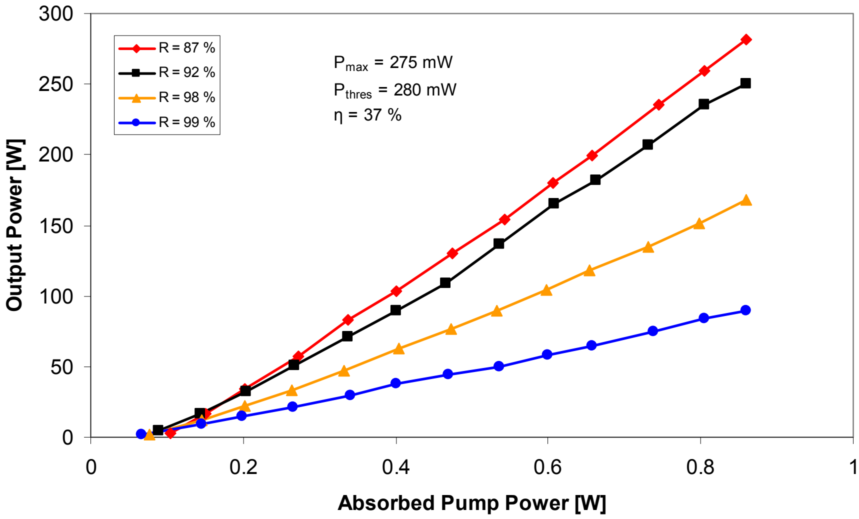

Figure 5.12 Power transfer characteristics of the Cr^{2+}:ZnSe laser using sample 3 placed at normal incidence.

With a maximum power of 280 mW and a slope efficiency of 37 % with respect to the absorbed pump power, no significant difference between the two crystal orientations was observed. At first, this seems surprising as one would expect the laser to work less efficiently with the additional Fresnel losses due to the crystal being placed at normal incidence. However, while losses are indeed increased these are compensated for by an etalon effect of the plane parallel crystal surfaces. In addition, the crystal appears longer to the pump light (see Figure 5.13). Of the 17.5 % reflected at the second crystal interface due to Fresnel reflection, 81.5 % is absorbed again (according to the absorption coefficient determined earlier). The none-absorbed part of this radiation undergoes another Fresnel reflection at the next crystal interface, from which 17.5 % is again being reflected and partially absorbed. At this point, the remaining light that would experience another Fresnel reflection reduced to 2 % of the overall pump light and was therefore be neglected. This increases the overall absorption by a ~5 % compared to neglecting the reabsorption of the internal Fresnel reflections.

It should be noted that with the crystal now being placed at normal incidence, the amount of pump light being reflected back into the SDL was increased significantly compared to the Brewster-angled crystal, however, no degradation of the SDL emission was observed.

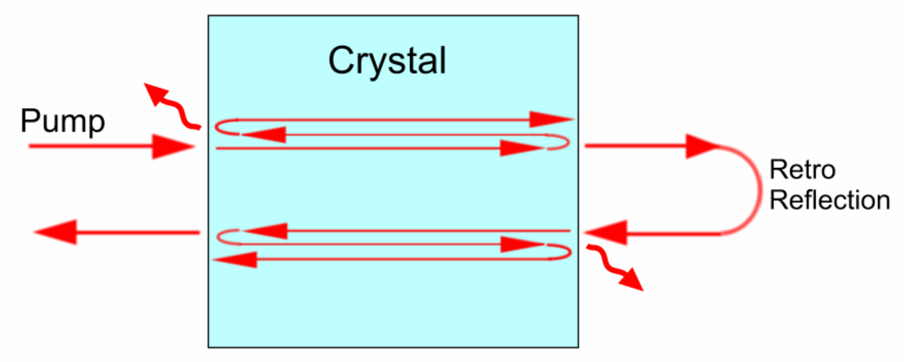

Figure 5.13 Schematic for the absorption and losses associated with the Cr^{2+}:ZnSe crystal when pumped at normal incidence.

To investigate the power scalability of this crystal, the pump power of the SDL was increased by using a 45 W pump diode laser. In addition, the retro-reflector was used to increase the absorbed pump power further. Using an R=87 % output coupler this led to a maximum output power from the Cr^{2+}:ZnSe laser of 982 mW with a maximum slope efficiency of 33 % with respect to the absorbed pump power (orange curve in Figure 5.14). As the curve shows, however, a reduction of the slope efficiency at the high end can be seen. This was associated to heating effects inside the crystal and could be eliminated by chopping the pump power and thereby reducing the overall heat introduced into the system. With a duty cycle of 50 %, this was enough to eliminate the thermal rollover of the power transfer curve resulting in a maximum on-time output power of 1.18 W. The use of water cooling of the brass mount was also used in an attempt to prevent roll-over. This, however, did not improve the performance.

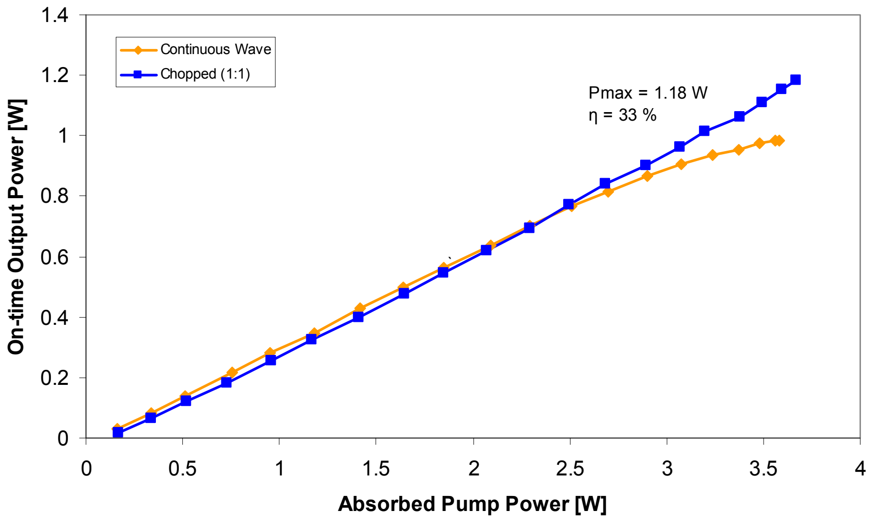

Figure 5.14 Power transfer for the SDL pumped Cr^{2+}:ZnSe laser in cw (orange curve) and quasi-cw (blue curve) operation.

To investigate whether this rollover was intrinsic to Cr^{2+}:ZnSe and its material properties, i.e. the change of refractive index with temperature, thermal conductivity or lifetime quenching, the next section will compare the results from this crystal with sample 4, a newer generation of material.

To be able to accurately compare the two samples, sample 4 was placed in a resonator identical to the one used in the previous section. For the comparison, the case of the normal incidence was used. Again, the power transfer characteristic was recorded to obtain an indication for the optimum output coupling for a given pump power (see Figure 5.15). However, this time the long arm was folded using flat output coupling mirrors to allow for higher output coupling. The total length of the resonator arm was kept the same as in the previous investigation and the angle between the resonator arms kept to a minimum. As the single pass absorption coefficient of this material was measured to be 3.9 cm^{-1} and therefore significantly smaller than the one of sample 3, the retro reflecting mirror M_p was used. This increased the overall absorption of the crystal from 60 to 72 % (taking Fresnel reflections into account).

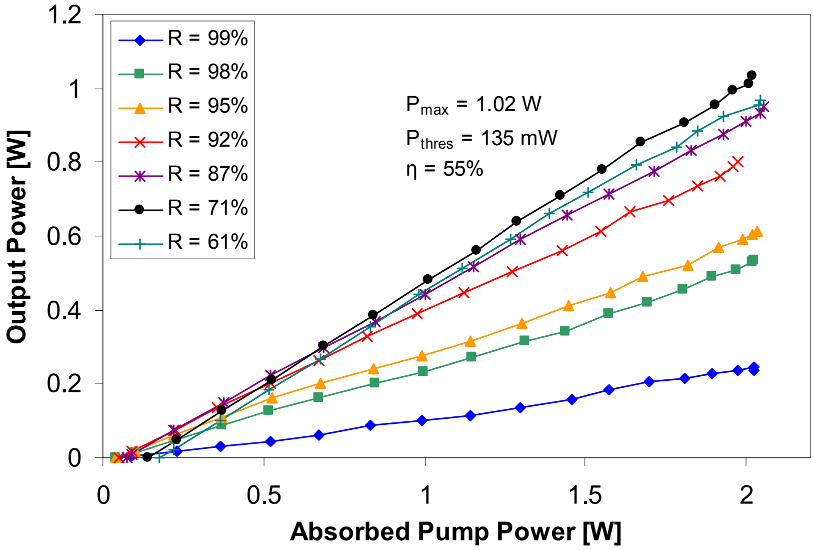

Figure 5.15 Power transfer characteristics of the SDL pumped Cr^{2+}:ZnSe using output couplers with reflectivities between 61 and 99 %.

Contrary to the previous sample, significantly higher output coupling (R=61 %) was inserted into this arrangement for an optimum output coupling at full pump power. This resulted in an output power of up to 1 W for 2 W of absorbed pump power. The resulting slope efficiency was measured to be 55 %. As the slope efficiency is proportional to T/(T+L) (where T is the output coupler transmission and L the parasitic losses in the resonator) this is a good first indication of the relatively low losses of the sample. To investigate this further, Findlay-Clay and Caird analysis were again carried out. The result of the Findlay-Clay analysis can be seen in Figure 5.16.

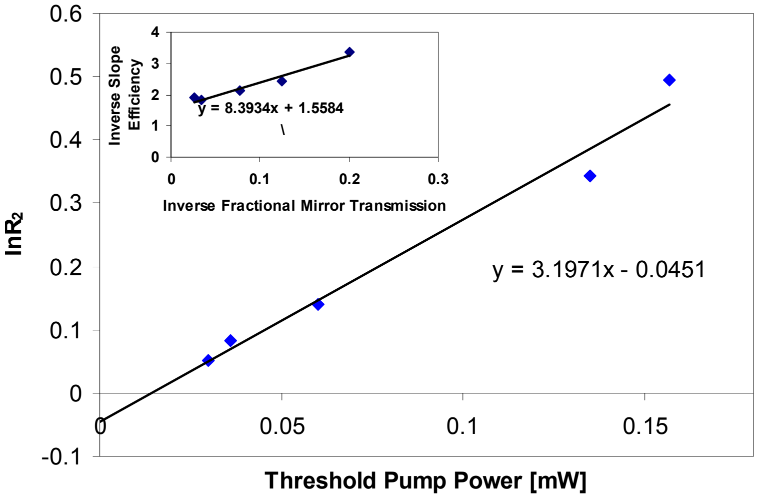

Figure 5.16 Loss analysis of the Cr^{2+}:ZnSe laser using the method suggested by Findlay and Clay revealing and Caird (Inset).

The resulting loss is 4.5±2.9 % and is a significant reduction compared to sample 3. The Caird analysis revealed a loss of 3.5±1.3 %.

Next it was investigated whether these reduced intrinsic losses allowed for higher output powers without thermal losses. For this the SDL was cooled to -15 °, delivering a maximum pump power of 5.8 W. With the pump retro reflecting mirror in place, this resulted in a total absorbed pump power of 3.8 W. The result of the power transfer can be seen in Figure 5.17.

Up to 1.8 W of output power was obtained from the laser with a maximum slope efficiency of 54 %. It should be noted, that again, no cooling of the Cr^{2+}:ZnSe crystal was employed. In contrast to sample 3, the power transfer for this sample did not show any degradation of the slope efficiency at higher pump powers. With similar absorbed pump power, crystal length and identical spot sizes of resonator and pump waist, the rollover can therefore be attributed to the high intrinsic losses of sample. These results are also in agreement with the recent results published by the University of Alabama group which reported output powers of 12 W without the need for special thermal management [13].

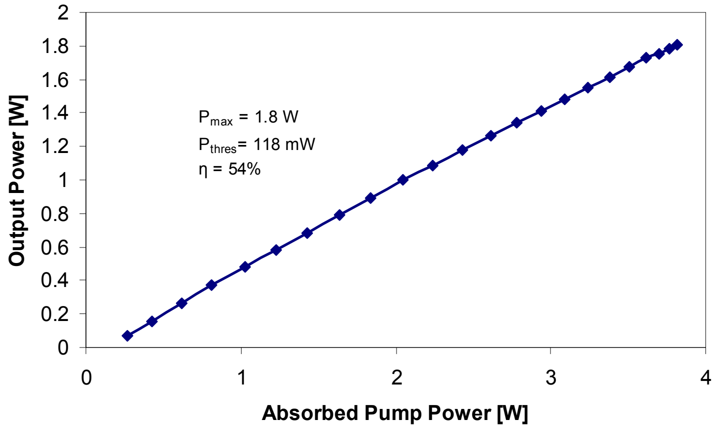

Figure 5.17 Power transfer for the SDL pumped Cr^{2+}:ZnSe laser using sample 4 with a maximum SDL output power of 5.8 W. The chromium laser exhibited a maximum output power of 1.8 W with a maximum slope efficiency of 54 %. N.B. No thermal rollover was observed.

5.3.2.1 1.9 µm SDL pumping of Cr^{2+}:ZnSe

The previous section of this chapter concentrated on the demonstration of a cw pumped Cr^{2+}:ZnSe laser using a 2.0 µm SDL as pump source. It was shown that very good slope efficiencies and powers could be obtained. Pumping at shorter wavelength can, however, be useful if the aim is to improve the overall laser efficiency (by shifting the pump wavelength closer to the absorption peak) or if emission from the Cr^{2+}:ZnSe laser is required at 2 µm or below [14]. This section will therefore discuss the use of the 1.9 µm SDL as pump source for Cr^{2+}:ZnSe.

Using the 1.9 µm SDL described in chapter 3, power transfer characteristic of the Cr^{2+}:ZnSe laser using sample 4 were carried out and are shown in Figure 5.18.

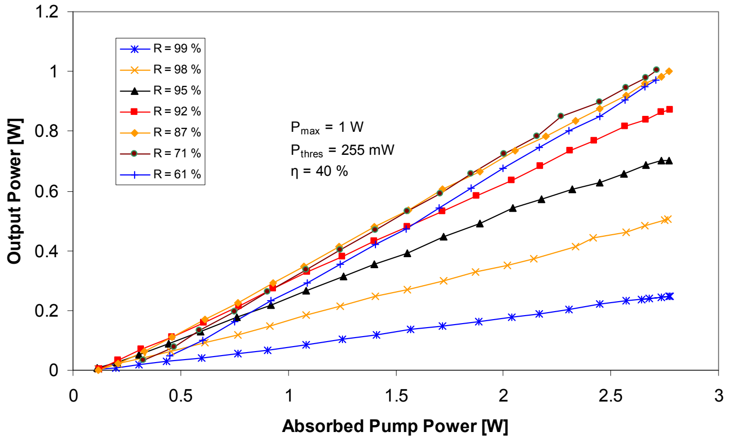

Figure 5.18 Power transfer characteristic of the 1.9 µm cw SDL-pumped Cr^{2+}:ZnSe laser using various output couplers with reflectivities between 61 and 99 %. The maximum output power was found to be 1 W with a slope efficiency of 40 % and a threshold of 255 mW.

From this set of data, the maximum power was found to be 1 W, limited by the available pump power, with a slope efficiency in respect to the absorbed pump power of 40 %. The single pump absorption was found to be 80 %, resulting in an absorption coefficient of 5.4 cm^{-1}. Compared to the 2.0 µm pump source we can see that the absorption coefficient increased by 1.5 cm^{-1} which is in good agreement to values in the literature [15].

5.4 Spectral tuning characteristics

While the wavelength coverage of chromium chalcogenide lasers is one of their most significant properties, harvesting the full potential is difficult as mirrors for this wavelength band are not as well developed as they are for the near infrared. To cover the full potential range of tuning from Cr^{2+}:ZnSe lasers, two options are possible. The first is the use of multiple mirror sets that can be installed according to the wavelength desired. This technique was successfully used by Demirbas et al. allowing the wavelength coverage from 1.88 to 3.10 µm using four-mirror sets centred at 2, 2.25, 2.6 and 2.9 µm [14].

Alternatively, mirrors coated to cover an exceptionally wide wavelength range can be used. These however, are difficult to fabricate as they demand layers with large thicknesses. They often require multiple growth runs that make it challenging to maintain growth quality and result in increased costs. Just recently, tuning over the range of 1973 to 3349 nm was demonstrated in a Cr^{2+}:ZnSe laser using a single set of mirrors [16].

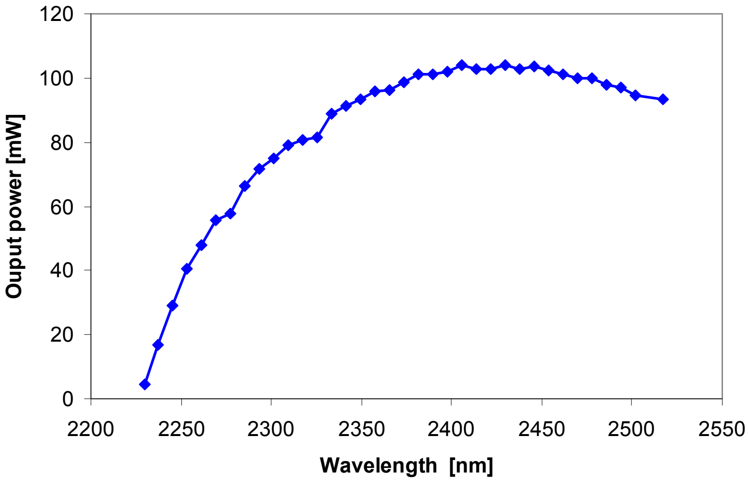

Figure 5.19 Tuning range of the Cr^{2+}:ZnSe laser using a prism as tuning.

For the tuning investigations, two mirror sets were available, both centred at ~2.45 µm. To tune the laser, a prism was inserted into the 4-mirror cavity as described in section 5.2. This spatially dispersed the different wavelength components of the intracavity field and allowed them to be selected by horizontally tilting the end mirror M_4. To reduce the threshold of the laser and maximise the tuning range, an output coupler with R = 98 % reflectivity was used. In this way, it was possible to tune the laser over a range of ~300 nm from 2.23-2.52 µm (Figure 5.19). With the emission centred at ~2.4 µm and the coatings specified for 2.35-2.55 µm, the edges of the tuning curve are strongly distorted by the coatings of the optics which caused the abrupt cut off of the tuning curve at 2.53 µm. Similar behaviour was observed from the second set of mirrors (see Figure 5.20).

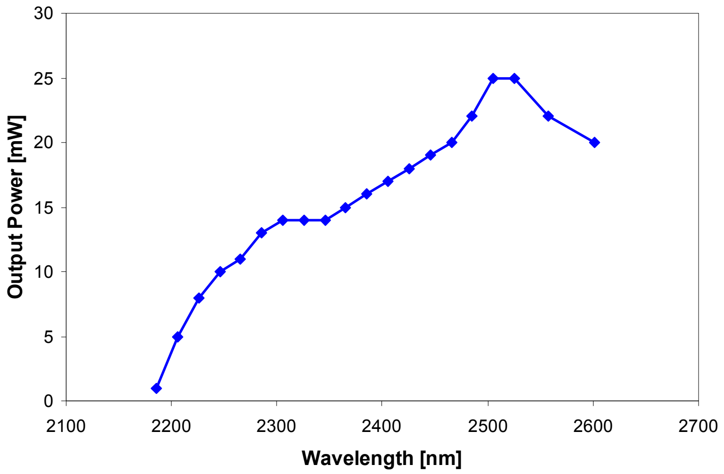

Figure 5.20 Wavelength tuning characteristics of the Cr^{2+}:ZnSe laser using the Layertech optic set with an output coupler with reflectivity R = 99 %.

For these measurements, an output coupler with a reflectivity of R=99 % had to be used, as this was the only value available from this mirror set, causing the output power of the laser to be significantly lower. While the mirror set allows an improved wavelength coverage from 2.19 to 2.60 µm, the shape of the tuning curve is strongly distorted for wavelengths >2.5 µm.

5.5 Intensity noise analysis

In previous sections, the insensitivity of the SDL towards feedback from the chromium laser was pointed out. The low noise properties of the SDL format has been investigated extensively before and shown that the SDL format permits relative intensity noise (RIN) levels less than -126 dB over a frequency range from 50 kHz to

500 MHz. This is a consequence of the short upper-state lifetime of the semiconductor material (in the order of nanoseconds) [17]. A short carrier lifetime also makes the SDL less sensitive to residual feedback from the pump laser – a serious problem in more conventional pump lasers such as the Tm^{3+}:$YAlO_3$ laser discussed in chapter 2.

In this section, the intensity noise of the Cr^{2+}:ZnSe laser is investigated. For the experiments, the 3-mirror resonator from section 5.2 is used with the crystal being placed at normal incidence. As a result of the crystal orientation, ~17.5 % of the pump radiation associated with the Fresnel reflection from the crystal facet was directly reflected back towards the SDL. The maximum output power of the SDL was 3.5 W.

To measure the intensity noise, a fast photodiode (Thorlabs PDA10D-EC) was used in conjunction with a fast digital oscilloscope (Agilent Infiniium 54830B). The output of the laser was recorded over a period of 10 s giving a total of $2 \cdot 10^6$ samples. The resulting frequency band is therefore 0.1 Hz to 100 kHz.

First measurements revealed strong intensity fluctuations from the Cr^{2+}:ZnSe laser which were traced back to the SDL. This was associated with the weak polarisation selectivity of the used 3-mirror resonator of the SDL, which allowed polarisation switching when perturbed by feedback from the pumped laser, leading to increased intensity noise. This effect, however, could be suppressed by increasing the polarisation selectivity of the resonator by inserting a Brewster-angled element such as a birefringent filter or simple glass substrate. For the laser discussed here, an uncoated, 6 mm thick, fused silica mirror substrate was inserted into the SDL resonator. This significantly reduced the intensity noise of the Cr^{2+}:ZnSe laser. Figure 5.21 shows a subset of the recorded intensity noise data of the Cr^{2+}:ZnSe laser in comparison to the electrical system noise of the measurement apparatus.

This reveals that the actual measurement is indistinguishable from the noise floor, setting the upper limit of the RMS intensity noise figure to 0.14 %. This value was found to be the same with the pump retro-reflecting mirror in place which increased the total light being back reflected towards the SDL by 5 % to 0.7 W.

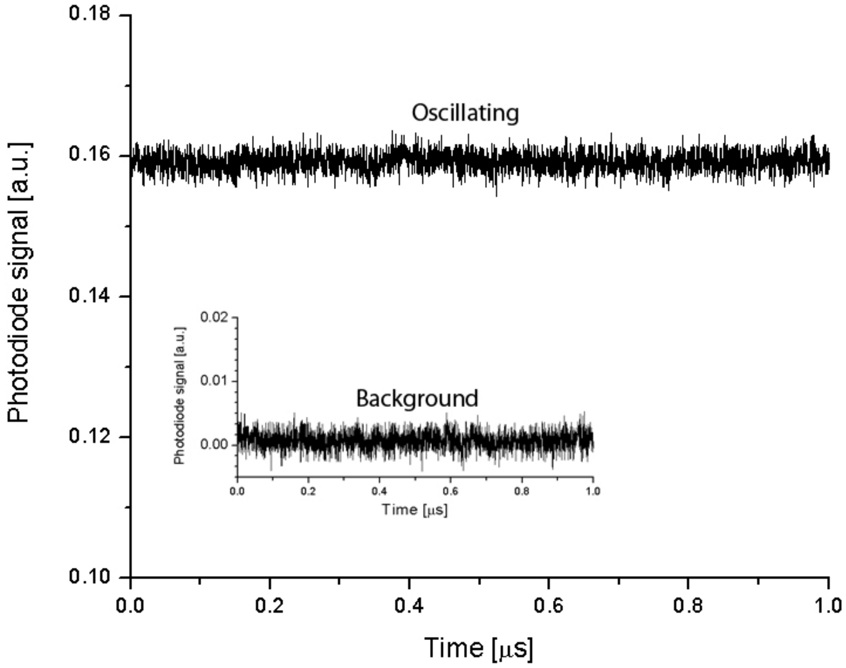

Figure 5.21 Subset of the intensity noise measurement for the Cr^{2+}:ZnSe laser.

These observations give clear indication that the SDL is an effective pump source to provide a low noise Cr^{2+}:laser in a straightforward manner without the need for optical isolation, reducing the overall cost of the system significantly.

5.6 Mode matching by brightness variation of the SDL

Throughout the Cr^{2+}:ZnSe laser experiments it was regularly observed, that the optimum performance of the chromium laser required adjustments to the SDL, specifically the overlap of pump and resonator mode.

As discussed in chapter 3, the mode overlap of the SDL resonator and pump waist causes the beam quality parameter of the SDL to change. In the context of using the SDL as pump source, the possibility of easy adjustment of the beam quality factor of the SDL can be utilized to improve the mode overlap of the SDL and the Cr^{2+}:ZnSe laser.

To investigate this theoretically, the mode profile for various Gaussian beams with different beam quality factors and identical spot sizes was plotted for a 2 μm source and compared to the mode of the fundamental Gaussian beam propagation of a 2.5 μm laser with identical waist radius.

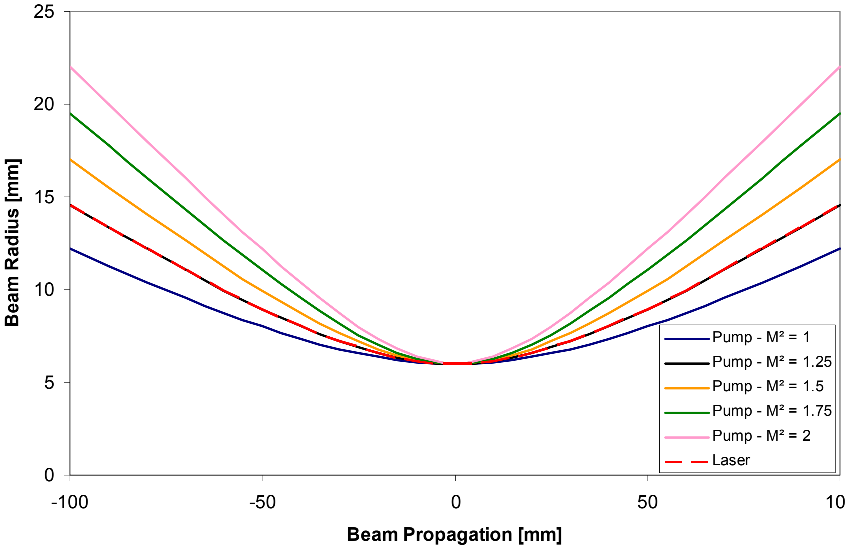

Figure 5.22 Modelled beam propagation of the pump source for different beam quality factors (M^2) compared to the laser resonator mode.

Here we can see that the resonator and pump mode overlap perfectly when the beam propagation parameter of the SDL is 1.25, which compensates for the increased diffraction at 2.4 µm. As a consequence, the resonator to pump mode overlap can be optimized for laser systems where the ratio of the laser to pump wavelength is within the range of the M^2 value of the SDL. In the case of the arrangement discussed in chapter 3 with a beam quality factor in the range of ~1-5 would allow the compensation of a laser to pump mode mismatch by a factor of 1-5.

These observations further underline the practicality of the SDL as flexible pump source not only for chromium chalcogenides but laser systems in general. With a wide range of wavelength in the UV, visible, as well as near and mid-infrared, the potential for SDL pumping of solid state lasers can be harvested over a wide range of systems.

5.7 Investigation of Cr^{2+}:CdZnTe as gain media

5.7.1 Experimental discussion

In addition to the investigations of pumping the well established Cr^{2+}:ZnSe using the SDL, this section will briefly investigate the SDL pumping of the novel chromium-doped chalcogenide host CdZnTe in respect to power transfer characteristics and thermal properties. As mentioned in the introduction to this chapter, CZT is available in high optical qualities due to it being used for gamma and x-ray detectors. Doped with chromium it could therefore be a readily available laser crystal for the generation of radiation in the 2-3 µm wavelength band.

For the experiments, two samples of Cr^{2+}:CdZnTe (sample 5 & 6) were prepared for laser operation. These two crystals were different in their doping concentration, a consequence of the diffusion gradient associated with the thermal diffusion process, with sample 5 being the one with the higher doping concentration.

The low thermal conductivity and heat capacity of CdZnTe mean that the efficiency of Cr^{2+}:CdZnTe laser is likely to be restricted by pump induced heating. For practical laser sources based on this material, the thermal management of the gain media is therefore critical. To be able to asses the performance of this material regardless of the thermal limitations, the laser was pumped using a quasi-cw 2.0 µm SDL (using an intracavity chopper) with a low duty cycles of 1.23 % and a pulse duration of 150 µs. This allowed eliminating the thermal effects due to pump induced heating. The experimental arrangement was the same as the 3-mirror resonator described in section 5.2 without the pump retro reflecting mirror in place. The crystals were placed at normal incidence, resulting in a resonator waist radius of 50 µm inside the crystal. The power transfer characteristic of sample 5 can be seen in Figure 5.23. Of the 1.15 W of available pump power 87 % was absorbed.

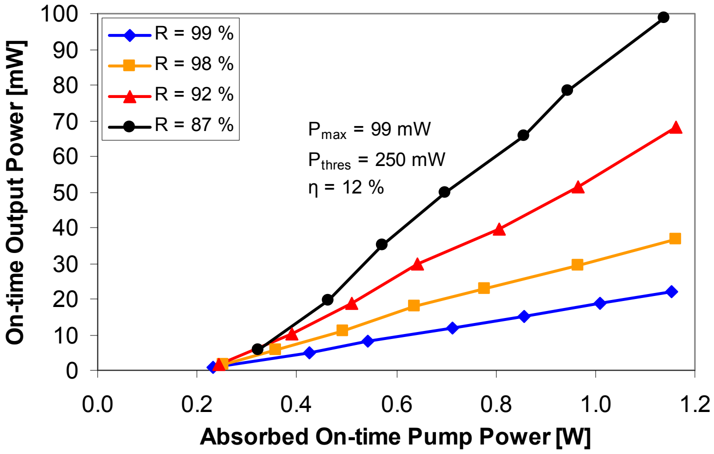

Figure 5.23 Power transfer characteristic for the 2.0 µm SDL pump Cr^{2+}:CdZnTe crystal with relatively high chromium concentration.

The sample with lower concentration of chromium showed a reduced absorption of only 72 %, however, with the slope efficiency and threshold being almost identical, the difference in doping concentration did not show significant differences in performance when operated in quasi-cw operation (see Figure 5.24).

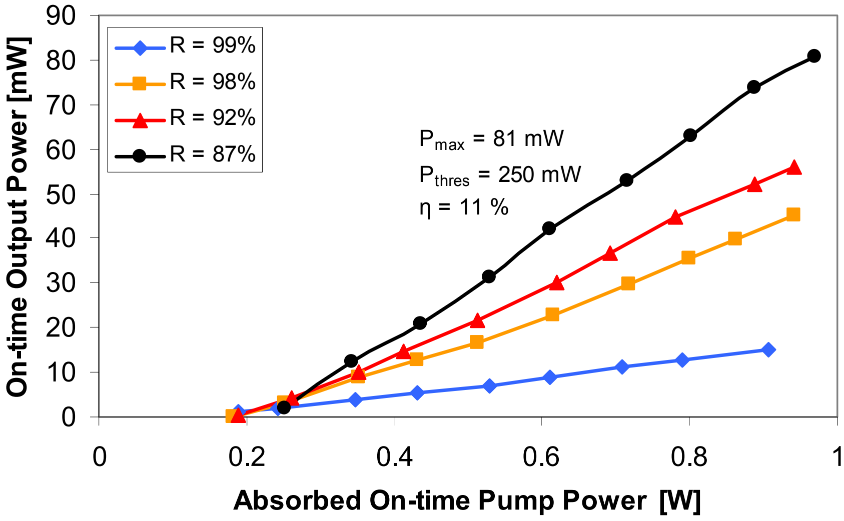

Figure 5.24 Power transfer characteristics of the 2.0 µm SDL pumped Cr^{2+}:CdZnTe crystal (lower chromium concentration) using different output couplers.

After these initial investigations, the Cr^{2+}:CdZnTe crystal was pumped with a higher power 2.0 µm SDL. The signal was still chopped at the same duty cycle and pulse duration as mention earlier. With an increased pump power of 4.7 W the chromium laser now delivered a maximum on-time output power of 540 mW using an output coupler with 87 % reflectivity (see Figure 5.25).

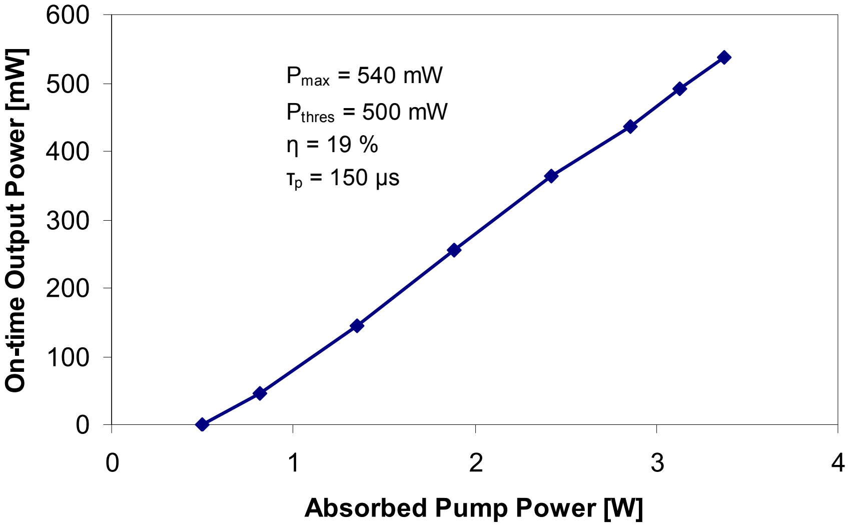

Figure 5.25 Power transfer characteristic of the high power 2.0 µm SDL pumped Cr^{2+}:CdZnTe laser.

While quasi-cw operation at low duty cycles and short pulse durations was readily achieved, cw operation was problematic due to the thermal limitations. With basic water cooling of the crystal to 15 °C, pump and resonator spot size of ~50 µm and 830 mW of pump power, cw operation was obtained with an average output power of <3 mW.

5.7.2 Thermal modelling

To investigate the thermal aspect of the laser crystal when pumped in pulsed and cw, a finite element analysis as described in chapter 4, section 4.7 was again carried out. For the model, the thermal conductivity was estimated to be 0.7 W/mK, based on the values for CdTe [18] and ZnTe [19] and the heat capacity of 219 J/(kg·K) used [20]. For comparison, the thermal conductivity and heat capacity of ZnSe are 19 W/mK [21] and 339 J/(kg·K) [22] respectively. The density for CdZnTe was 5730 kg/m^3 (5270 kg/m^3 for ZnSe) [20,22]. For simplicity, the scenario was modelled for a rod of 3 mm radius (cooled around the edge) with the 1.15 W of incident cw pump power (1 W absorbed) focused into a spot radius of about 40 µm. The resulting temperature distribution in the crystal can be seen in Figure 5.26. The estimated peak temperature rise is of the order of 100 K.

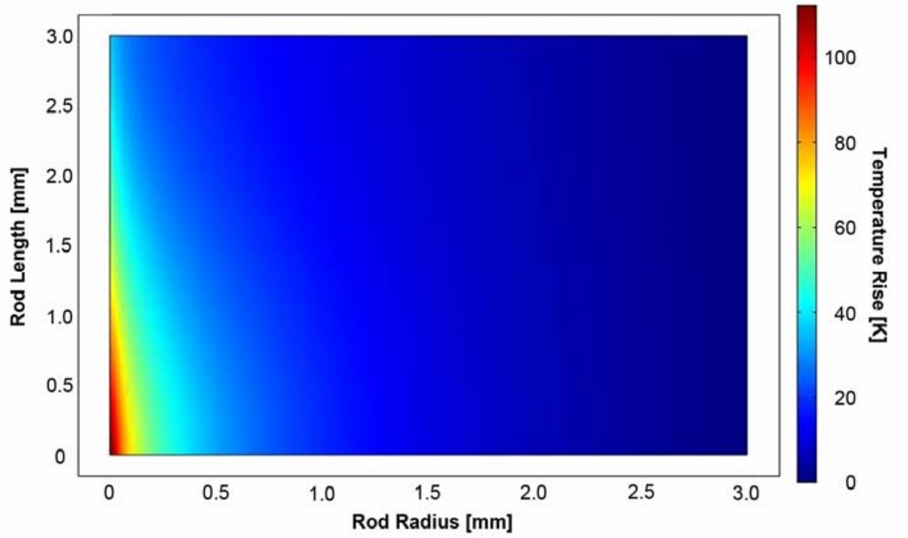

Figure 5.26 Temperature distribution of the Cr^{2+}:CdZnTe crystal when pumped with 1.1 W of cw power.

Taking into account the lifetime quenching of the upper laser level in Cr^{2+}:CdZnTe reported by Cerny et al. with a lifetime of 1.1 µs at room temperature [5], this temperature rise would strongly reduce the efficiency of the system and underlines the previously observed low output power when pumped in cw. Higher output powers in this mode of operation can therefore only be expected if significant measures are undertaken to address the thermal management of the crystal. As such, one might envisage the use of thin disk approaches potentially in combination with heatspreader approaches, as previously discussed for SDL. It should be noted, however, that diamond would be problematic in the context of Cr^{2+}-laser systems as the transparency of diamond reduces significantly above 2.5 µm [23]. Although silicon carbide has somewhat lower thermal conductivity, its superior transmission at longer wavelengths makes it an interesting alternative.

As discussed in section 5.7.1, an alternative approach of mitigating thermal effects in Cr^{2+}:CdZnTe lasers is the use of pulsed pump sources. To gain an insight into the thermal response of Cr^{2+}:CdZnTe when pumped with pulses, a transient analysis of the model was carried out. In contrast to cw-pumping, the temperature rise of the crystal when pumped in pulsed mode is insignificant and less than 1 K for an absorbed pump power of 1 W in a 40 µm radius waist and a pulse duration of 60 µs (Figure 5.27, left).

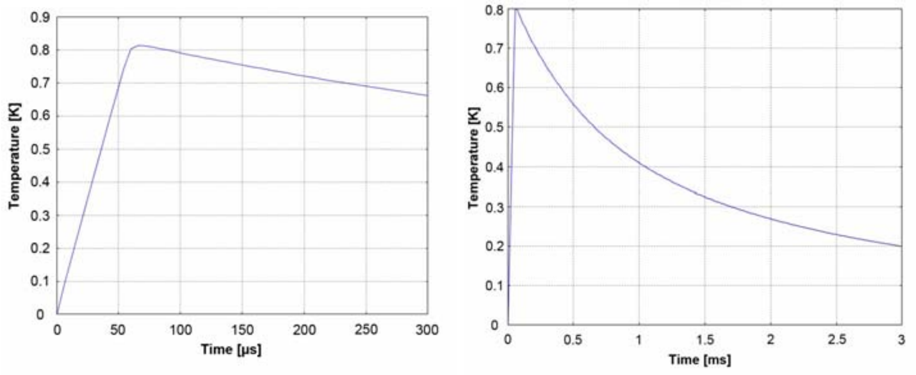

Figure 5.27 Temperature change of the Cr^{2+}:CdZnSe crystal when pumped with 1.1 W of on-time pump power in a pump pulse duration of 60 µs over 300 µs (left) and 3 ms (right).

It can also be seen that the cooling time is in the order of a few milliseconds indicating that no significant pulse to pulse heating is present in the laser.

If the transient temperature rise after turning on a cw pump beam is considered (Figure 5.28), it can be seen that 90 % of the temperature rise happens in the first 3 to 4 s. However, a significant rise of 30 K occurs already within the first 10 µs. This would suggest that for athermal-pumping the pulse durations of the pump source would need to be kept to <1 ms.

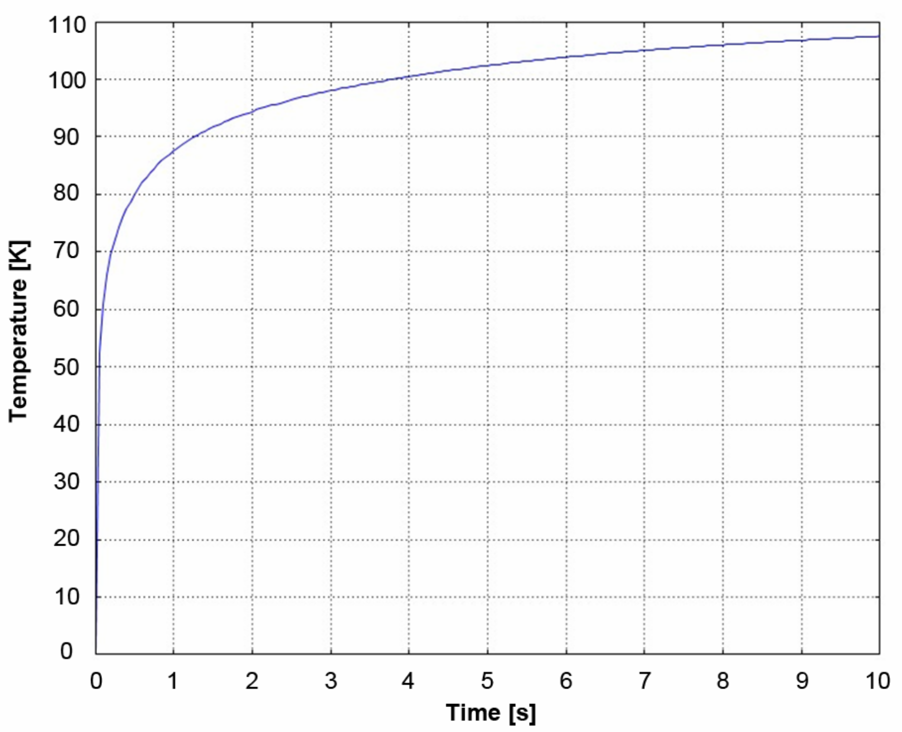

Figure 5.28 Temperature change of the Cr^{2+}:CdZnTe when pumped at 1.1 W showing a temperature rise of ~100 K.

Even though limited in performance, chromium-doped CdZnTe could potentially be a useful laser crystal for applications where cost effectiveness and sample-to-sample quality are of great importance. While the material can not provide the efficiencies and high cw output powers of other chromium-doped chalcogenide crystals such as Cr^{2+}:ZnSe, the on-time output power of 550 mW obtained in the context of this work could well be adequate for short range sensing applications such as process monitoring. Using more advanced methods for thermal management could potentially increase the output powers in both, cw and pulsed operation.

5.8 Conclusion

The use of 1.9 and 2.0 µm SDLs as a stable and flexible pump sources for Cr^{2+}:chalcogenide lasers has been discussed and compared to a more conventional pump source for these gain materials, i.e. a Tm^{3+}:$YAlO_3$ laser. In this context, various Cr^{2+}:ZnSe as well as Cr^{2+}:CdZnTe crystals were investigated. Using the Tm^{3+}:$YAlO_3$ laser resulted in strong system instabilities originating from the feedback induced intensity noise fluctuations despite the use of active, electronic feedback in the $Tm^{3+}:YAlO_3$ laser. The SDL pump sources did not exhibit these instabilities and delivered stable output radiation without the need for any optical isolation or active stabilisation. Using the 1.9 µm SDL to pump Cr^{2+}:ZnSe resulted in a maximum output power of up to 1 W (limited by the available pump power of 3.8 W) with a slope efficiency of up 40 % and a threshold of 255 mW.

When pumping the Cr^{2+}:ZnSe laser using the 2.0 µm SDL, with the pump wavelength now in the wings of the absorption band of Cr^{2+}:ZnSe, the absorption coefficient of the material was reduced from 5.4 to 3.9 cm^{-1} . This, however, did not significantly reduce the efficiency of the whole system. The higher pump power of 5.8 W available from the 2.0 µm SDL resulted in cw output powers of up to 1.8 W from the Cr^{2+}:ZnSe laser with a slope efficiency of 54 %. While these efficiencies are one of the highest reported in Cr^{2+}:ZnSe so far, the output power of the SDL pumped Cr^{2+}:ZnSe laser is somewhat lower than the 12 W recently reported by Mirov et al. [24]. It should be noted, however, that the pump source for this high power result is a Tm-fibre laser providing up to 30 W. When comparing to the more rigid and compact direct diode-pumped embodiments of Cr^{2+}:ZnSe laser, the SDL-pumped Cr^{2+}:ZnSe laser shows great advantages with output powers and slope efficiencies well above the ones obtained from diode-pumped embodiments where output powers are restricted to <100 mW and slope efficiencies of <40 % [25-27].

Using a prism or BRF to tune the laser, a maximum tuning range between 2.25 and 2.55 µm was achieved limited by the coatings of the mirrors. Using mirrors with broader coatings or multiple mirror sets should in principle allow use of the full emission band of the chromium gain media; however, it should be noted that for emission from the chromium laser below 2 µm, the use of the 2.0 µm SDL pump is not suitable as a population inversion would not be possible. To extend the tuning range to shorter wavelengths, pumping closer to the absorption peak of Cr^{2+}:ZnSe at around 1.8 µm would be required.

To further underline the practicality of the SDL as a pump source the intensity noise of the SDL-pumped Cr^{2+}:ZnSe laser was investigated without using any form of optical isolation between the SDL and the Cr^{2+}:ZnSe laser. This revealed an RMS intensity noise level of <0.14 %, limited by the resolution of the measurement apparatus. The strong intensity fluctuations and the damage caused to the

Tm^{3+}:$YAlO_3$ laser did not permit a comparative analysis of the two systems, however, the insensitivity of the SDL towards feedback is a significant advantage if one is pursuing the aim of practical laser sources for the mid-infrared wavelength band as the use of expensive optical isolators is not required and thereby greatly reducing the overall system complexity and cost.

In addition to the demonstration of the SDL as a pump source for the well established Cr^{2+}:ZnSe material, the novel host CdZnTe was investigated for laser operation. With up to 550 mW of on-time output power, the material performed significantly poorer compared to Cr^{2+}:ZnSe in quasi-cw operation with a factor of two smaller output power for the same pump power. At the same time, cw operation of Cr^{2+}:CdZnTe was strongly limited due to the poor thermal properties of the material to a few mW. Finite element analysis suggested that for the given experimental circumstances this limitation is associated with a strong temperature rise of the chip in the order of 100 K when pumped continuously. When pulsed-pumped, the temperature rise is insignificant with a rise of less than 1 K for pulse durations of 60 μs and with a cooling time of several milliseconds, pulse to pulse heating can be neglected. The model also revealed that significant heating of the crystal took place in the first 10 μs after the pump pulse is turned on, suggesting that the limits for athermal-pumping of Cr^{2+}:CdZnTe is in the order of 1 ms pulse duration and repetition rates of up to 100 Hz. For cw operation, significant measures would need to be required to reduce heating of the device significantly.

References

[1] H. L. Glass, A. J. Socha, C. L. Parfeniuk, and D. W. Bakken, "Improvements in production of CdZnTe crystals grown by the Bridgman method," J. Cryst. Growth **184-185**, 1035 (1998).

[2] I. S. Moskalev, V. V. Fedorov, and S. B. Mirov, "10 Watt, pure continuous-wave, polycrystalline Cr^{2+}:ZnS laser," Opt. Express **17**, 2048 (2009).

[3] Photonics Innovations Ltd., http://photonicsinnovations.com

[4] II-VI Infrared, http://www.ii-vi.com

[5] P. Cerny, H. Sun, and D. Burns, "Spectroscopic investigation and continuous-wave laser demonstration utilizing single crystal Cr^{2+}:CdZnTe," presented at the Advanced Solid-State Photonics, Viena, (2005).

[6] N. Hempler, J. M. Hopkins, B. Rosener, N. Schulz, M. Rattunde, J. Wagner, U. N. Roy, A. Burge, and D. Burns, "Semiconductor Disk Laser Pumped Cr^{2+}:Chalcogenide Lasers," CLEO, 284 (2008).

[7] Laseroptik GmbH, http://www.laseroptik.de

[8] CSPE, http://www.cspe-laseroptic.com

[9] IPG Photonics Ltd., http://www.ipgphotonics.com

[10] D. Findlay and R.A. Clay, "The measurement of internal losses in 4-level lasers," Phys. Lett. **20**, 227 (1966).

[11] J. A. Caird, S. A. Payne, P. R. Staver, A. J. Ramponi, L. L. Chase, and W. F. Krupke, "Quantum Electronic-Properties of the $Na_3Ga_2Li_3F_{12}$-Cr^{3+} Laser," IEEE J. Quantum Eelect. **24**, 1077 (1988).

[12] S. A. Payne, L. L. Chase, H. W. Newkirk, L. K. Smith, and W. F. Krupke, "$LiCaAlF_6$-Cr^{3+} - a Promising New Solid-State Laser Material," IEEE J. Quantum Eelect. **24**, 2243 (1988).

[13] S. Mirov, V. Fedorov, I. Moskalev, D. Martyshkin, and C. Kim, "Progress in Cr^{2+} and Fe^{2+} doped mid-IR laser materials," Laser & Photonics Review, NA (2009).

[14] U. Demirbas and A. Sennaroglu, "Intracavity-pumped Cr^{2+}:ZnSe laser with ultrabroad tuning range between 1880 and 3100 nm," Opt. Lett. **31**, 2293 (2006).

[15] U. Hommerich, X. Wu, V. R. Davis, S. B. Trivedi, K. Grasza, R. J. Chen, and S. Kutcher, "Demonstration of room-temperature laser action at 2.5 µm from Cr^{2+}:$Cd_{0.85}Mn_{0.15}Te$," Opt. Lett. **22**, 1180 (1997).

[16] E. Sorokin, I. T. Sorokina, M. S. Mirov, V. V. Fedorov, I. S. Moskalev, and S. B. Mirov, "Ultrabroad Continuous-Wave Tuning of Ceramic Cr:ZnSe and Cr:ZnS Lasers," presented at the ASSP, San Diego, CA, USA, (2010).

[17] Ghaya Baili, Fabien Bretenaker, Mehdi Alouini, Loïc Morvan, Daniel Dolfi, and Isabelle Sagnes, "Experimental Investigation and Analytical Modeling of Excess Intensity Noise in Semiconductor Class-A Lasers," J. Lightwave Technol. **26**, 952 (2008).

[18] S. Kuppurao, S. Brandon, and J. J. Derby, "Modeling the Vertical Bridgman Growth of Cadmium Zinc Telluride .1. Quasi-Steady Analysis of Heat-Transfer and Convection," J. Cryst. Growth **155**, 93 (1995).

[19] V. Kishore, R. Sharma, Vibhav K. Saraswat, N. S. Saxena, Kananbala Sharma, and T. P. Sharma, "Temperature dependence of effective thermal conductivity and diffusivity of Zn_xTe_{1-x} ($x = 5$, 10, 30 and 50) chalcogenide material," Applied Thermal Engineering **27**, 1552 (2007).

[20] R. Cerný, A. Kalbác, and P. Prikryl, "Computational modeling of CdZnTe crystal growth from the melt," Computational Materials Science **17**, 34 (2000).

[21] I. T. Sorokina, E. Sorokin, S. Mirov, V. Fedorov, V. Badikov, V. Panyutin, A. Di Lieto, and M. Tonelli, "Continuous-wave tunable Cr^{2+}:ZnS laser," Appl. Phys. B **74**, 607 (2002).

[22] CRYSTRAN, http://www.crystran.co.uk/zinc-selenide-znse.htm.

[23] A. A. Kaminskii, V. G. Ralchenko, and V. I. Konov, "CVD-diamond - a novel X^3-nonlinear active crystalline material for SRS generation in very wide spectral range," Laser Physics Letters **3**, 171 (2006).

[24] S. B. Mirov, V. V. Fedorov, I. S. Moskalev, D. V. Martyshkin, and C. Kim, "Progress in Cr^{2+} and Fe^{2+} dopded Mid-IR Laser Materials," Laser Photonics Rev. **DOI 10.1002/Ipor.200810076** (2009).

[25] M. Mond, D. Albrecht, E. Heumann, G. Huber, S. Kuck, V. I. Levchenko, V. N. Yakimovich, V. G. Shcherbitsky, V. E. Kisel, and N. V. Kuleshov, "1.9

μm and 2.0 μm laser diode pumping of Cr^{2+}: ZnSe and Cr^{2+}:CdMnTe," Opt. Lett. **27**, 1034 (2002).

[26] I. Moskalev, A. Gallian, V. Fedorov, S. Mirov, V. Badikov, V. Panyutin, D. Garbuzov, I. Kudryashov, and S. Todorov, "Continuous-wave polycrystalline Cr^{2+}:ZnSe laser pumped by a 1.85 μm InGaAsP/InP laser diode," presented at the Conference on Lasers and Electro-Optics/International Quantum Electronics Conference and Photonic Applications Systems Technologies, (2004).

[27] E. Sorokin and I. T. Sorokina, "Tunable diode-pumped continuous-wave Cr^{2+}:ZnSe laser," Appl. Phys. Lett. **80**, 3289 (2002).

Chapter Six

Pulsed Cr^{2+}:ZnSe laser

6.1 Introduction

In the previous chapter, the SDL format was demonstrated to be a practical pump source for solid state lasers such as chromium-doped chalcogenide lasers. After the promising results in cw and quasi-cw operation, this chapter will concentrate on the use of SDLs to pulsed-pump Cr^{2+}:ZnSe lasers.

The pulsed operation of lasers is vital for many applications. While nonlinear processes often require the high intensities available from pulsed sources, applications like LIDAR benefit from high pulse energies. The use of pulses also allows easier recognition of a signal when the signal to noise ratio is low. Additionally, the pulsed-pumping of laser systems can save energy compared to cw operation and thereby increasing the overall system efficiency and reducing cost.

So far, chromium-doped chalcogenide lasers have been demonstrated in various modes of pulsed operation: mode-locked, Q-switched and gain-switched. Motivated by the aim of developing a *mid-IR Ti:Sapphire* laser, a lot of attention has been paid to the development of mode-locked Cr^{2+}:ZnSe arrangements. The first demonstration used an acousto-optic modulator, leading to pulse durations of 4.4 ps [1]. However, passively mode-locked embodiments using saturable absorbers or Kerr lens modelocking soon followed with pulse durations significantly reducing to 80 fs [2,3].

Q-switching of Cr^{2+}:II-VI lasers has so far been of less interest. This is likely to be associated with the relatively short upper-state lifetime of the order of microseconds (4 μs for Cr^{2+}:ZnSe), compared to some of the rare-earth materials available which posses upper-state lifetimes in the order of milliseconds. However, pulsed microchip embodiments have been realised in Cr^{2+}:ZnSe with pulses of up to 1 mJ [4].

In this chapter, the focus will be the development of passively Q-switched and gain switched Cr^{2+}:ZnSe lasers.

The concept of Q-switching was introduced in chapter 3. Gain switching is similar in that the energy is stored in the population inversion before oscillation is enabled, allowing relatively high energy pulses to be extracted [5]. Instead of an active or passive element inside the resonator, however, gain-switching relies on the resonator and population dynamics to form the pulses (Figure 6.1).

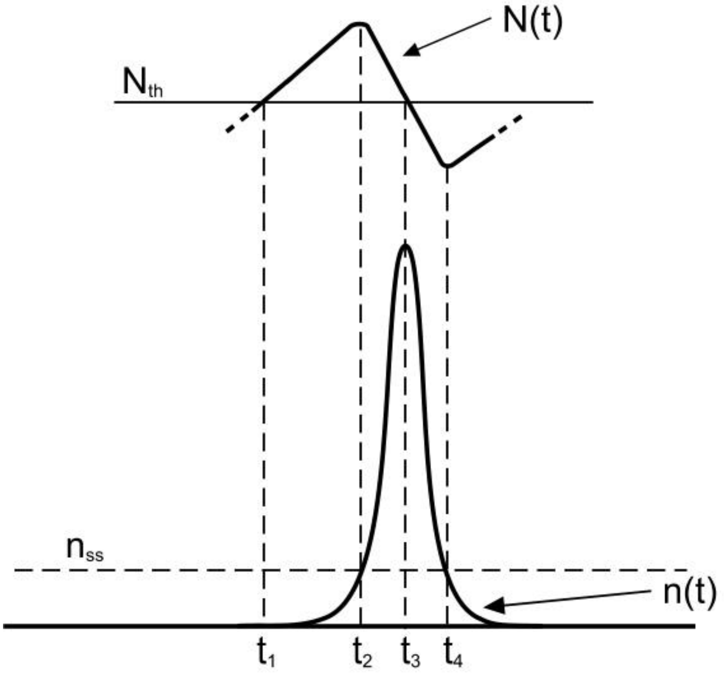

Figure 6.1 Schematic of the pulse formation in a gain-switched laser showing the temporal evolution of the population inversion N_{th} and the photon number n(t) after [5].

Here it is assumed that the pump pulse turns on somewhat before time t_1 so that the inversion population N(t) passes the threshold level N_{th} at a time t_1. Before this time, the photon number inside the resonator is essential zero but starts to build up according to the build up time of the resonator, after the population reaches threshold. Once the photon number passes the steady state value at the time t_2, the upper laser level population is rapidly extracted by stimulated emission, resulting in the steep rise of the intracavity field. Once the population is reduced below the threshold level (t_3), the photon number starts to reduce until the resonator field is below the steady state and the photons no longer deplete the population inversion. At this point (t_4), the inversion will start to increase again and the process repeats itself. For continuous pumping, this process will repeat itself over and over again, with the peak power of the pulses reducing and the output approaching a steady state level. The result is the formation of relaxation oscillation (see Figure 6.2)

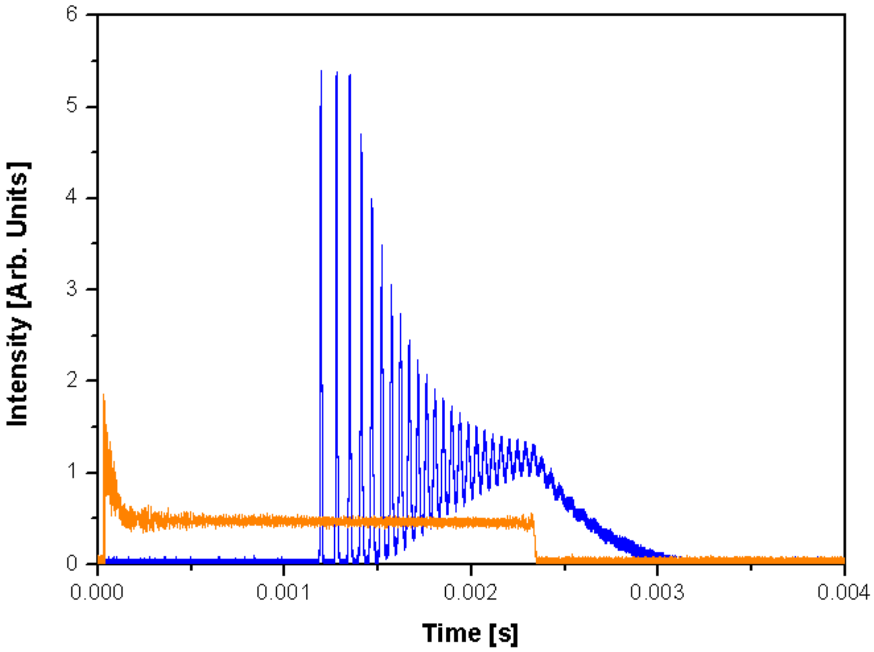

Figure 6.2 Schematic of relaxation oscillation in a laser (blue trace) after the turn on of the laser when pumped with a pulsed signal (orange trace). The spiking at the beginning of the pulse changes to sinusoidal oscillations towards the end of the pulse.

This relaxation to the steady state can be suppressed, however, when the laser is pumped with pulses of durations similar in length to the cavity build up time. This leads to the formation of individual pulses without the need for any additional intracavity elements. The result is a potential compact, sturdy and low cost system that is capable of supplying energetic pulses.

After the discussion of using a 2.3 µm SDL chip as a variable saturable absorber to Q-switch and control the mode of operation of a Cr^{2+}:ZnSe laser, the pulsed-pumped 1.9 µm SDL discussed in chapter 4 will be used as pump source for a gain switched Cr^{2+}:ZnSe laser.

6.2 Passive Q-switching

6.2.1 Experimental arrangement

For this experiment, a z-folded resonator was set up (see Figure 6.3). The folding mirrors (M_1 and M_2) were chosen to have 100 mm radius of curvature and the arm lengths were set to 300 mm resulting in a resonator waist inside the crystal of 72 x 52 µm (Figure 6.4). This was matched by focusing the radiation of the 2.0 µm SDL pump source using a 70 mm lens (f_1) into the 3 mm thick piece of Cr^{2+}:ZnSe (sample 4). Another resonator waist was formed by employing a 50 mm radius of curvature mirror (M_4) to focus one of the resonator arms onto the intracavity SDL chip.

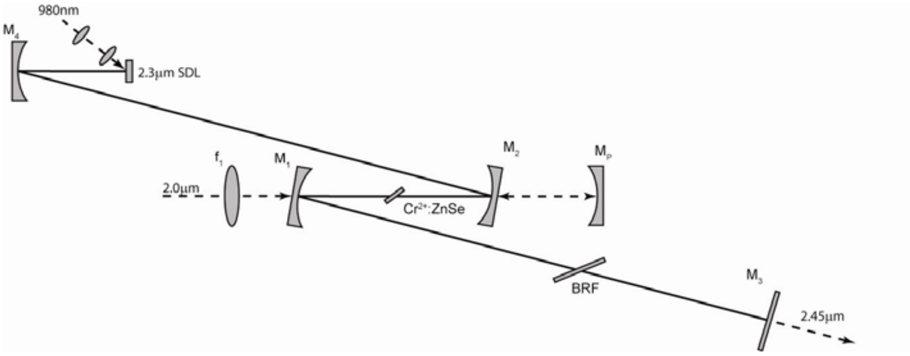

Figure 6.3 Experimental arrangement for the passively Q-switched Cr^{2+}:ZnSe laser comprising of a f_1=70mm focusing lens, r=-50 mm radius of curvature mirrors (M_1, M_2 and M_4), a pump retro-reflecting mirror M_P, an output coupler M_3, an intracavity 2.3 µm SDL and a birefringent filter (BRF).

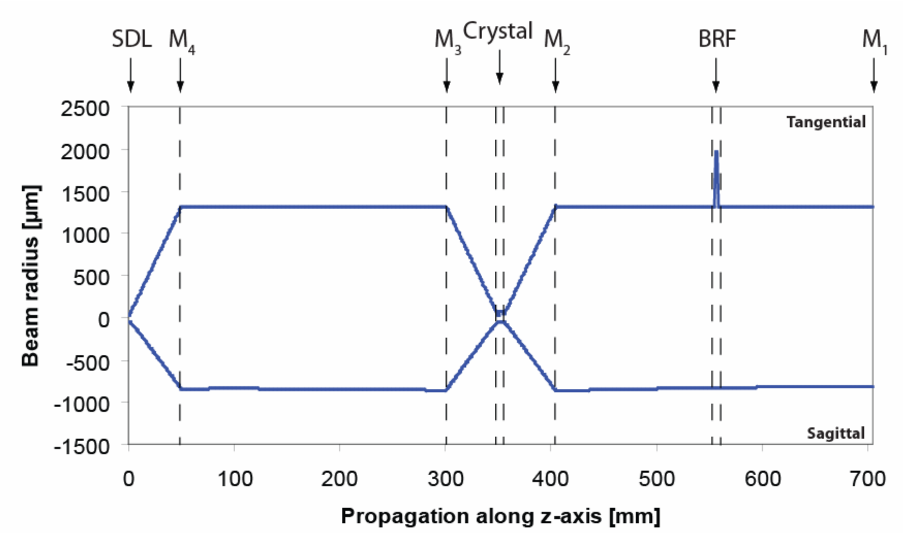

Figure 6.4 Resonator mode size for the Q-switched Cr^{2+}:ZnSe laser showing a mode size of 52 x 72 µm inside the crystal.

Instead of a conventional saturable absorber, a semiconductor disk laser chip designed for 2.3 µm emission [6] was used as passive Q-switch. Using a fibre-coupled (100 µm) diode laser emitting at 980 nm it is possible to bleach the absorbing quantum wells of the SDL which in turn allows switching between different modes of operation [7]. To match the emission of the chromium laser to the 2.3 µm, a BRF was used to tune the resonator wavelength.

6.2.2 Experimental discussion

Without any pump light applied to the intracavity absorber, Q-switched operation was readily obtained. For an incident pump power of 3.1 W and an output coupler reflectivity of 87 % the pulses were recorded using a fast photodetector. This revealed a repetition rate of 830 kHz and 90 ns pulse duration (Figure 6.3).

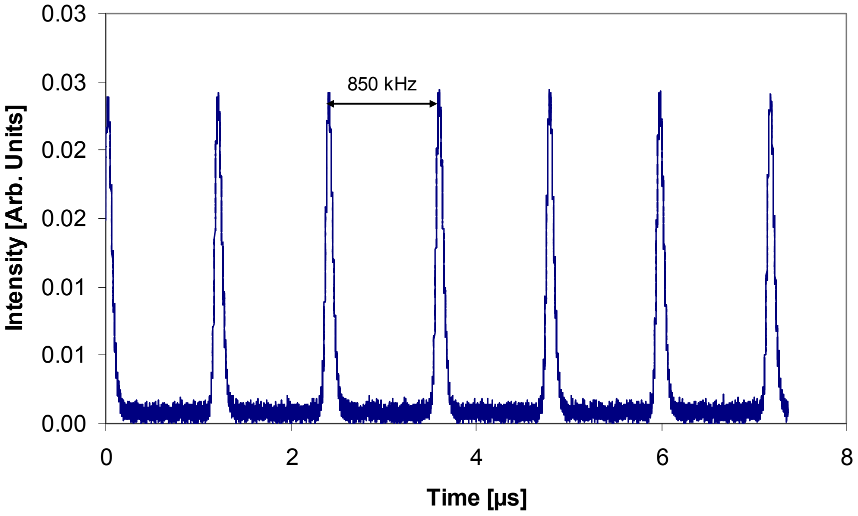

Figure 6.5 7 consecutive pulses from the passively Q-switched Cr^{2+}:ZnSe laser using the 2.3 µm SDL as variable saturable absorber.

The average output power was measured using a laser power meter and was measured to be 535 mW, resulting in a pulse energy of 0.6 µJ.

To determine the jitter of the output pulses, the relative position of 7 consecutive pulses was recorded and averaged 4000 times (see Figure 6.5). The resulting trace is showing a broadening of the consecutive pulses. This change in pulse width is not associated with broadening of the actual pulses but rather related to the temporal distribution of the pulse. The information can therefore be used to determine the jitter by subtracting the initial pulse width from the width of the averaged pulse. As the temporal displacement of a single pulse accumulates with every consecutive pulse, the widths of the peaks grow linearly from pulse to pulse (see inset of Figure 6.8). In this way, a pulse to pulse jitter of 113 ns was determined. In this context it was important to add a polarisation defining element into the SDL resonator. Otherwise the jitter increased strongly due to polarisation switching in the SDL resonator arising from optical feedback from the chromium laser. Figure 6.5 also shows that after the fourth peak, the trace does not reach zero anymore. This is an indication that the distribution functions of neighbouring pulses are blending into each other and the temporal position of the pulses is not fully distinguishable anymore.

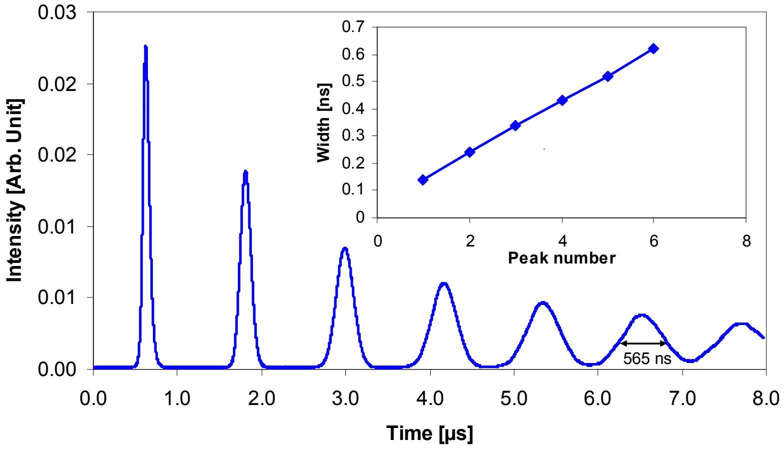

Figure 6.6 Output pulses recorded from the Q-Switched Cr^{2+}:ZnSe laser averaged over 4000 times pulses. The increased pulse width is indication for the jitter of the laser. **Inset:** Change of the half maximum width with number of peaks away from the triggered peak.

For the power transfer, output couplers with reflectivities between 87 and 99 % were used. The maximum average output power was obtained using the R=87 % output coupler resulting in 535 mW average power for 1.9 W of absorbed pump power. The maximum slope efficiency was 31 %. This slope efficiency is smaller than for cw operation discussed in chapter 6 using the same sample; however, this is to be expected due to increased losses inside the resonator associated with the absorber.

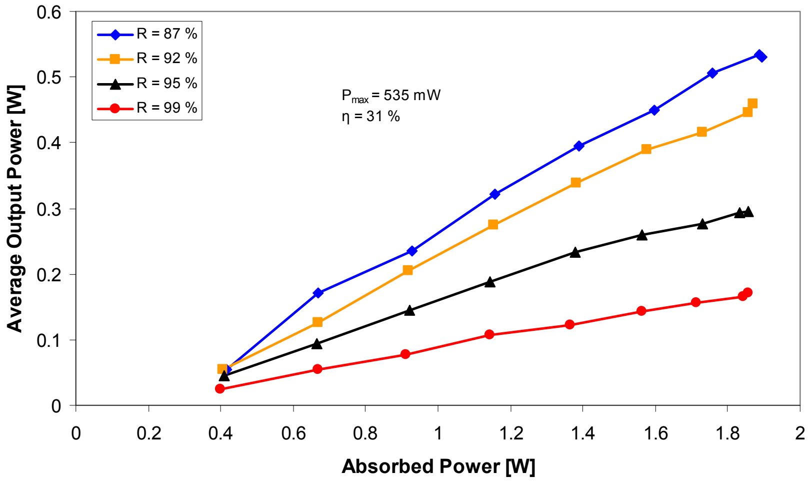

Figure 6.7 Power transfer showing the relation between incident pump power and average output power, revealing a maximum average output power of 535 mW for 87 % output coupling.

From the average power and repetition rate the pulse energy was calculated. The output pulse energy over the absorbed pump power for various output couplers is depicted in (Figure 6.8). For output coupling with a mirror of 87 % reflectivity, the maximum pulse energy was found to be 507 nJ.

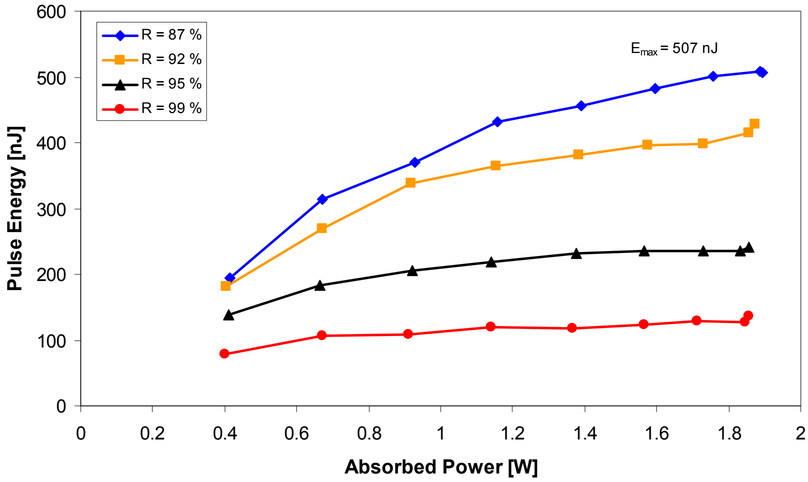

Figure 6.8 Power transfer characteristic of the Q-switched Cr^{2+}:ZnSe laser revealing a maximum pulse energy of 500 nJ.

As the saturable absorber requires a certain photon flux to saturate and become transmissive, i.e. allow the stored energy inside the crystal, to be emitted in form of a pulse, the pulse duration and repetition rate is directly depending on the ration of the absorbed pump power to the threshold pump power. For a given passively Q-switched system, the repetition rate and pulse duration therefore changes with pump power. For an output coupler with a reflectivity of 87 %, this relation can be seen in Figure 6.9 and its inset.

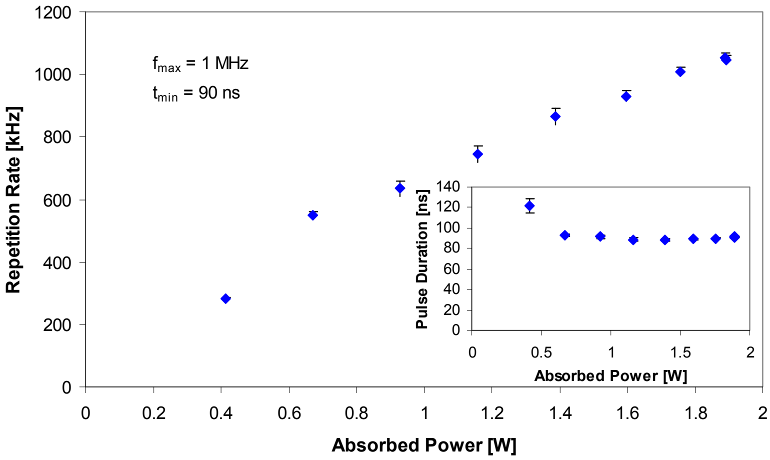

Figure 6.9 Change of the repetition rate of the Q-switched Cr^{2+}:ZnSe laser with pump power. **Inset:** Change of the pulse duration with pump power.

This shows, that the repetition rate changes between 280-1050 kHz while the pulse duration drops from 122 to 91 ns. As a consequence, the case of passive Q-switching imposes restrictions on the output parameters that can be obtained from a laser. If a smaller repetition rate was required, while maintaining the pulse duration, no obvious solution is available without changing the saturation fluence, by either varying the spot size on the saturable absorber or redesigning the absorber itself. If, for example, pulse duration could be sacrificed, it would be possible to increase the threshold of the laser by increasing the spot sizes of the cavity mode inside the active medium or by changing the output coupling and reduce the repetition rate in this way.

6.2.3 Switching between modes of operation

The use of an SDL chip as absorber has no particular advantage for solely Q-switched lasers compared to the use of conventional absorbers; however, it does enable the use of an additionally pump source to bleach the chip and change the saturation fluence. As demonstrated in reference [7], this can be used to switch between different operational modes of the laser. While continuous-wave operation requires a highly bleached SDL to allow efficient oscillation without significant losses, Q-switching needs a significant modulation depth to hold back the oscillation and to allow the storage energy inside the crystal. Mode-locked operation requires a relatively small modulation depth that does not prevent cw-operation but just modulates the signal to encourage the longitudinal modes of the resonator to lock in phase. To achieve this, the absorption spectrum of the chip can be modified either by bleaching it using the pump laser or by changing the temperature of the chip, which will cause a wavelength shift of the absorption profile. If the point of operation is on a slope of the absorption profile, tuning can be achieved with small temperature changes. While the bleaching of the chip is achieved using a 980 nm fibre-coupled diode laser, the temperature shift can be achieved by either using a direct temperature control of the chip by, e.g. thermo-electric cooling/heating or by optical pumping.

As reported in the previous section, the Cr^{2+}:ZnSe laser exhibited Q-switched pulses when the intra-cavity chip is not pumped or heated. However, when applying a pump signal of 2.4 W to the SDL chip, the mode of operation changed to cw. This switching took 450 μs from the moment the diode laser driver was triggered to the moment when the Cr^{2+}:ZnSe laser emitted cw radiation (see Figure 6.10). The majority of this time, however, was attributed to the turn-on delay of the diode laser from the moment the driver was triggered. The optical to optical turn-on delay was therefore on the order of 50 µs, which is in good agreement with the results reported in reference [7].

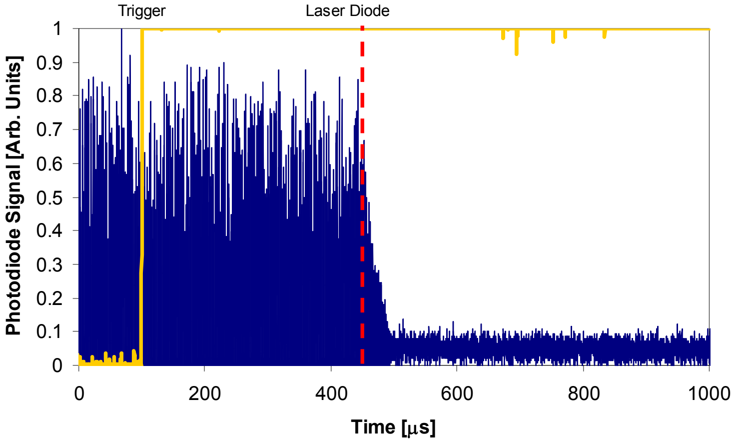

Figure 6.10 Output of the Cr^{2+}:ZnSe laser recorded before and after switching the operational mode from cw to Q-switching, revealing a total delay of 450 µs and a 50 µs optical to optical time constant.

Applying a Fourier transformation [8] to the data reveals the Q-switching operation for times <500 ns and cw operation of >500 ns (see Figure 6.11 and inset). The peaks in the main plot are the fundamental and harmonics of the Q-switched pulse in frequency space, separated by the repetition rate (f=825 kHz) of the Q-switched signal. The inset does not show any distinguishable frequency components as would be expected from a cw signal.

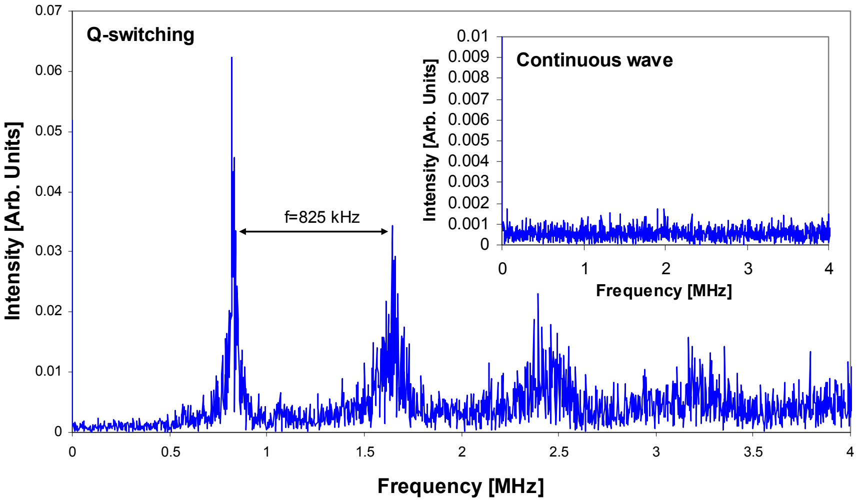

Figure 6.11 Fast Fourier analysis of the output signal of the Cr^{2+}:ZnSe laser before and after (inset) applying pump light to the intra-cavity SDL.

To investigate the possibility of modelocking the Cr^{2+}:ZnSe laser using the SDL as a saturable absorber the pump power on the intracavity SDL chip had to be increased compared to the Q-switched operation to reduce the modulation depth of the chip. Decreasing the power to 1.8 W resulted in the formation of a pulse train as visible in the inset of Figure 6.12. It should be noted, that the floor of the measured signal did not reach zero, which is associated with the speed of the photodetector which would not to fully resolve the individual pulses.

When analysing the output power using an RF spectrum analyser (Agilent 86142B) a strong peak was observed at a repetition rate of 130 MHz which was the frequency expected from a resonator with a roundtrip length of 2.3 m.

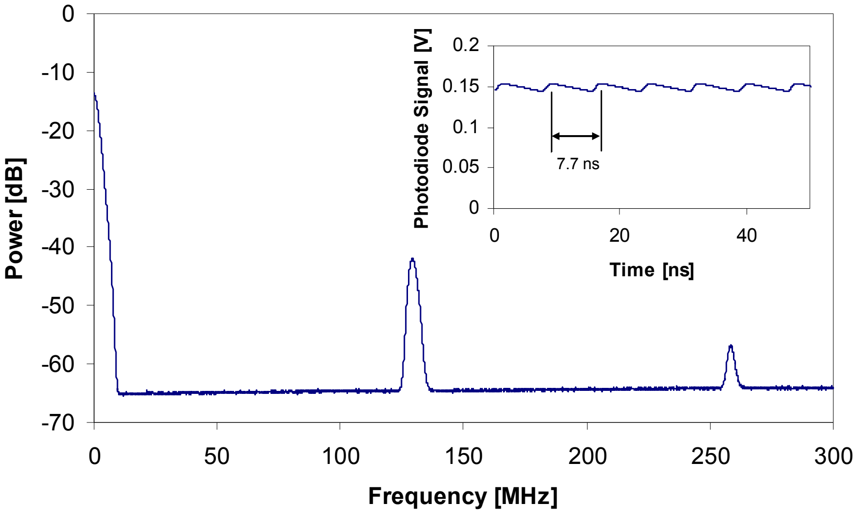

Figure 6.12 RF spectrum of the pulses at a cavity repetition rate of 130 MHz with 7.7 ns pulse separation (inset). The pulses in the inset were resolution limited by the photo detector.

To encourage the formation of ultra-short pulses, two ZnSe prisms were inserted into the resonator to introduce negative dispersion to balance the positive dispersion introduced by the optical components and encourage the formation of short pulses.

As the pulse width of a mode-locked laser is directly related with its spectral width by the time bandwidth product, a real time spectrometer can be used to observe the pulse width. The spectrum should broaden significantly when the laser operates in pulsed regime rather than cw. However, as real time spectrometers for this wavelength are not readily available, an in-house build scanning Fabry-Perot interferometer (SFPI) was build. A SFPI is based on the effect known from etalons, where a spectral filter function is created when two surfaces with reflecting properties for the wavelength band of interest are brought in close proximity and aligned parallel to each other. The result is that specific wavelengths are resonant with the microcavity. When resonant, the detected intensity of the wavelength after the SFPI is higher compared to the non-resonant wavelength. The result is a filter function as shown in Figure 6.13.

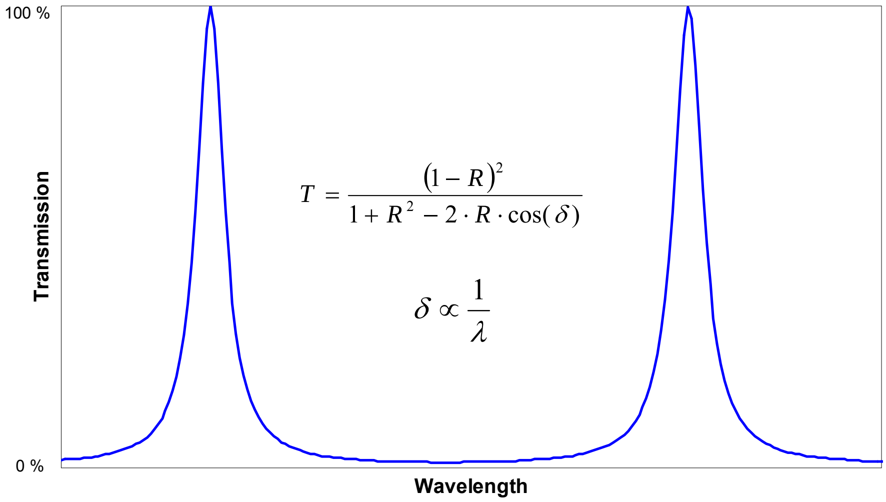

Figure 6.13 Transmission of an etalon formed by two reflective mirrors parallel to each other and in close proximity. The equation shows the dependence of the transmission on the reflectivity (R) of the mirrors, and the phase difference (δ).

When one of the surfaces is vibrated, e.g. by a piezo-actuator modulated by a function generator, the filter function of the etalon can be changed, resulting in a sweep through a range of wavelengths. In this fashion, the output spectrum of a laser can be transformed from the frequency into the temporal domain and can be visualized on an oscilloscope. As the SFPI used for this work was not calibrated, a grating monochromator was used as reference.

In cw operation, the spectrum was measured to be ~10 nm with prisms in place and with the SDL chip being pumped to transparency. For a transform limited 100 fs sech^2 pulse, the bandwidth of the laser would need to be in excess of 65 nm (assuming a time bandwidth product 0.315). Adjusting the laser for mode-locked operation, however, did not increase the bandwidth, a clear indication that no short pulses were formed.

Investigating the laser in respect to bandwidth limiting properties revealed that the output bandwidth was limited by water absorption features around 2.4 µm (Figure 6.14).

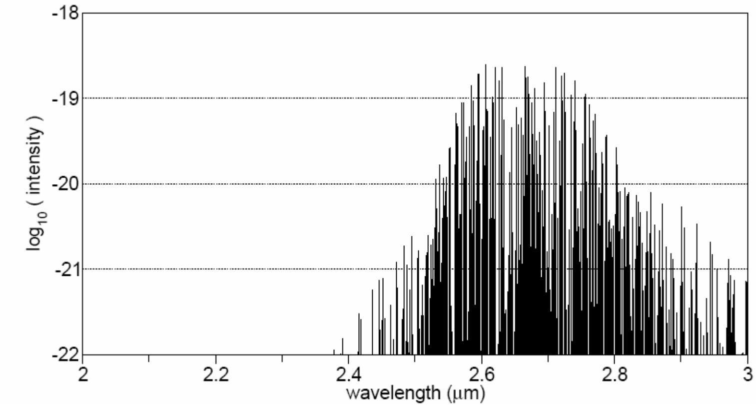

Figure 6.14 Water absorption with an intensity of $1 \cdot 10^{-22}$ $cm^{-1}/(mol \cdot cm^{-2})$ lines between 2-3 µm. (Data obtained from the HITRAN database through www.spectralcalc.com).

Enclosing the resonator in an air tight box and purging it with nitrogen ensured elimination of these features; however, this was not enough to enable the formation of broad enough output spectrum. The bandwidth limiting effect of SDLs was observed elsewhere and is related to the micro cavity resonance of the SDL [9]. Antiresonant SDL structures could be envisaged to overcome this issue.

6.3 Gain switching of Cr^{2+}:ZnSe

While the previously discussed Cr^{2+}:ZnSe laser is very flexible in its mode of operation and can therefore be used for many applications, often the need for practical and specific laser sources is more important to satisfy the need for applications. In this section, a gain-switched, low-cost Cr^{2+}:ZnSe laser is discussed using the pulsed-pumped 1.9 µm SDL as pump source and thereby replacing bulky and actively cooled conventional cw diode lasers.

6.3.1 Experimental arrangement

The experimental arrangement of the 1.9 µm SDL is the fibre-coupled 2-mirror arrangement discussed in chapter 4. This delivered a maximum on-time pump power of 12 W with a pulse duration of ~160 ns and a maximum repetition rate of 1 kHz to the Cr^{2+}:ZnSe laser.

The chromium laser consisted of a short hemispheric 2-mirror resonator in which the Cr^{2+}:ZnSe crystal was placed directly in front of a high reflectivity plane mirror, with the coating centred at 2.45 µm. The cavity was terminated by a curved output coupler with a curvature of 50 mm and a reflectivity of 92 %, placed 50 mm away from the plane mirror.

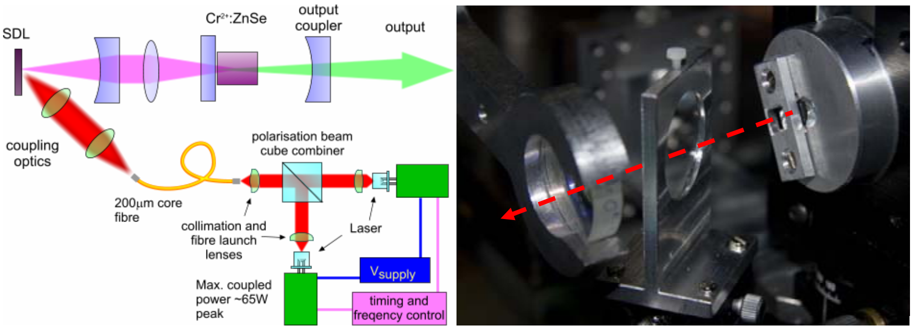

Figure 6.15 Left: Experimental arrangement of the gain-switched Cr^{2+}:ZnSe laser comprising of the 1.9 µm pulsed-pumped SDL pumped by the OSRAM SPL PL90_3 pulsed diode lasers. **Right:** Picture of the hemispheric Cr^{2+}:ZnSe laser including a BRF.

This configuration resulted in a fundamental resonator waist of 69 µm inside the crystal. To focus the pump radiation into the crystal, a 100 mm focal length lens was used which was empirically determined to be the best choice of the available lenses to optimise the output power.

6.3.2 Experimental discussion

In the previously described arrangement, the Cr^{2+}:ZnSe crystal exhibited stable output pulses with pulse durations of 20 ns at a repetition rate of 10 kHz (dictated by the repetition rate of the pulsed-pumped SDL).

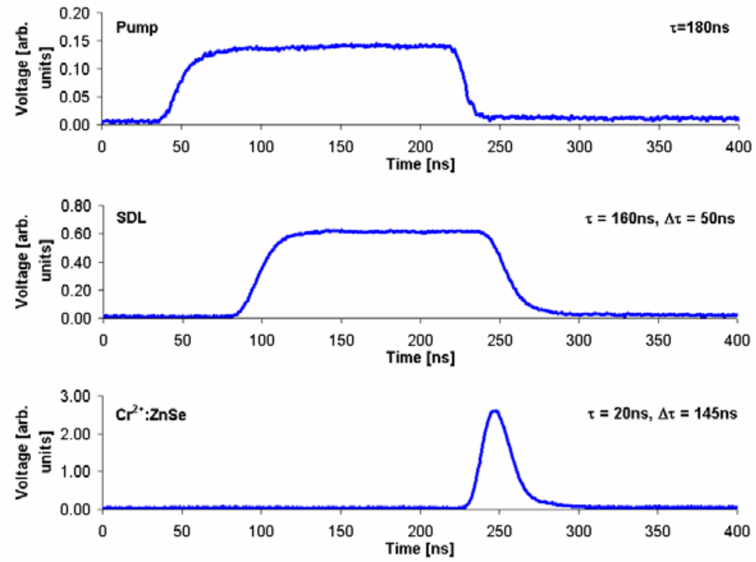

Figure 6.16 Recorded pulse timing of the pulsed-pumped Cr^{2+}:ZnSe laser showing the pulse of the 905 nm nanostack pulsed diode laser, the 1.9 µm SDL and the Cr^{2+}:ZnSe laser.

The timing diagram of the pulsed diode laser, SDL and Cr^{2+}:ZnSe laser reveals a significant delay of the pulse emitted from the chromium laser to the very end of the pump pulse (Figure 6.16). This delay was, however, intentional as it allowed the population inversion in the gain media to build up over the whole duration of the pump pulse and thereby maximize the stored energy.

To achieve this, the build up time (t_B) of the resonator was adjusted to match the pump pulse duration using equation 6.1 [10].

$$t_B \approx \frac{\tau_c}{r-1} \ln\left(\frac{I_{SS}}{I_0}\right) \qquad \text{Equation 6.1}$$

Here, τ_c is the cavity decay time, r the times above threshold and I_{SS}/I_0 the ratio of final oscillation level to the initial noise level. This shows that an optimized resonator build-up time for a gain-switched laser is only valid for a given pump power. If the pump power was increased above this value, the pulse would turn on earlier and therefore caused the laser to work less efficiently. If this reduced -on time was significant enough, the laser would not only exhibit the first spike but multiples, before ultimately reaching the sinusoidal part of the relaxation oscillations as discussed in the introduction of this chapter.

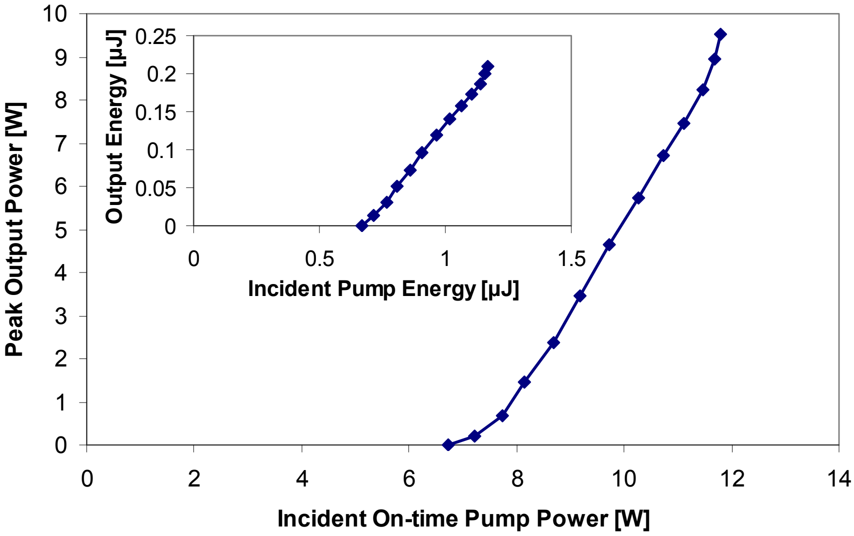

Figure 6.17 Power transfer characteristic of the gain switched Cr^{2+}:ZnSe laser with a maximum peak output power of ~10 W. **Inset:** Energy transfer the gain switched Cr^{2+}:ZnSe laser.

With the resonator build up being optimised for maximum pump power, the power transfer was recorded. For this, the peak intensity was recorded using a fast photodiode (Thorlabs PDA10D-EC). This measurement was calibrated using the average output power of the Cr^{2+}:ZnSe laser at maximum pump power measured using a Coherent Field Mate power meter in combination with a Coherent PM10 thermopile head. The resulting power transfer using a 92 % output coupler can be seen in Figure 6.17 and shows a maximum peak power of 10 W.

Compared to the power transfer curves of the Cr^{2+}:ZnSe laser recorded in the previous chapter, the plot shows significant non-linear parts at the top and bottom of the curve. The top part is likely to be associated with transverse mode changes of the resonator. This was associated with a mode match of pump and resonator mode not being optimised for single-mode operation but for multi-mode operation to extract maximum power from the laser. The lower non-linear part of the power transfer curve is associated with a significant change of the pulse duration around threshold which for a given pump energy will reduce the peak power and thereby result in a distortion of the power transfer plot. If the energy transfer curve is plotted, this effect disappears (see insert Figure 6.17) and reveals a fairly constant slope efficiency of 40 % and maximum pulse energy of 210 nJ.

When investigating the output spectrum of the pulsed-pumped Cr^{2+}:ZnSe laser, no chirp of the output pulses was observed, showing that the intrinsic chirp of the pulsed-pumped SDL was not imposed on the Cr^{2+}:ZnSe laser. Instead, pulses were emitted stably with a free-running wavelength of 2.48 μm. It was also possible to tune the output wavelength of the laser using a BRF. For this, a 1.5 mm thick quartz BRF was used, allowing wavelength tuning between 2465-2573 nm (see Figure 6.18). As this range was lower than expected, it was first assumed that the BRF was limiting the tuning range. As the limiting factor would be the free spectral range of the 2 mm thick quartz BRF, this was calculated using the equation 6.2 [11].

$$\upsilon_{fsr} = \frac{c}{(n_e - n_o) \cdot L_e} \qquad \text{Equation 6.2}$$

Here, c is the speed of light, n_e and n_0 the ordinary and extraordinary refractive index of the BRF material and L_e the length of the BRF. With a thickness of the quartz BRF of 2 mm and an extraordinary and ordinary refractive index of 1.5195 and 1.5116 respectively [12], a free spectral range of 330 nm was obtained. It should be noted that this equation assumes that the value of n_e and n_o do not change significantly over the wavelength band of interest. The value of 330 nm is therefore an approximation of the actual value. The result, however, shows that the BRF does not limit the tuning range of the laser.

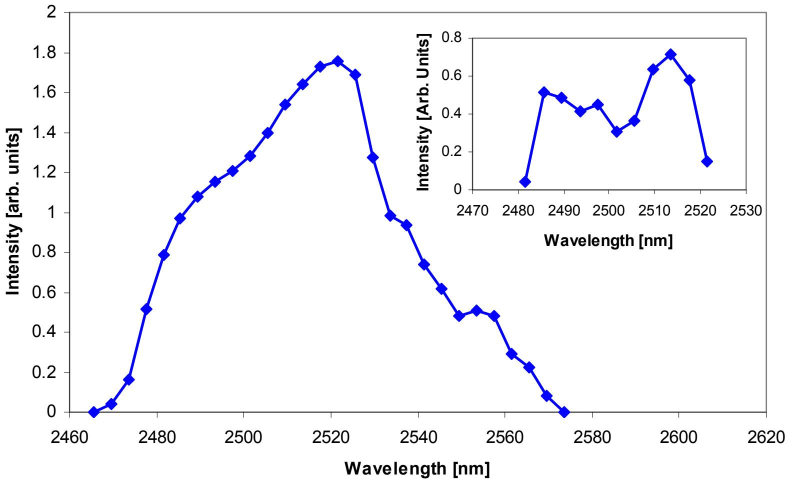

Figure 6.18 Tuning characteristic of the gain-switched Cr^{2+}:ZnSe laser using a 1.5 mm thick BRF. **Inset:** Spectral tuning range of the laser using prism tuning.

To investigate this further an intracavity ZnSe prism was used as alternative to the BRF (Figure 6.19). As previous experiments have shown, prism tuning should allow access to the full tuning range possible with the mirror set used. With the prism in place tuning of the laser between 2481-2521 nm (inset of Figure 6.18) was possible. Compared to the >300 nm cw tuning range obtained from the cw Cr^{2+}:ZnSe laser, the results from the gain switched laser are again limited. The reason for this is so far not fully understood and would require further investigation of the system.

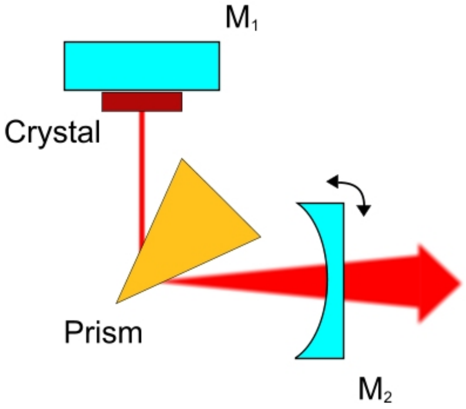

Figure 6.19 Schematic for the tuneable gain-switched Cr^{2+}:ZnSe laser using a prism as wavelength selective element.

6.3.3 Modelling

To investigate the potential of the pulsed-pumped Cr^{2+}:ZnSe laser, a numerical model based on coupled rate equations (equation 6.3 and 6.4) was used [13].

$$\frac{dN_2}{dt} = R_p - \frac{\sigma \cdot c \cdot \phi \cdot N_2}{V} - \frac{N_2}{\tau} \qquad \text{Equation 6.3}$$

$$\frac{d\phi}{dt} = \frac{V_a \cdot \sigma \cdot c \cdot \phi \cdot N_2}{V} - \frac{\phi}{\tau_c} \qquad \text{Equation 6.4}$$

Here, R_P is the pumping rate; the second term represents the stimulated emission where N_2 is the population of the upper laser level, Φ the number of photons inside the cavity, c the speed of light, σ the stimulated emission cross section and V the mode volume of the resonator. For the cavity rate equation 6.4 the first term represents the growth rate of the photon population in the cavity due to stimulated emission where V_a is the volume of the mode in the active medium. The second term expresses the losses inside the resonator where τ_c is photon lifetime.

The model was set up using the software MathCAD 14 and the solution for the equations found using a Runge-Kutta algorithm [14]. The material parameters used in these calculations are shown in Table 6.1

Parameter	Value	Unit
Emission cross section	$1.3\cdot10^{-22}$	M²
Upper state lifetime	$4\cdot10^{-6}$	s
Pump power	12	W
Laser wavelength	2450	nm
Pump laser wavelength	1900	nm
Laser repetition rate	100	Hz

Table 6.1 Material parameters for the coupled rate equations model of the gain-switched Cr^{2+}:ZnSe laser obtained from reference [15].

To compare the modelled results with the experiments, the input parameters for the models were based on the experimental arrangement discussed in the previous section with the resonator length being set to 50 mm, the output coupler to a reflectivity of 96 %, a spot size of 90 μm radius and a pump pulse duration of 160 ns. It should be noted that any additional intracavity losses were neglected. The trace calculated by the model, can be seen in Figure 6.20.

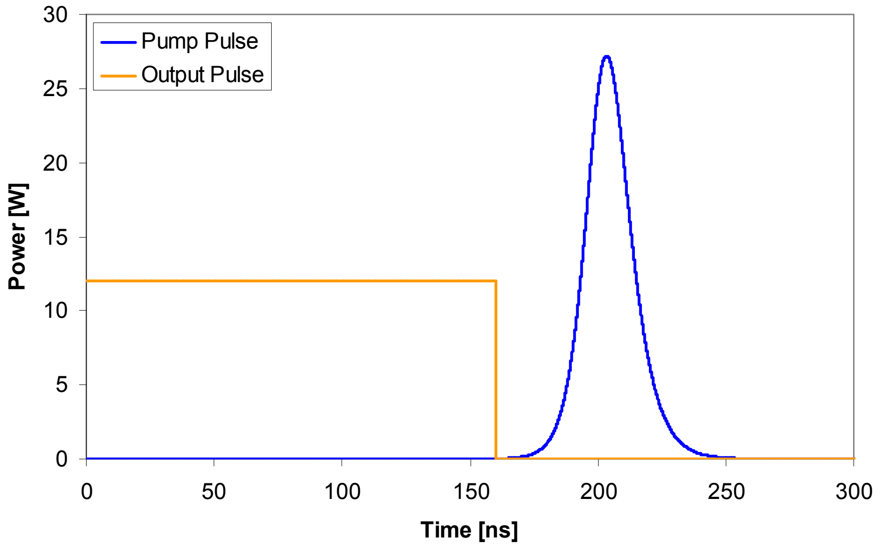

Figure 6.20 Output pulse of the gain-switched Cr^{2+}:ZnSe laser as modelled numerically using coupled rate equations.

The comparison with the experimental results shows that while the general trend of the model is in agreement, the exact values of pulse duration, peak power and turn on delay differ. As the material parameters used for the model were obtained from the literature, this discrepancy is expected; however the model can still be used to obtain relative trends of the system performance and give indications of how to improve the laser.

In the following, the input parameters of the resonator waist, output coupler reflectivity, cavity length and pump pulse duration were varied and the resulting output parameters plotted. For this, only a single parameter was changed at a time while leaving the rest constant.

First, the response of the laser output to varying the resonator waist was investigated. As an example, the modelled peak output power and the pulse duration are shown in Figure 6.21. This shows that the pulse peak power is maximised at around 60 W for a resonator waist of 75 µm. Further reduction of the resonator waist does not increase the peak power which levels off, until the resonator waist reaches 65 µm. For values lower than this, no single pulses are obtained from the laser but double pulsing occurs. This is not desirable as it reduces the peak power and energy of the individual pulses.

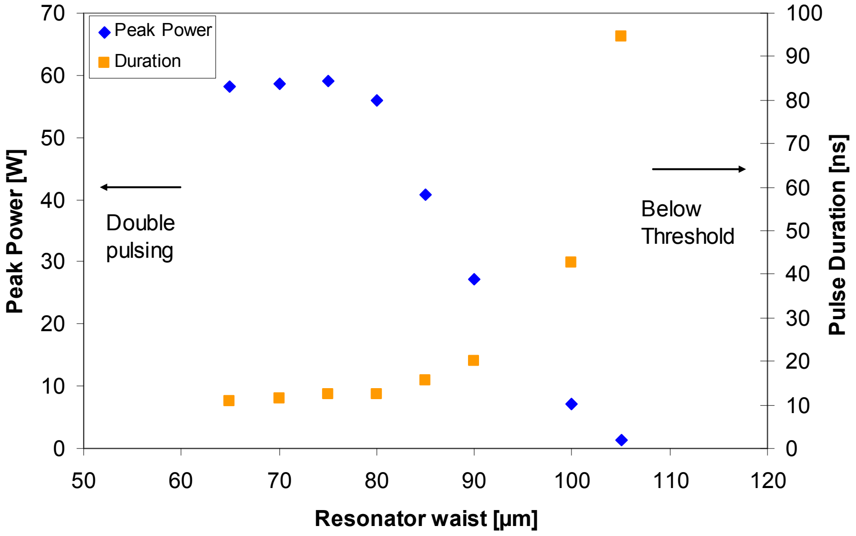

Figure 6.21 Modelled change of peak pulse power and pulse duration over resonator waist radius of the Cr^{2+}:ZnSe laser.

While the pulse peak power maximises at 75 µm cavity waist, the pulse duration reaches a minimum of 8 ns at this point. This pulse duration increases near exponentially for larger resonator waists until the laser is below threshold for mode sizes >105 µm.

When plotting the pulse energy and optical to optical efficiency as a function of the resonator mode radius, the resulting plot closely follows the shape of the peak power curve, with optimised values of 45 % efficiency and 800 nJ for a resonator waist of 75 µm. The pulse turn on delay with respect to the beginning of the pump pulse follows the trend of the pulse duration and saturates at the same point. As a result, an optimum resonator waist for this set of parameters can be found from the model with the value being 75 µm.

After investigating the influence of the resonator waist on the output parameters of the laser, the effect of the output coupler reflectivity was examined. The peak pulse power and pulse durations were plotted as a function of the output coupler reflectivity (see Figure 6.22).

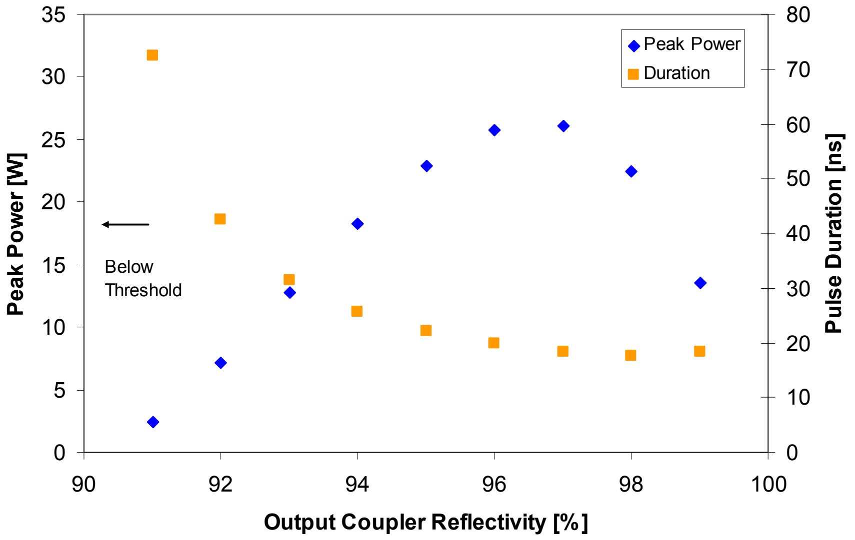

Figure 6.22 Modelled change of peak pulse power and pulse duration over output coupler reflectivity of the Cr^{2+}:ZnSe laser.

Here it can be seen that an optimum solution for the peak power is obtained for an output coupler reflectivity of 97 % with the pulse duration being at its minimum of 8 ns for a reflectivity of 98 %. Again, the lower end of the reflectivities is determined by the laser being below threshold. The optical to optical efficiency and the pulse energy curves again follow the pulse peak power while the turn on delay follows the pulse duration. For this set of parameters, an optimum output coupling can be found for ~97.5 % output coupler reflectivity.

In the same fashion as with the resonator waist and output coupler reflectivity, an optimum pump pulse duration of 240 ns can be found for this parameter range, where the pulse peak power, energy and optical to optical efficiency are maximised.

When considering the rearrangement of the resonator in respect to the length (see Figure 6.23), the model suggests that a shorter resonator is strongly beneficial to obtain the shortest pulses which would result in a maximum pulse peak power. This observation suggest, that a microchip implementation of a gain-switched Cr^{2+}:ZnSe laser could potentially enable pulse durations as short as 1 ns. This, however, would require the shortening of the pump pulse, as otherwise, strong relaxation oscillation would be obtained due to the short build-up time of the resonator field.

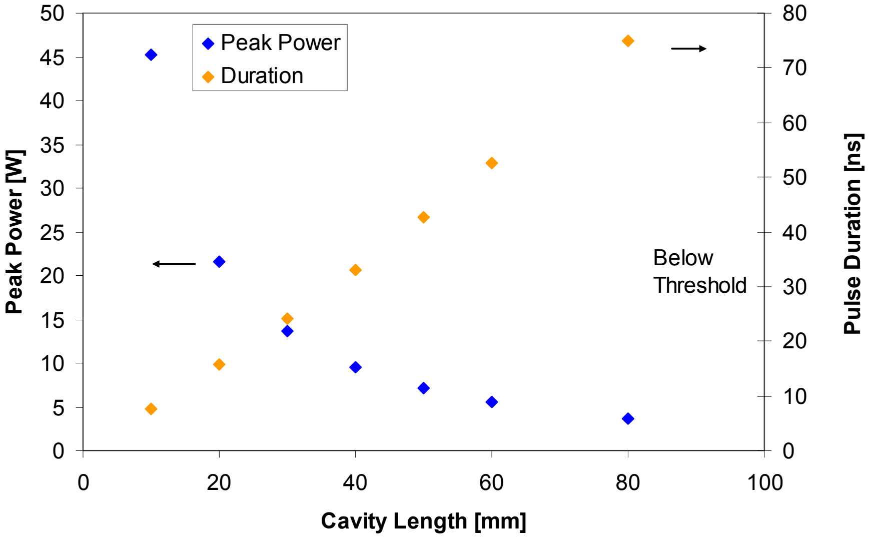

Figure 6.23 Modelled change of peak pulse power and pulse duration over cavity length of the Cr^{2+}:ZnSe laser.

The shortening of the resonator length does not, however, increase the energy of the output pulses. If maximising the pulse energy of the system is desired the turn-on time of the resonator would need to be increased by, e.g. increasing the resonator length and/or pump spot size or by reducing the output coupler reflectivity. This would allow the storage of more energy from the pump pulses with extended durations and thereby increase the output energy of the output pulses. If parameters such as the output coupling, resonator length and pump/resonator mode size are restricted but larger turn-on times are still required, it is also possible to insert active or passive elements such as Q-switches or saturable absorbers into the resonator. This would allow to hold off of the oscillation build-up for the desired duration but at the same time maintain compactness of the system.

6.4 Conclusion

The pulsed operation of a Cr^{2+}:ZnSe laser was demonstrated. Using an optically pumped SDL chip as variable intracavity absorber resulted in Q-switched operation of the chromium lasers with average output power of 535 mW, pulse duration of 90 ns, pulse energy of 0.5 µJ and repetition rate of up to 1GHz. The pulse jitter of the system was found to be 113 ns.

Pumping the intracavity SDL with 2.4 W allowed bleaching of the SDL chip and thereby switching the mode of operation of the chromium laser from Q-switching to cw. The switching time between the two states was found to be 50 µs for the optical to optical change, and 450 µs taking into account the delay introduced by the diode driver unit.

Rather than using the SDL as intracavity element, it was also possible to use the pulsed-pumped SDL introduced in chapter 4 to pump the Cr^{2+}:ZnSe laser, resulting in gain-switched operation. From this laser pulses with a pulse energy and pulse duration of 210 nJ and 20 ns respectively were obtained in a cost effective and practical format. Inserting a BRF into the resonator allowed tuning of the output wavelength of the chromium laser from 2465-2573 nm. With a ZnSe prism inside the resonator, tuning from 2481-2521 nm was possible.

Using a model based on the coupled rate equation allowed the further investigation of the resonator parameters and their influence. While not in total agreement with the experimental results, the model allowed to investigate relative changes of the laser properties for changing input parameters allowing to propose micro-chip arrangements of a gain-switched Cr^{2+}:ZnSe laser that could produce significantly shorter pulses in the order of a few nanoseconds.

For comparison, the results of the two types of pulsed operation used in this chapter, i.e. Q-switching and gain-switching, are shown in Table 6.2.

	Q-Switched	**Gain-Switched**
Pulse energy [nJ]	0.50	0.21
Peak power [W]	5.5	10
Pulse duration [ns]	90	20
Repetition rate [Hz]	$1 \cdot 10^6$	$1 \cdot 10^3$
Average power [mW]	535	2

Table 6.2 Comparison of the results obtained from the Q-switched and gain-switched Cr^{2+}:ZnSe laser.

It shows that the Q-switched operation is superior to the gain-switched mode of operation for these specific systems with higher repetition rates, and pulse energies. However, with shorter pulse durations and pulse energy and peak power in the same order of magnitude as the Q-switched arrangement, the gain switched system can be considered more appropriate for applications where more simplistic systems are required. The shortcomings with regards to pulse energy of this system can potentially be reduced by increasing the pump power using the extended pulsed-pumped SDL as demonstrated in chapter 4 or by using more individual devices to power scale the pulsed-pumped SDL power and in turn, the power of the gain switched system.

References

[1] T. J. Carrig, G. J. Wagner, A. Sennaroglu, J. Y. Jeong, and C. R. Pollock, "Mode-locked Cr^{2+}:ZnSe laser," Opt. Lett. **25**, 168 (2000).

[2] I. S. Moskalev, V. V. Fedorov, and S. B. Mirov, "Self-Starting Kerr-Mode-Locked Polycrystalline Cr2+:ZnSe Laser," CLEO, 104 (2008).

[3] I. T. Sorokina and E Sorokin, "Chriped-mirror dispersion controlled femtosecond Cr:ZnSe laser," presented at the ASSP, Paper WA7, (2007).

[4] S. Mirov, V. Fedorov, I. Moskalev, D. Martyshkin, and C. Kim, "Progress in Cr^{2+} and Fe^{2+} doped mid-IR laser materials," Laser & Photonics Review, NA (2009).

[5] A. E. Siegman, in *Lasers*, edited by A. Kelly University Science Books, Sausalito, CA, pp. 962 (1986).

[6] J. M. Hopkins, A. J. Maclean, D. Burns, E. Riis, N. Schulz, M. Rattunde, C. Manz, K. Kohler, and J. Wagner, "Tunable, single-frequency, diode-pumped 2.3 µm VECSEL," Opt. Express **15**, 8212 (2007).

[7] V. G. Savitski, D. Burns, and S. Calvez, "Optically-pumped saturable absorber for fast switching between continuous-wave and passively mode-locked regimes of a $Nd:YVO_4$ laser," Opt. Express **17**, 5373 (2009).

[8] L. Papula, in *Mathematik fuer Ingenieure und Naturwissenschaftler* Vieweg, Braunschweig, Vol. 2, pp. 158 (2000).

[9] V. G. Savitski 2009.

[10] A. E. Siegman, in *Lasers*, edited by A. Kelly University Science Books, Sausalito, CA, pp. 492 (1986).

[11] O. Svelto, in *Principles of Lasers*, edited by D. C. Hanna Springer, New York, pp. 280 (1998).

[12] ISP Optics, http://www.ispoptics.com (2010).

[13] O. Svelto, in *Principles of Lasers*, edited by D. C. Hanna Springer, New York, pp. 249 (1998).

[14] L. Papula, in *Mathematik fuer Inginieure und Naturwissenschaftler* Vieweg, Braunschweig, Vol. 2, pp. 563 (2000).

[15] I. T. Sorokina, "Cr^{2+}-doped II-VI materials for lasers and nonlinear optics," Opt. Mater. **26**, 395 (2004).

Chapter Seven

Conclusion and future work

7.1 Continuous wave SDL-pumped chalcogenide laser

The (AlGaIn)(AsSb)-based semiconductor disk laser has been demonstrated to be a novel pump source for Cr^{2+}:chalcogenide lasers. With two chips optimised for emission at 1.9 and 2.0 µm, the quantum well structure allowed precise control of the peak emission wavelength which could be utilised to pump the Cr^{2+}:ZnSe laser in either its absorption wing or closer to the absorption peak (1.78 µm). With a cw output power of up to ~6 W from the 2 µm SDL, the Cr^{2+}:ZnSe delivered up to 1.8 W of output power, showing that this pump source is able to provide multi-Watt level laser operation in the mid-IR. While similar and higher output powers have been reported from Cr^{2+}:chalcogenide lasers using other pump sources [1], the SDL format has various advantages that make it a more favourable pump source for applications where high power is not important: The short carrier lifetime in a semiconductor makes the SDL insensitive to feedback. This eliminates the need for optical isolation, a requirement for the conventional pump sources discussed elsewhere [2-4] and for the Tm^{3+}:$YAlO_3$ laser discussed in this work. The external cavity of the SDLs also offers added flexibility (typical of bulk solid-state lasers) because intracavity elements can be added for, e.g., wavelength tuning and polarisation definition.

For applications that require higher pump powers than the ones achieved in this work, multiple SDL chips within a single cavity can be used to distribute the pump-induced heating between multiple gain elements [5]. This approach was investigated in this work using two semiconductor chips, but more engineered solution such as the one demonstrated by Coherent Inc. at a wavelength of 1µm could also be envisaged at 2µm [5]. In this way, the output power of these systems could be scaled to tens of Watts of output powers, making the SDL a contender as pump source for high power embodiments of Cr^{2+}:II-VI lasers. It should be noted, however, that the use of multiple gain elements significantly increases the complexity of these systems. As an alternative, therefore, multiple pump and resonator spots on the same chip could be used. If this is to be equivalent to using multiple chips, the separation of the individual spots on the chip needs to be large enough to prevent thermal interaction between adjacent spots (see Figure 7.1). This approach would reduce the number of intracavity SDL chips, but each gain region would still require an individual pump source and focussing lenses. To simplify this further, the use of diode laser bars could be envisaged. Rather than pumping individual spots, a diode laser bar could be used to illuminate a stripe on the chip. The available pumped region could then be utilised using a resonator geometry that consists of multiple reflections on the chip (see Figure 7.2).

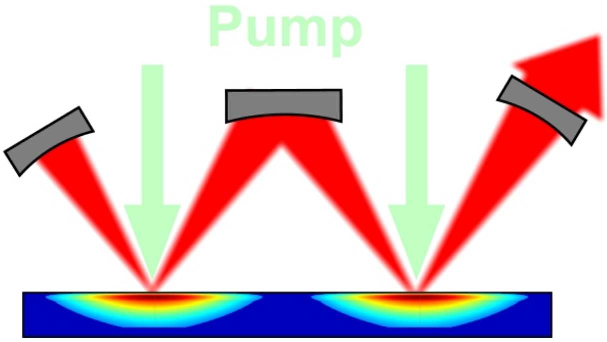

Figure 7.1 Pumping scheme using multiple pump and resonator waists on the same chip without the pump induced heating interfering between individual spots.

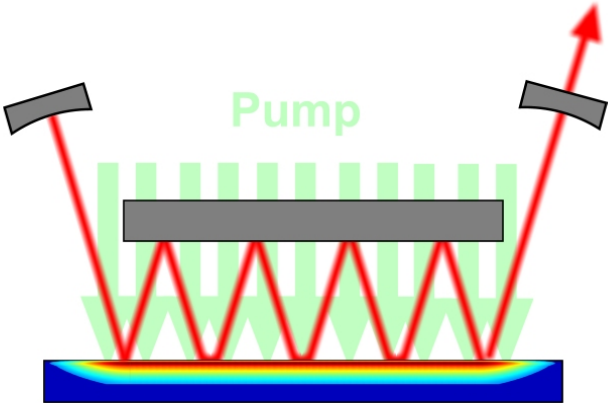

Figure 7.2 Pumping scheme using a diode laser bar and multiple resonator reflections along the pumped area.

In this way, the output power of the SDL could potentially be significantly enhanced while still offering a compact format.

Power scaling, however, is not the only areas where there is scope for future developments. In addition to the use of (AlGaIn)(AsSb)-based SDLs emitting around 2 µm to pump chromium-chalcogenide lasers, advances in this field have led to emission at 2.8 μm [6]. This wavelength is interesting for pumping iron-doped chalcogenides such as Fe^{2+}:ZnSe [7]. The absorption peak is at 3.1 μm but the absorption coefficient does not reduce significantly at 2.8 μm [8]. However, Fe^{2+}:ZnSe is not as developed as its chromium-doped counterparts and suffers from strong lifetime quenching. Continuous wave operation at room temperature is therefore difficult and typically strong cooling of the crystal is required, making the system significantly more complex [9]. To counteract some of the detrimental effects such as loss and crystal quality, intracavity pumped schemes could be envisaged [10]. A schematic of this approach can be seen in Figure 7.3.

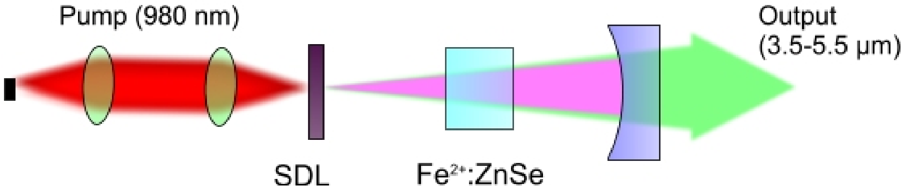

Figure 7.3 Schematic of an intracavity-pumped Fe^{2+}:ZnSe laser using an SDL as pump source.

For intracavity pumping arrangements, the Fe^{2+}:ZnSe crystal would not be pumped at its absorption peak but in the wings of the absorption. Indeed, an absorption of <10 % per round trip would be required as otherwise the absorption (which the SDL would see as intracavity losses) would exceed the available gain of the SDL and, as a consequence, prevent oscillation of the SDL. The intracavity approach offers several advantages. It provides a very high power optical field which would favour the use of lightly-doped or short crystals. While the lightly-doped crystals would permit better thermal management, a shorter crystal would benefit from reduced intrinsic and parasitic losses. Intracavity-pumping would also provide a uniform longitudinal pump profile which would prevent strong local heating of the crystal as is typically encountered in end-pumped geometries. In addition, the requirement for lower absorption would enable the use of a wider range of pump wavelengths, which would be beneficial in the case of SDL pumping as the available power from the GaSb-based systems strongly decreases towards longer wavelengths around 3 μm.

While the lack of available pump sources in the mid-IR make the SDL a valuable pump source for chromium-chalcogenide laser, SDL pumping could also be extended into other wavelength bands. While in the near infrared between 800-980 nm a variety of diode lasers are available, SDL pumping of rare-earth materials such as ytterbium, neodymium and erbium could be advantageous if complex pumping geometries are required that would benefit from a high brightness pump source. This technology therefore offers the potential for a wide range of applications and offers the laser engineer more flexibility in designing application-focused laser systems.

7.2 Pulsed SDL-pumped chalcogenide laser

In the pulsed-pumped domain, the SDL format has shown interesting properties such as the intra-pulse wavelength shift associated with the heating of the device [11]. While this is not an advantage for pumping Cr^{2+}:ZnSe lasers, it is of interest for spectroscopic applications. Here, the intrinsic chirp of the pulsed-pumped SDL could be used to scan a wavelength region, e.g. for the detection of a specific trace gas. Rather than analysing the signal in the spectral domain, the required information could be extracted in the temporal domain, which would only require a photodetector rather than an expensive spectrum analyser. This functionality could further be extended if one considers pulsed-pumping of OPOs. Using SDLs for pumping OPOs has already been demonstrated in cw operation [12]. Pulsed-pumping would potentially build on this by reducing overall power consumption for the same on-time powers, but it would also translate and increase the chirp of the pulsed-pumped SDL, resulting in a larger scan within a single pulse.

Pulsed-pumping also allows the scaling of on-time output powers to levels significantly higher than those obtained for cw operation. While this can not be utilised to scale the average output power of Cr^{2+}:chalcogenide lasers, it enables low-cost embodiments of these devices in a compact format. The output energies of the gain-switched Cr^{2+}:ZnSe system reported in chapter 6 are relatively low but could significantly be increased if the pulse duration and/or on-time power of the pulsed-pumped SDL would be increased. For this, multiple approaches could be investigated. In the same way as for cw operation, multiple chips within the same SDL resonator could be used and pumped using polarisation combined pulsed diode lasers to increase the output power of the laser. As no indication of strong thermal rollover was present in the experimental investigations in chapter 4, however, power scaling approaches in a single pump spot could be considered first. For this, multiple sets of polarisation combined pulsed diode lasers could focus onto the same spot, thereby potentially multiplying the on-time output power of these systems.

Ultimately, this approach will be limited by the complexity of the pulsed-diode laser arrangements or the thermal roll-over of the laser.

To reduce complexity, one could use multiple pulsed diode lasers and arrange them in an array – each of them collimated in the fast axis individually and focused using a single lens (see Figure 7.4). In this way, the polarising beam cubes could be removed, resulting in a more compact pump arrangement.

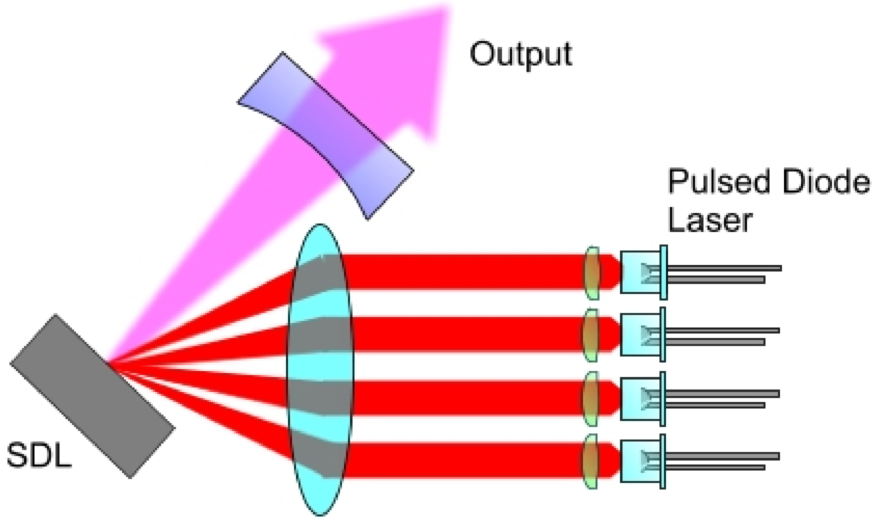

Figure 7.4 Pulsed diode laser array where each individual diode is collected and all are focused by a single lens onto the SDL chip.

Multiple pulsed diode lasers pumping the same spot can potentially also be advantageous for extending the pulse duration from the SDL. This can be achieved by multiplexing the diodes so that the individual diode laser or diode laser arrays are turn on sequentially. For pumping of Cr^{2+}:II-VI materials, the maximum pulse duration would be in the order of the fluorescence lifetime of the material (a few microseconds) as otherwise the population would not increase but fluorescence would deplete the upper laser level. It should also be noted, that the pulse duration of the SDL can not be increased indefinitely as thermal effects will eventually cause the system to roll over, limiting powers to those obtained for cw-pumped operation.

While this limits the maximum pulse durations obtainable from pulsed-pumped SDLs, the maximum on-time power could be increased significantly as long as the pulse duration is limited to durations where no significant heat diffusion occurs. This would result in a mode of operation that is akin towards disk arrangements which would allow the scaling of the output power by increasing pump and resonator spot sizes, which is not something that can typically be achieved with SDLs [13].

Another approach to higher powers would be the use of commercially available pulsed diode laser arrays such as the SPL AH90_3 available from OSRAM. These are 12 channel laser arrays with individual on-time output powers of up to 75 W with a total of 900 W on-time power. These could be used in as illustrated in fig. 7.2: a stripe of the SDL is pumped and multiple reflections of the resonator mode on the chip extract the available energy.

With these short pulse, high-power pulsed-pumped SDLs one could also envisage gain-switched microchip embodiments of Cr^{2+}:ZnSe. While the energy of the output pulses would be limited by the population that could build up during the resonator build-up time (if the build-up time is shorter than the laser level lifetime), high peak powers with short pulse durations in the order of a few nanoseconds could be achieved.

Pulse-pumping could also be used in the context of Fe^{2+}:ZnSe. While the cw operation of this material is more challenging than in Cr^{2+}:ZnSe, pulsed-pumping would be advantageous as the short pulse would permit the extraction of the stored energy before spontaneous emission and non-radiative decay would deplete the upper laser level. This approach could also be combined with the intracavity pumping scheme proposed in the previous section and would allow significant advances towards useful laser sources based on Fe^{2+}:ZnSe.

Overall, the SDL has shown great promise as a pump source for mid-infrared solid-state lasers. With room for improvements of the systems and the extension into different wavelength bands, this technology can enhance the performance of new as well as established laser systems.

References

[1] S. Mirov, V. Fedorov, I. Moskalev, D. Martyshkin, and C. Kim, "Progress in Cr^{2+} and Fe^{2+} doped mid-IR laser materials," Laser & Photonics Review, NA (2009).

[2] I. T. Sorokina, E. Sorokin, A. Di Lieto, M. Tonelli, R. H. Page, and K. I. Schaffers, "Efficient broadly tunable continuous-wave Cr^{2+}: ZnSe laser," J. Opt. Soc. Am. B-Opt. Phys. **18**, 926 (2001).

[3] K. L. Schepler, R. D. Peterson, P. A. Berry, and J. B. McKay, "Thermal effects in Cr^{2+}:ZnSe thin disk lasers," IEEE J. Sel. Top. Quantum Electron. **11**, 713 (2005).

[4] I. S. Moskalev, V. V. Fedorov, and S. B. Mirov, "10 Watt, pure continuous-wave, polycrystalline Cr^{2+}:ZnS laser," Opt. Express **17**, 2048 (2009).

[5] J. Chilla, S. Butterworth, A. Zeitschel, J. Charles, A. Caprara, M. Reed, and L. Spinelli, "High power optically pumped semiconductor lasers," Solid State Lasers Xiii: Technology and Devices **5332**, 143 (2004).

[6] N. Hempler, J. M. Hopkins, and M. Rattunde, "Tuning and brightness optimisation of high-performance GaSb-based semiconductor disk lasers from 1.86 to 2.80 µm," presented at the European Conference on Lasers and Electro-Optics, Munich, (2009).

[7] U. Demirbas, A. Sennaroglu, and K. Adnan, "Preparation and Spectroscopic Investigation of Diffusion-Doped Fe^{2+}:ZnSe and Cr^{2+}:ZnSe," presented at the Advanced Solid-State Photonics, Washington, D.C, (2005).

[8] V. V. Fedorov, S. B. Mirov, A. Gallian, D. V. Badikov, M. P. Frolov, Y. V. Korostelin, V. I. Kozlovsky, A. I. Landman, Y. P. Podmar'kov, V. A. Akimov, and A. A. Voronov, "3.77-5.05 µm tunable solid-state lasers based on Fe^{2+}-doped ZnSe crystals operating at low and room temperatures," IEEE J. Quantum Eelect. **42**, 907 (2006).

[9] V. I. Kozlovsky, V. A. Akimov, M. P. Frolov, V. Korostelin Yu, A. I. Landman, V. P. Martovitsky, V. V. Mislavskii, P. Podmar'kov Yu, K. Skasyrsky Ya, and A. A. Voronov, "Room-temperature tunable mid-infrared lasers on transition-metal doped II-VI compound crystals grown from vapor phase," physica status solidi (b) **247**, 1553.

[10] D. W. Anthon, J. H. Clark, L Johnson, and T. J. Pier, USA (1991).

[11] N. Hempler, J. M. Hopkins, A. J. Kemp, N. Schulz, M. Rattunde, J. Wagner, M. D. Dawson, and D. Burns, "Pulsed pumping of semiconductor disk lasers," Opt. Express **15**, 3247 (2007).

[12] D. J. Stothard, J. M. Hopkins, D. Burns, and M. H. Dunn, "Stable, continuous-wave, intracavity, optical parametric oscillator pumped by a semiconductor disk laser (VECSEL)," Opt. Express **17**, 10648 (2009).

[13] A. J. Kemp, J. M. Hopkins, A. J. Maclean, N. Schulz, M. Rattunde, J. Wagner, and D. Burns, "Thermal management in 2.3 µm semiconductor disk lasers: A finite element analysis," IEEE J. Quantum Eelect. **44**, 125 (2008).

List of Publications

Journal Papers:

1. N. Hempler, J.-M. Hopkins, A. J. Kemp, N. Schulz, M. Rattunde, J. Wagner, M. D. Dawson and D. Burns “Pulsed pumping of semiconductor disk lasers,“ Opt. Express, **15** (6), 3247-3256 (2007).
2. J.-M. Hopkins, N. Hempler, B. Rösener, N. Schulz, M. Rattunde, C. Manz, K. Köhler, J. Wagner, and D. Burns, “High-power, (AlGaIn)(AsSb) semiconductor disk laser at 2.0 µm,“ Opt. Letters, **33** (2), 201-203 (2008).
3. N. Hempler, J.-M. Hopkins, B. Rösener, M. Rattunde, J. Wagner, V. V. Fedorov, I. S. Moskalev, S. B. Mirov and David Burn, “Semiconductor disk laser pumped Cr^{2+}:ZnSe laser,” Opt. Express, **17** (20), 18136–1814 (2009).

Conferences proceedings:

1. J.-M. Hopkins, N. Hempler, A. J. Maclean, A. J. Kemp, M. D. Dawson, E. Riis, N. Schulz, M. Rattunde, C. Manz, K. Köhler, J. Wagner and D. Burns, “High performance, GaSb-based, optically-pumped semiconductor disk lasers (Invited),” 8th International Conference on Mid-Infrared Optoelectronics: Materials and Devices, Bad Ischl, Austria, 2007.
2. N. Hempler, J-M. Hopkins, A.J. Kemp, M.D. Dawson, D. Burns, N. Shultz, M. Rattunde, J. Wagner, “Pulsed pumping of a 2.3 µm InGaAsSb Semiconductor Disk Laser”, Presented at the Conference on Lasers and Electro-Optics (CLEO), Baltimore (2007).
3. N. Hempler, J.-M. Hopkins, B. Rösener, N. Schulz, M. Rattunde, J. Wagner, U. N. Roy, A. Burger and D. Burns,” Semiconductor Disk Laser Pumped $Cr^{2+:}$Chalcogenide Lasers” Presented at the Conference on Lasers and Electro-Optics (CLEO), Santa Clara (2008).
4. N. Hempler, J.-M. Hopkins, B. Rösener, N. Schulz, M. Rattunde, J. Wagner, and D. Burns, “5W Mid-IR Optically-pumped Semiconductor Disk Laser”, Presented at the Conference on Lasers and Electro-Optics (CLEO), Santa Clara (2008).
5. N. Hempler, J.-M. Hopkins, B. Rösener, M. Rattunde, J. Wagner, I. S. Moskalev, V. Fedorov, S. S. Mirov and D. Burns, “Semiconductor disk laser pumped

Cr^{2+}:Chalcogenide lasers”, Mid-Infrared Optoelectronics: Materials and Devices IX, Freiburg (2008).

6. N. Hempler, J.-M. Hopkins, B. Rösener, M. Rattunde, J. Wagner, I. S. Moskalev, V. Fedorov, S. S. Mirov and D. Burns, “Pulsed pumping of 1.9um and 2um semiconductor disk lasers and their use as pump sources for $Cr^{2+:}$ZnSe”, Presented at the conference for Middle Infrared Coherent Sources (MICS), Freiburg (2008).
7. M. Rattunde, B. Rösener, N. Hempler, J.-M. Hopkins, D. Burns, R. Moser, C. Manz, K. Köhler, J. Wagner, „Power scaling of GaSb-based semiconductor disk lasers for the 2.X µm wavelength range“, Presented at the conference for Middle Infrared Coherent Sources (MICS), Trouville (2009).
8. N. Hempler, J.-M. Hopkins, M. Rattunde, B. Rösener, R. Moser, C. Manz, K. Köhler, J. Wagner and D. Burns1, “Tuning and brightness optimization of high-performance GaSb-based semiconductor disk lasers from 1.86 to 2.80µm”, Presented at the Conference on Lasers and Electro-Optics Europe (e-CLEO), Munich (2009).
9. N. Hempler, J.-M. Hopkins, A. Kemp, B. Rösener, M. Rattunde, J. Wagner, D. Burns, “20W, Quasi-cw GaSb-Based Semiconductor Disk Laser”, Advanced Solid State Photonics (2010).